

Alma Mater Studiorum – Università di Bologna

DOTTORATO DI RICERCA IN

CHIMICA

Ciclo 35

Settore Concorsuale: 03/B1-FONDAMENTI DELLE SCIENZE CHIMICHE E SISTEMI INORGANICI

Settore Scientifico disciplinare: CHIM/03-CHIMICA GENERALE E INORGANICA

TITOLO TESI

STRATEGIES FOR LOWERING THE ENVIRONMENTAL IMPACT OF
DIFFERENT ELECTROCHEMICAL ENERGY STORAGE SYSTEM

Presentata da: Alessandro Brilloni

Coordinatore Dottorato

Prof. Luca Prodi

Supervisore

Prof. Francesca Soavi

Co-supervisore

Prof. Fabrizio Passarini

Esame finale anno 2023

Summary

Abstract	
Chapter 1: Introduction	1
1.1 Climate, energy landscape and prospective	1
1.2 Energy Storage Systems: need for batteries	6
1.3 Electrochemical Energy Storage Systems	11
1.3.1 Lithium-ion batteries: principle, manufacturing, sustainability	13
1.3.2 Electrical double-layer supercapacitors	16
1.3.3 Redox Flow Battery	21
Chapter 1 References	25
Chapter 2: Green Li-ion Batteries	32
2.1 Water processable binders: Pullulan and PEDOT:PSS	32
2.2 Easy recovery of wasted Li-ion cathodes	34
2.3 Pullulan and PEDOT:PSS: performance comparison	47
2.4 Chapter 2 Conclusion	60
Reference Chapter 2	62
Chapter 3: Semi-solid electrodes	65
3.1 Chapter 3 Conclusion	79
Reference Chapter 3	80
Chapter 4: Green Supercapacitors	82
4.1 Chapter 4 Conclusion	101
Reference Chapter 4	102
Chapter 5: Supercapacitor for improved RFBs performances in hybrid systems	103
5.1 High Power Vanadium Redox Flow Battery	104
5.2 Commercial Supercapacitors	110
5.3 Combining high power VRFC with Supercapacitors	113
5.4 Chapter 5 Conclusion	118
Reference Chapter 5	120
Chapter 6: Conclusion	121

7 Project, publication and contribution.....	125
7.1 National and International Projects	125
7.2 List of Publication	125
7.3 List of Contribution to Conferences: posters and oral presentations	126

Abstract

The continuous growth of global population brings an exponential increase on energy consumption, especially by those fast growing Countries like India. This phenomenon leads also to an increase of greenhouse gas emission in the atmosphere and to increasing temperature of the planet. In order to contain this sequence of events we need to put in place technologies that allow the population to grow without affecting the environment. Among the technological solutions with the greatest impact is the adoption of renewable energy production systems like photovoltaic or wind power: unfortunately, the main limit of these technologies is the natural intermittence of the energy sources that limits their applicability.

The key enabling technology for a widespread usage of clean power sources are electrochemical energy storage systems, most commonly known as batteries. Batteries will enable the storage of energy during overproduction period and the release during low production period stabilizing the power outcome, allowing the connection to the main grid and increasing the applicability of renewable energy sources.

Batteries are not only used in connection with energy production systems. They will also help reducing gas emission through the widespread diffusion of electrical vehicles and electrical mobility devices. The automotive sector is nowadays the leading industry for the adoption, use and consumption of the most famous lithium-ion battery.

Despite the high number of benefits that the widespread use of batteries will bring, starting from the reduction of CO₂ emitted in the atmosphere, it is necessary also to take care of the environmental impact of processes and materials used for the production of electrochemical storage systems. In addition, there are many different battery systems, with different chemistries and designs that require specific strategies.

Nowadays, the most part of the materials and chemicals used for battery production are toxic for humans and the environment. For this reason, with the developing mass production of battery devices, there is the risk to only shift the environmental impact of our activities into another form. Decreasing the environmental impact of batteries production becomes of fundamental importance for the transition to a low carbon society.

For this reason, this Ph.D. thesis addresses the challenging scope of lowering the environmental impact of manufacturing processes of different electrochemical energy storage systems using natural

derived or low carbon footprint materials while increasing the performances with respect to commercial devices. New designs and innovative manufacturing processes are also investigated.

Chapter 1 introduces the context of the energy transition and the different technologies investigated, reporting the reasons for adoption and application of diverse electrochemical storage systems.

New materials and production strategies for green Lithium-ion batteries are investigated in Chapter 2. The manufacturing process is reconsidered in the light of the use of green materials and easy recycling of the battery.

In Chapter 3 a new innovative design is proposed for redox-flow battery: semi solid electrodes are investigated and proposed as a technology that eliminates the use of the binder and lower the manufacturing costs of the battery.

Similar strategies and materials exploited in Chapter 2 are also tested for the production of green supercapacitors in Chapter 4.

Finally, in the Chapter 5, a new explorative way of combining different electrochemical storage systems, namely Supercapacitors and Redox-Flow Batteries, in order to exploit the advantages of both systems in combination, is proposed.

Overall, the activities carried out during my Ph.D. project are extremely challenging because they cover a high number of different electrochemical storage systems involving a wide range of electrochemical processes from capacitive to faradic. New materials, different production processes and new battery design, all in view of sustainability and low environmental impact, increased the innovative and challenging aspects of this work.

Therefore, the main novelty of my work is i) the use of a low carbon footprint materials that allow the production of lithium-ion batteries and supercapacitors with a reduced environmental impact while maintaining similar performances compared to commercial devices, and ii) the introduction of semi-solid slurries, a new component for designing innovative flowable systems that can increase overall performances and material exploitation.

The interdisciplinarity of my work was strengthened by the opportunity to collaborate with different research groups of the University of Bologna, starting from the Department of Chemistry “Giacomo Ciamician” (Polymer science and biomaterials Lab – Prof. ML. Focarete and Prof. C.Gualandi), the department of Industrial Chemistry “Toso Montanari (Analytical Chemistry Lab – Prof. Marco Giorgetti) and with the University of Landshut (Technologiezentrum Energie -TZE- Prof K.H. Pettinger).

These extremely fruitful collaborations were carried out under different national and international projects, namely ISARP 2018-2020/Italy-South Africa joint Research Programme 2018-2020 (Italian Ministers of Foreign Affairs and the Environment and NRF of South Africa, grant No. 113132), Fondazione CARISBO/Progetto ricerca n° 354, Piano Triennale di Realizzazione 2019-2021/Progetto ricerca n° 354 and the HyFlow project (funding from the European Union's Horizon 2020 research and innovation programme under grant agreement No 963550) and “Piano Triennale di Realizzazione 2019–2021, Accordo di Programma Ministero dello Sviluppo Economico” - ENEA (PTR MISE-ENEA 2019-2021).

The outcomes of my Ph.D. work have contributed to 6 papers published on peer-review international scientific Journals and 12 oral and poster presentations at Conferences.

Chapter 1: Introduction

1.1 Climate, energy landscape and prospective

Today the destructive effects of climate change affect every part of the world, from glacier melting at the poles and on mountain chains, to increased desertification in Africa and more frequent flooding events in urbanized areas. Scientists are confident that the results of the climate change will turn out worse every year if humans will continue warming up the planet with greenhouse gas emission at current rate. This condition represents an urgent and potential irreversible threat to human societies and the planet as it is now. To address this issue, the majority of the countries in the world adopted, during the 21st Conference of the Parties (COP21) in December 2015, the Paris Agreement. Along with the help of the scientific community, the countries subscribed the intention of pursuing all efforts necessary to limit global temperature rise to +1.5°C with respect to the pre-industrial level [1].

Nowadays, the link between the human activities and the rise of the temperature is clear: human emission of greenhouse gases, especially of carbon dioxide (CO₂), are the primary cause of the temperature increase [2]. To have a clearer overview, in Figure 1.1 the trend of the average temperature of the Earth between 1850 and 2020 is shown. It is clear that over the past few decades,

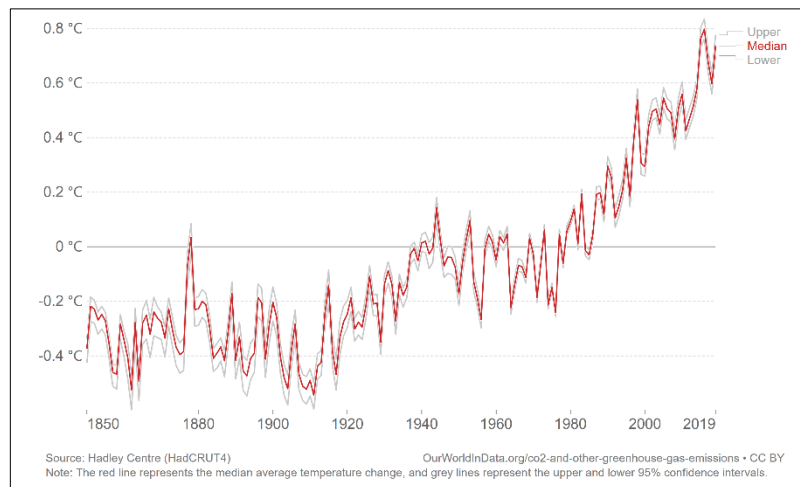


Figure 1.1: Average temperature anomaly: Global average land-sea temperature anomaly relative to the 1961-1990 average temperature

global temperature has risen rapidly to up 0.7°C higher than the baseline. Overall, from the 1850, the era of industrialization, the temperature has already rise on an average of 1.1°C. A rise of such small amount of temperature might seems small if taken in other contest, but it is true that 1°C of rapid warming can, and is having, significant impact on climate and natural systems. It has also to be considered that the average temperature is given as the combined temperature of both sea and land surface: it's important to note that land areas change temperature in both directions, warming and cooling, much more than oceanic areas. Therefore, it results that the land increased by c.a. 1.56°C and the sea by 0.76°C in 2020 [3]. Given that the northern hemisphere has more land mass, it resulted

that the rise in average temperature at north of the equator has been higher than in the south. At very high latitudes, especially near the Poles, average temperature has risen upwards of 3°C, and in some cases exceeding 5°C. These are also the regions that could experience the largest impacts such as sea ice, permafrost, and glacial melt causing sea level rise and disturbing the delicate balance between warm, cold, and salty water streams. This difference in temperature between the hemisphere also affects the geographical distributions of water availability over continents, changing profoundly both precipitation and evaporation events. [4,5].

In order to slow down the rising temperature and preserve the climate that allowed the world population to grow, it is urgent to lower the emission of CO₂ and other greenhouse gases in the atmosphere in order to restore the energy balance of the Earth.

The energy balance is maintained between the net incoming shortwave solar radiation (downward) and the outgoing longwave terrestrial radiation (upward) at the top of the atmosphere. Assuming that the Earth-atmosphere system radiates as a blackbody, according to the Stefan–Boltzmann law of blackbody radiation, the Earth surface temperature can be estimated as –18.7°C. This temperature is different from the global mean temperature of Earth’s surface of +14.5°C. This difference happens thanks to the atmosphere so-called *greenhouse effect*, that increase the temperature by as much as 33°C. Greenhouse gases such as, CO₂, nitrous oxides (N₂O), methane (CH₄), chlorofluorocarbons (CFCs) and water vapor (H₂O) act absorbing substantially the upward flux of longwave radiation emitted by the Earth’s surface before it reaches the top of the atmosphere, helping to maintain the warm climate at Earth’s surface. If a greenhouse gas increases its concentration in the atmosphere, the infrared opacity of air increases, thereby enhancing the capacity of absorbing the upward longwave radiation in the atmosphere. This effect increases the overall temperature of the coupled surface-atmosphere system and it is the so-called “*Global Warming*”. An important factor that affects the magnitude of global warming is the “positive feedback process” that involves water vapor. Water vapor strongly absorbs and emits most of the spectral range of terrestrial longwave upward radiation. Along with the increase of water and land temperature, the evaporation and, therefore, the amount of H₂O in the atmosphere increases consequently. This process contributes to the “*water vapor positive feedback*” effect and label H₂O as a major contributor for the powerful greenhouse effect of the atmosphere, although it is not to be considered as greenhouse gas but as a consequence of the global warming [5].

Data from the “World resource institute on Climate watch 2020” reports for the year 2016 that CO₂ was the largest contributor of global greenhouse gas emission, accounting for around three-quarters

(74.4%) of total emissions, while methane contributed for 17.3%; nitrous oxide 6.2%; and other gas emissions (HFCs, CFCs, SF₆) for 2.1% [6]. These data must be read also considering the “*Global warming potential of greenhouse gas*”, the GWP₁₀₀¹: for example, methane has a GWP 28 time higher than CO₂, while N₂O is 265-fold higher, which means that per unit of gas emitted, they are much more dangerous [7]. Considering all the contributions, the major cause of global warming has therefore to be attributed mainly to the emission in the atmosphere of CO₂ and other greenhouse gasses. In Figure 1.2a the global average concentrations of CO₂ in the atmosphere over the past 800,000 years are shown.

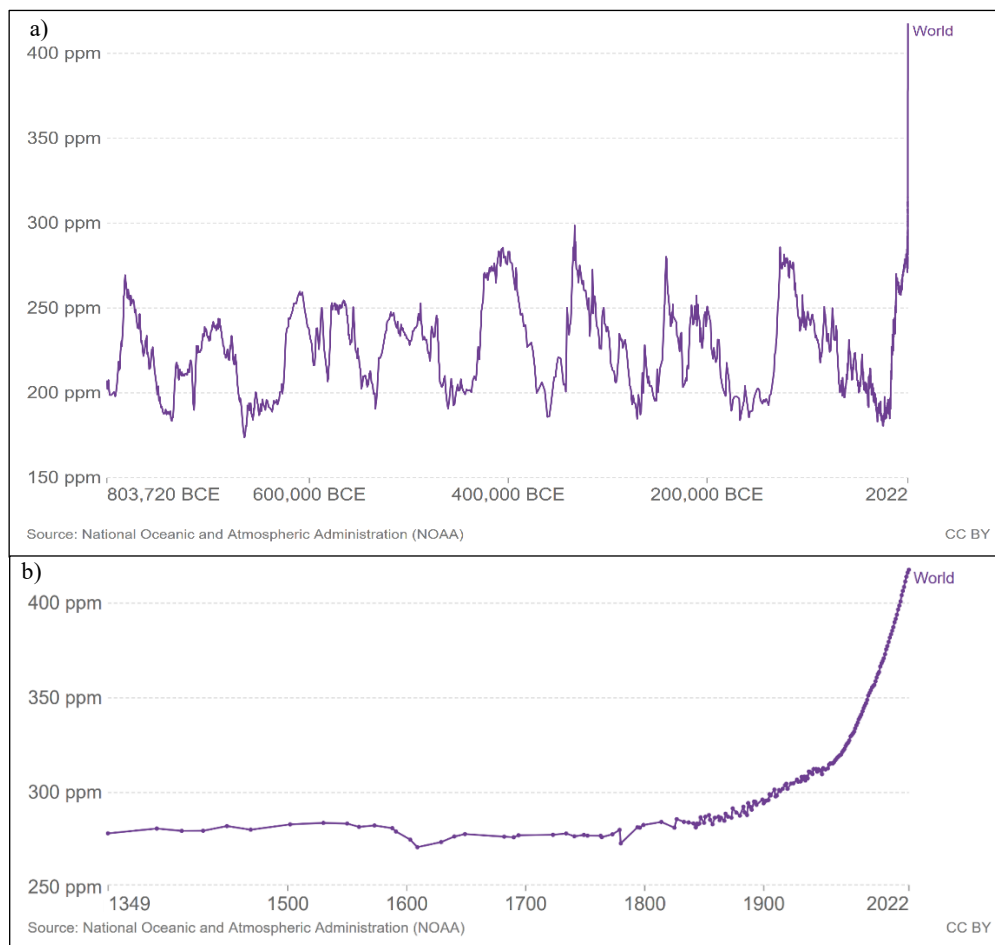


Figure 1.2 Global average concentrations of CO₂ in the atmosphere over the past a) 800,000 years and over the last centuries b) [9].

In this period consistent fluctuations in CO₂ concentrations are evident and can be attributed to the onset of ice ages (low CO₂) and interglacial (high CO₂), caused by changes in the Earth’s orbit around the sun, called Milankovitch cycles, but the concentration of CO₂ never exceeded 300 parts per million (ppm) [8]. This trend changed in more recent year, with the industrial revolution and the

¹ GWP measures the relative warming impact of one unit mass of a greenhouse gas relative to carbon dioxide. A GWP₁₀₀ value of 28 therefore means one ton of methane has 28 times the warming impact of one ton of carbon dioxide over a 100-year timescale.

increase of human emissions of CO₂ from burning fossil fuels, as shown in Figure 1.2b. Only in the recent past few decades, the concentration has raised from around 270ppm over 400ppm in a very short time, giving also less time to the ecosystem to adapt.

The data on the CO₂ concentration in the atmosphere (Figure 1.2) has to be compared with Figure 1.3 that show the cumulated annual CO₂ emissions from fossil fuels and by world region per year, starting from the industrial revolution. The correspondence between the two curves reveals the direct connection between the concentration of greenhouse gases and human activities mainly based on the burning of fossil fuels. In a continuous growing trend, only in the 2020 were emitted in the atmosphere a total amount of around 34 billion tons of CO₂. In the 20th century, more than 90% of emission were produced in Europe and USA, but in the recent years this trend has changed, and the most significant share of emission is produced by developing countries like China, which produced 10.68 billion tons of CO₂ in 2020.

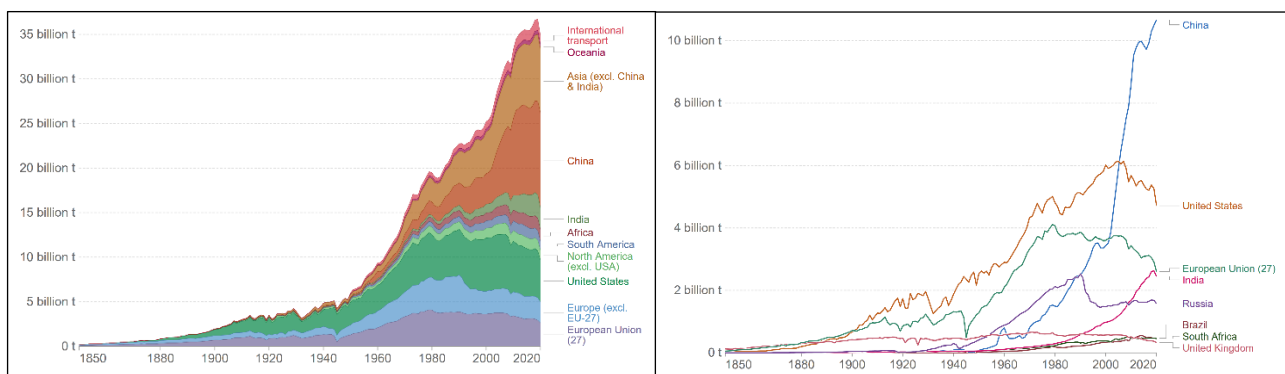


Figure 1.3 Cumulated annual CO₂ emissions only from fossil fuels and non-cumulated by world region per year, in Btons[10].

Taking into account the global emission of CO₂, not only those related to fossil fuels, Asia region is the largest emitter, accounting for 53% of global emissions, being also home to 60% of the world's population. China is, by a significant margin, Asia's and the world's largest emitter. This rapid rise in emissions has only occurred in very recent decades along with the massive improvements in living standards since 1950. North America is the second largest regional emitter with a share of 18% of global emissions (USA 15%), followed by Europe with 17%². Africa and South America are both small emitters, accounting for 3-4% of global emissions each. The world in 2019 has emitted 50 billion of cumulated CO₂eq emission³. CO₂eq emission are originated in different amount by different sector⁴: 73.2% are to be accounted for Energy (electricity, heat and transport), 18.4% to agriculture,

² In this data the 28 countries of the European Union are grouped together since they typically negotiate and set targets as a collective body.

³ Carbon dioxide-equivalents sum all of the warming impacts of the different greenhouse gases together in order to give a single measure of total greenhouse gas emissions.

⁴ Percentages are calculated on the values of equivalent carbon dioxide CO₂eq emission per sector.

forestry and land use, 5.2% to direct industrial processes and 3.2% to waste and waste management. The sector that produces the highest share of emission is the energy: 16.2% for transportation, 24.2% for energy used in industrial processes, 17.5% energy used in building, 5.8% comes from fugitive emission from energy production and last 10% from other smaller activities related to energy production.

On the basis of these data and many more, the Intergovernmental Panel on Climate Change (IPCC), supported by the scientific community with more than 6000 peer-reviewed publications, presented the “*Special Report on Global Warming*” in 2019 [1]. The report highlights how important is limiting the rise of medium temperature to +1.5°C and outlines possible scenarios of warming temperature based on the prediction of climate policies application, shown in Figure 1.4.

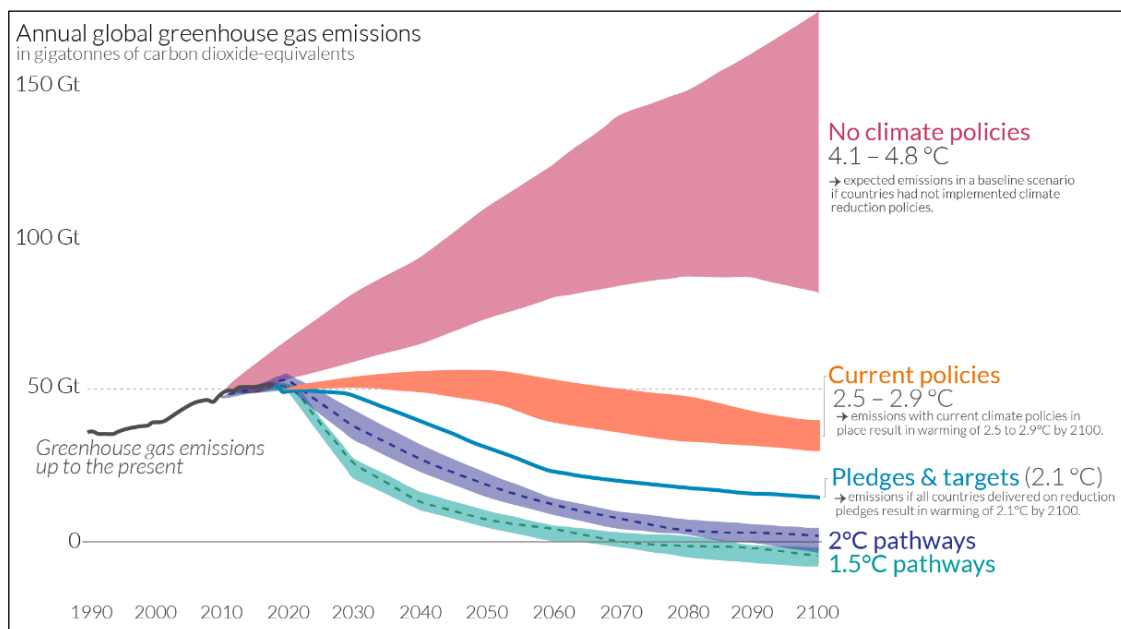


Figure 1.4: Global greenhouse gas emission and warming scenarios [11]

The IPCC report, and the scenarios described in Figure 1.4, also shows that recent trends in emissions and the level of international ambition indicated by nationally determined contributions within the Paris Agreement, will not be sufficient to reduce to the target of 1.5°C the temperature (Pledges & Targets blue line). To reach the 1.5°C pathway the world needs to be decarbonized at least six times faster than the actual rate. The transition towards climate neutrality by 2100 gives to the energy sector a central role, as it is today responsible for around 73% of the global greenhouse gas emissions.

In order to achieve these goals, research and innovation are critical for delivering the solutions and system transformations required. The key to decarbonizing the world’s production systems and activities is a massive electrification powered by renewable energy sources, electric mobility, smart buildings, and smart cities. Use of solar, wind, hydropower and other low-carbon technologies will

pave the way to the shift to a green economy. Therefore, the share of power production from renewable energy sources (RES) must be drastically increased along with the efficiency of the whole renewable energy value chain integrating sustainability and circularity throughout it. In parallel, it is mandatory to develop and demonstrate novel and disruptive renewable energy technologies and energy storage solutions. Carbon capture and storage (CCS) technology will be needed then to tackle remaining emissions. In all scenarios shown in Figure 1.4, renewables are projected to lead the power generation mix, reaching 80-90% in 2050. In the “Pledge and Target” scenario, RES share is expected to double in the next 15 years, from 29% to 60%. Most of the growth in RES is expected to come from solar and onshore wind, due to declining costs, and they are projected to make up 43% and 26% of generation respectively in 2050 [12].

The downside that energy from renewable energy sources brings is their natural intermittency: wind and sun do not allow a constant energy production and this condition negatively affects the energy grid and energy production if RES are consistently implemented. In order to mitigate this effect and allow a strong implementation of RES into the grid, the contemporary deployment of flexible solutions for power generation and smart monitoring of the grid is required, but most of all, the implementation of energy storage systems (ESS) is of fundamental importance. ESS will play a key role for the penetration of RES into the grid system thanks to their ability to store energy when is overproduced and provide energy only when is needed: this feature strongly mitigates the intermittency of power production from RES, stabilizing the power grid making it more efficient. Many ESS are available on the market, with high efficiency values and different impacts on the grid, and they will be shortly presented in the next section.

1.2 Energy Storage Systems: need for batteries

The power grid needs to be kept in balance between the incoming and the outgoing power flux. ESSs can shift the higher peak load to off-peak hours in order to level the generation requirement, allowing generators to run more efficiently at a stable power level, potentially decreasing the average cost of electricity. Additionally, increased energy storage capacity can defer or avoid generation capacity increases, decrease transmission congestion (and thereby transmission losses), therefore improving the reliability and dynamic stability of the power grid facilitating the connection of RES to the electric grid. A high number of different types of energy storage options are available for use

in the energy sector and more are emerging as the technology becomes a key component in the energy systems of the future. The different types of energy storage systems can be grouped into five technology categories: pumped hydro, mechanical, thermal, electrical, chemical, electrochemical.

Each technology has advantages and disadvantages e.g. related to energy density, capacity, price and potential for scale-up. This is shown in Figure 1.5 with discharge time as a function of system size [13]. The interaction of electricity storage with generation, transmission, distribution and consumption is of extreme importance. This interaction may occur in two levels. First, storage may be deployed together with power generation projects (especially based on renewable energy, high power, long discharge time) or at the end-user level (especially when combined with self-production of renewable electricity, low power and short discharge time). Along with this, discharge/response time of the energy source is of fundamental importance because it determines at what level of the grid the source can be connected and the type of intervention that can operate [14]. Electrochemical and electrical energy storage e.g. batteries and supercapacitors, respectively, cover the mid-time range, minutes to hours and allow scale-up to MW-size. Potential mechanical energy as pumped-hydro and compressed air energy storage may reach GW size (Figure 1.5).

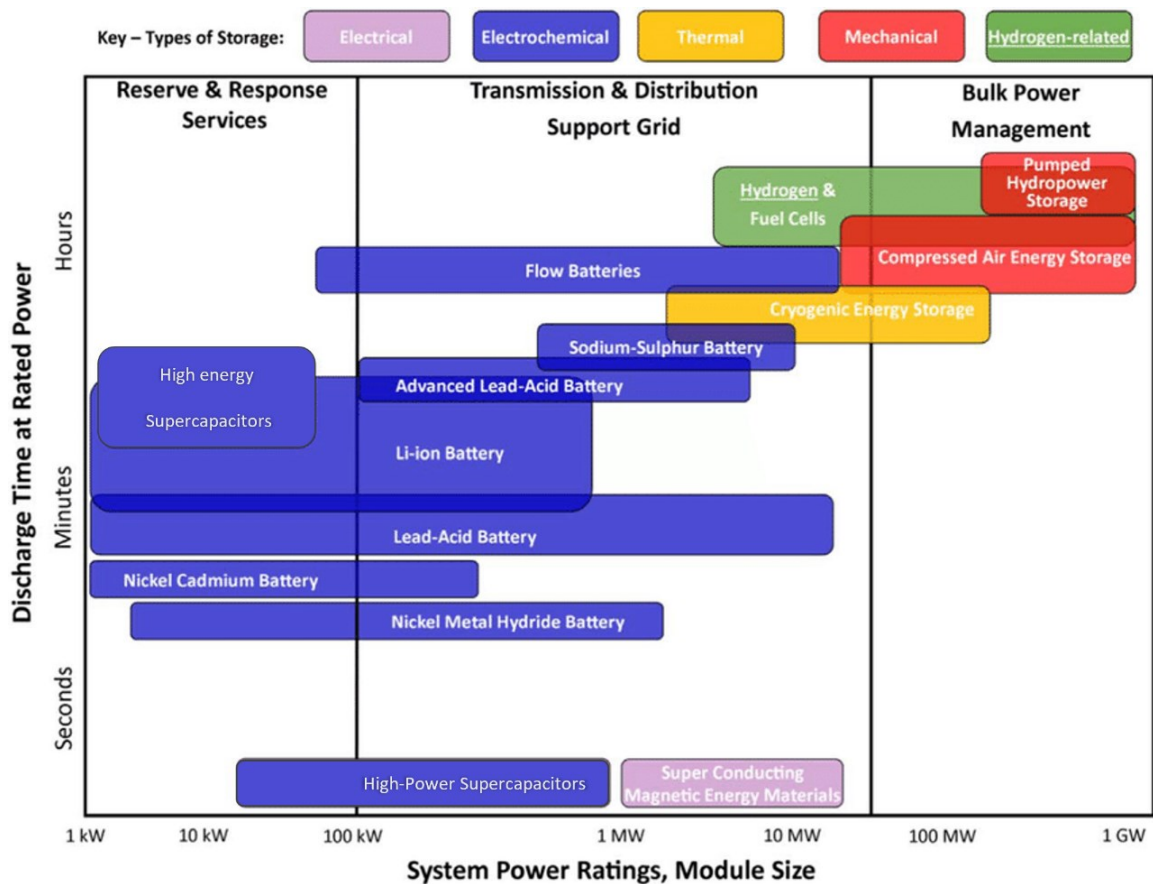


Figure 1.5 Comparison of key-type energy storage technologies in sense of storage capacity and discharge power duration (modified from [13])

Pumped Hydro Energy Storage (PHES) systems are based on large water reservoirs. Such systems require water cycling between two reservoirs at different levels with the energy stored in the water in the upper reservoir, which is released when the water is released to the lower reservoir. The technology has been widely implemented over much of the past century to become the most common form of utility-scale storage globally: PHES systems cover nearly 90% of the world's electric storage capacity [14]. Its simplicity of design, relatively low cost, and similarity in operation to hydroelectric power has made it the industry standard for storage for a century. The round-trip efficiency of this process depends on pumping system, motor, turbine and generator efficiencies as well as evaporation rates and it is assessed between 70% and 85%. The storage capacity depends on the size of the reservoirs, while the power depends on the flow and height of the water. However, this type of energy storage largely depends on the geographical conditions and the availability of suitable sites, a condition that limits its applicability. These systems also have significant impacts on the local wildlife, especially if one or both of the reservoirs needs to be constructed. Also, the fluctuating water levels can significantly disrupt the inhabitants of the reservoirs. [15].

Among the mechanical energy storage systems, worth mentioning are the Compressed Air Energy Storage (CAES) and Flywheel. In CAES systems, off-peak grid power is used to pump air underground until it reaches a high pressure. Air remains underground in a geologic formation until energy is needed, then it is released and heated, and passing through a turbine, generates power. The downside of this system is that to produce power air is mixed with fuel in a gas turbine, therefore emitting CO₂ into the atmosphere [16]. Flywheels have been in existence for centuries, however, over the past few decades they have been considered as forms of bulk energy storage. A simple form of kinetic energy storage, these systems are extremely rapid in their response time and, with recent developments in bearing design, have been able to achieve high efficiencies for short durations of storage. Their disadvantages are that they have a high rate of self-discharge due to frictional losses, and their relatively high initial costs [17].

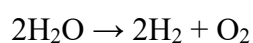
Thermal energy storage (TES) systems are specially designed to store heat energy by cooling, heating, melting, condensing, or vaporizing a substance. Depending on the operating temperature range, the materials are stored at high or low temperatures in an insulated repository. Later, the energy recovered from these materials is used for various residential and industrial applications, such as space heating or cooling, hot water production, or electricity generation, depending on the operating temperature range [15]. Despite the total cycle efficiency of TES systems is low compared to other ESS, low as 30%-50%, this technology comes with advantages such as: low daily self-discharge (~1%), good energy density (specific energy 80-250 Wh/kg), environment friendliness together with low capital

cost investment. Finally, this technology results in a good choice for large energy storage without any major hazards in many applications [15,18].

An additional electrical energy storage is the Superconducting Magnetic Energy Storage (SMES). This technology is based on the main feature of superconductive materials: when a current flux is flowing into a superconductive material, the current will continue to flow even after the voltage across it has been removed. When the superconductor coil is cooled below its superconducting critical temperature it has negligible resistance, hence current will continue to flow (even after a voltage source is disconnected). The energy is stored in the form of a magnetic field generated by the current in the superconducting coil and it can be released by discharging the coil. The coils are usually made of niobiumtitanium (NbTi) filaments which have a critical temperature of around 9 °K. Since SMES can store “current”, no conversion system is required. Therefore, the efficiencies of SMES systems are very high and they can switch from full discharge to full charge very quickly and vice versa. Due to its very high cycling capacity and high efficiency over short time periods SMES is very well suited to high power short duration applications. They are used in many voltage stability and power quality applications, for example to provide very clean power in microchip manufacture. The biggest problem with SMES is the very high capital costs of the cooling units required and the related high self-discharge rate due to the energy expenditure of cooling via cryogenic liquid, which uses either liquid helium at 4.2K or super-fluid helium at 1.8 °K [19].

In the category of chemical energy storage systems, the most important is Hydrogen Energy Storage (HES). The high energy density of hydrogen makes it one of the most promising future fuels. Hydrogen contains 33.33 kWh kg⁻¹ compared to 12 kWh kg⁻¹ of petrol and diesel [20, 21]. However, the major limit comes with the volume necessary for storing it: hydrogen has an extremely low volumetric energy content of 0.01 MJ/L at ambient conditions, while, in comparison, the volumetric energy contents of methane and gasoline are 0.04 MJ/L and 32 MJ/L, respectively [22].

Among the different H₂ production methods, steam reforming, coal gasification and electrolysis of water are majorly used today at industrial level. With the declining cost for renewable electricity, there is a growing interest in water electrolytic H₂ production. The H₂ production by water splitting uses an aqueous medium and an electrolysis cell: two electrodes are placed in the aqueous electrolyte solution and are connected to the power supply. When a sufficiently high voltage is applied between the electrodes, water is decomposed to produce H₂ on the cathode and O₂ at the anode. Regardless to the electrolyte used, the overall main reaction is always the same:



Hydrogen can then be converted back into electricity through fuel cell (FC), which is the preferable way to maximize the potential benefits of H₂: FC convert the chemical energy of H₂ into electrical energy directly so that the efficiency can be as high as 60%–80%, with only water as a byproduct [23]. Fuel cells are now commercially applied in a variety of stationary and transportation applications. The main concern for a wide application of hydrogen as a HES system is the low volumetric energy density which is a limit in the economic and efficient storage of hydrogen.

Compared to other ESS, H₂ has the advantages of being capable of higher energy storage capacity, long storing period and flexibility. For these reasons, HES systems find their best application in stationary implants where they can smooth out the energy volatility and peak shaving absorbing especially the excess of renewable energy generation. As regards the mobility sector, despite the high number of projects worldwide on hydrogen mobility [24], the main limit remains the overall efficiency, known as “wheel to wheel efficiency”, of the whole process that is limited between 25-35%, as shown in Figure 1.6 .

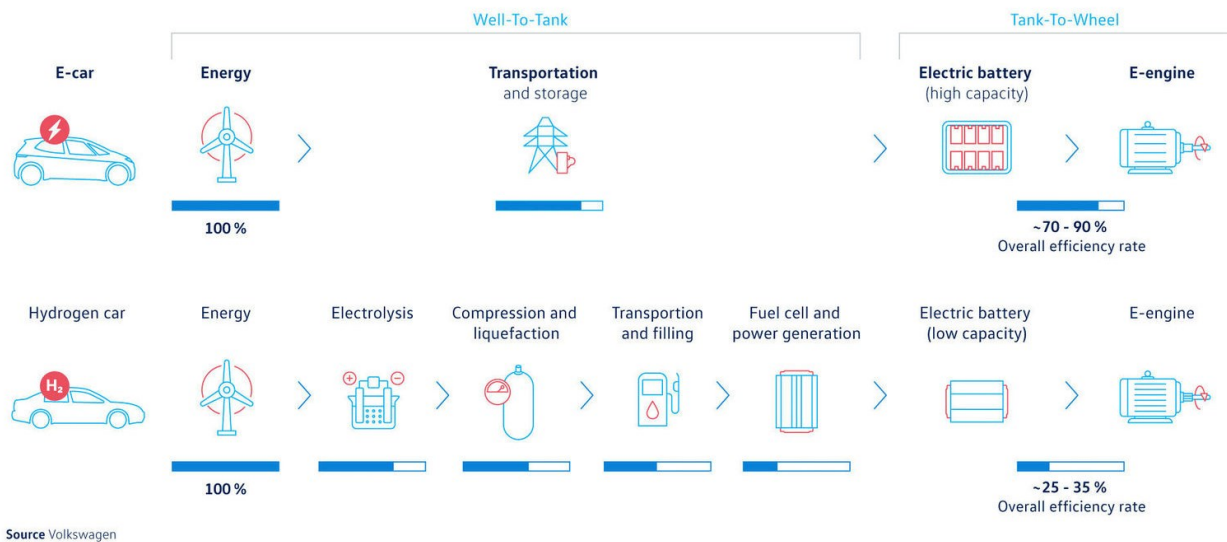


Figure 1.6 Comparison of the wheel to wheel efficiency for hydrogen and battery energy storage system; figure modified from [25]

The last category, which my thesis work focuses on, is the Electrochemical Energy Storage systems (EESS). In EESS a reversible electrochemical reaction occurs at the electrode active material: chemical energy is converted through a redox reaction into electricity and vice versa. These reactions occur at two different electrodes (positive and negative) that are electrically connected through an external circuit and physically separated by an ionically conducting medium called electrolyte.

Through the years, since Alessandro Volta first conceived the idea of the Volta pile in the early 19th century, EESS have been the subject of years of research, development, demonstration and

commercialization. In the past years the greatest example was the lead-acid battery, mainly used for starting combustion engines and for back-up powers in homes, that now gave the stage to the Lithium-ion cell technology, thanks to the exponential growth of electronic devices and the increased performances. The research on EESS brought also to the development and commercialization of Supercapacitors, which are based on a non-Faradaic process, and to the Redox Flow Battery (RFB), which stores energy in liquid electrodes. Energy density of these devices can range from 20 Wh kg⁻¹ of the RFBs to around 270 Wh kg⁻¹ of the most performing Li-ion cells and they feature different design and power/energy ratio. Compared to TES or mechanical energy storage technologies, EESS have higher energy densities that are surpassed only by chemical energy storage, and can achieve generally really high values of roundtrip efficiency, close to 95%. Because of their compact footprint and independence from geographical and geological resources they face fewer siting restrictions than, for example, PHES. Because EESS typically provide more power for a given area in case of stationary storage and are simpler in designing plant, batteries are a versatile technology that can be readily deployed at a variety of scales, from centralized large-scale facilities of MW of power, down to the level of distributed residential users, or to mobility applications with kW of power, application that push the research on more compact cell formats with higher capacity densities [26]. The different types of EESS, that are also the subject of this work, are detailed and discussed in the next section.

1.3 Electrochemical Energy Storage Systems

The category of electrochemical energy storage and conversion system is comprehensive of many different chemistries and devices that can vary from type of end application, are different in size, energy that can deliver, time of discharge, power and most of all, electrochemical mechanism that drives their functioning principle. In Figure 1.7 a comprehensive classification of these systems based on the chemistry and design is shown.

The main difference, that divides EESS into three different branches, is the working principle. Electrochemical capacitors, more commonly known as Electrical Double Layer Capacitors (EDLC) are driven by non-Faradaic processes and store energy by an electrostatic process, more precisely at the electrical double layer that is set at the electrode/electrolyte interface. On the other hand, Electrochemical Batteries are driven by Faradaic processes in which the current flows due to an

electrochemical reaction that is taking place at the two electrodes. Both the process that drives batteries and EDLC are reversible.

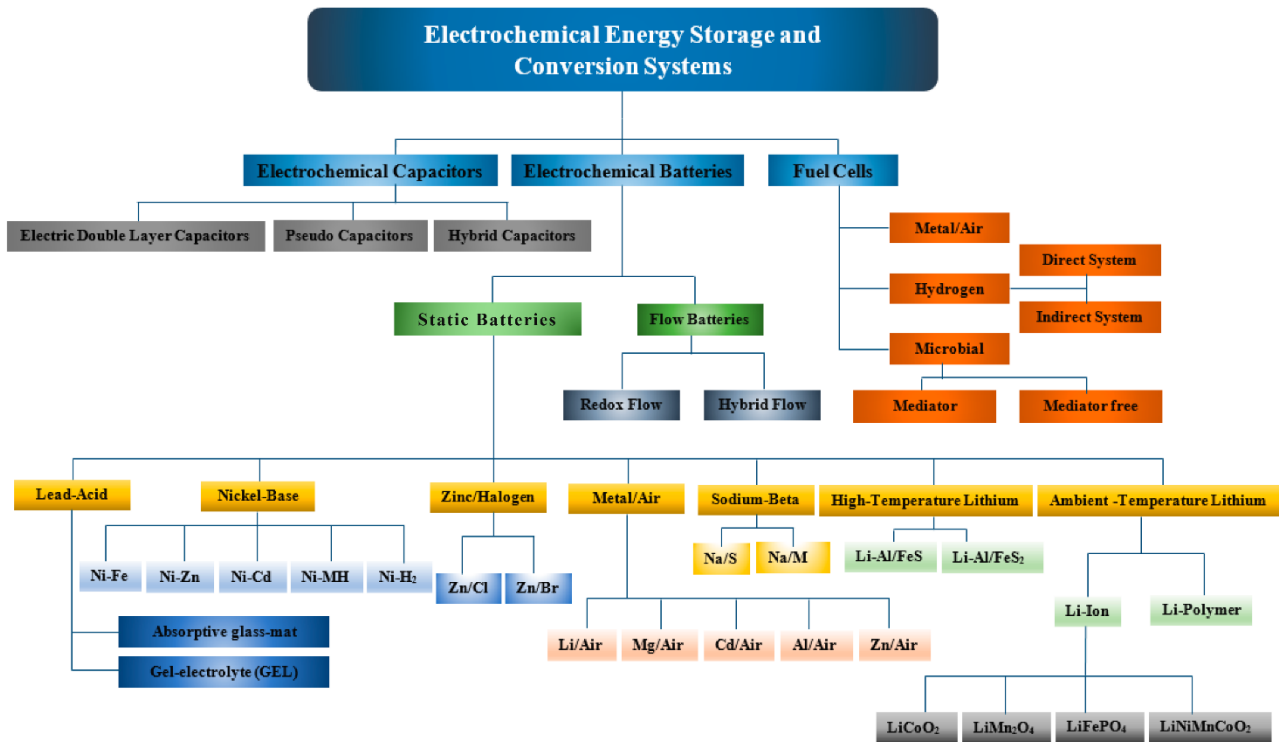


Figure 1.7 Classification of electrical energy storage system for accumulation and conversion devices. Modified from [27]

Fuel cells instead, are classified as electrochemical conversion systems. This means that, on the contrary to what happens in batteries and EDLC, the reaction at the base of these devices is not reversible. A fuel cell is a device which allows the direct conversion of chemical energy into an electrical form and can be fed continuously with reagent, so that the electrical power output can be maintained for a long time. The most diffused fuel cell is the Hydrogen Fuel Cell (HFC) [28]. HFCs produce only water as a byproduct of the chemical reaction, have high energy efficiency and longer life span with respect to batteries. The downside comes mainly with the cost of the materials for the manufacturing of the fuel cell and the infrastructure for the handling of hydrogen [28, 29].

Considering the branch of Electrochemical Batteries in Figure 1.7, the first difference that must be underlined is between Flow Batteries and Static Batteries. The redox flow battery differs due to the use of liquid electrolytes that flow inside the battery and in which active materials are dissolved. The main advantage of this technology is the possibility to decouple energy and power and the long cycle life. Regarding the static batteries branch, the most diffused technology is represented by lithium-ion batteries (LIBs). Due to its high specific capacity, high energy density and good cycling stability, LIBs have the dominant share of the rechargeable batteries market and are applied in a vast number

of application fields, from medical to automotive [30]. In the next sections we will analyze in deep the technologies of LIBs, EDLC and RFBs.

1.3.1 Lithium-ion batteries: principle, manufacturing, sustainability

LIBs utilize lithium-ion intercalation compounds at both the negative and positive electrodes as hosts for reversible lithium-ion storage. In current LIBs, graphite is used as anode and a metal oxide (or phosphate) is used as cathode. A scheme of a lithium-ion (Li-ion) cell is represented in Figure 1.8. During discharge, lithium ions diffuse internally from the negative electrode to the positive electrode through a liquid electrolyte, while electrons simultaneously move in the same direction through an external circuit, powering the external load to which the battery is connected. During charge, the process is reversed, with lithium ions

diffusing from the positive to the negative electrode, and electrons flowing through the external circuit, under voltage supplied by an external power source. State-of-the-art LIBs cells have a nominal voltage of 3.6 – 4.5 volts (V), a specific energy (or gravimetric energy density) between 100 and 270 watt-hours per kilogram (Wh/kg), and an energy density between 300 and 650 watt-hours per liter (Wh/L). They have high roundtrip energy

efficiency (85%–98%, depending on the rate of charge and discharge), low maintenance requirements, cycle life up to 5/6 thousand full charge/discharge cycles), and a low self-discharge rate. A Li-ion cell contains several key components that can be identified in Figure 1.8: a positive electrode, a negative electrode, aluminum and copper foil current collectors to which the positive and negative electrodes are respectively adhered, a liquid electrolyte, and a porous separator to electrically isolate the two electrodes from one another. The positive electrode is typically composed of lithium transition-metal oxides, such as lithium cobalt oxide (LCO), lithium manganese oxide (LMO), lithium nickel-manganese-cobalt oxide (NMC), or lithium iron phosphate (LFP), and conductive carbon powder to enhance electrical conductivity. Recently, with the increasing demand for energy density, Li-rich Mn-based materials have attracted more attention because of their high capacity of

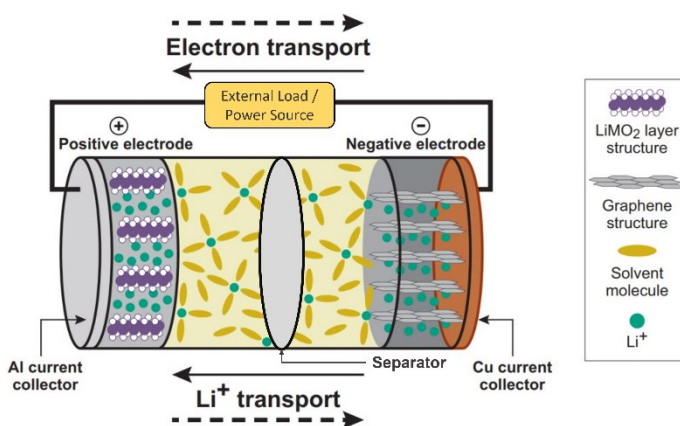


Figure 1.8 Schematic representation of a Li-ion battery. Dashed line indicates discharge directions of ions and electrons, while solid line indicates charging direction. [modified from 26]

$>250 \text{ mAh g}^{-1}$ and high voltage $>4.5 \text{ V}$ [31]. The active powders are held together by a polymeric binder that gives the solid structure and mechanical characteristic to the electrode. The negative electrode is typically a graphite-based material also mixed with conductivity enhancers and binders.

Currently, most research studies on LIBs have been focused on lowering the price of diverse active electrode materials and looking for suitable electrolytes for high cut-off voltage applications, especially the nickel-rich and/or cobalt-free cathode materials. Although the price of LIB has drop from 1000 \$/kWh in 2010 to 200 \$/kWh of today and it is forecasted to be 132 \$/kWh in 2030 [32], progress in LIB manufacturing process remained the same on the principles and not much progress has been made, despite the fact that manufacturing contributes about 25% of the cost of LIBs [33]. Currently, the manufacturing of LIBs still needs to go through slurry mixing, coating, drying, calendaring, slitting, vacuum drying, jelly roll fabrication (stacking for pouch cells and winding for cylindrical and prismatic cells), welding, packaging, electrolyte filling, formation, and aging, a multi-staged process being adopted by industry. The sequences of the manufacturing process are represented in Figure 1.9.

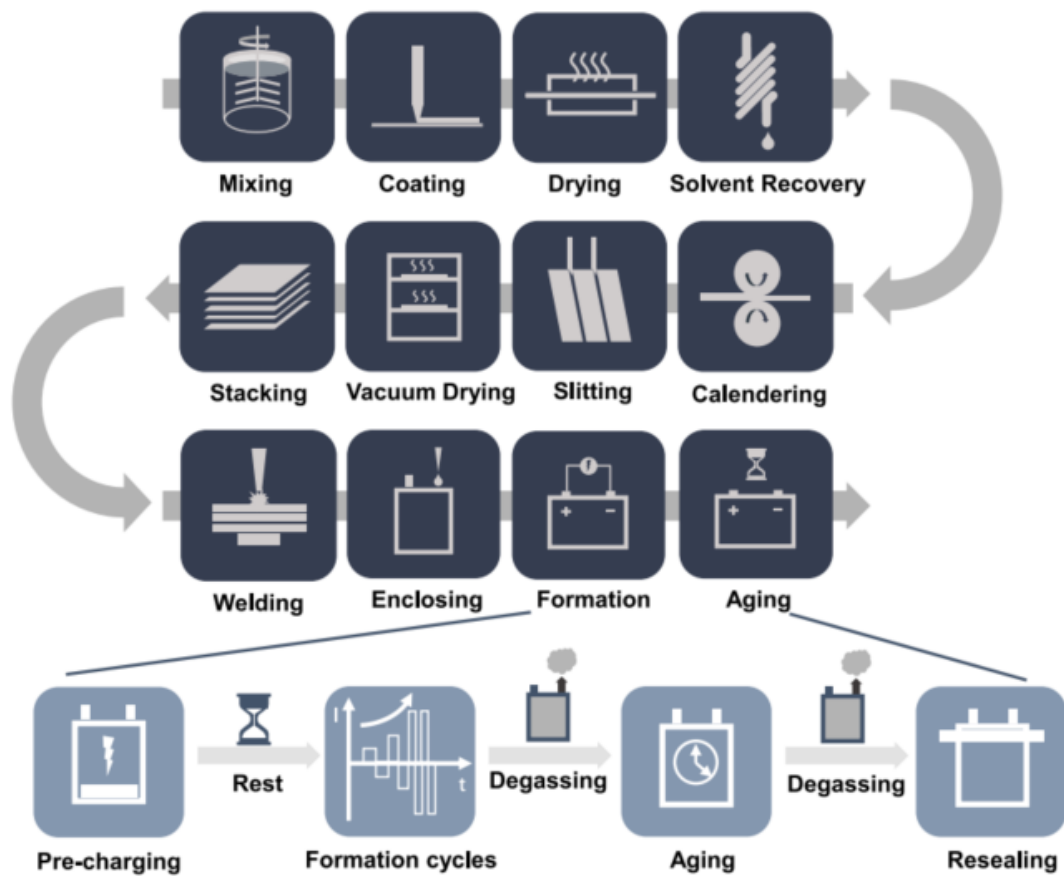


Figure 1.9 Schematic of LIBs manufacturing process [34]

Following Figure 1.9, at first the active material (metal oxide powder), conductive carbonaceous additive, and binder are mixed to form a uniform slurry with the solvent. For the cathode, N-methyl pyrrolidone (NMP) is normally used to dissolve the binder, which is polyvinylidene fluoride (PVDF). For the anode, the styrene-butadiene rubber (SBR) binder is dissolved in water with carboxymethyl cellulose (CMC). The slurry is then pumped into a slot die, coated on both sides of the current collector (Al foil for cathode and Cu foil for the anode), and delivered to drying equipment to evaporate the solvent. The common organic solvent (NMP) for cathode slurry is toxic, both for humans and the environment, and has strict emission regulations. Thus, a solvent recovery process is necessary for the cathode production during the drying step and the recovered NMP is reused in battery manufacturing with 20%–30% loss [35]. For the water-based anode slurry, the harmless vapor can be exhausted to the ambient environment directly. The following calendaring process can help adjust the physical properties (bonding, conductivity, density, porosity, etc.) of the electrodes. After all these processes, the finished electrodes are stamped and slitted to the required dimension to fit the cell design. The electrodes are then sent to the vacuum oven to remove the excess water. After the electrodes are well prepared, they are sent to the dry room with dried separators for cell production. The electrodes and separator are wound or stacked layer by layer to form the internal design of a cell, The cell stack is then transferred to the designed enclosure that is filled with electrolyte before the final sealing and completes the cell production [34]. After these steps, before considering the cell as a final product, it needs to go under the electrochemical activation that consists in formation cycles of charging and discharging in which the solid electrolyte interface (SEI) is formed. The cost estimation and evaluation of energy consumption for these manufacturing steps is critical to help determine the steps that need the most research and innovation in order to lower the price. As an example, the energy consumption of a 32-Ah lithium manganese oxide (LMO)/graphite cell production was measured from an industrial pilot-scale manufacturing facility by Yuan et al. [36] and the results are reported in Figure 1.10.

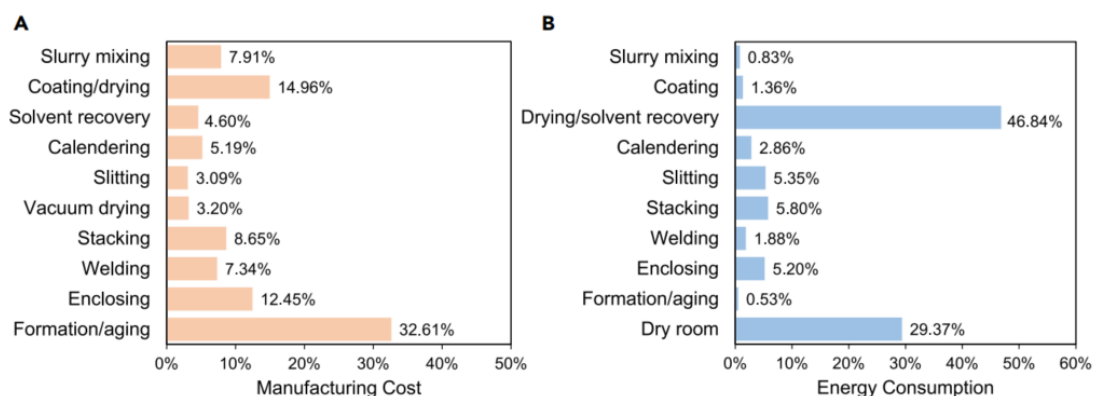


Figure 1.10 A) Cost breakdown and B) energy consumption breakdown for every step of the manufacturing process of LIBs [34]

Figure 1.10 clearly shows that the highest energy consumption step is drying and solvent recovery (about 47% of total energy) due to the long-time heating and off-gas cooling and the cost of treating the toxic fumes of NMP. The transition to the use of aqueous electrode preparation also for the cathode by nontoxic binders can provide a great step forward towards an ideally sustainable and environmentally friendly manufacturing process for LIBs. A simple comparison of binder and solvent costs already indicates the convenience of water-based electrode processing. NMP is rather expensive and costs 1–3 \$ kg⁻¹ compared to about 0.015 \$ L⁻¹ for water, and so is PVdF with a price of 8–10 \$ kg⁻¹. Therefore, this approach can accelerate the fall in prices for LIBs while dramatically lower environmental impact during the manufacturing. Natural polymers, like cellulose, alginate, guar gum have already been reported as viable alternatives to PVdF in many published works [37-40]. The use of water processable binder will also help the recycling of LIBs and the end-of-life management of aqueous binders: this approach opens a new path towards the design for a “direct recycling” of LIBs.

1.3.2 Electrical double-layer supercapacitors

Electrical double layer capacitors (EDLC), also known as supercapacitors, differ from LIBs because they operate with a non-faradaic storage mechanism. In EDLCs the charge is stored at the surface of the active material by electrostatic accumulation of electrolyte ions, which form an electrical double layer (EDL) at each electrode. This mechanism of storing energy gives to EDLCs the possibility to be charged and discharged in a really short time, between second and some minute, featuring extremely high power density, from 500 to 30 000 W kg⁻¹. However, since the EDL occurs only at the surface of the active materials, the energy density of EDLCs is much lower than that of batteries, being typically less than 10 Wh kg⁻¹. Thanks to a robust construction and simplicity of the electrochemical process that does not deteriorate the electrodes over cycling, EDLCs have impressive cycle life and can operate for more than 10⁶ cycles [41]. This characteristic makes EDLCs suitable for application like engine start-up, service for high quality power transmission and frequency regulation control for the grid, stabilization of fluctuant loads from renewable energy sources and ultimately, kinetic energy recovery systems in which a fraction of the kinetic energy of vehicles during breaking is stored and then released again upon accelerating [41].

The aforementioned EDL, formed by accumulation of charges, is described in detail by the Helmholtz model. This model describes the charge separation at the electrode/electrolyte interface when an

electrode of a certain surface area S (m^2) is polarized building up a double layer of thickness d , where d indicates the EDL thickness, namely the distance between the first layer of ions and the electrode surface. This simplified Helmholtz double-layer can be regarded as an electrical capacitor of a certain capacitance defined by Equation 1.1

$$C = \varepsilon_0 \varepsilon_r \cdot \frac{S}{d} \quad (1.1)$$

where ε_0 and ε_r are the permittivity of vacuum and of the solvent, respectively. From Equation 1.1 is clear that the capacitance of the EDL, that affects the overall capacitance, is strongly dependent from the surface of the electrode. Therefore, it is clear that the adoption of electrodes with high surface area, like activated carbons that feature up to 2000 m^2/g , is fundamental. From Equation 1.1 is clear that the capacitance of the EDL, that affect the overall capacitance, is strongly dependent from the surface of the electrode. Therefore, is clear that the adoption of cathodes with high surface area is fundamental.

Conventional EDLC are composed of i) two electrodes, which are composed of high surface area carbon, binder, current collector and, in most cases, a conductive agent like carbonaceous powder, ii) an electrolyte, which is comprised of solvent and salt, but solvent-free electrolytes are also possible, iii) a separator to prevent physical contact and short circuit of the electrodes and finally iv) of the casing and mechanical components ensuring a reliable connection for high currents within the capacitor as well as a connection to the respective application.

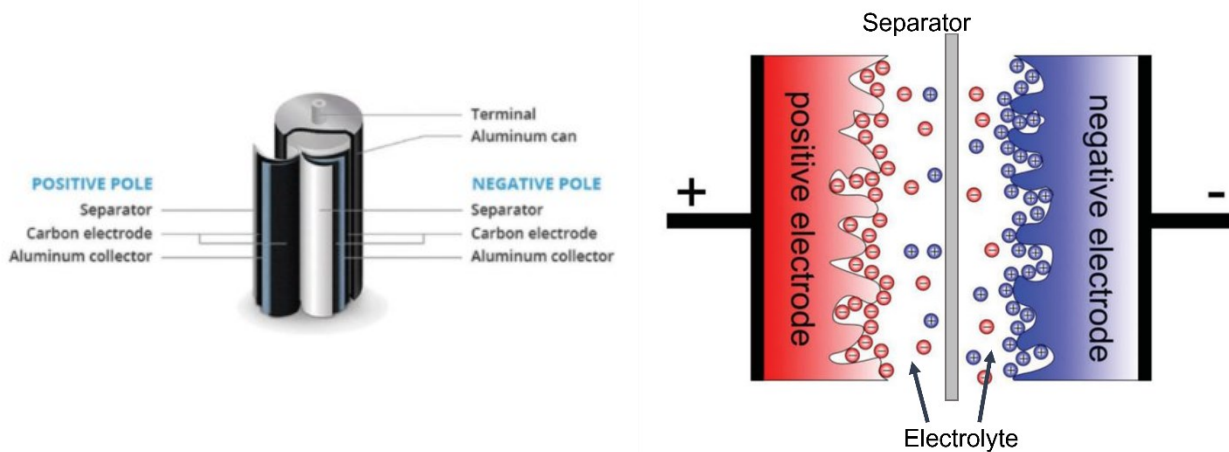


Figure 1.11 a) cross section of a commercial EDLC b) Representation of the charged state of a symmetric electrical double-layer capacitor using porous electrodes [modified from 43]

Upon charge, the EDL is setup at each electrode, hence the EDLC cell can be modeled with two capacitive elements (one for each electrode) in series with a resistance that is termed Equivalent Series Resistance (ESR). The overall cell capacitance C_{cell} is hence:

$$\frac{1}{C_{cell}} = \frac{1}{C_{negative\ el.}} + \frac{1}{C_{positive\ el.}} \quad (1.2)$$

The ESR includes the ionic resistance of the electrolyte (in the electrolyte and in the porous architecture of the carbon electrodes) and the electronic resistances of the electrodes. The capacitance C (F) of a EDLC can be calculated from Equation 1.3

$$C = q/V \quad (1.3)$$

where q is the charge, expressed in Coulomb, and V is the voltage. More precisely the capacitance of an EDLC is expressed in Equation 1.4, which shows the direct relation between time and voltage upon a galvanostatic test run at the I current:

$$C = \frac{\Delta Q}{\Delta V} = \frac{I \cdot \Delta t}{\Delta V} \quad (1.4)$$

Therefore, the “linear” dependence of the voltage over time allows to calculate C with the use of slope s of the V vs t plot ($s = \Delta V/\Delta t$).

Figure 1.11 present a typical galvanostatic discharge profile of an EDLC. The delivered energy (Wh) can be calculated from the discharge profile by Equation 1.4

$$E = I \cdot \int_0^t \frac{V}{3600} \cdot dt \quad (1.4)$$

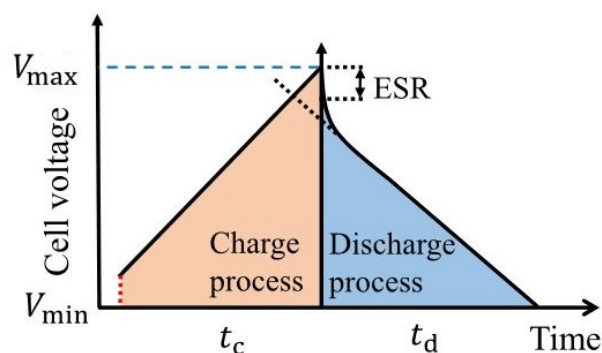


Figure 1.12 Schematic representation of constant current profile for a typical capacitive EDLC device

Since the EDL occurs only at the surface of the active material, this needs to have well-developed specific surface area (SSA), high microporosity, chemical and thermal stability, good conductivity and tailorable porosity. The typical choice for active materials in EDLCs are carbonaceous compounds that thanks to their tunability of surface chemistry, microstructure and morphology, chemical and thermal stability are the most adopted solution. More precisely, Activate Carbons (ACs) are the preferred ones, in both research and industry, because they have relatively low costs and high SSA ($>1500 \text{ m}^2 \text{ g}^{-1}$) when estimated by the Brunauer–Emmett–Teller (BET) method. Abundantly

available organic materials, including food waste [44,45], are a particularly attractive natural resource for the production of ACs, such as those derived from coconut shells or charcoal, which are the most common commercially used porous carbons. As examples, porous carbons derived from pyrolysis of lignin from bio-digester plants are reported to be activated with KHCO_3 and obtained a high specific surface area of $1879 \text{ m}^2 \text{ g}^{-1}$ and high pore volume of $0.75 \text{ cm}^3 \text{ g}^{-1}$ [46]. Other studies report S_{BET} values of more than $3000 \text{ m}^2 \text{ g}^{-1}$ for coal and semi-coke activated in KOH for 5 h at $800 \text{ }^\circ\text{C}$ [47]. Similarly, hydrothermal treatment of eucalyptus wood sawdust and subsequent KOH activation at $800 \text{ }^\circ\text{C}$ yielded up to S_{BET} of $2967 \text{ m}^2 \text{ g}^{-1}$ [48]. Since the conductivity of ACs for electrochemical storage devices is typically quite low, a small amount of additive needs to be added during electrode preparation to increase the electric conductivity of the electrode. This conducting agent needs to be highly conductive and its particle size should be orders of magnitude smaller than that of the active material so it can easily fill the voids between the individual particles of the active material and also between the active material and current collector, therefore contributing to lower the ESR. Carbon blacks are the most prominent material used as conducting agent in both research in industry so far. Like in batteries manufacturing process, supercapacitors electrodes need a binder to hold together ACs and conductive materials. As of today, the most used binders are polytetrafluoroethylene (PTFE), polyvinylidene fluoride (PVdF), and sodium carboxymethyl cellulose (Na-CMC) [42]. Binders can be categorized by their electrolyte compatibility, which is dependent on their solubility in the electrolyte's solvent, or whether or not they contain fluorine. Binders not containing fluorine may be preferred in terms of environmental compatibility making the recycling at the end of the device's lifetime easier. Other advantages of fluorine-free binders are their lower density as well as their lower cost. In EDLCs, electrolytes play a crucial role in the energy storage mechanism. Their ions are adsorbed on the electrode surface enabling the storage of energy in the double layer actively taking part in the storage mechanism. The main criteria for selection of an electrolyte are the electrochemical stability window, viscosity and the ionic conductivity. The electrolyte should have high electrochemical stability, which would enable high operative voltages and, therefore, high energy and power of the final device. The last two characteristics determine how fast and how easy the ions can move through the electrolyte. Low viscosities and high conductivities are preferred if pursuing high power devices because they allow ion of the electrolyte to "move" faster.

Commercially available EDLCs typically use organic solvent based electrolytes. These electrolytes have the advantage of having higher electrochemical stability compared to aqueous electrolytes, while still maintaining acceptable values for conductivity and viscosity. The main solvent for the industry is acetonitrile (ACN) and Et_4NBF_4 is mainly used as conductive salt. Since the operating voltage is a fundamental characteristic that directly influences the performance, scientists are looking for

increasing the electrochemical stability window using for example ionic liquids (ILs) or highly concentrated aqueous electrolytes [50-52]. ILs, thanks to their low flammability, represent an even safer alternative to the more volatile acetonitrile solutions. In addition, ILs are known for their high thermal stability, good conductivity and wide electrochemical stability window (>3 V). The most investigated ILs for EDLCs are based on the bis(trifluoromethanesulfonyl)imide (TFSI) anion [53,54]. Despite these characteristics, ILs are not used in commercial devices due to drawbacks like high costs, low transport properties which result in low conductivity, and they cannot be considered as totally green and strategies to recover them after use are needed.

The two EDLC electrodes need to be physically separated from each other to prevent short circuits, and a separator is used for this purpose. Separators are typically made of natural or synthetic polymers (cellulose or polypropylene). The polymer fibers are connected with each other forming a net that the ions of the electrolyte can pass through, but at the same time is able to prevent the physical contact of the electrodes. Separators based on glass fibers or ceramics can be used as well, but their cost limits them for research purposes, while separators based on synthetic or natural polymers made through electrospinning technique are revealed to have good mechanical and electrochemical properties [55,56].

When it comes to the manufacturing of supercapacitors, the costs are divided as shown in Figure 1.13. The electrode and the electrolyte materials are the biggest share of the overall EDLC cost, sharing 28% and 27% respectively. Nevertheless, the cost of the separator as well as the costs of the cell parts and construction are not much lower (23 and 22% for separator and cell components, respectively). The biggest share of the electrolyte cost is the conductive salt (about 60%) and the remaining part is attributed to the solvent. For the electrodes, the biggest cost factors are the foil (about 60%) and the carbon (about 40%). The cost of binder and conductive additive can be considered negligible toward the overall electrode costs ($\leq 1\%$).

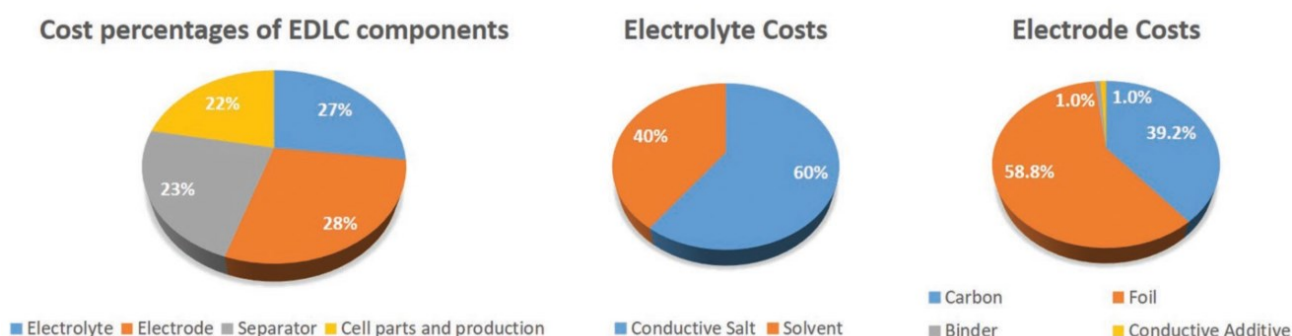


Figure 1.13 Cost percentages of the individual EDLC components [42]

1.3.3 Redox Flow Battery

Redox flow battery (RFBs) is a completely different class of battery. RFBs store energy by the use of two different soluble redox couple dissolved into two flowable electrodes. A schematic representation of a RFB is shown in Figure 1.14. The two fluid solutions, defined as electrolytes, are contained into two tanks and are pumped into the stack where the electrochemical reaction occurs and chemical energy is transformed into electrical energy, and vice versa. Inside the single vanadium cell, the ion exchange membrane prevents the contact of the two solutions allowing the electrochemical reaction to occur. RFBs can decouple energy and power design because the energy depends on the total volume of the liquid electrolytes contained into the tanks, while the power that the RFB can deliver depends on the design of the cell stack, and, mainly, on the electrode's area. RFBs have high round trip efficiency (RTE), high Depth of discharge (DoD), long cycle life, fast responsiveness, high scalability, and they are cost-effective. These are the key features for the technology successful deployment. RFBs are adopted mainly for large-scale grid storage, which requires long life-low cost batteries, considering both cyclability, calendar life, and round-trip efficiency. The downside of RFBs, in terms of performance, relates to the low energy density (c.a. 25

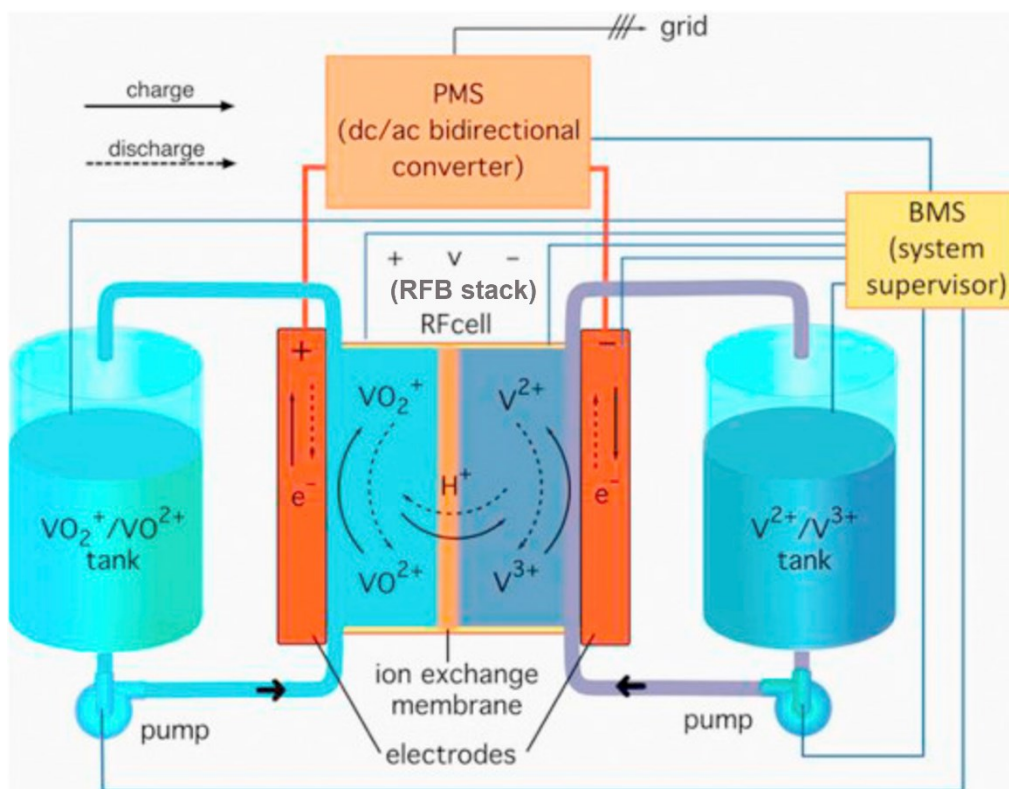
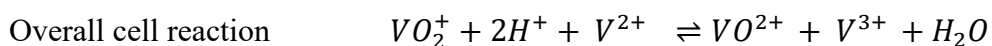
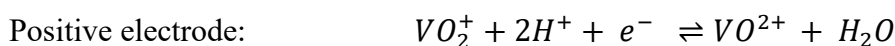


Figure 1.14 Scheme of a single-cell electrochemical vanadium redox flow battery [modified from 57]

Wh/L), while in terms of applicability, the installation and maintenance costs are still the main barriers for their penetration as storage units in the grid.

RFBs technology has been investigated using many different redox couple, employing sustainable redox active organic molecules based on Earth abundant elements [58], or using metal redox couple as active material like the Vanadium–bromine [59]. Moving from the redox couple, also alternative designs like membraneless RFBs [60] or RFB with insoluble solid active materials [61] have been proposed.

Among the different RFB chemistries, Vanadium Redox Flow Battery (VRFB) is the most and successful diffused. The Vanitec website (Global vanadium organization) lists 26 companies as producers of this technology and several plants have been installed globally. It is worth mentioning the 100 MW and 400 MWh VRFB of the Dalian Flow Battery Energy Storage Peak-shaving Power Station [62]. Thanks to the ability of vanadium to exist in solution in four different oxidation states, vanadium ions are used at both compartments, namely vanadium IV-V (tetravalent-pentavalent VO^{2+} and VO_2^+) in the positive electrolyte and vanadium II-III (bivalent-trivalent V^{2+} and V^{3+}) in the negative electrolyte. The electrochemical reactions produced by these solutions in the cells are:



The corresponding standard cell voltage is $E_0 = 1.26$ V at 25 °C and 50% SoC. The practical open circuit voltage (OCV) of a fully charged cell is expected to be 1.4 V [63]. Typically, the electrolyte is composed of a 1.6–1.7 M vanadium V_2O_5 dissolved in a 2 M sulfuric acid solution. As said before, the energy density of VRFB is the main limit because it ranges between 25 Wh L^{-1} and 35 Wh L^{-1} , much less than LIBs (c.a. 250 Wh L^{-1}). Using the same metal in both electrolytes prevents cross-contamination, allowing for a lifespan longer than any other solid-state or flow battery, which is typically 15.000–20.000 charge/discharge cycles as compared to the top figure of 5.000 typical of other batteries. In such a well-established technology, efforts are devoted at improving efficiency and increasing defined current and power densities. The typical current density of commercial VRFBs is in the order of 80–100 mA cm^{-2} , corresponding to power density of maximum 100 mW cm^{-2} . Most of the research to increase these values is focused on the membrane and the electrodes.

The VRFB membrane keeps the positive (catholyte) and negative (anolyte) electrolyte solutions from mixing. While preventing the cross mixing of the electrolyte solution, the membrane must facilitate the redox reaction by allowing hydrogen ions to pass through, balancing and completing the net cell reaction. Therefore, the most important parameters for optimal membrane are high ion conductivity, great chemical and mechanical stability, low cross-over rates, low voltage resistance and low swelling. Research studies on membranes focus on the development of ion-exchange membranes with excellent balance between ionic conductivity and vanadium-ion permeability, by tuning the material composition, optimizing membrane thickness and pore size distribution. Today, the most used membranes are based on cationic exchange membrane (CEM) like Nafion®. This class of membrane shows high ionic conductivity, excellent chemical stability and good mechanical properties in high acidic environment. The main disadvantage of the Nafion® based membranes is the high cost, that inhibits the broad application in commercial systems, and high crossover rates that will eventually increase the maintenance cost of the whole system. An alternative class of membrane type is the Anionic Exchange Membrane (AEM). These membranes are positively charged with surface functional groups and repulse the positive ions of vanadium electrolytes. Therefore, AEM can significantly reduce the crossover of vanadium phenomenon. In addition, AEMs can be synthesized at a lower cost than CEM, making this membrane more appealing for industrial application. The downside of using an AEM comes with a lower chemical stability and higher resistance that limits discharge currents and durability [64,65]. One of the emerging separator technologies is the nanofiltration membrane that, unlike the traditional ion exchange membrane, exploits a pressure difference to drive the ion diffusion through the membrane that is composed of many small pores. Since the radius of vanadium and its ions are much larger than that of H^+ , nanofiltration membranes use basic geometry (pore size) as a permeation gate. Hence, the pore size of the membrane selects and allows the passage of the hydrogen ions by excluding vanadium ion's [66,67]. The electrode is the component that facilitates the oxidation and reduction reactions within the flow battery. The surface of the electrode acts as a catalyst for the reaction and its porous surface provides the reaction sites for the electrolyte solution. The most used electrode materials are graphitized polyacrylamide (PAN) and Rayon (cellulose fibers) in carbon paper and carbon felt forms [68]. Research focuses on surface modification of the carbon felt with, as an example, graphene coating or metal oxide deposition in form of TiO_2 or TiN nanowires [69]. Nevertheless, the major limits of VRFB still remain the low energy density, the initial manufacturing cost and the fact that vanadium is classified as a strategic material, being mined in few non-European nations all over the world, making his price highly volatile [70].

Regarding the energy density, conventionally designed RFBs scales with solubility of the electroactive species employed, which is typically in the range of 1–2 M. An emerging strategy, that is being pursued to circumvent the low solubility of the active species, is the use of solid active materials suspended in the catholytes and/or anolytes. This approach opens to the possibility of achieving unprecedented values of energy density for RFBs [57] by the design of Semi-Solid flow Battery (SSFBs). In SSFBs, the electrolyte solution with the soluble active species is replaced by a suspension of solid particles that form a slurry, also termed semi-solid electrode. A representation of a SSFB is shown in Figure 1.15. Working prototypes of SSFBs using flowable suspensions reached up to ≈ 12 M concentration of electroactive materials. This concept was extended to other battery chemistries based on non-aqueous electrolytes [71] and aqueous electrolytes [72], as well as organic particulate materials [73] and capacitive materials like a flowable supercapacitor [74]. This concept was also applied to metal-air batteries, allowing energy density up to 500 Wh/kg on a lab scale [75,76].

Carbon particles are added into the active particle slurry to provide the required electrical connection between the active species and the current collector. The carbon particle should provide an electrically conductive percolating network that enables to increase the electrochemical surface area when the slurry flows through the reactor. A high carbon content enables high electrical conductivity and high current density. Unfortunately, this approach dramatically increases the viscosity and ionic resistance of the slurry, so that a compromise value of carbon content must be found. In parallel, surfactants and dispersing agents should be used to improve the rheological properties and stability of semi-solid electrodes. The use of suspensions of solid particles requires changes in the internal design of a conventional RFBs. In particular, the reactor should allow solid particles to flow through it and therefore carbon felt electrodes with high surface area cannot be used because they would be prone to clogging. 3D electrodes made by conductive materials and high percentage of void must be adopted to allow the circulation of the viscous slurries [77]. Although the promising results, many improvements are still needed, both at material and cell engineering level, to accelerate SSFB market penetration.

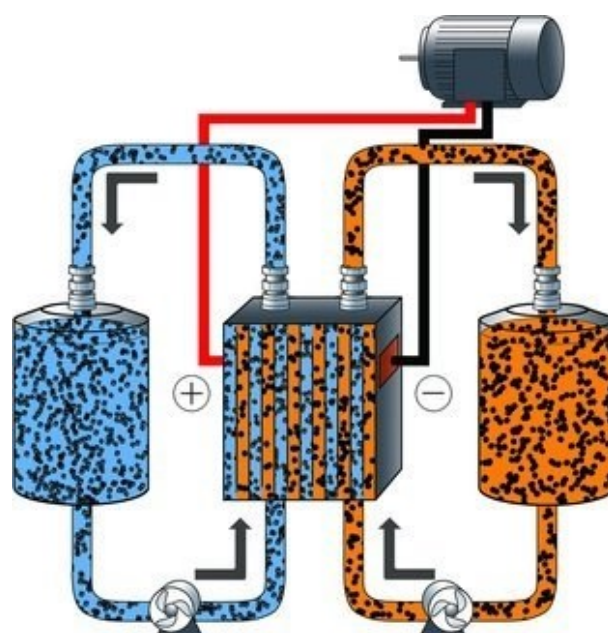


Figure 1.15 Scheme of a semi-solid flow battery

Chapter 1 References

- [1] Intergovernmental Panel on Climate Change (IPCC). (2022). *Global Warming of 1.5°C: IPCC Special Report on Impacts of Global Warming of 1.5°C above Pre-industrial Levels in Context of Strengthening Response to Climate Change, Sustainable Development, and Efforts to Eradicate Poverty*. Cambridge: Cambridge University Press. Doi:10.1017/9781009157940
- [2] Lacis, A. A.; Schmidt, G. A.; Rind, D; Ruedy, R. A.; “Atmospheric CO₂: Principal Control Knob Governing Earth’s Temperature”, *Science*, 2010, 330, 356-359.
DOI:10.1126/science.1190653
- [3] National Centers for Environmental Information, <https://www.ncei.noaa.gov/cag/global/time-series/globe/land/12/12/1880-2020>
- [4] Berkeley Earth. *Global Temperature Report for 2019*. <http://berkeleyearth.org/archive/2019-temperatures/>.
- [5] Manabe, S.; Role of greenhouse gas in climate change. *Tellus A: Dynamic Meteorology and Oceanography*, 2019, 71(1), p.1620078. DOI: <http://doi.org/10.1080/16000870.2019.1620078>
- [6] Climate watch: the world resource institute, 2020, <https://www.climatewatchdata.org/>
- [7] Pachauri, R. K. , Allen, M. R. , Barros, V. R. , Broome, J. , Cramer, W. , Christ, R. , Church, J. A. , Clarke, L. , Dahe, Q. , Dasgupta, P. , Dubash, N. K. , Edenhofer, O. , Elgizouli, I. , Field, C. B. , Forster, P. , Friedlingstein, P. , Fuglestvedt, J. , Gomez-Echeverri, L. , Hallegatte, S. , Hegerl, G. , Howden, M. , Jiang, K. , Jimenez Cisneroz, B. , Kattsov, V. , Lee, H. , Mach, K. J. , Marotzke, J. , Mastrandrea, M. D. , Meyer, L. , Minx, J. , Mulugetta, Y. , O’Brien, K. , Oppenheimer, M. , Pereira, J. J. , Pichs-Madruga, R. , Plattner, G. K. , Pörtner, H. O. , Power, S. B. , Preston, B. , Ravindranath, N. H. , Reisinger, A. , Riahi, K. , Rusticucci, M. , Scholes, R. , Seyboth, K. , Sokona, Y. , Stavins, R. , Stocker, T. F. , Tschakert, P. , van Vuuren, D. and van Ypserle, J. P. (2014): Climate Change 2014: Synthesis Report. Contribution of Working Groups I, II and III to the Fifth Assessment Report of the Intergovernmental Panel on Climate Change / R. Pachauri and L. Meyer (editors) , Geneva, Switzerland, IPCC, 151 p., ISBN: 978-92-9169-143-2 .
- [8] Bereiter, B., Eggleston, S., Schmitt, J., Nehrbass-Ahles, C., Stocker, T. F., Fischer, H., Kipfstuhl, S., and Chappellaz, J. (2015), Revision of the EPICA Dome C CO₂ record from 800 to 600 kyr before present, *Geophys. Res. Lett.*, 42, 542– 549, doi:[10.1002/2014GL061957](https://doi.org/10.1002/2014GL061957).
- [9] Global Monitoring Laboratory, Earth System Research Laboratories.
<https://gml.noaa.gov/ccgg/trends/global.html>
- [10] Global Carbon Project. (2021). Supplemental data of Global Carbon Budget 2021 (Version 1.0) [Data set]. Global Carbon Project. <https://doi.org/10.18160/gcp-2021>
- [11] Climate Action Tracker, <https://climateactiontracker.org/global/temperatures/>
- [12] McKinsey & Company, *Global Energy Perspective 2022*, April 26 2022, <https://www.mckinsey.com/industries/oil-and-gas/our-insights/global-energy-perspective-2022>

- [13] Møller, K. T.; Jensen, T. R.; Akiba, E.; Li, H; Hydrogen – A sustainable energy carrier *Progress in Natural Science: Materials International*, 2017, 27, 34-40
<http://dx.doi.org/10.1016/j.pnsc.2016.12.014>
- [14] European Commission, Directorate-General for Energy, Andrey, C.; Barberi, P.; Nuffel, L.; (2020). *Study on energy storage: contribution to the security of the electricity supply in Europe*, Publications Office. <https://data.europa.eu/doi/10.2833/077257>
- [15] Mitali, J.; Dhinakaran, S.; Mohamad, A. “Energy storage systems: a review”, *Energy Storage and Saving*, 2022, 1, 166-216, <https://doi.org/10.1016/j.enss.2022.07.002>.
- [16] King, M.; Jain, A.; Bhakar, R.; Mathur, J. & Wang, J. “Overview of current compressed air energy storage projects and analysis of the potential underground storage capacity in India and the UK” , *Renewable and Sustainable Energy Reviews*, 2021, 139, 110705
<https://doi.org/10.1016/j.rser.2021.110705>.
- [17] Amiryar, M.E.; Pullen, K.R. A Review of Flywheel Energy Storage System Technologies and Their Applications. *Applied Science*. 2017, 7, 286. <https://doi.org/10.3390/app7030286>
- [18] Nadeem F.; Hussain S. M. S.; Tiwari P. K.; Goswami A. K.; Ustun T. S., “Comparative Review of Energy Storage Systems, Their Roles, and Impacts on Future Power Systems,” in *IEEE Access*, vol. 7, pp. 4555-4585, 2019, doi: 10.1109/ACCESS.2018.2888497.
- [19] Ali M. H., Wu B. , Dougal R. A., “An Overview of SMES Applications in Power and Energy Systems,” in *IEEE Transactions on Sustainable Energy*, vol. 1, no. 1, pp. 38-47, April 2010, doi: 10.1109/TSTE.2010.2044901.
- [20] Yue, M.; Lambert, H.; Pahon, E.; Roche, R.; Jemei, S. & Hissel, D. Hydrogen energy systems: “A critical review of technologies, applications, trends and challenges” *Renewable and Sustainable Energy Reviews*, 2021, 146, 111180 <https://doi.org/10.1016/j.rser.2021.111180>.
- [21] Handwerker, M.; Wellnitz, J.; Marzbani, H. Comparison of Hydrogen Powertrains with the Battery Powered Electric Vehicle and Investigation of Small-Scale Local Hydrogen Production Using Renewable Energy. *Hydrogen* 2021, 2, 76-100. <https://doi.org/10.3390/hydrogen2010005>.
- [22] Usman, M. R.; “Hydrogen storage methods: Review and current status” *Renewable and Sustainable Energy Reviews*, 2022, 167, 112743, <https://doi.org/10.1016/j.rser.2022.112743>.
- [23] Mekhilef, S.; Saidur, R.; Safari, A.; “Comparative study of different fuel cell technologies” *Renewable and Sustainable Energy Reviews*, 2012, 16, 981-989, <http://dx.doi.org/10.1016/j.rser.2011.09.020>,
- [24] Horizon 2020, Hydrogen Mobility Europe, internet site accessed 16/10/2022
<https://cordis.europa.eu/project/id/671438>
- [25] Volkswagen Newsroom, “Battery or fuel cell, that is the question”, internet site accessed 16/10/2022, <https://www.volkswagen-newsroom.com/en/stories/battery-or-fuel-cell-that-is-the-question-5868>
- [26] “The Future of Energy Storage, An interdisciplinary MIT study”, Massachusetts Institute of Technology, 2022, <https://energy.mit.edu/research/future-of-energy-storage/>

- [27] Abbas, Q.; Mirzaeian, M.; Hunt, M.R.C.; Hall, P.; Raza, R. “Current State and Future Prospects for Electrochemical Energy Storage and Conversion Systems”. *Energies* 2020, 13, 5847. <https://doi.org/10.3390/en13215847>
- [28] Felseghi, R.-A.; Carcadea, E.; Raboaca, M.S.; TRUFIN, C.N.; Filote, C. “Hydrogen Fuel Cell Technology for the Sustainable Future of Stationary Applications”. *Energies* 2019, 12, 4593. <https://doi.org/10.3390/en12234593>
- [29] Manoharan, Y.; Hosseini, S.E.; Butler, B.; Alzahrani, H.; Senior, B.T.F.; Ashuri, T.; Krohn, J. “Hydrogen Fuel Cell Vehicles; Current Status and Future Prospect.” *Applied Science* 2019, 9, 2296. <https://doi.org/10.3390/app9112296>
- [30] Yang, Y.; Okonkwo, E. G.; Huang, G.; Xu, S.; Sun, W.; He, Y.; “On the sustainability of lithium ion battery industry – A review and perspective “ *Energy Storage Materials*, 2021, 36, 186-212, <https://doi.org/10.1016/j.ensm.2020.12.019>.
- [31] Ji, X.; Xia, Q.; Xu, Y.; Feng, H.; Wang, P.; Tan, Q.; “A review on progress of lithium-rich manganese-based cathodes for lithium ion batteries “ *Journal of Power Sources*, 2021, 487, 229362, <https://doi.org/10.1016/j.jpowsour.2020.229362>.
- [32] Mauler, L.; Duffner, F.; Zeier, W. G.; Leker, J.; “Battery cost forecasting: a review of methods and results with an outlook to 2050” *Energy Environ. Sci., The Royal Society of Chemistry*, 2021, 14, 4712-4739, <https://doi.org/10.1039/D1EE01530C>
- [33] Kwade, A.; Haselrieder, W.; Leithoff, R.; Modlinger, A.; Dietrich, F.; Droeder, K.; “Current status and challenges for automotive battery production technologies.” 2018 *Nature Energy* 3, 290–300
- [34] Liu, Y.; Zhang, R.; Wang, J. & Wang, Y. “Current and future lithium-ion battery manufacturing” *iScience*, 2021, 24, 102332. <https://doi.org/10.1016/j.isci.2021.102332>
- [35] Ahmed, S.; Nelson, P.A.; Gallagher, K.G.; Dees, D.W; “Energy impact of cathode drying and solvent recovery during lithium-ion battery manufacturing” *J. Power Sources*, 2016, 322, 169–178, <https://doi.org/10.1016/j.jpowsour.2016.04.102>
- [36] Yuan, C.; Deng, Y.; Li, T. & Yang, F. “Manufacturing energy analysis of lithium ion battery pack for electric vehicles” , *CIRP Annals* , 2017, 66, 53-56, <https://doi.org/10.1016/j.cirp.2017.04.109>
- [37] Bresser, D.; Buchholz, D.; Moretti, A.; Varzi, A.; Passerini, S.; “Alternative binders for sustainable electrochemical energy storage – the transition to aqueous electrode processing and bio-derived polymers “ *Energy Environmental Science, The Royal Society of Chemistry*, 2018, 11, 3096-3127, <https://doi.org/10.1039/C8EE00640G>
- [38] Wood, D. L.; Quass, J. D.; Li, J.; Ahmed, S.; Ventola, D.; Daniel, C.; “Technical and economic analysis of solvent-based lithium-ion electrode drying with water and NMP “ *Drying Technology, Taylor & Francis*, 2018, 36, 234-244 <https://doi.org/10.1080/07373937.2017.1319855>
- [39] Li, J.; Lu, Y.; Yang, T.; Ge, D.; Wood, D. L.; Li, Z. “Water-Based Electrode Manufacturing and Direct Recycling of Lithium-Ion Battery Electrodes—A Green and Sustainable Manufacturing System “; *iScience*, 2020, 23, 101081 <https://doi.org/10.1016/j.isci.2020.101081>

- [40] Brilloni, A.; Poli, F.; Spina, G. E.; Samorì, C.; Guidi, E.; Gualandi, C.; Maisuradze, M.; Giorgetti, M.; Soavi, F. “Easy recovery of Li-ion cathode powders by the use of water-processable binders” *Electrochimica Acta*, 2022, 418, 140376, <https://doi.org/10.1016/j.electacta.2022.140376>.
- [41] Zhao, J.; Burke, A. F. “Review on supercapacitors: Technologies and performance evaluation” *Journal of Energy Chemistry*, 2021, 59, 276-291 <https://doi.org/10.1016/j.jechem.2020.11.013>.
- [42] Schütter, C.; Pohlmann, S.; Balducci, A. “Industrial requirements of materials for electrical double layer capacitors: impact on current and future applications.”, *Advanced Energy Materials*, 9.25,(2019), 1900334. <https://doi.org/10.1002/aenm.201900334>
- [43] Béguin, F.; Presser, V.; Balducci, A.; Frackowiak, E. “Carbons and Electrolytes for Advanced Supercapacitors “ *Advanced Materials*, 2014, 26, 2219-2251 <https://doi.org/10.1002/adma.201304137>
- [44] Rufford, T. E.; Hulicova-Jurcakova, D.; Zhu, Z. ;Lu, G. Q. “Nanoporous carbon electrode from waste coffee beans for high performance supercapacitors” *Electrochemistry Communications*, 2008, 10, 1594-1597 <https://doi.org/10.1016/j.elecom.2008.08.022>
- [45] Kosheleva, R.I., Mitropoulos, A.C.; Kyzas, G.Z. “Synthesis of activated carbon from food waste” *Environ Chem Lett* **17**, 429–438 (2019). <https://doi.org/10.1007/s10311-018-0817-5>
- [46] Mutuma, B. K.; Sylla, N. F.; Bubu, A.; Ndiaye, N. M.; Santoro, C.; Brilloni, A.; Poli, F.; Manyala, N. ; Soavi, F. “Valorization of biodigester plant waste in electrodes for supercapacitors and microbial fuel cells “ *Electrochimica Acta*, 2021, 391, 138960, <https://doi.org/10.1016/j.electacta.2021.138960>.
- [47] Kierzek, K.; Frackowiak, E.; Lota, G.; Gryglewicz, G. ; Machnikowski, J. “Electrochemical capacitors based on highly porous carbons prepared by KOH activation” *Electrochimica Acta*, 2004, 49, 515-523 <https://doi.org/10.1016/j.electacta.2003.08.026> .
- [48] Wei, L.; Sevilla, M.; Fuertes, A. B.; Mokaya, R. ; Yushin, G. “Hydrothermal Carbonization of Abundant Renewable Natural Organic Chemicals for High-Performance Supercapacitor Electrodes” *Advanced Energy Materials*, 2011, 1, 356-361. <https://doi.org/10.1002/aenm.201100019>
- [49] Portet, C.; Lillo-Rodenas, M. A.; Linares-Solano, A.; Gogotsi, Y.; “Capacitance of KOH activated carbide-derived carbons” *Physical Chemistry Chemical Physics*. 2009, 11, 4943
- [50] DeVos, N.; Maton, C.; Stevens, C. V. “Electrochemical Stability of Ionic Liquids: General Influences and Degradation Mechanisms.” *ChemElectroChem* 2014, 1, 1258–1270. <https://doi.org/10.1002/celec.201402086>
- [51]. González, A.; Goikolea, E.; Barrena, J.A.; Mysyk, R. “Review on supercapacitors: Technologies and materials” *Renewable and Sustainable Energy Reviews*, 2016, 58, 1189–206 <https://doi.org/10.1016/j.rser.2015.12.249>
- [52]. Lazzari, M.; Mastragostino, M.; Soavi, F. “Capacitance response of carbons in solvent-free ionic liquid electrolytes.” *Electrochemistry Communications* 2007, 9, 1567–1572. <https://doi.org/10.1016/j.elecom.2007.02.021>

- [53] Krause, A.; Balducci, A. “High voltage electrochemical double layer capacitor containing mixtures of ionic liquids and organic carbonate as electrolytes.” *Electrochemistry Communications*. 2011, *13*, 814–817. <https://doi.org/10.1016/j.elecom.2011.05.010>
- [54] Krummacher, J.; Balducci, A. “Al(TFSI)₃ as a Conducting Salt for High-Voltage Electrochemical Double-Layer Capacitors.” *Chemistry of Materials* **2018**, *30*, 4857–4863. <https://doi.org/10.1021/acs.chemmater.8b02253>
- [55] Li, Y.; Li, Q.; Tan, Z. “A review of electrospun nanofiber-based separators for rechargeable lithium-ion batteries” *Journal of Power Sources*, 2019, *443*, 227262 <https://doi.org/10.1016/j.jpowsour.2019.227262>.
- [56] Banitaba, S. N.; Ebadi, S. V.; Salimi, P.; Bagheri, A.; Gupta, A.; Arifeen, W. U.; Chaudhary, V.; Mishra, Y. K.; Kaushik, A.; Mostafavi, E. “Biopolymer-based electrospun fibers in electrochemical devices: versatile platform for energy, environment, and health monitoring” *Materials Horizons*, *The Royal Society of Chemistry*, 2022, <https://doi.org/10.1039/D2MH00879C>
- [57] Sánchez-Díez, E.; Ventosa, E.; Guarnieri, M.; Trovò, A.; Flox, C.; Marcilla, R.; Soavi, F.; Mazur, P.; Aranzabe, E.; Ferret, R. “Redox flow batteries: Status and perspective towards sustainable stationary energy storage “ *Journal of Power Sources*, 2021, *481*, 228804, <https://doi.org/10.1016/j.jpowsour.2020.228804>.
- [58] Winsberg, J.; Hagemann, T.; Janoschka, T.; Hager, M. D.; Schubert, U. S. “Redox-Flow Batteries: From Metals to Organic Redox-Active Materials” *Angewandte Chemie International Edition*, 2017, *56*, 686-711. <https://doi.org/10.1002/anie.201604925>
- [59] Vafiadis, H.; Skyllas-Kazacos, M. “Evaluation of membranes for the novel vanadium bromine redox flow cell” *Journal of Membrane Science*, 2006, *279*, 394-402 <https://doi.org/10.1016/j.memsci.2005.12.028>.
- [60] Bamgbopa, M. O.; Almheiri, S. & Sun, H.” Prospects of recently developed membraneless cell designs for redox flow batteries” *Renewable and Sustainable Energy Reviews*, 2017, *70*, 506-518 <https://doi.org/10.1016/j.rser.2016.11.234>
- [61] Wang, X.; Chai, J.; Jiang, J. “J. “Redox flow batteries based on insoluble redox-active materials. A review “ *Nano Materials Science*, 2021, *3*, 17-24 <https://doi.org/10.1016/j.nanoms.2020.06.003>.
- [62] Vanitec Transforming Possibilities, Vanadium Redox Flow Battery Company, 2022. <http://www.vanitec.org/vanadium-redox-flow-battery-vrfb-companies>. (Accessed on the 29 October 2022)
- [63] Knehr, K.; Kumbur, E. “Open circuit voltage of vanadium redox flow batteries: Discrepancy between models and experiments” *Electrochemistry Communications*, 2011, *13*, 342-345 <https://doi.org/10.1016/j.elecom.2011.01.020>.
- [64] Tempelman, C.H.L.; Jacobs, J.F.; Balzer, R.M.; Degirmenci, V. “Membranes for all vanadium redox flow batteries” *Journal of Energy Storage*, 2020, *101754*, <https://doi.org/10.1016/j.est.2020.101754>.

- [65] Zeng, L.; Zhao, T.S.; Wei, L.; Jiang, H.R.; Wu, M.C.; Anion exchange membranes for aqueous acid-based redox flow batteries: Current status and challenges, *Applied Energy*, 2019, Vol. 233–234, 622-643, <https://doi.org/10.1016/j.apenergy.2018.10.063>.
- [66] Lourenssen, K.; Williams, J.; Ahmadpour, F.; Clemmer, R. ; Tasnim, S. “Vanadium redox flow batteries: A comprehensive review” *Journal of Energy Storage*, 2019, 25, 100844 <https://doi.org/10.1016/j.est.2019.100844>
- [67] Shi, X.; Esan, O. C.; Huo, X.; Ma, Y.; Pan, Z.; An, L. ; Zhao, T. “Polymer Electrolyte Membranes for Vanadium Redox Flow Batteries: Fundamentals and Applications” *Progress in Energy and Combustion Science*, 2021, 85, 100926 <https://doi.org/10.1016/j.pecs.2021.100926>
- [68] Eifert, L.; Banerjee, R.; Jusys, Z.; Zeis, R. “Characterization of Carbon Felt Electrodes for Vanadium Redox Flow Batteries: Impact of Treatment Methods” *Journal of The Electrochemical Society, The Electrochemical Society*, 2018, 165, A2577
- [69] Gencten, M.; Sahin, Y. “A critical review on progress of the electrode materials of vanadium redox flow battery.” *International Journal of Energy Research* 2020; 44: 7903– 7923. <https://doi.org/10.1002/er.5487>
- [70] Minke, C.; Kunz, U.; Turek, T. “Techno-economic assessment of novel vanadium redox flow batteries with large-area cells” *Journal of Power Sources*, 2017, 361, 105-114, <https://doi.org/10.1016/j.jpowsour.2017.06.066>.
- [71] Ventosa, E.; Buchholz, D.; Klink, S.; Flox, C.; Chagas, L. G.; Vaalma, C.; Schuhmann, W.; Passerini, S.; Morante, J. R. “Non-aqueous semi-solid flow battery based on Na-ion chemistry. P2-type $\text{Na}_x\text{Ni}_{0.22}\text{Co}_{0.11}\text{Mn}_{0.66}\text{O}_2\text{-NaTi}_2(\text{PO}_4)_3$ ” *Chemical Communication, The Royal Society of Chemistry*, 2015, 51, 7298-7301, <https://doi.org/10.1039/c4cc09597a>
- [72] Ventosa, E.; Amedu, O.; Schuhmann, W. “Aqueous mixed-cation semi-solid hybridflow batteries” *ACS Applied Energy Materials* 1 (2018) 5158–5162, <https://doi.org/10.1021/acsaem.8b01418>
- [73] Yan, W.; Wang, C., Tian, J.; Zhu, G.; Ma, L.; Wang, Y.; Chanr, R.; Hu, Y.; Wang, L.; Chen, T.; Ma, J.; Jin, Z. “All-polymer particulate slurry batteries.” *Nature Communication* 2019, **10**, 2513 , <https://doi.org/10.1038/s41467-019-10607-0>.
- [74] Presser, V.; Dennison, C. R.; Campos, J.; Knehr, K. W.; Kumbur, E. C.; Gogotsi, Y. “The Electrochemical Flow Capacitor: A New Concept for Rapid Energy Storage and Recovery” *Advanced Energy Materials*, 2012, 2, 895-902, <https://doi.org/10.1002/aenm.201100768>.
- [75] Ruggeri, I.; Arbizzani, C.; Soavi, F. “A novel concept of Semi-solid, Li Redox Flow Air (O₂) Battery: a breakthrough towards high energy and power batteries” *Electrochimica Acta*, 2016, 206, 291-300, <https://doi.org/10.1016/j.electacta.2016.04.139>
- [76] Ruggeri, I.; Arbizzani, C.; Soavi, F. “Carbonaceous catholyte for high energy density semi-solid Li/O₂ flow battery” *Carbon*, 2018, 130, 749-757, <https://doi.org/10.1016/j.carbon.2018.01.056>.

[77] Poli, F.; Ghadikolaei, L.K.; Soavi, F. “Semi-empirical modeling of the power balance of flow lithium/oxygen batteries” *Applied Energy*, 2019, 248, 383-389.
<https://doi.org/10.1016/j.apenergy.2019.04.133>

Chapter 2: Green Li-ion Batteries

This Chapter reports and discusses the results achieved in manufacturing green Li-ion batteries (LIB) with the scope of lowering energy consumption and eliminating the use of potentially dangerous chemicals.

The main scope of this part of my work is devoted to the exploitation of novel aqueous processable polymers, such as Pullulan (PU) or the bifunctional electronically conductive poly(3,4-ethylenedioxythiophene)-poly (styrene sulfonate) (PEDOT:PSS), as binders for manufacturing Li-ion batteries. The first one was used to investigate the complete life cycle of a LIB and the latter to compare the performances of water processable binder with conventional one.

The use of these materials will allow the development of a sustainable LIB value chain, where devices are designed in view of recovery of the critical and valuable materials at their end of life. The results of this approach have been published in the two articles attached in this chapter [1, 2].

2.1 Water processable binders: Pullulan and PEDOT:PSS

In order to design a more sustainable manufacturing process while lowering the price for LIBs production, a lot of effort is being devoted to the substitution of F-based binders like poly(vinylidene difluoride) (PVdF) which needs N-methyl-2-pyrrolidone (NMP) as solvent/dispersant, both very toxic for humans and the environment. The use of these chemicals for electrodes manufacturing processes requires the need for expensive atmosphere cleaning and monitoring systems. In addition, during the traditional incineration process at the end of life of the LIB, the presence of the F-containing polymers might generate volatile and toxic fluorocarbons [3-5].

Water processable binders for aqueous electrode preparation can provide a leap forward towards an ideally sustainable cycle life of LIBs, from manufacturing to the disposal of devices, opening a new approach towards the design for recycling [5-7].

In this work, I explored the applicability of two different water processable polymers as binders for LIBs, such as pullulan (PU) and the bifunctional electronically conductive poly(3,4-ethylenedioxythiophene)-poly (styrene sulfonate) (PEDOT:PSS).

Pullulan (PU) is a bio-derived polymer, more precisely an exopolysaccharide produced from starch by *Aureobasidium pullulans*. Pullulan films exhibit excellent mechanical properties, are edible, biodegradable, O₂-impermeable, resistant in an alkaline environment, and highly water-soluble. For these characteristics, pullulan is attracting much attention for pharmaceutical and biomedical applications [8].

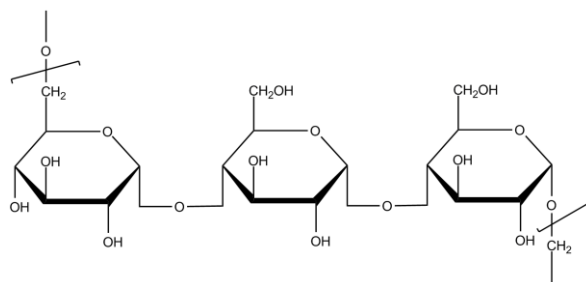


Figure 2.1: Chemical structure of Pullulan

On the other hand, PEDOT is an electronically conductive polymer that has been widely proposed as a key component for the next-generation consumer electronics and energy storage devices [9,10]. PEDOT doped with poly (styrene sulfonate) (PSS) anion (PEDOT:PSS) features high conductivity (10-102 S cm⁻¹), and nowadays commercial aqueous solutions of PEDOT:PSS are available. Along with its binding ability, PEDOT:PSS provides conductive bridges between individual particles which can improve the electron transport within the electrode components [11].

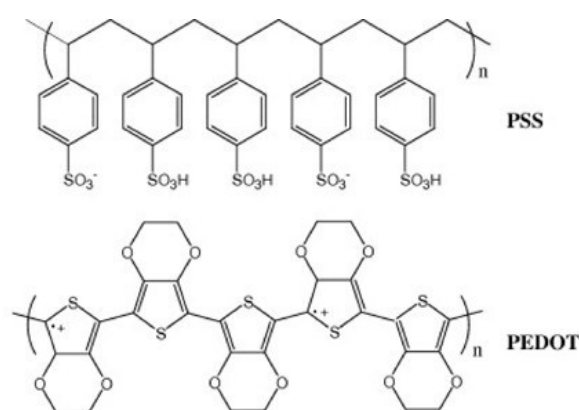


Figure 2.2 : PEDOT:PSS

2.2 Easy recovery of wasted Li-ion cathodes

I started my work exploiting PU as a water processable binder for $\text{Li}(\text{Ni}_{0.5}\text{Mn}_{0.3}\text{Co}_{0.2})\text{O}_2$ (NMC532) based cathodes, aiming at demonstrate that PU-processed electrodes can be viewed as LIB components “designed in view of recycling”. The PU was used in combination to glycerol (PUGLY), a plasticizer that confers suitable mechanical properties to the PUGLY-NMC cathodes.

At first, a detailed manufacturing process was developed, following the conventional step of dry milling, wet milling, casting, heating and pressing but using water and pullulan in an open air environment. The last part of the process includes the recovering and recycling of the materials used by dissolving the PUGLY binder electrodes with water spray by an aerograph fed with compressed air.

In order to validate the feasibility of the process, the pristine powders, the manufactured electrodes and the recovered black powder were analyzed with X-ray diffraction (XRD) and X-ray absorption spectroscopy (XAS). XRD results obtained for the pristine NMC532 powder are similar to those evaluated for the PUGLY-NMC electrode, therefore suggesting that the bulk lattice of NMC was well maintained after electrode processing by PUGLY. This conclusion was further supported by XAS analyses. XAS technique confirmed the same chemical and structural environment of Mn, Co and Ni in the pristine and recovered powders and electrodes. This fact is outstanding, also taking into consideration that the XAS probes not only the surface of a sample but also its bulk behavior.

The electrochemical performance of PUGLY-NMC electrodes were tested in coin cells with Li-metal anodes and were compared to that of cathodes featuring PVdF, similar to commercial ones. The two electrodes featured similar mass loading of ca. 5.5 mg cm^{-2} . At first the two electrodes were compared through cycling voltammetry (CVs) at $20 \mu\text{V/s}$, before and after the rate capability test in a reduced electrochemical window of 4.2 V. The results show that the first CVs tests function as an activation phase for the electrodes in which the 34oltametric capacity increased from $103 \text{ mAh g}_{\text{NMC}}^{-1}$ to $121 \text{ mAh g}_{\text{NMC}}^{-1}$ for PUGLY-NMC electrodes. The two electrodes featured similar behavior also during the rate capability tests.

When the C/rate increased from C/10 to 1C, the specific capacity of PVdF-NMC decreased from $115 \text{ mAh g}_{\text{NMC}}^{-1}$ to $99 \text{ mAh g}_{\text{NMC}}^{-1}$ and from $115 \text{ mAh g}_{\text{NMC}}^{-1}$ to $96 \text{ mAh g}_{\text{NMC}}^{-1}$ for PUGLY-NMC. After the first conditioning cycles, the PUGLY-NMC cathode was further tested in a wider electrode potential range by setting the charge cut-off voltage at 4.5 V for over 500 cycles carried out at C/3 and 1C. The 1C rate was considered an accelerated aging test condition and the cell showed an

outstanding cycle stability. Only after 450 cycles, 200 of each carried out at 1C, the capacity started to slightly fade. The PUGLY-NMC cathodes featured 153 mAh g⁻¹ at C/3 taking into account just the NMC content. Therefore, the electrochemical tests indicated that PUGLY can be considered as a valuable green alternative to PVdF. Indeed, the nominal performance of the NMC cathode powder, as for the manufacturer is > 150 mAh g⁻¹.

After the recovery of the powders used for casting electrodes and the XRD and XAS analysis, the aerobic and anaerobic biodegradability of the PUGLY and PVdF binders was evaluated to demonstrate the possibility of managing the waste waters used to wash and recover the NMC-carbon powders from the PUGLY-NMC electrodes through conventional biological treatments. It resulted that under aerobic conditions, PUGLY reached 34% of biodegradation in 50 days, while a complete biodegradation was achieved in just 15 days under anaerobic conditions indicating that bio-based binders can effectively enable a design-for-recycling electrode process where the binder impact is completely reduced, and the active valued powders recovered.

The use of PUGLY binder will not only reduce the environmental impact of LIBs, but will also decrease electrode manufacturing costs. Here I report an example considering the electrode production cost based solely on the materials, which includes the cost of active materials, carbon, and the binder solution used for the slurry. The evaluation has been done considering the production of composite electrodes featuring 5% binder, by using inks (including powders, binder and solvent) prepared with 40% of solvent (as in this work), i.e. with a binder concentration in the solution of 7.5%. The cost of a binder solution featuring PVdF (8 – 10 USD kg⁻¹) in NMP (1 – 3 USD kg⁻¹) can be as high as 3.5 USD kg⁻¹ [5]. For PVdF-based solutions, the major cost comes from NMP. Substitution of NMP with water (0.015 USD kg⁻¹) dramatically decreases the cost of the binder solution. A solution of 7.5% PUGLY (PU 20 – 30 USD kg⁻¹, [12]) in water, with 1:1 PU:GLY (0.4 – 0.5 USD kg⁻¹ [13]) ratio, costs only 1,0 USD kg⁻¹. This specific cost is 70% lower than that of the PVdF-NMP solution. Despite being affected by the binder to solvent ratio, and binder content in the composite electrodes, these cost values indicate the potential cost reduction by transitioning to water-based electrodes from the materials' point of view. In addition, it must be underlined that using the aqueous solution would avoid the need of the environments with controlled atmosphere required for processing NMP, with further advantages in terms of costs.

The experimental methods and the results of this study are reported in [1], which is here attached as complete publication.



Easy recovery of Li-ion cathode powders by the use of water-processable binders

Alessandro Brilloni^a, Federico Poli^a, Giovanni Emanuele Spina^a, Chiara Samorì^a, Elena Guidi^a, Chiara Gualandi^a, Mariam Maisuradze^b, Marco Giorgetti^{b,c}, Francesca Soavi^{a,c,*}

^a Department of Chemistry "Giacomo Ciamician", Alma Mater Studiorum Università di Bologna, Via Selmi 2, Bologna 40126, Italy

^b Department of Industrial Chemistry "Toso Montanari", Alma Mater Studiorum Università di Bologna, Via del Risorgimento 4, Bologna 40136, Italy

^c National Reference Center for Electrochemical Energy Storage (GISEL) - INSTM, Via G. Giusti 9, Firenze 50121, Italy

ARTICLE INFO

Keywords:

Water-processable cathodes
NMC
Lithium battery
Recycling
Pullulan

ABSTRACT

The continuous growth of the lithium battery market calls for strategies that simultaneously target high energy/power system performance, sustainable manufacturing processes, exploitation of green raw materials and easy recycling of batteries. Here we propose the use of pullulan, a water-soluble and biodegradable polymer, as a binder for the production of LIB cathodes based on $\text{Li}(\text{Ni}_{0.5}\text{Mn}_{0.3}\text{Co}_{0.2})\text{O}_2$ (NMC532). We aim to contribute to the development of a sustainable LIB value chain, where devices are designed in view of the recovery of critical elements at their end-of-life. In fact, the aqueous manufacturing of the cathodes represents a green, cheap and easy procedure to produce electrodes with reduced environmental impact and recover Li-ion cathode powders from spent LIBs. The cathodes exhibited up to 135 mAh g^{-1} of composite material and 167 mAh g^{-1} of NMC, and excellent cycling stability over 500 cycles along with good capacity retention at high C-rates. NMC and carbon black were directly recovered by dissolving the binder through a water-fed aerograph in less than 2 min. Notably, the waste waters used to wash and recover the NMC-carbon powders were biodegradable, which is of great importance to close the "sustainability chain" loop.

1. Introduction

Lithium-ion batteries (LIBs) are considered one of the main enabling technologies within the European Green Deal roadmap [1,2]. In fact, LIBs are even more irrupting into e-mobility and energy storage from intermittent renewable energy sources. In this scenario, strategies that simultaneously target high energy/power performance, sustainable manufacturing processes, valorisation of green raw materials and easy recycling of LIBs are urgently needed [3,4].

As it concerns LIB manufacturing, the transition towards the use of low cobalt content cathodes, like $\text{Li}(\text{Ni}_x\text{Mn}_y\text{Co}_z)\text{O}_2$ (NMC), is considered a good option. It features a specific capacity that can be higher than 160 mAh/g (depending on the Ni:Mn:Co stoichiometry) and a working potential higher than $4 \text{ V vs Li}^+/\text{Li}$ [4,5]. In addition, to meet the requirements of sustainable and cheaper production processes, much effort is being devoted to the substitution of F-based components with alternative ones. Indeed, today the commonly used binders are F-based polymers, like poly(vinylidene difluoride) (PVdF) which needs

N-methyl-2-pyrrolidone (NMP) as solvent/dispersant, both very toxic for humans and the environment. Europe has included NMP in the list of substances of very high concern and has recently set severe limits on its use [6]. Today, the use of PVdF for electrode processing requires expensive atmosphere-controlled environments and has a great economic and environmental impact on LIBs manufacturing [7–9]. Furthermore, the presence of F-containing polymers might generate volatile and toxic fluorocarbons during the traditional incineration of spent LIBs [7].

Transition to aqueous electrode preparation by nontoxic binders is expected to provide a great step forward towards an ideally sustainable and environmentally friendly technology for energy storage systems. Furthermore, the low environmental impact during the manufacturing and end-of-life management of aqueous binders open a new approach towards the design for recycling of LIBs [7–13]. Natural polymers, like cellulose, alginate, guar gum have already been reported as viable alternatives to PVdF [7–17].

Pullulan (PU) is an exopolysaccharide produced from starch by

* Corresponding author at: Department of Chemistry "Giacomo Ciamician", Alma Mater Studiorum Università di Bologna, Via Selmi 2, Bologna 40126, Italy.
E-mail address: francesca.soavi@unibo.it (F. Soavi).

<https://doi.org/10.1016/j.electacta.2022.140376>

Received 13 January 2022; Received in revised form 24 March 2022; Accepted 10 April 2022

Available online 11 April 2022

0013-4686/© 2022 Elsevier Ltd. All rights reserved.

Aureobasidium pullulans. It is based on linked maltotriose repeating units that confer high film- and fiber-forming characteristics to pullulan. Pullulan films exhibit excellent mechanical properties, are edible, biodegradable, O₂-impermeable, resistant in an alkaline environment, and highly water-soluble. For these characteristics, pullulan is attracting much attention for pharmaceutical and biomedical applications and, more recently, as a component (binder and/or separator) of electrochemical energy storage devices, like supercapacitors and high-voltage LNMO LIBs [18–20]. Specifically, pullulan:glycerol with 1:1 mixtures (PUGLY) were used for their excellent binding properties. Indeed, glycerol acts as a plasticizer and improves the mechanical properties of the polymer film [21]. Pullulan was also reported as a component of binder formulations for silicon anodes of LIBs [22]. Beside cell manufacturing, LIB component recycling is also a key topic that has to be addressed to fulfill the system sustainability challenge. The increasingly growing LIB market brings about an increasing demand for lithium and cobalt, with the consequent price increase and related concerns about the future and long-term material availability [23–25].

End-of-life LIBs are managed by three main approaches: rebuild, retrofit and recycle. Recycling is the best option. It enables the inclusion of exhausted LIBs within a circular economy approach, considering them as resources rather than waste to be disposed of. Hence, used or exhausted batteries can be considered as a huge reserve of raw material, reusable for the construction of new LIBs [23–27].

Critical metals from exhausted LIB electrodes can be recovered by pyrometallurgical, hydrometallurgical, electrochemical methods that can be also combined [28]. The first step is the mechanical separation of LIB components that usually takes place by breaking or shredding off electrodes. Alternatively, it is possible to separate the current collector sheets from the composite material through thermal processes that degrade the binder at 150–500 °C or pyrolysis [28]. In such processes,

however, HF can develop due to the degradation of the electrolyte. Direct recycling by the dissolution of the PVdF binder through the use of NMP, γ -butyrolactone, dimethylformamide or dimethyl sulfoxide is a valuable alternative. However, even in this case, toxic solvents that require controlled work environments are required [24,26,28]. Cathodes manufactured with water-soluble binders can be directly recycled to recover the black mass (active cathode powder and carbon additive) by physical separation from metal current collectors through a simple immersion in water and avoiding any harmful organic solvent, which dramatically reduces the recycling environmental impact and cost. This approach has been successfully demonstrated for Li(Ni_{0.5}Mn_{0.3}Co_{0.2})O₂ (NMC532) cathodes processed by several binders like carboxymethyl cellulose (CMC), styrene-butadiene rubber (SBR), and PVdF latex NMC532 powders that were recollected by sonication, washing and sintering at 700 °C [9].

It is worth noting that failure in manufacturing of LIBs, i.e. electrode cutting (for pouch cells) or cell assembly errors, could impact on the total manufacturing costs by ca. 26%, which may lead to the loss material during the manufacturing process, causing to lowering the yield to 75%. Direct and easy recycling of scraps electrodes produced by aqueous binders could decrease the overall manufacturing costs by reintroducing valuable active materials in the manufacturing stream [9–11].

Here we propose the use of the water-soluble and biodegradable polymer pullulan (PU) to manufacture NMC532 cathodes (hereafter labelled with PUGLY-NMC). PU allows a green, cheap and easy procedure to produce electrodes and recover Li-ion cathode powders from spent LIBs. Indeed, black mass was directly recovered by dissolving the binder through a water-fed aerograph, without any additional sintering step. The PUGLY-NMC production and direct recycling concept is depicted in Fig. 1.

The electrochemical performance of PUGLY-NMC electrodes tested

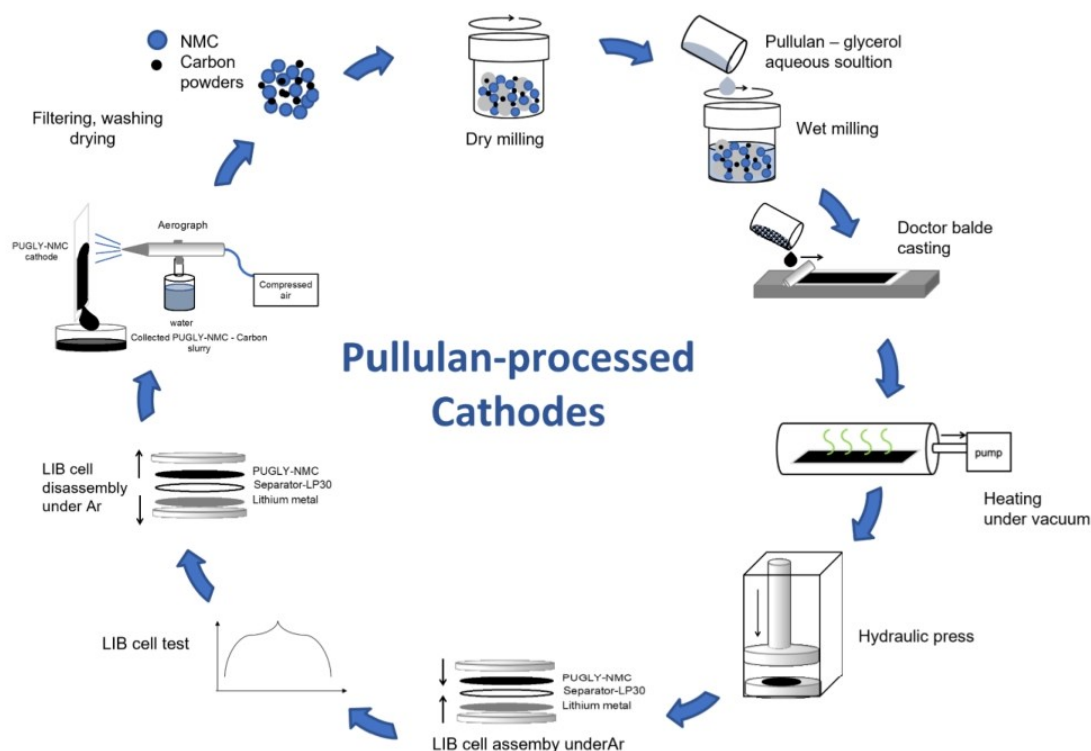


Fig. 1. PUGLY-NMC cathode production process and schematic of the entire direct recycling process. In this paper, direct recycling was demonstrated on fresh-prepared cathodes (not cycled).

in cells with Li-metal anodes is reported and compared to that of cathodes featuring PVdF. Electrochemical tests are complemented with structural and morphological analyses of fresh, aged cathodes and recovered powders (from production wastes). In addition, the aerobic and anaerobic biodegradability of the PUGLY and PVdF binders is evaluated to demonstrate the possibility of managing the waste waters used to wash and recover the NMC-carbon powders from the PUGLY-NMC electrodes through conventional biological treatments. Hence, overall, this paper aims at demonstrating that PU-processed electrodes can be viewed as LIB components “designed in view of recycling” and manufactured in compliance with the green chemistry principles [29]. Indeed, LIB cathode manufacturing by water-based processes in the ambient atmosphere, as well as the easy NMC powder recovery (from aged cells and/or cathode production wastes), enable to address the principles “1. Prevention”, “3 Less Hazardous synthesis”, “4. Design Safer Chemicals”, “5. Use of Renewable Feedstocks”, “6. Reduce derivatives” and “7. Inherently Safer Chemistry for Accident Prevention”.

2. Experimental

2.1. PUGLY-NMC cathode preparation

PUGLY-NMC cathodes were produced using a commercial NMC532 powder (Shandong Gelon Lib.Co) with stoichiometry $\text{Li}(\text{Ni}_{0.5}\text{Mn}_{0.3}\text{Co}_{0.2})\text{O}_2$ (see EDS data in the Supplementary Information section, Fig. S1) and particle size 9–12 μm [30].

Electrodes were produced by casting NMC-based composites on aluminum current collectors (20 μm -thick). Before casting, aluminum foils were treated to remove passivation layers. Specifically, the foils were immersed in a 5% wt KOH aqueous solution for 1 min, washed with milliQ water and dried in an oven overnight at 80 °C.

NMC and carbon conductive additive (SuperC45, Imerys Graphyte Carbon), with a mass ratio 89.5:10.5 were dry-milled at 250 rpm over 30 min by a planetary ball mill (FRITSCH, Pulverisette) using tungsten jar (12 mL) and spheres (10 spheres, 5 mm diameter). This step enabled a good dispersion of the carbon particles within the oxide grains.

Then, the aqueous solution of pullulan (binder, TCI Europe, Zwijndrecht, Belgium) and glycerol (plasticizer, Sigma-Aldrich) with 1:1 mass ratio and 40% w/ w_{total} of milliQ was added in the jar, to obtain a slurry that was milled at 250 rpm over 20 min. The slurry milling time and the amount of water were kept as small as possible in order to minimize side reactions between NMC and water. In fact, it has been reported that exchange $\text{Li}^+ \leftrightarrow \text{H}^+$ reactions can take place during immersion of NMC cathode powders in water [31]. In turns this might bring about the formation of LiOH and to the increase of pH. Such increase could favor the formation of Li_2CO_3 , by the reaction with CO_2 from the atmosphere, and promote aluminum corrosion during the casting procedure [13,17]. The pH of the slurry was checked and resulted in 10.67 ± 0.02 . The pH of the PUGLY solution, without NMC and carbon was 6.7 ± 0.02 . To avoid a prolonged contamination with the atmosphere, PUGLY-NMC layers were casted immediately after slurry milling on pre-etched aluminum foils. The final composition of the PUGLY-NMC cathodes was: 85% NMC, 10% carbon conductive additive, 5% PUGLY. The composite slurry was casted on the aluminum foil by a Mini Coating Machine (Hohsen Corporation) at 0.3 cm s^{-1} and with a bar distance of 200 μm . The coated films were dried at 60 °C overnight in a thermostatic oven, pressed at 4 Ton/cm^2 , and dried again under dynamic vacuum (BUCHI oven) at 120 °C overnight to eliminate any trace of water. Finally, they were transferred in a dry box under Argon atmosphere (MBraun, H_2O and $\text{O}_2 < 1$ ppm).

Cathodes featuring PVdF binder were produced by a similar approach that is detailed in Supplementary Information.

2.2. Chemical-physical analyses

The morphological characterization of the materials was carried out

using a Zeiss EVO 50 electron scanning microscope (SEM) equipped with an energy-dispersive X-ray analyzer (EDS) from Oxford INCA Energy 350 system. Low magnification images of bent cathodes were collected by a Skybasic digital microscope (1000X). X-ray diffraction (XRD) spectra were collected by a PANalytical X'Pert PRO powder diffractometer equipped with a X'Celerator detector ($\text{CuK}\alpha$ radiation, $\lambda = 1.5406 \text{ \AA}$, 40 mA, 40 kV), radiation source and Ni filter by continuous scanning mode (step 0.017° 2 θ step size, 10 s/step scan rate). The reported XRD patterns have been corrected for the background and, in the case of the electrodes, for a 0.3 mm displacement of the XR beam focal plane.

Thermogravimetric Analysis (TGA) was performed by a TA Thermal Analysis Q50 equipment, under Argon/ O_2 flow (60 mL/min) with a scan rate of 10 °C/min up to 650 °C. Dynamic Mechanical Analysis (DMA) were performed with a dynamic mechanical analyzer DMA Q800 TA Instrument on rectangular samples in tensile mode and under strain control. The storage (E') and loss modulus (E'') were monitored for 10 min while applying a strain amplitude of 0.06% at an oscillation frequency of 1 Hz.

2.3. Electrochemical tests

PUGLY-NMC electrodes (0.9 cm diameter) were tested in 2-electrode Swagelok cells in Teflon with AISI 316 L connectors. Lithium metal was used as the negative electrode. Before the use, lithium was mechanically treated and laminated to remove any passivation layer. The separator used to assemble the cell was a Celgard (2300, 25 μm -thick) film. The electrolyte used was 1 M LiPF_6 in 1:1 (w:w) ethylene carbonate (EC): dimethyl carbonate (DMC) (LP30, Selectolyte BASF, Germany). The cells were assembled in a dry box. The electrochemical measurements were carried out at 30 °C by a multi-channel VMP (Perkin Elmer, Waltham, MA, USA) potentiostat/galvanostat.

At first, PUGLY-NMC cathodes were subjected to a conditioning protocol that consisted in voltammetric (CV) and galvanostatic charge/discharge cycles that were carried out with a charge cut-off voltage of 4.2 V vs. Li^+/Li . Afterwards, electrochemical tests were performed increasing the charge cut-off at 4.5 V vs. Li^+/Li . For the galvanostatic tests, the C-rate was calculated on the basis of the nominal specific capacity provided by the NMC provider, i.e. 150 mAh g^{-1} [30].

2.4. NMC-carbon recovering and biodegradation studies

The NMC-carbon recovery process was tested on large PUGLY-NMC foils (area of 56 cm^2) that were not cycled to get quantitative data. The average areal mass loading of the composite layer was $6 \pm 1 \text{ mg cm}^{-2}$. The films were weighed and then the PUGLY-NMC composite was collected by dissolving the PUGLY binder with water spray by an aerograph fed with compressed air. The obtained aqueous suspension containing dissolved PUGLY and the NMC-carbon black mass was filtered by a syringe filter (Millex-GV Millipore Coop., 0.22 μm) that was also used to wash with hot water the powder trapped in the filter. The filter with the black mass was removed from the filter holder, dried at 120 °C in a thermostatic oven. Finally, the NMC-carbon composite was collected from the filter.

To evaluate the biodegradability of the waste-waters used to wash and recover the NMC-carbon powders from the electrodes, aerobic and anaerobic tests were carried out on aqueous solutions of PUGLY and PVdF. Aerobic biodegradation was determined by a ready biodegradability test in an aqueous medium according to the OECD (Organization for Economic Cooperation and Development) guideline 301 F, “Manometric respirometry”, using an activated sludge taken from a treatment plant receiving domestic sewage located in Ravenna, Italy, as the bacterial inoculum [32]. The anaerobic degradation was performed at 55 °C for 15 days by using a mix of anaerobically-digested sewage sludge from local waste-water treatment plants of different agro-food industries, and following the procedure reported in ref. [33] (the amount of biogas

produced was evaluated by visual quantification of the volume produced every day, while the percentage of methane was determined by analysing 10 mL of the biogas through a GC-TCD, Agilent 78120A).

2.5. X-ray absorption spectroscopy measurements

X-ray absorption spectroscopy (XAS) experiments at the Ni, Mn and Co K-edges were performed at Elettra Sincrotrone Trieste (Italy), at the XAFS 11.1 beamline [34]. The storage ring operated at 2.4 GeV in top-up mode with a typical current of 160 mA. Data were recorded in transmission mode using ionization chambers filled with a mixture of Ar, N₂, and He to have 10, 70, and 95% of absorption in the I0, I1, and I2 chambers, respectively. An internal reference of nickel, manganese and cobalt foil was used for energy calibration. The white beam was monochromatized using a fixed exit monochromator equipped with a pair of Si (111) crystals. Spectra were collected with a constant k-step of 0.03 Å⁻¹ with 2 s per point acquisition time from 6345 to 7090 eV, from 7515 to 8320 eV, and from 8155 to 8820 eV around Mn, Co and Ni K-edges, respectively.

3. Results

3.1. PUGLY-NMC cathode production

PUGLY-NMC cathodes were obtained following the steps described in Section 2.1 and in Fig. 1.

Figs. 2 and 3 report the SEM images and XRD patterns of the pristine NMC powder and PUGLY-NMC cathodes. The comparison of Fig. 2a and 2b suggests that the ball milling step is beneficial to get a homogeneous dispersion of carbon and binder among the NMC grains, and to reduce the size of the largest NMC agglomerates (> 10 μm). In addition, no significant difference was observed in the XRD spectra after the water processing (see also XRD reflection positions in Table S1). All the patterns display a single-phase α-NaFeO₂-type structure [35]. No additional reflections that could be ascribed to contaminants like LiOH or Li₂CO₃ were observed in the X-ray patterns. The split of the (006)/(102) and (108)/(110) doublets indicates a good hexagonal ordering that is representative of the layered structure, and that was kept before and after electrode processing [34,35]. Table 1 reports lattice parameters *a* and *c* refined by the rhombohedral system with R-3 m space group, as

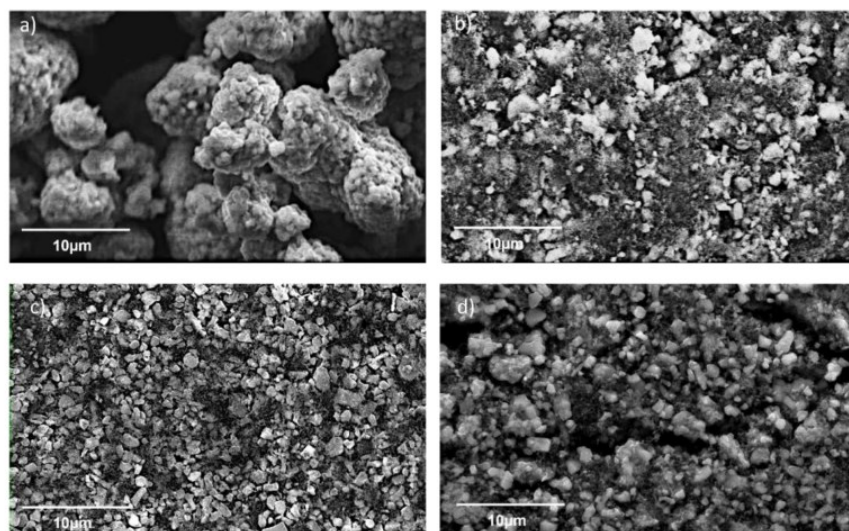


Fig. 2. SEM images of (a) pristine NMC powder, (b) pristine PUGLY-NMC electrode, (c) PUGLY-NMC electrode after 500 galvanostatic cycles, and (d) recovered black mass.

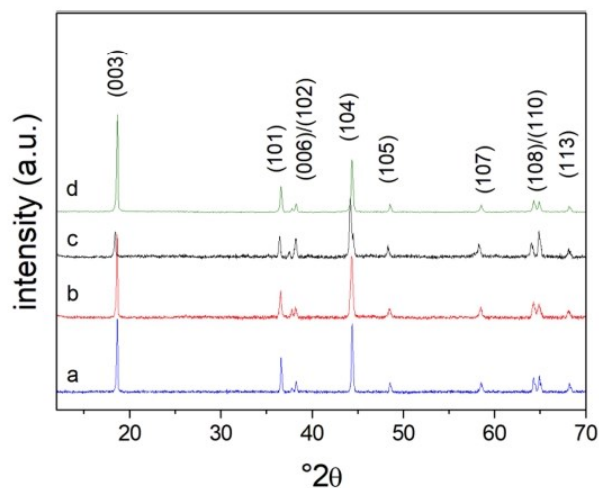


Fig. 3. XRD patterns of (a) pristine NMC powder, (b) pristine PUGLY-NMC electrode, (c) PUGLY-NMC electrode after 500 galvanostatic cycles, (d) NMC-carbon powder recovered from waste cathode (not cycled).

Table 1

Lattice parameters *a*, *c*, ratios of the integrated intensities of the (003) and (104) reflections (I_{003}/I_{104}), and EDS stoichiometric ratio of Ni, Mn and Co.

Sample	XRD		I_{003}/I_{104}	EDS atomic ratio		
	<i>a</i> (Å)	<i>c</i> (Å)		Ni	Mn	Co
Pristine NMC powder	2.87	14.21	0.96	4.9	3.1	2.0
Fresh PUGLYNMC electrode	2.86	14.19	0.93	4.8	3.0	2.0
Cycled PUGLYNMC electrode	2.85	14.16	0.33	4.8	3.1	2.0
Recovered NMC-carbon powder	2.87	14.17	1.10 ^a	4.7	2.9	2.0

^a averaged over several spectra.

well as the ratio of the integrated intensities of the (003) and (104) reflections (I_{003}/I_{104}), that is taken as an indicator of cation mixing, i.e. the partial occupation of Ni²⁺ lattice sites by Li⁺. High (I_{003}/I_{104}) indicates

small $\text{Li}^+/\text{Ni}^{2+}$ cation mixing [36]. For the pristine NMC532 powder, the a and c parameters are 2.87 Å and 14.21 Å, and the I_{003}/I_{104} ratio is 0.93. Table 1 reports the Ni, Mn and Co atomic ratio evaluated by SEM-EDS that confirmed the NMC532 stoichiometry. Both XRD parameters and EDS results obtained for the pristine NMC532 powder are similar to those evaluated for the PUGLY-NMC electrode, therefore suggesting that the bulk lattice of NMC was well maintained after electrode processing by PUGLY. This conclusion was further supported by XAS analyses, discussed in Section 3.4, that indicated that the pristine NMC bulk chemical and structural environment of Mn, Co, and Ni was retained in PUGLY-NMC electrodes.

The average mass loading of the PUGLY-NMC coating was evaluated by weighing different samples cut as disks (0.9 cm diameter) from the main aluminum coated strip (Fig. 4a). Up to $6 \pm 1 \text{ mg cm}^{-2}$ of composite layer and 4.8 mg cm^{-2} of NMC was deposited on Al. The layer was well stuck on the current collector and no cracks were observable even at a millimetric magnification (Fig. 4b).

Electrode manufacturing upscale by automatic roll machine requires that high bending flexibility and resistance to elongation are achieved without damaging the composite material coating. In addition, for cost- and time-effective electrode production, high temperatures are often used to dry electrodes [37]. We tested the flexibility of the PUGLY-NMC cathode strips (9 cm width and c.a. 15 cm long) by wrapping them around a 5 cm diameter steel cylinder. Fig. 4c, d reports the images of the flexibility study and show that the PUGLY-NMC cathodes exhibited excellent mechanical properties, with no crack formation after the test.

Electrode integrity was also evaluated during a DMA analysis where small deformations were applied to the electrode for a prolonged time. The measurements were carried out to compare the behavior of PU based and PVdF based electrodes under the same test condition. The measurements were performed under controlled strain at room temperature by applying an oscillating strain of $\epsilon = 0.06\%$ for 10 min. The application of a higher strain of 0.08% resulted in the break of the aluminum current collector. Fig. 5 shows that both storage modulus and loss modulus did not change during the DMA test, meaning that both electrodes maintained their mechanical properties without being

damaged under the investigated conditions.

Fig. 6 shows the TGA profiles under Ar/O_2 of the milled black mass (NMC and carbon, without binder) and of a PUGLY-NMC cathode (the aluminum mass has been excluded). In absence of binder, i.e. in the case of the black mass sample, the mass loss between 270 °C and 300 °C can be attributed to surface carbonates formed after exposure to water and air [38]. Oxygen evolution from the NMC lattice at these temperatures can be appreciated only in delithiated samples [39] (for a comparison, see also the TGA analysis of the pristine NMC powder without carbon, Fig. S3). This loss partially overlaps with the binder degradation, as evidenced by the comparison of the curve of the black powder and of the PUGLY-NMC cathode. Indeed, pullulan is known to exhibit a high thermal stability at temperatures even up to 200 °C in an inert atmosphere [40,41]. The mass loss before 200 °C of the cathode (black line) can be attributed to the PUGLY binder that under oxygen atmosphere loses 50% of its weight as shown in Fig. S3. The additional 10% mass loss between 450 and 500 °C is related to the combustion of the carbonaceous component.

3.2. PUGLY-NMC cathode electrochemical test

At first, the electrodes were cycled in a narrow electrode potential window, i.e. between 2.5 V and 4.2 V vs Li^+/Li in $\text{Li}/\text{LP30}/\text{NMC}$ cells. Fig. 7 compares the results of the voltammetric and galvanostatic tests run in this potential range of PUGLY-NMC and PVdF-NMC electrodes featuring the same mass loading (ca. 5.5 mg cm^{-2}). Specifically, the following test protocol was adopted: 5 CVs at 20 $\mu\text{V/s}$, galvanostatic cycles at C/10, C/5, C/3, C/1 and C/5 (both for charge and discharge), and 3 CVs at 20 $\mu\text{V/s}$. Fig. 7a compares the CVs of the two electrodes before and after the galvanostatic cycles at C/10. For both PUGLY-NMC and PVdF-NMC, galvanostatic cycling improved electrode response. Indeed, for PUGLY-NMC, the voltammetric capacity increased from 103 $\text{mAh g}_{\text{NMC}}^{-1}$ to 121 $\text{mAh g}_{\text{NMC}}^{-1}$. For the PVdF-NMC it changed from 106 $\text{mAh g}_{\text{NMC}}^{-1}$ to 125 $\text{mAh g}_{\text{NMC}}^{-1}$. This behavior could be explained with the improvement of electrode wettability by the electrolyte promoted by cycling. After this sort of activation, the CVs of PUGLY-NMC

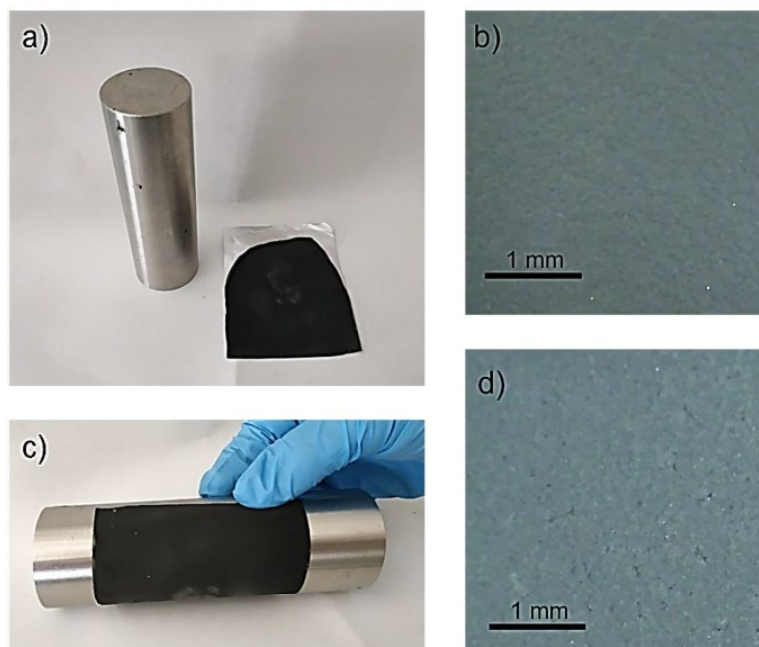


Fig. 4. (a) PUGLY-NMC coated aluminum strip, (b) magnification of the coating layer, (c) flexibility test, (d) magnification of the coating layer during flexibility test.

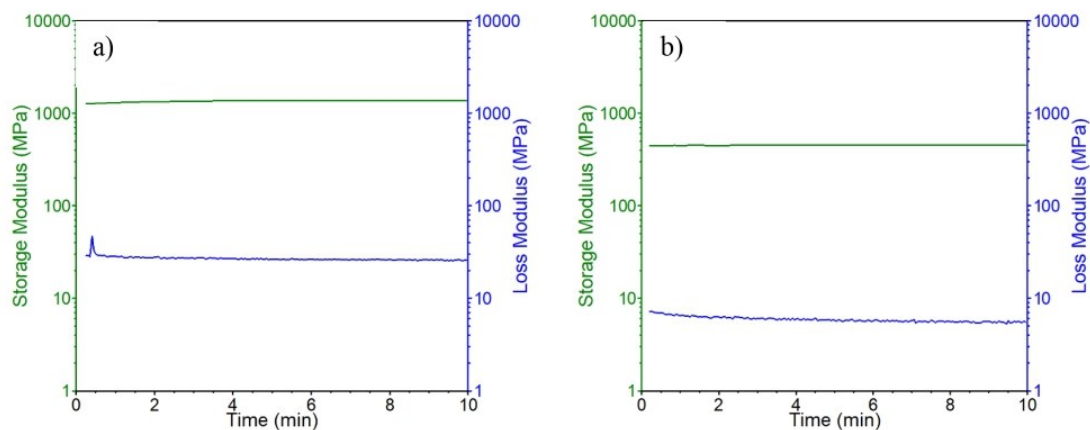


Fig. 5. DMA measurements under controlled strain at RT by applying a 0.06% strain of (a)PU electrode and (b) PVdF electrode.

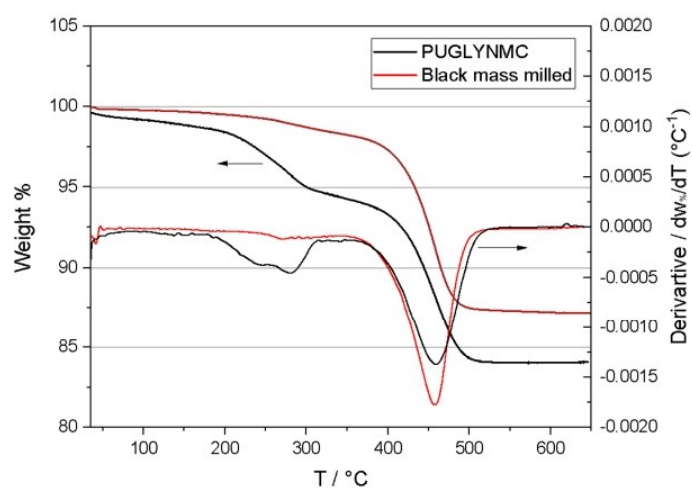


Fig. 6. TGA profiles under Ar/O₂ and their derivatives of the milled black mass (NMC and carbon, red line), and of the pristine PUGLY-NMC cathode (the aluminum mass has been excluded, black line).

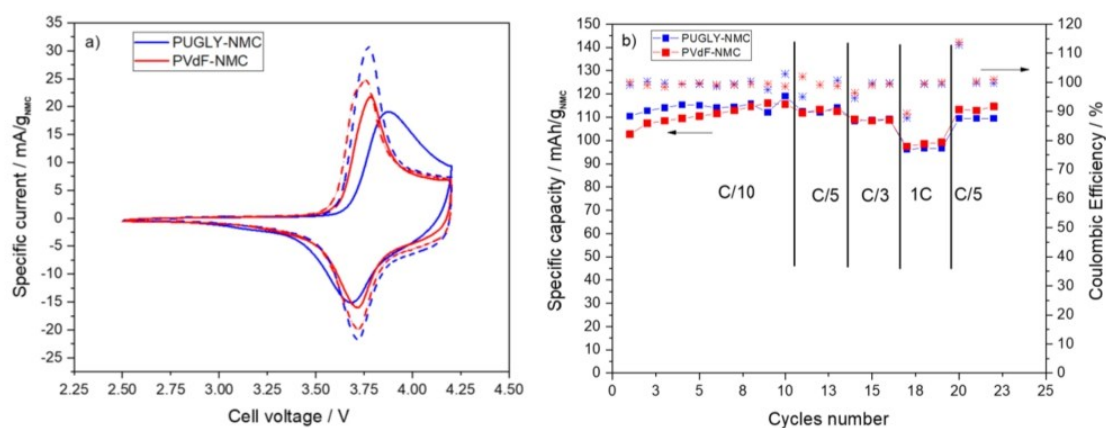


Fig. 7. (a) Cyclic voltammograms at $20 \mu\text{Vs}^{-1}$ before (solid lines) and after (dashed lines) the galvanostatic tests, and (b) trends of the specific capacity (squares) and coulombic efficiency (asterisks) under the rate capability tests at C/5, C/3 and 1C of Li/LP30/NMC cells with PUGLY-NMC or PVdF electrodes (ca. 5.5 mg cm^{-2}) with cell cut-off voltages 2.5 V - 4.2 V. Specific current and capacity values are calculated on the content of NMC.

and PVdF-NMC overlapped. Figs. 7b and S4 show that even under galvanostatic test, the two electrodes feature similar behavior. Also, the capacity retention of the electrodes was similar. Indeed, when the C-rate increased from C/10 to 1C, the specific capacity of PVdF-NMC decreased from $115 \text{ mAh g}_{\text{NMC}}^{-1}$ to $99 \text{ mAh g}_{\text{NMC}}^{-1}$. For PUGLY-NMC, specific capacity correspondingly decreased from $115 \text{ mAh g}_{\text{NMC}}^{-1}$ to $96 \text{ mAh g}_{\text{NMC}}^{-1}$.

After the first conditioning cycles, the PUGLY-NMC cathode was further tested in a wider electrode potential range, by setting the charge cut-off voltage at 4.5 V. Fig. 8a reports the trend of the cycled capacity and coulombic efficiency over 500 cycles carried out at C/3 and 1C. The 1C rate was considered an accelerated aging test condition. The cell featured an outstanding cycle stability. Only after 450 cycles, 200 of each carried out at 1C, the capacity started to slightly fade. Worth noting, we used an as received lithium metal anode and no SEI forming additives were present in the electrolyte. Therefore, the observed fading could be ascribed not only to the cathode, but also to the lithium anode operation. Periodically, C-rate capability tests with charge/discharge at C/5, C/3, 1C and C/5 (4 cycles for each C-rate) were run as a diagnostic tool to check the cell state-of-health. As an example, Fig. 8b reports the capacity and coulombic efficiency trends during one of the C-rate capability tests. Fig. 8c shows representative galvanostatic profiles at different C-rates of the cell. The PUGLY-NMC cathodes featured 165

mAh g^{-1} , 153 mAh g^{-1} , 147 mAh g^{-1} , 126 mAh g^{-1} , and 85 mAh g^{-1} , when calculated taking into account just the NMC content. Therefore, the electrochemical tests indicated that PUGLY can be considered as a valuable green alternative to PVdF. Indeed, the nominal performance of the NMC cathode powder, as for the manufacturer, is $> 150 \text{ mAh g}^{-1}$ [30]. After the full electrochemical characterization, after 500 cycles, the Li/LP30/PUGLY-NMC was disassembled in a dry box and the PUGLY-NMC recovered and washed with acetonitrile. The electrode was analyzed by SEM-EDS and XRD and the results are reported in Figs. 2c and 3c, and in Table 1. The comparison with the data collected with the pristine PUGLY-NMC cathodes highlights that the material did not undergo significant structural and morphological changes after cycling. However, after cycling, I_{003}/I_{104} decreased from 0.93 to 0.33, hence suggesting Ni and Li ions interchange with each other's sites in the crystal lattice.

In order to approach practical conditions, the mass loading of PUGLY-NMC electrodes was doubled. Fig. 8a and 8b include the results of the galvanostatic cycling tests for an electrode featuring 9.9 mg cm^{-2} of PUGLY-NMC. The increase of the mass loading brings about the decrease of the cycled capacity, presumably because of a lack of optimized ionic and electronic connections of NMC particles. However, it is worth noting that PUGLY enables good mechanical and electrochemical stability even at higher mass loadings. Indeed, the thicker electrode kept

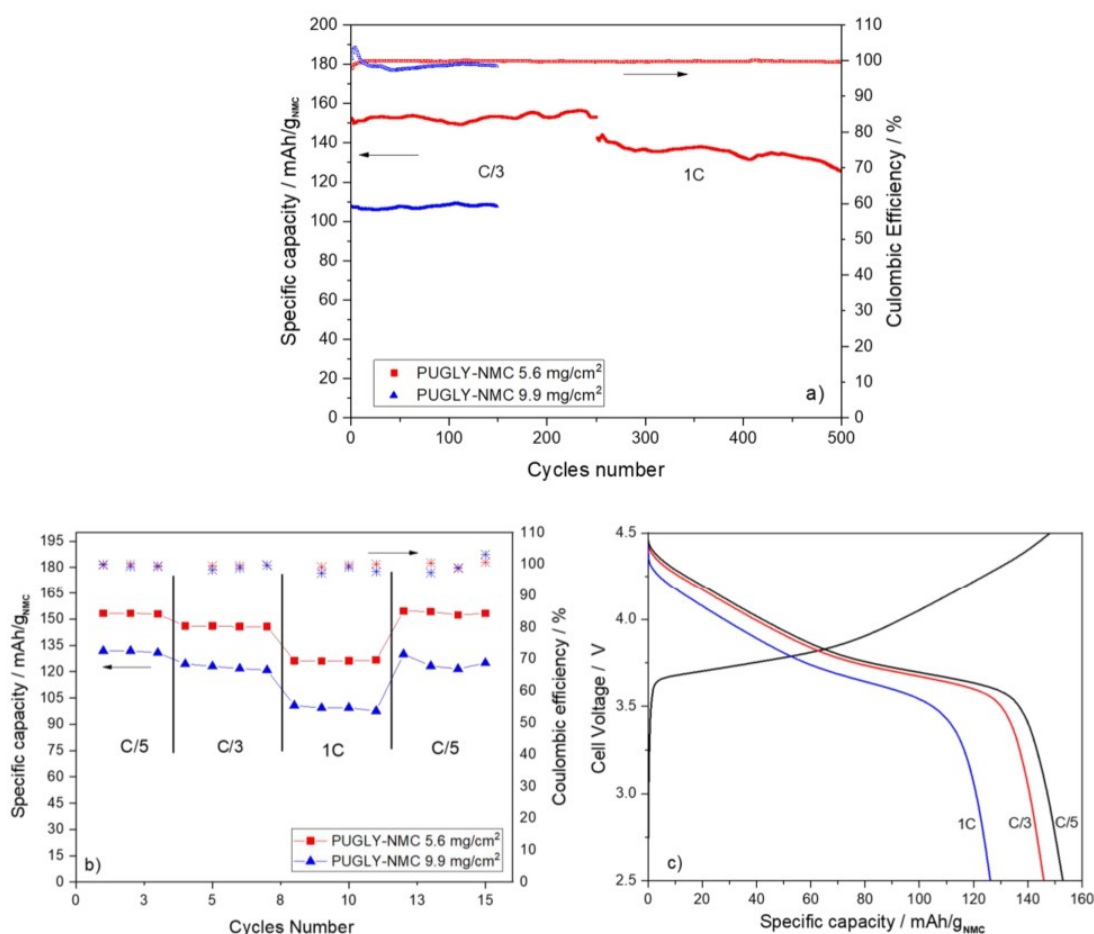


Fig. 8. Galvanostatic tests of the Li/LP30/PUGLY-NMC (5.6 mg cm^{-2}) cell at 4.5 V cut-off potential: trends of the specific capacity and coulombic efficiency (a) over repeated cycles at C/3 and C/1, and (b) under the rate capability tests at C/5, C/3, 1C, (c) galvanostatic profiles for selected C-rates. Specific capacity values are calculated on the content of NMC. Fig. (a) and (b) include the capacity trend over cycling of a thicker electrode featuring 9.9 mg cm^{-2} of PUGLY-NMC.

100% of its initial capacity over 150 cycles.

3.3. PUGLY-NMC electrode direct recycling

An easy method to recover NMC from composite electrodes was set up. The cycled electrodes featured only 0.9 cm diameter and, hence, few mg of PUGLY-NMC, which is too low to quantitatively demonstrate the recycling process and to recover enough material for further analysis. Therefore, the direct recycling method was demonstrated using large PUGLY-NMC cathode films casted on aluminum, freshly prepared (not cycled). Specifically, in the first step, the films were weighed and then the PUGLY-NMC composite was collected by dissolving the PUGLY binder with water spray by an aerograph fed with compressed air. Second step is the water filtering of the composite powder, which was performed with a syringe and a disk filter by firstly pumping the water resulting from the first step and later with demineralized water. Fig. 9 shows procedure and that PUGLY-NMC easily detached from the aluminum layer in a few seconds.

Finally, the biodegradability of the PUGLY solution obtained after the recovery of the binder from the electrode was tested and compared to that of PVdF, both under aerobic and anaerobic conditions (Fig. 10). Under aerobic conditions, PUGLY reached 34% of biodegradation in 50 days, while a complete biodegradation was achieved in just 15 days under anaerobic conditions. As expected, PVdF was highly persistent under both the aerobic and anaerobic conditions tested (0–2% of biodegradation observed in 50–60 days). These results demonstrate the environmental potential of binders like PUGLY if compared to the conventional PVdF binder, indicating these bio-based binders enable the design of a manufacturing-to recycling electrode process where the binder impact is completely reduced.

The collected powder was filtered and washed with water and finally dried at 120 °C overnight. The powder, shown in Fig. 9, consists of an NMC-carbon composite.

XRD, EDS, and XAS analyses (Fig. 3, Table 1 and Section 3.4) indicated that the crystalline domain of the NMC active material is retained.

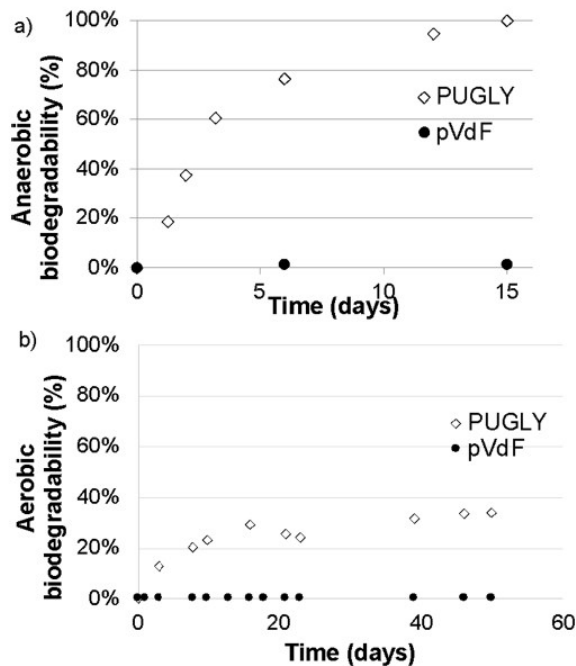


Fig. 10. Biodegradability of PUGLY and PVdF binders under (a) anaerobic and (b) aerobic conditions.

In fact, XRD NMC patterns of the recovered powder overlap those of the pristine one.

Given that delithiated NMC tends to release oxygen above 250 °C [39], and that carbon burns above 400 °C (Fig. 6), direct recycling of the

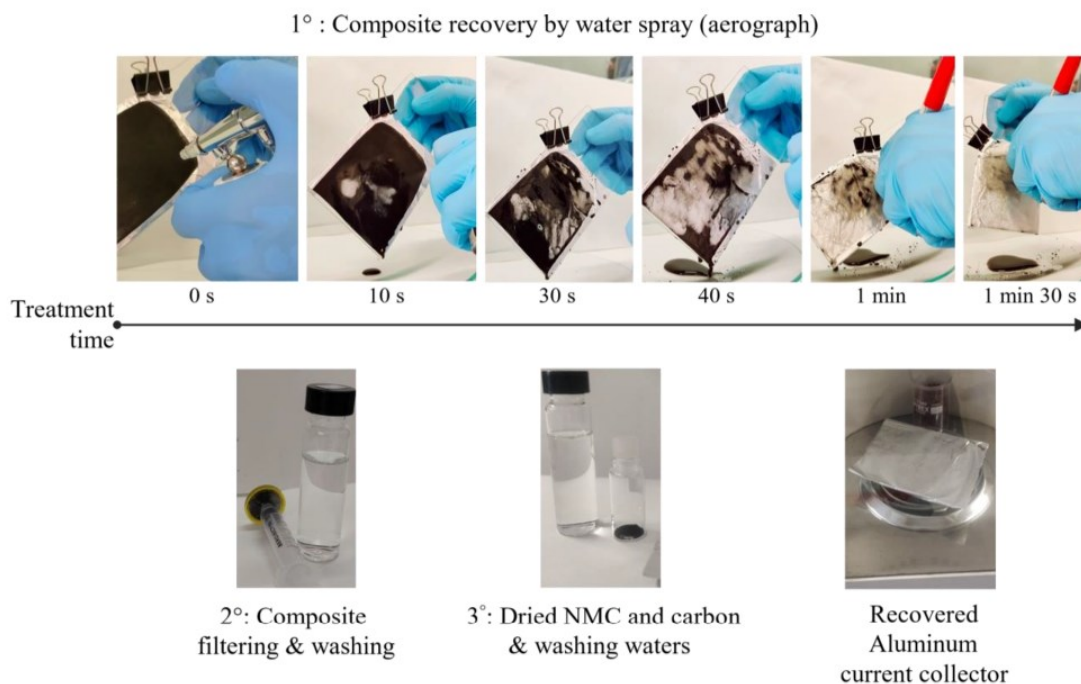


Fig. 9. Procedure to recover PUGLY-NMC composite from casted electrodes by water-spray divided in three steps.

black composite can be a viable approach to keep the pristine chemical and structural features of the active material. Therefore, the NMC-carbon mixture can be reused to produce new PUGLY-NMC electrodes, closing the recycling loop, as demonstrated by Fig. 11 that compares the first CVs of thick PUGLY-NMC electrodes assembled with the fresh NMC powder and the recovered black mass. The voltammograms of the two electrodes are comparable, suggesting that the electrochemical behavior of NMC is preserved after the recovery process. The specific capacity of the recovered electrode is $76 \text{ mAh g}_{\text{NMC}}^{-1}$, lower than that of the fresh one ($95 \text{ mAh g}_{\text{NMC}}^{-1}$), but this difference has to be mainly explained with the high loading of the former electrode (15.6 mg cm^{-2}) vs. the latter (9.9 mg cm^{-2}) and with the fact that it was not galvanostatically activated.

In any case to restore NMC degradation, a process of revitalization, i. e. correction of the lithium stoichiometry, could be performed. Many approaches have been proposed, like NMC reconditioning through conventional solid-state reactions by adding external Li sources (e.g., carbonate or sulfate) [42]. NMC treatment with concentrated Li-ion solutions, through hydrothermal process and subsequent heating steps regenerated the lattice and electrochemical features of NMC with limited cost ($< 10 \text{ \$ Kg}$) [43]. As it concerns pullulan, we consider it as a waste that being biodegradable does not need to be recovered, as well as further purification of waste waters is not needed. In any case to recover PU, heating and precipitation steps can be performed, following the procedure already proposed for its fermentative production [44].

3.4. XAS analyses

To validate the recovery process, an X-ray absorption spectroscopic study has been conducted on the pristine NMC powder, the fresh PUGLY-NMC electrode, and the recovered black powder. The results are presented in Fig. 12. By using the strong selectivity of the XAS probe for the atomic species, the local structure and oxidation state changes associated with the manganese, nickel and cobalt can be revealed. As seen from the different panels of the Fig. 12, which represent nickel, manganese and cobalt K edges of recovered powder compared to the pristine powder and pristine electrode, the three spectra have a close match for all the three elements, indicating the absence of the structural and chemical modification of the local coordination of those metals during the recovery process. The only difference is slight decrease of edge jump peak intensity of Ni and Mn (very little in case of Co) of PUGLY-NMC electrode, which is understandable, as additional

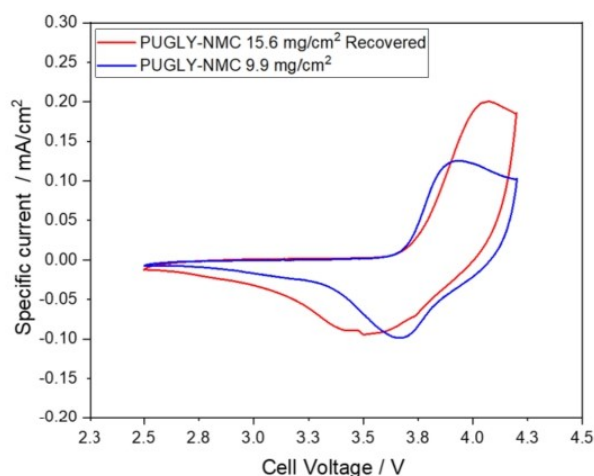


Fig. 11. Comparison of the CVs at $20 \mu\text{Vs}^{-1}$ of a fresh PUGLY-NMC electrode (9.9 mg cm^{-2}) and of an electrode produced by using the recovered black mass (15.6 mg cm^{-2}).

compounds are present in the electrode formulation, whereas recovered powder spectra follows the spectra of the pristine powder. Furthermore, each set of spectra characterized by a pre-edge peaks, here depicted as A, position of which is indicative of the formal charge and then the oxidation state [45]. Once again, no shift in the energy position of such a feature is detected in the three panels. The absence of any detectable shift in the edge position of the spectra suggests that the local charges associated with Mn, Co and Ni are the same while comparing pristine and the recovered powder. This is also confirmed by the EXAFS data (Fig. S5). In all cases two shells are visible: metal (Ni, Mn, or Co respectively) oxygen interaction as the first shell and interaction to metal as the second one: Ni(Mn, Co)-M(Ni, Mn, Co). No local structural changes are visible.

Overall, XAS technique confirmed the same chemical, and structural environment of Mn, Co and Ni in the pristine and recovered powders and electrodes. This fact is striking, also taking into consideration that the XAS probes not only the surface of a sample but also its bulk behavior.

4. Conclusions

Overall, our study demonstrates that the use of water-soluble and biodegradable polymer pullulan for the manufacturing of LIB cathodes is a valuable alternative to traditional binders based on fluorine polymer and has a potential to the development of a sustainable LIB value chain, where devices are designed in view of the recovering of critical elements at their end-of-life.

Specifically, the high-potential cathodes PUGLY-NMC, based on NMC532 and pullulan, were produced in the ambient atmosphere, by avoiding the use of toxic solvents and fluorinated binders. Not only the cathodes featured mechanical properties that are suitable for an automatic production by roll-to-roll equipment, but, and mainly, they exhibited excellent cycling stability over 500 cycles along with good capacity retention at high C-rates.

The use of PUGLY binder will, first of all, decrease electrode manufacturing costs. Electrode production cost based solely on the materials, includes the cost of active materials, carbon, and the binder solution used for the slurry. Table S2 (supplementary information) reports the costs of different binder solutions. The evaluation has been done considering the production of composite electrodes featuring 5% binder, by using inks (including powders, binder and solvent) prepared with 40% of solvent (as in this work), i.e. with a binder concentration in the solution of 7.5%. The cost of a binder solution featuring PVdF ($8\text{--}10 \text{ USD kg}^{-1}$) in NMP ($1\text{--}3 \text{ USD kg}^{-1}$) can be as high as 3.5 USD kg^{-1} [7]. For PVdF-based solutions, the major cost comes from NMP. Substitution of NMP with water ($0.015 \text{ USD kg}^{-1}$) dramatically decreases the cost of the binder solution. As an example, 7.5% wt. CMC ($2\text{--}5 \text{ USD kg}^{-1}$) aqueous solutions, even with the addition of other polymers/plasticisers, like styrol-butadien rubber (SBR, $2\text{--}3 \text{ USD kg}^{-1}$), will cost lower than 0.36 USD kg^{-1} [7].

At present PU ($20\text{--}30 \text{ USD kg}^{-1}$, [46]) is more expensive than CMC, but its mechanical properties are superior [47], as well its increasing market is forecasting a significant cost reduction. However, a solution of 7.5% PUGLY in water, with 1:1 PU:GLY ($0.4\text{--}0.5 \text{ USD kg}^{-1}$ [48]) ratio, costs only 1.0 USD kg^{-1} . This specific cost is 70% lower than that of the PVdF-NMP solution. Despite being affected by the binder to solvent ratio, and binder content in the composite electrodes, these cost values indicate the potential cost reduction by transitioning to water-based electrodes from the materials' point of view. In addition, it has to be underlined that using the aqueous solution would avoid the need of the environments with controlled atmosphere required for processing NMP, with further advantages in terms of costs. In addition, the use of the water processable binder could enable a green, cheap, fast and easy procedure to recover the Li-ion cathode black powders from the cathodes. Indeed, we directly recovered NMC by dissolving the binder and collecting the powders in less than 2 min by means of a water-fed aerograph. The waste-waters used to wash and recover the

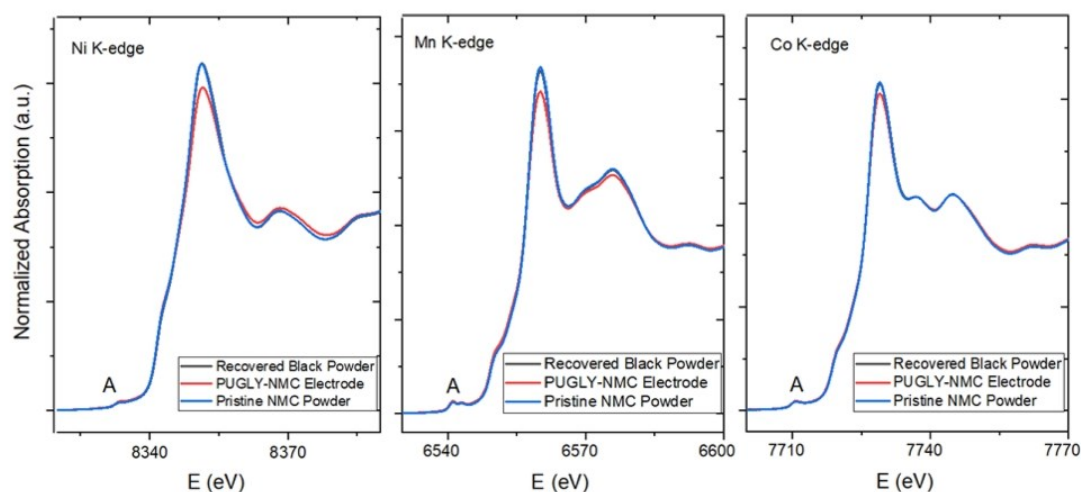


Fig. 12. XAS signals of the pristine NMC powder, the fresh PUGLY-NMC electrode, and the recovered NMC-carbon black powder.

NMC-carbon powders are biodegradable, which is of great importance to close the “sustainability chain” loop. In addition, NMC active material does not suffer any structural and chemical modifications after the recovery process, as verified by the bulk and atomic sensitive XAS investigation.

The size (0.9 cm diameter) of the cycled electrodes was too low to recover enough material for further analysis. Hence, at present, the recovery process has been demonstrated only by using large PUGLY-NMC cathode films casted on aluminum, freshly prepared (not cycled). Work on the assembly and direct recovery of large pouch cells, that will further strengthen our concept, is planned. In any case, the proposed procedure could pave the way towards a further reduction of LIB manufacturing costs by reducing active material losses related to production errors and inaccuracies which today account for the 26% of the total manufacturing costs. Indeed, NMC could be easily recovered from production scraps and put back in the main production stream.

Supporting Information: PVdF-NMC cathode preparation process; SEM pictures and EDS spectra of the pristine NMC523 powder, TGA profiles under argon of the pristine NMC powder and PUGLY polymer composite, TGA profile under O₂ of the PU/GLY polymer composite, galvanostatic profiles for selected C-rates of PUGLY-NMC and PVdF-NMC electrodes, and comparison of the k₂-extracted EXAFS signal taken at the Mn, Ni and Co K-edges and their corresponding Fourier Transform, for all investigated electrodes and powders.

CRedit authorship contribution statement

Alessandro Brilloni: Methodology, Validation, Formal analysis, Investigation, Data curation, Writing – original draft, Visualization. **Federico Poli:** Methodology, Formal analysis, Investigation, Data curation, Writing – original draft, Visualization. **Giovanni Emanuele Spina:** Formal analysis, Investigation, Data curation, Visualization. **Chiara Samori:** Formal analysis, Investigation, Data curation, Writing – original draft, Visualization. **Elena Guidi:** Formal analysis, Investigation, Data curation, Visualization. **Chiara Gualandi:** Formal analysis, Investigation, Data curation, Writing – original draft, Visualization. **Mariam Maisuradze:** Formal analysis, Investigation, Data curation, Visualization. **Marco Giorgetti:** Formal analysis, Investigation, Resources, Data curation, Writing – original draft, Visualization. **Franческа Soavi:** Conceptualization, Methodology, Investigation, Resources, Data curation, Writing – original draft, Visualization, Supervision.

Declaration of Competing Interest

The authors declare that they have no known competing financial interests or personal relationships that could have appeared to influence the work reported in this paper.

Acknowledgments

“Piano Triennale di Realizzazione 2019–2021, Accordo di Programma Ministero dello Sviluppo Economico” – ENEA and “New generation of electrochemical energy storage systems”- Progetto Alte Competenze per la Ricerca e il Trasferimento Tecnologico POR FSE 2014/2020 - REGIONE EMILIA ROMAGNA are acknowledged for the financial support. Measurements at ELETTRA were funded by the Ceric project number 20212162 (M. Giorgetti as PI).

Supplementary materials

Supplementary material associated with this article can be found, in the online version, at doi:10.1016/j.electacta.2022.140376.

References

- [1] European Commission, The European Green Deal, European Commission, Brussels, 2019, 11.12.2019, COM640 final, https://ec.europa.eu/info/strategy/priorities-2019-2024/european-green-deal_en. Date of access 02/11/2021.
- [2] M. Killer, M. Farrokhsheer, N.G. Paterakis, Implementation of large-scale Li-ion battery energy storage systems within the EMEA region, *Appl. Energy* 260 (2020), 114166.
- [3] S. Dühnen, J. Betz, M. Kolek, R. Schmich, M. Winter, T. Placke, Toward green battery cells: perspective on materials and technologies, *Small Methods* 4 (2020), 2000039.
- [4] L. Mauler, F. Duffner, J. Leker, Economies of scale in battery cell manufacturing: the impact of material and process innovations, *Appl. Energy* 286 (2021), 116499.
- [5] A. Manthiram, A reflection on lithium-ion battery cathode chemistry, *Nat. Commun.* 11 (2020) 1550.
- [6] European Commission, Annex XVII to REACH (Regulation concerning the Registration, Evaluation, Authorisation and Restriction of Chemicals, European Commission, Brussels, 2019, 9.4.2019 SWD1300 final, <https://eur-lex.europa.eu>. Date of access 02/11/2021.
- [7] D. Bresser, A. Moretti, A. Varzi, S. Passerini, Alternative Binders for sustainable electrochemical energy storage—the transition to aqueous electrode processing and bio-derived polymers, *Energy Environ. Sci.* 11 (2018) 3096.
- [8] D.L. Wood, J.D. Quass, J. Li, S. Ahmed, D. Ventola, C. Daniel, Technical and economic analysis of solvent-based lithium-ion electrode drying with water and NMP, *Dry. Technol.* 36 (2018) 234–244.
- [9] J. Li, Y. Lu, T. Yang, D. Ge, D.L. Wood, Z. Li, Water-based electrode manufacturing and direct recycling of lithium-ion battery electrodes—a green and sustainable manufacturing system, *iScience* 23 (2020), 101081.

- [10] R. Schröder, M. Aydemir, G. Seliger, Comparatively assessing different shapes of lithium-ion battery cells, *Proced. Manuf.* 8 (2017) 104–111.
- [11] Y. Liu, R. Zhang, J. Wang, Y. Wang, Current and future lithium-ion battery manufacturing, *iScience* 24 (2021), 102332.
- [12] C.M. Costa, E. Lizundia, S. Lanceros-Méndez, Polymers for advanced lithium-ion batteries: state of the art and future needs on polymers for the different battery components, *Prog. Energy Combust. Sci.* 79 (2020), 100846.
- [13] M. Wood, J. Li, R.E. Ruther, Z. Du, E.C. Self, H.M. Meyer, C. Daniel, I. Belharouak, D.L. Wood, Chemical stability and long-term cell performance of low-cobalt, Ni-Rich cathodes prepared by aqueous processing for high-energy Li-Ion batteries, *Energy Storage Mater.* 24 (2020) 188–197.
- [14] P.P. Prosini, C. Cento, M. Carewska, A. Masci, Electrochemical performance of Li-ion batteries assembled with water-processable electrodes, *Solid State Ion.* 274 (2015) 34–39.
- [15] F. Bigoni, F. De Giorgio, F. Soavi, C. Arbizzani, Sodium alginate: a water-processable binder in high-voltage cathode formulations, *J. Electrochem. Soc.* 164 (2016) A6171.
- [16] F. De Giorgio, A. La Monaca, A. Dinter, M. Frankenberger, K.-H. Pettinger, C. Arbizzani, Water-processable $\text{Li}_4\text{Ti}_5\text{O}_{12}$ electrodes featuring eco-friendly sodium alginate binder, *Electrochim. Acta* 289 (2018) 112–119.
- [17] M. Kuenzel, D. Bresser, T. Diemant, D. Vieira Carvalho, G.-T. Kim, J. Behm, S. Passerini, Complementary strategies toward the aqueous processing of high-voltage $\text{LiNi}_{0.5}\text{Mn}_{1.5}\text{O}_4$ lithium-ion cathodes, *ChemSusChem* 11 (2018) 562–573.
- [18] F. Poli, D. Momodu, G.E. Spina, A. Terella, B.K. Mutuma, M.L. Focarete, N. Manyala, F. Soavi, Pullulan-ionic liquid-based supercapacitor: a novel, smart combination of components for an easy-to-dispose device, *Electrochim. Acta* 338 (2020), 135872.
- [19] G.E. Spina, F. Poli, A. Brilloni, D. Marchese, F. Soavi, Natural polymers for green supercapacitors, *Energies* 13 (2020) 3115–3131.
- [20] A. Brilloni, F. Marchesini, F. Poli, E. Petri, F. Soavi, Performance comparison of LMNO cathodes produced with pullulan or PEDOT:PSS water-processable binders, *Energies* 15 (7) (2022) 2608.
- [21] P.R. Vuddanda, M. Montenegro-Nicolini, J.O. Morales, S. Velaga, Effect of plasticizers on the physico-mechanical properties of pullulan based pharmaceutical oral films, *Eur. J. Pharmaceut. Sci.* 96 (2017) 290–298.
- [22] A.N. Preman, H. Lee, J. Yoo, I.T. Kim, T. Saito, S. Ahn, Progress of 3D network binders in silicon anodes for lithium ion batteries, *J. Mater. Chem. A* 8 (2020) 25548–25570.
- [23] X. Zheng, Z. Zhu, X. Lin, Y. Zhang, Y. He, H. Cao, Z. Sun, A mini-review on metal recycling from spent lithium ion batteries, *Engineering* 4 (2018) 361.
- [24] M. Greenwood, M. Wentker, J. Leker, A region-specific raw material and lithium-ion battery criticality methodology with an assessment of NMC cathode technology, *Appl. Energy* 302 (2021), 117512.
- [25] E. Fan, L. Li, Z. Wang, J. Lin, Y. Huang, Y. Yao, R. Chen, F. Wu, Sustainable recycling technology for Li-ion batteries and beyond: challenges and future prospects, *Chem. Rev.* 120 (2020) 7020.
- [26] C. Liu, J. Lin, H. Cao, Y. Zhang, Z. Sun, Recycling of spent lithium-ion batteries in view of lithium recovery: a critical review, *J. Clean. Prod.* 228 (2019) 801.
- [27] L. Oliveira, M. Messagie, S. Rangaraju, J. Sanfelix, M. Rivas, J. Mierlo, Key issues of LIBs from resource depletion to environmental KPI, *J. Clean. Prod.* 108 (2015) 354.
- [28] Y. Yao, M. Zhu, Z. Zhao, B. Tong, Y. Fan, Z. Hua, Hydrometallurgical processes for recycling spent lithium-ion batteries: a critical review, *ACS Sustain. Chem. Eng.* 6 (2018) 13611–13627.
- [29] <https://www.acs.org/content/acs/en/greenchemistry>. Date of access 12/04/2022.
- [30] <http://www.libgroup.net/index.html>. Date of access 12/04/2022.
- [31] I.A. Shkrob, J.A. Gilbert, P.J. Phillips, R. Klie, R.T. Haasch, J. Barenó, D. P. Abraham, Chemical weathering of layered Ni-rich oxide electrode materials: evidence for cation exchange, *J. Electrochem. Soc.* 164 (2017) A1489.
- [32] G. Torri, D. Fabbri, Biochar enables anaerobic digestion of aqueous phase from intermediate pyrolysis of biomass, *Bioresour. Technol.* 172 (2014) 335–341.
- [33] Secretary-General of the OECD., Guideline For Testing of Chemicals: Ready Biodegradability; OECD Guideline 301, Organization for Economic Cooperation and Development, Paris, 1992.
- [34] G. Aquilanti, M. Giorgetti, R. Dominko, L. Stievano, I. Arcon, N. Novello, L. Olivi, Operando characterization of batteries using x-ray absorption spectroscopy: advances at the beamline XAFS at synchrotron Elettra, *J. Phys. D Appl. Phys.* 50 (2017), 074001.
- [35] T. Li, X.Z. Yuan, L. Zhang, D. Song, K. Shi, C. Bock, Degradation mechanisms and mitigation strategies of nickel-rich NMC-based lithium-ion batteries, *Electrochem. Energy Rev.* 3 (2020) 43–80.
- [36] X. Zhang, W.J. Jiang, A. Mauger, Qilu, F. Gendron, C.M. Julien, Minimization of the cation mixing in $\text{Li}_{1-x}(\text{NMC})_{1-x}\text{O}_2$ as cathode material, *J. Power Sources* 195 (2010) 1292–1301.
- [37] P. Ruschhaupt, A. Varzi, S. Passerini, Natural polymers as green binders for high-loading supercapacitor electrodes, *ChemSusChem* 13 (2020) 763–770.
- [38] J. Sicklinger, M. Metzger, H. Beyer, D. Pritzl, H.A. Gasteiger, Ambient storage derived surface contamination of NCM811 and NCM111: performance implications and mitigation strategies, *J. Electrochem. Soc.* 166 (2019) A2322–A2335.
- [39] S. Min Bak, E. Hu, Y. Zhou, X. Yu, S.D. Senanayake, S.J. Cho, K.B. Kim, K.Y. Chung, X.Q. Yang, K.W. Nam, Structural changes and thermal stability of charged $\text{LiNi}_x\text{MnyCo}_z\text{O}_2$ cathode materials studied by combined *in situ* time-resolved XRD and mass spectroscopy, *ACS Appl. Mater. Interfaces* 6 (2014) 22594–22601.
- [40] C. Gualandi, A. Zucchelli, M. Fernández Osorio, J. Belcari, M.L. Focarete, Nanovascularization of polymer matrix: generation of nanochannels and nanotubes by sacrificial electrospun fibers, *Nano Lett.* 13 (2013) 5385–5390.
- [41] P. Oguzhan, F. Yanglar, Pullulan, Production and usage in food industry, *J. Food Sc. Tech.* 4 (3) (2013) 57–63.
- [42] C. Ferrara, R. Ruffo, E. Quartarone, P. Mustarelli, Circular economy and the fate of lithium batteries: second life and recycling, *Adv. Energy Sustain. Res.* 2 (2021), 2100047.
- [43] S.E. Sloop, L. Crandon, M. Allen, M.M. Lerner, H. Zhang, W. Sirisaksoontorn, L. Gaines, J. Kim, M. Lee, Cathode healing methods for recycling of lithium-ion batteries, *Sustain. Mater. Technol.* 22 (2019) e00113.
- [44] G.V.S.R. Krishna, K. Srinivasulu, M. Usha, B. Bodaiah, Y.V.V. Kumar, M. Vijaya, P. Sudhakar, Sequential heating and solvent precipitation for effective pullulan recovery from jaggery based fermentation broths, *J. Pharm. Res.* 10 (2016) 296–300.
- [45] D. Buchholz, J. Li, S. Passerini, G. Aquilanti, D. Wang, M. Giorgetti, X-ray absorption spectroscopy investigation of lithium-rich, cobalt-poor layered-oxide cathode material with high capacity, *ChemElectroChem* 2 (2015) 85–97.
- [46] S. Farris, I.U. Unalan, L. Introzzi, J.M. Fuentes-Alventosa, C.A. Cozzolino, Pullulan-based films and coatings for food packaging: present applications, emerging opportunities, and future challenges, *J. Appl. Polym. Sci.* 131 (2014) 40539.
- [47] A.N. Preman, H. Lee, J. Yoo, I.T. Kim, T. Saito, S. Ahn, Progress of 3D network binders in silicon anodes for lithium ion batteries, *J. Mater. Chem. A* 8 (2020) 25548–25570.
- [48] A.R. Abdul Aziz, W. Tan Hooi, B. Archina, Two-step purification of glycerol as a value added by product from the biodiesel production process, *Front. Chem.* 7 (2019) 2296.

2.3 Pullulan and PEDOT:PSS: performance comparison

After exploiting PU, the investigation on water processable binders was focused on a different class of polymers, namely electronically conductive polymers. Among the conducting polymers, poly(3,4-ethylenedioxythiophene) (PEDOT) is one of the most popular and it has been already demonstrated as a valuable component of cathode in LIBs [14-17]. In recent works, PEDOT has been doped with poly(styrene sulfonate) (PSS) anion to form PEDOT:PSS reaching high conductivity as $10\text{-}10^2\text{ S cm}^{-1}$, but it has been exploited limited to coating particles that afterwards have been used to prepare electrodes with PVdF binder [18-20].

In this part of the work, I wanted to compare the performances of PEDOT:PSS and PU as water processable binders for high-voltage lithium-metal battery cells. Specifically, $\text{LiNi}_{0.5}\text{Mn}_{1.5}\text{O}_4$ (LMNO) electrodes were fabricated using PU (LMNO-PU) or PEDOT:PSS (LMNO-PE), assembled with Li-metal anode and 1M LiPF₆ in 1:1 (v:v) ethylene carbonate (EC): dimethyl carbonate (DMC) (LP30 electrolyte), and compared to that of cells assembled with LMNO featuring PVdF.

Thermogravimetric analysis (TGA) was performed at first to determine if there is any difference in the maximum working temperature of the different binders. All the three binders, namely PU, PEDOT:PSS and PvDF remain stable before 200 °C. Afterwards, the voltametric and galvanostatic tests were performed. The tests indicated that PU-based electrodes perform like the conventional PVdF-based ones and that the use of PEDOT:PSS significantly improves specific capacity and capacity retention at different current rates and over cycling.

For example, LMNO-PE electrodes featured 130 mAh g⁻¹ at C/10, which is slightly higher than the nominal value reported by the LMNO powder provider (125 mAh g⁻¹). Moreover, lithium metal cells assembled with PEDOT:PSS-based cathode showed an outstanding capacity retention of 100% over 200 cycles carried out at 1C and with a high cut-off voltage of 5 V. The good cycling stability of LMNO-PE was related to the ability of PEDOT:PSS to be a “barrier” against undesired side reactions of LMNO with the electrolyte, an effect that has been already observed for cathodes produced with PVdF binder and PEDOT:PSS-coated LMNO particles [18-20].

At each C-rate, the highest specific capacity was achieved with LMNO-PE, while LMNO-PU cathodes performed very similarly to LMNO-PvDF cathodes. Indeed, at C/5 LMNO-PE featured 136 mAh g⁻¹. This value decreased by 17% (to 113 mAh g⁻¹) when current increased at C/1. For LMNO-PU and LPNMO-PvDF, the specific capacity at C/5 was 111 mAh g⁻¹ and 114 mAh g⁻¹ and it decreased to 103 mAh g⁻¹ at C/1.

The results of this work demonstrate that PU and PEDOT:PSS are valuable green water processable binder alternative to PVdF for high voltage cathode that can guarantee high performance and, in the case of PEDOT:PSS, enhance the cycling stability. This conclusion opens the concrete possibility of designing a sustainable manufacturing process for LIBs with polymers of different origins and different outcomes.

What is left to demonstrate is the biodegradability of PEDOT:PSS binder and the impact that will have at the end of life in order to be fully comparable with PU and close the cycle life of green sustainable Lithium-ion batteries. The experimental methods and the results of this study are reported in [2], which is here attached as complete publication.

Article

Performance Comparison of LMNO Cathodes Produced with Pullulan or PEDOT:PSS Water-Processable Binders

Alessandro Brilloni ¹ , Francesco Marchesini ¹, Federico Poli ¹, Elisabetta Petri ¹ and Francesca Soavi ^{1,2,3,*} 

¹ Department of Chemistry “Giacomo Ciamician”, Alma Mater Studiorum University of Bologna, Via Selmi 2, 40126 Bologna, Italy; alessandro.brilloni2@unibo.it (A.B.); francesco.marchesini@studio.unibo.it (F.M.); federico.poli8@unibo.it (F.P.); elisabetta.petri2@unibo.it (E.P.)

² ENERCube, Centro Ricerche Energia, Ambiente e Mare, Centro Interdipartimentale per la Ricerca Industriale Fonti Rinnovabili, Ambiente, Mare ed Energia (CIRI-FRAME), Alma Mater Studiorum University of Bologna, Viale Ciro Menotti 48, 48122 Marina di Ravenna, Italy

³ National Reference Center for Electrochemical Energy Storage (GISEL)-INSTM, Via G. Giusti 9, 50121 Firenze, Italy

* Correspondence: francesca.soavi@unibo.it



Citation: Brilloni, A.; Marchesini, F.; Poli, F.; Petri, E.; Soavi, F. Performance Comparison of LMNO Cathodes Produced with Pullulan or PEDOT:PSS Water-Processable Binders. *Energies* **2022**, *15*, 2608. <https://doi.org/10.3390/en15072608>

Academic Editors: Carlos Miguel Costa and Daniel-Ioan Stroe

Received: 25 February 2022

Accepted: 25 March 2022

Published: 2 April 2022

Publisher’s Note: MDPI stays neutral with regard to jurisdictional claims in published maps and institutional affiliations.



Copyright: © 2022 by the authors. Licensee MDPI, Basel, Switzerland. This article is an open access article distributed under the terms and conditions of the Creative Commons Attribution (CC BY) license (<https://creativecommons.org/licenses/by/4.0/>).

Abstract: The aim of this paper is to demonstrate lithium metal battery cells assembled with high potential cathodes produced by sustainable processes. Specifically, $\text{LiNi}_{0.5}\text{Mn}_{1.5}\text{O}_4$ (LMNO) electrodes were fabricated using two different water-processable binders: pullulan (PU) or the bifunctional electronically conductive poly(3,4-ethylenedioxythiophene)-poly(styrene sulfonate) (PEDOT:PSS). The cell performance was evaluated by voltammetric and galvanostatic charge/discharge cycles at different C-rates with 1M LiPF_6 in 1:1 (v:v) ethylene carbonate (EC):dimethyl carbonate (DMC) (LP30) electrolyte and compared to that of cells assembled with LMNO featuring poly(vinylidene difluoride) (PVdF). At C/10, the specific capacity of LMNO-PEDOT:PSS and LMNO-PU were, respectively, 130 mAh g^{-1} and 127 mAh g^{-1} , slightly higher than that of LMNO-PVdF (124 mAh g^{-1}). While the capacity retention at higher C-rates and under repeated cycling of LMNO-PU and LMNO-PVdF electrodes was similar, LMNO-PEDOT:PSS featured superior performance. Indeed, lithium metal cells assembled with PEDOT:PSS featured a capacity retention of 100% over 200 cycles carried out at C/1 and with a high cut-off voltage of 5 V. Overall, this work demonstrates that both the water-processable binders are a valuable alternative to PVdF. In addition, the use of PEDOT:PSS significantly improves the cycle life of the cell, even when high-voltage cathodes are used, therefore demonstrating the feasibility of the production of a green lithium metal battery that can exhibit a specific energy of 400 Wh kg^{-1} , evaluated at the electrode material level. Our work further demonstrates the importance of the use of functional binders in electrode manufacturing.

Keywords: lithium-ion battery cathode; LMNO; pullulan; PEDOT:PSS; water processable binder; electronically conducting polymer

1. Introduction

The transition towards the use of cobalt-free, high voltage, and capacity cathode active materials (CAM), such as $\text{Li}(\text{Ni}_x\text{Mn}_y)\text{O}_2$ (LMNO), will bring about the so-called cell generation Gen3b [1]. $\text{LiNi}_{0.5}\text{Mn}_{1.5}\text{O}_4$ is one of the most promising cathode formulations, featuring a theoretical specific capacity of 145 mAh g^{-1} with working potential of ca. 4.7 V vs. Li^+/Li [2].

While it displays good electronic and Li^+ conductivities, and excellent rate capability, it may exhibit severe capacity fade over cycling, especially at elevated temperatures [3,4]. To address the European Battery Alliance (EBA) goal [5], a valuable practical strategy that is being pursued is the shifting of the electrode productive process from organic solvents through to aqueous ones exploiting bio-derived and water processable binders [6].

Nowadays, poly(vinylidene difluoride) (PVdF) is commonly used for its good chemical and electrochemical stability, and solubilized N-methyl-2-pyrrolidone (NMP). NMP has been listed by Europe as a high concern substance [6,7]. It is toxic and requires expensive atmosphere-controlled environments, affecting the economic and environmental impact on cathode and Lithium Batteries (LIBs) manufacturing. Indeed, it has been reported that electrode drying and NMP recovery process imposes an energy demand of ~10 kWh per kg of NMP as it evaporates at 200 °C [6,8].

Commonly used aqueous binders are less expensive than PVdF and require a lower drying temperature and time [6]. Furthermore, for their low environmental impact during the manufacturing and the end-of-life management, they open new approaches towards the design for recycling of LIBs [9,10]. Water-processable polymers, such as cellulose, alginate, guar gum, have already been reported as successful alternatives to PVdF for CAMs [6,8–13].

Pullulan, for its high water-solubility, excellent mechanical properties, O₂-impermeability, stability at high pH, and biodegradability, is emerging as a green electrode binder. Pullulan has been reported as a binder component of silicon anodes, as well as pullulan: glycerol 1:1 mixture (PU) exhibited excellent binding capability for thick carbon electrodes of supercapacitors and Li(Ni_{0.5}Mn_{0.3}Co_{0.2})O₂ (NMC532) cathodes [10,13–15]. Supercapacitors working with PU-based electrodes and separators, combined with ionic liquid electrolyte, were demonstrated to be stable over thousands of cycles operated with a cell voltage of 3.2 V [14,15]. In [10], we demonstrated PU-based NMC532 featuring up to 167 mAh g⁻¹ of NMC532, and excellent cycling stability over 500 cycles. On the other hand, electronically conductive polymers conjugate the typical characteristics of polymeric materials, such as the high chemical inertia, good mechanical properties, and lightness with the ability to conduct electrons. Among the conducting polymers, poly(3,4-ethylenedioxythiophene) (PEDOT) is one of the most popular and it has been widely proposed as a key component for the next-generation consumer electronics and energy storage devices [16,17]. PEDOT has been already demonstrated as a valuable component of cathodes in lithium-ion batteries. Ozerova et al. showed that mechanical mixing of LiFePO₄/C with pre-polymerized PEDOT particles, in the presence of different surfactants (Triton X-100 and cetyltrimethylammonium bromide) improved the cathode specific capacity by 20% with respect to the uncoated LiFePO₄, reaching 81 mAh g⁻¹ at 1600 mA g⁻¹ [18]. In situ oxidative polymerization of 3,4-ethylenedioxythiophene (EDOT) in acidic media has been used by Jinfeng Liu et al. to coat particles of LMNO with PEDOT. The resulting material has been exploited to prepare electrodes with a PVdF-binder. PEDOT-coated LMNO particles featured a better capacity retention with respect to the pristine material, with improved gravimetric capacity [19]. Laisuo et al. showed that a protective thin film of PEDOT on LMNO obtained by chemical vapor deposition (CVD) increases the rate capacity and extends the high temperature (50 °C) cycle life of LiMn₂O₄ by over 60% [20]. Moreover, by operando synchrotron X-ray diffraction, they demonstrated that PEDOT further improves current homogeneity in LiCoO₂ electrodes during cycling [21].

PEDOT doped with poly(styrene sulfonate) (PSS) anion (PEDOT:PSS) features high conductivity (10–10² S cm⁻¹), and nowadays commercial aqueous solutions of PEDOT:PSS are available. PEDOT:PSS has been exploited to coat particles that have been used to prepare electrodes with PVdF binder. PEDOT:PSS-coated Li_{1.2}Ni_{0.2}Mn_{0.6}O₂ featured 286 mAh g⁻¹ at 0.1 C and 146 mAh g⁻¹ at C/1 after 100 cycles [22]. Electrospun of LMNO nanoparticles coated with 1%wt of PEDOT:PSS exhibited improved cycle stability as side reactions with the electrolyte were alleviated. By this approach, up to 128 mAh g⁻¹ were achieved, but cycling stability was demonstrated only over 30 cycles [23].

The availability of commercial, aqueous PEDOT:PSS solutions opens the possibility to use it both as CAM coating and as a “bifunctional”, green, electronically conductive binder. Along with its binding ability, PEDOT:PSS provides conductive bridges between individual particles, which can improve the electron transport within the electrode components [24]. Furthermore, PEDOT:PSS is attracting much interest as self-healing material, i.e., as a material that is able to recover its functionalities after being damaged. This property could

be seen as an additional advantage that might positively impact on the cathode cycling stability and LIB safety [25]. The good mechanical properties of PEDOT:PSS binder have also been demonstrated with silicon-based anodes, which are known for their relevant volume expansion/contraction during the lithiation/delithiation processes [26–28].

While PEDOT:PSS binder has been successfully demonstrated for LiFePO_4 , LiCoO_2 , and NMC composite electrodes [17,29], to the best of our knowledge, PEDOT:PSS has not been reported as bifunctional binder for high-voltage LMNO electrodes, yet.

The aim of this work is to demonstrate high-voltage lithium metal battery cells, assembled with a cathode produced by sustainable processes. Specifically, LMNO electrodes were fabricated using two different water-processable binders: pullulan (PU) or the bifunctional electronically conductive poly(3,4-ethylenedioxythiophene)-poly(styrene sulfonate) (PEDOT:PSS). While PU and PEDOT:PSS feature different structure and chemical-physical properties, they share three important features: they both (i) have high technological and market relevance, (ii) can be aqueous processed, and (iii) are biocompatible. Pullulan is indeed attracting much attention in the packaging industry, mainly in pharmaceuticals and food [30,31]. In turn, PEDOT:PSS has been demonstrated to be a key material for organic electronics, sensing, and wearable applications [16]. In these fields, processability and technological exploitation of these polymers have been widely demonstrated. With our study we aim to further demonstrate the use of these two polymers in an additional, strategic technological sector, namely, LIB manufacturing.

The performance of the cells assembled with the two different aqueous binders was evaluated by voltammetric and galvanostatic charge/discharge cycles at different C-rates with 1M LiPF_6 in 1:1 (v:v) ethylene carbonate (EC):dimethyl carbonate (DMC) (LP30 electrolyte) and compared to that of cells assembled with LMNO featuring poly(vinylidene difluoride) (PVdF). The results demonstrated that PU and PEDOT:PSS are valuable green water processable binder alternatives to PVdF for high-voltage cathode that can guarantee high performance and, in the case of PEDOT:PSS, enhance the cycling stability.

2. Materials and Methods

2.1. Preparation of the Electrodes

Electrodes were prepared using the commercial LMNO powder, purchased from NANOMYTE[®] SP-10 (NEI Corporation, Somerset, NJ, USA), as active material. The powder stoichiometry is $\text{LiMn}_{1.5}\text{Ni}_{0.5}\text{O}_4$, the average particle size is 4–7 μm , and the nominal capacity (at C/10, between 3.5 and 5 V vs. Li^+/Li) is 125 mAh g^{-1} . Different cathodes formulations have been studied. The identification codes and the areal mass loadings of the composites and LMNO of the electrodes produced by different binders are reported in Table 1. In LMNO-PU electrodes, the utilization of the bio derived, water processable binder pullulan:glycerol 1:1 in weight (PU) was investigated. They featured 85% LMNO, 10% carbon conductive additive (Super C45, Imerys, Paris, France), and 5% PU (2.5% pullulan and 2.5% glycerol). LMNO-PU composite mass loading was 2.1 mg cm^{-2} . The effect of the use of the bifunctional binder PEDOT:PSS was explored with LMNO-PE electrodes that featured 85% LMNO, 10% conductive carbon (Super C45), and 5% PEDOT:PSS. LMNO-PE composite mass loading was 3.8 mg cm^{-2} . As a benchmark, electrodes were also produced with PVdF binder and processed with NMP solvent, and they are labelled in the following text as LMNO-PVdF. Their composition was 85% LMNO, 10% conductive carbon (Super C65, Imerys), and 5% PVdF, the composite mass loading was 3.7 mg cm^{-2} . For LMNO-PU production, at first, pullulan powder (TCI) was dissolved in Milli-Q water with Glycerol (GLY, Sigma-Aldrich, Merck Life Science S.r.l., Milan, Italy) with a mass ratio 1:1 and stirred for 30 min. LMNO and carbon conductive additive (Super C45), with a mass ratio 85:10 was added in a jar with the binder obtaining a slurry that was milled at 250 rpm for 30 + 30 (reverse) min in a planetary mill (FRITSCH, Pulverisette, Lainate, Milan, Italy). The slurry was subsequently casted on aluminum foil by a Mini Coating Machine (Hohsen Corporation, Osaka, Japan) at 0.3 cm s^{-1} and with a bar distance of 8 mil (250 μm). The coated films were dried at 60 °C overnight in a thermostatic oven, pressed at

4 ton cm^{-2} , and dried again under dynamic vacuum (Büchi glass oven B-585) overnight at 60 °C to eliminate any water trace. The LMNO-PE electrodes were prepared by mixing the LMNO powder and the conductive carbon, with a mass ratio of 85:10 by dry milling at 250 rpm for 5 min in the planetary mill. Then, the aqueous solution of PEDOT:PSS (Sigma-Aldrich, 1.1%) was added to the jar, resulting in a slurry that was milled at 250 rpm for 1 h (30 min reverse). The slurry was subsequently casted on aluminum foil, dried, and pressed following the same procedure used for LMNO-PU electrodes. For the LMNO-PVdF production, LMNO and the conductive carbon powders with a mass ratio of 85:10, were dry milled at 250 rpm for 5 min. Then, a solution of PVdF in NMP was added to the jar, resulting in a slurry that was milled at 250 rpm for 1 h (30 min reverse). The slurry was subsequently casted on aluminum foil, dried at 60 °C overnight in a thermostatic oven, pressed, and dried again under dynamic vacuum at 120 °C to eliminate any solvent trace.

Finally, all the prepared electrodes were transferred and stored in a dry box under Argon atmosphere (MBraun, H_2O and $\text{O}_2 < 1$ ppm).

Table 1. Acronyms, and composite and LMNO areal loadings of the cathodes produced with pullulan or PEDOT:PSS or PVdF binders.

Electrode Name	Binder	Composite Mass Loading (mg cm^{-2})	LMNO Mass Loading (mg cm^{-2})
LMNO-PU	Pullulan	2.1	1.8
LMNO-PE	PEDOT:PSS	3.8	3.2
LMNO-PVdF	PVdF	3.7	3.2

2.2. Chemical–Physical Analyses

X-ray diffraction (XRD) spectra were collected by a PANalytical X'Pert PRO powder diffractometer equipped with a X'Celerator detector ($\text{CuK}\alpha$ radiation, $\lambda = 1.5406 \text{ \AA}$, 40 mA, 40 kV), radiation source, and Ni filter by continuous scanning mode (step 0.017° 2θ step size, 10 s/step scan rate). Thermogravimetric Analysis (TGA) were performed by a TA Thermal Analysis Q50 equipment, under O_2 flow (60 mL min^{-1}) with a scan rate of $10 \text{ }^\circ\text{C min}^{-1}$ up to $550 \text{ }^\circ\text{C}$.

2.3. Lithium Metal/LMNO Coin Cell Prototype Assembly

The prepared electrodes were cut into 18 mm disks and tested as cathode of 2032 coin cells 2032 featuring 200 μL of a 1M LiPF_6 in 1:1 (*v:v*) ethylene carbonate (EC): dimethyl carbonate (DMC) (LP30, Selectilyte BASF, Ludwigshafen, Germany) solution as electrolyte with commercial Celgard 2300 as separator, and metallic lithium 16 mm as quasi-reference counter electrode. All the tested cells were assembled in a dry box (Labmaster 130, H_2O , and $\text{O}_2 < 0.1$ ppm MBraun, Garching, Germany).

2.4. Electrochemical Characterization

The electrochemical test consisted in cyclic voltammetry (CV) and galvanostatic charge/discharge cycles with potential limitation (GCPL). The electrochemical tests were performed in a thermostatic oven at 30 °C with a BioLogic VSP multichannel potentiostat/galvanostat/FRA. The measurements were carried with a two-electrode set up, in which the working electrode was the tested material, and the counter-reference was the lithium disk (see Section 2.3). All the Li/LMNO cells were tested with charge and discharge cell cut-off voltages of 5 V and 3.5 V, respectively. In particular, the test protocol consisted of a preliminary galvanostatic charge/discharge cycles at C/10 (conditioning cycles), carried out to form a stable CEI (Cathode Electrolyte Interface), required to let the electrode working above 4 V. The C/rate currents were set referring to the experimental specific capacity declared by the LMNO manufacturer, i.e., 125 mAh g^{-1} . This step was followed by 3 cyclic voltammetries (CVs) at $50 \mu\text{V s}^{-1}$ to highlight any side electrochemical signals that could impact on cycling performance of the cell. CV discharge curves were analyzed to obtain a first evaluation of the specific capacity that was calculated from the integral of

the cathodic current under the CV test; the obtained charge values were divided by the composite mass of the working electrode. The electrode areal capacity (mAh cm^{-2}) was obtained considering only the cathodic surface directly faced to lithium metal, i.e., 2 cm^2 (1.6 cm diameter). Subsequently, a series of galvanostatic cycles run with the same charge current ($C/5$) at increasing discharge currents ($C/5$, $C/3$, and $C/1$) were performed to investigate how increasing currents could affect electrode performances. Finally, repeated charge/discharge cycles at $C/1$ to evaluate the cell stability under prolonged cycling of the different formulations were performed.

3. Results

Figure 1a reports the weight loss normalized to mass variation evaluated by TGA under Ar/O_2 of the LMNO cathodes with PU, PEDOT:PSS, and PVdF binders, and of the pristine LMNO powders, the characteristic decomposition temperatures are highlighted by the derivatives of the TGA profiles reported in Figure 1b. While the curve for LMNO-Powder indicates that no significant mass variation occurs, for the composite electrodes two minima exist. The first one is located below $400 \text{ }^\circ\text{C}$ and is related to the binder degradation. The second one, more evident, at around $500 \text{ }^\circ\text{C}$ is related to the combustion of the carbonaceous content (Super C45 or Super C65). All the binders degrade above $200 \text{ }^\circ\text{C}$ with pullulan being the less stable. PEDOT:PSS binder shows a more constant decomposition rate with the derivative minimum at $400 \text{ }^\circ\text{C}$.

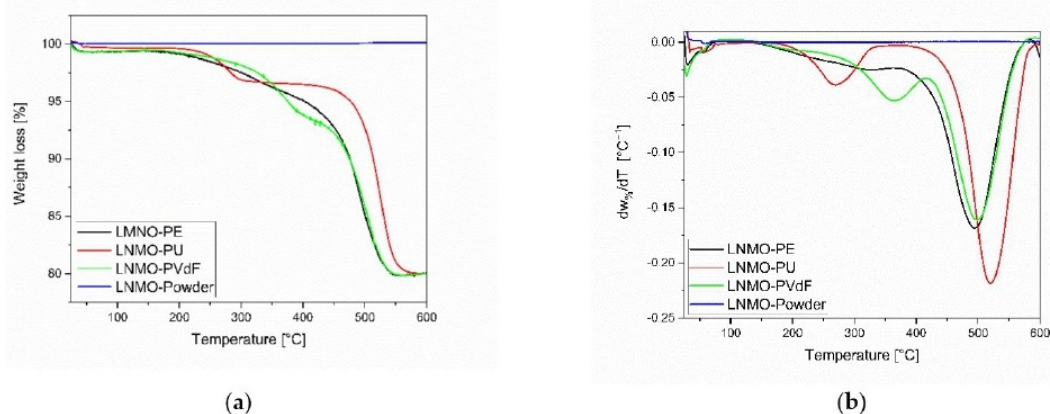


Figure 1. (a) Weight loss normalized to mass variation and (b) Derivatives of the TGA profiles under Ar/O_2 of the three electrodes (the aluminum mass has been excluded) and of the pristine LMNO powder.

The XRD patterns of the pristine LMNO powder and of the LMNO-PU, LMNO-PE, and LMNO-PVdF electrodes are reported in Figure 2. The patterns overlap and no significant difference was observed in the XRD spectra after the water processing. This suggests that the bulk lattice of LMNO was well maintained after electrode production by PU or PEDOT:PSS.

At first, galvanostatic charge/discharge cycles at a C-rate of $C/10$ were performed to form a stable CEI and to evaluate the specific capacity of the tested formulations. Selected cell voltage profiles of the conditioning cycles are reported in Figure 3.

The cell voltage profiles reported in Figure 3a feature the plateau expected for LMNO electrodes. The discharge curve derivatives shown in Figure 3b enabled a better evaluation of the cell voltage plateau. The plateau at 3.97 V is related to the $\text{Mn}^{3+}/\text{Mn}^{4+}$ pair, the one at 4.67 V is related to $\text{Ni}^{2+}/\text{Ni}^{3+}$, and that at 4.72 V corresponds to the $\text{Ni}^{3+}/\text{Ni}^{4+}$ redox couples. [4]. The PEDOT:PSS water-based formulation, featured the highest specific LMNO discharge capacity (130 mAh g^{-1}), followed by LMNO-PVDF (124 mAh g^{-1}) and LMNO-PU (119 mAh g^{-1}). After the GCPL conditioning cycles at $C/10$, CVs at $50 \mu\text{Vs}^{-1}$ were carried out to highlight the presence of any secondary faradaic reactions related to

the different exploited binders. The voltammograms are reported in Figure 4. For all the tested cells, the CVs overlap and show well defined redox peaks that are related to the $\text{Mn}^{3+}/\text{Mn}^{4+}$, $\text{Ni}^{2+}/\text{Ni}^{3+}$ and $\text{Ni}^{3+}/\text{Ni}^{4+}$ redox pairs. No additional signals can be appreciated. The voltammetric test confirmed that LMNO-PE is outperforming in terms of specific capacity. It featured 130 mAh g^{-1} with a coulombic efficiency of 99%. LMNO-PU exhibited 127 mAh g^{-1} with a coulombic efficiency of 96.5%. For LMNO-PVdF the specific capacity and coulombic efficiency were 124 mAh g^{-1} and 97.6%, respectively.

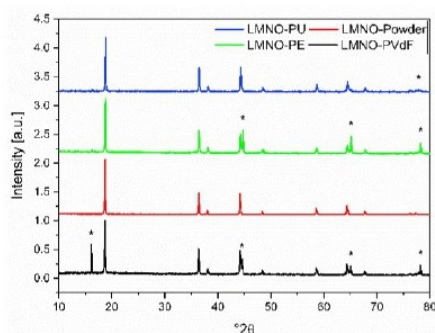


Figure 2. XRD patterns of the pristine LMNO powder and of the LMNO-PU, LMNO-PE, and LMNO-PVdF electrodes. (* Sample holder).

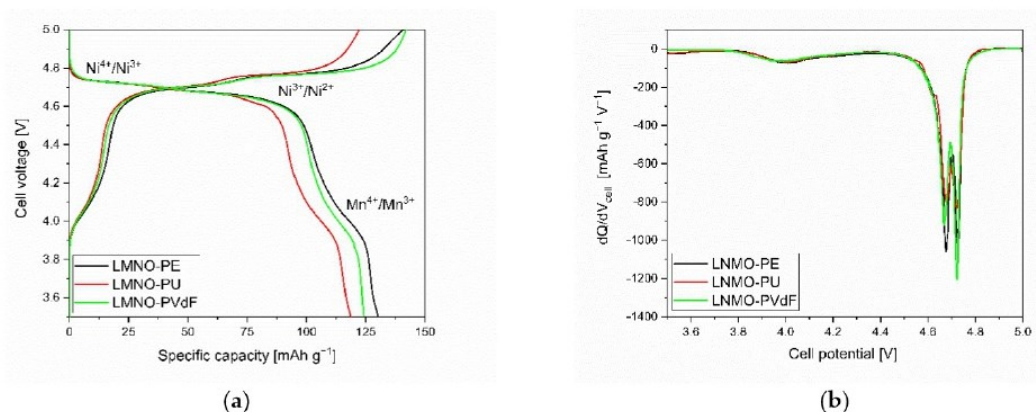


Figure 3. (a) Cell voltage profile vs. specific capacity and (b) derivative of the specific discharge capacity vs. cell voltage at C/10 of the different coin cells assembled with LMNO-PU, LMNO-PE, or LMNO-PVdF.

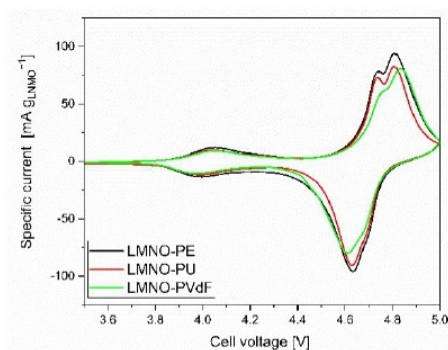


Figure 4. Cyclic voltammogram of the coin cells assembled with LMNO-PU, LMNO-PE, or LMNO-PVdF at $50 \mu\text{Vs}^{-1}$.

To investigate the response of the proposed electrodes formulations at high current, GCPL tests at increasing discharge current were carried out. In particular, the cells were charged with a C/5 current (calculated on the nominal capacity of LMNO) up to 5 V and discharged to 3.5 V at increasing C-rates, namely, C/5, C/3, and C/1. Figure 5 reports the trend of the specific capacity delivered at each cycle and current. All the cells featured a good rate capacity. At each C-rate, the highest specific capacity was achieved with LMNO-PE. Indeed, at C/5, LMNO-PE featured 136 mAh g⁻¹. This value decreased by 17% (to 113 mAh g⁻¹) when the current increased at C/1. For LMNO-PU and LPNMO-PVdF, the specific capacity at C/5 was 111 mAh g⁻¹ and 114 mAh g⁻¹, respectively, and it decreased to 103 mAh g⁻¹ at C/1. Overall, the CV and GCPL data demonstrate the feasibility of the use of water processed, high voltage cathodes based on the biopolymer pullulan or the electronically conducting PEDOT:PSS. Moreover, the good performance of the PEDOT:PSS-based formulation, suggests that the electronically conducting nature of the PEDOT:PSS binder, improves the electronic percolation network of the LMNO particles, and enables a better exploitation of the active materials even at high currents.

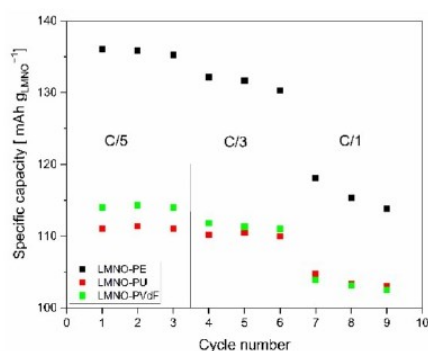


Figure 5. Specific capacity normalized to the LMNO content of the lithium metal cells with LMNO-PE, LMNO-PU, or LMNO-PVdF cathodes, under galvanostatic discharge at increasing current.

The GCPL at different C-rates have been analyzed to calculate the cell energy and power density reported in the Ragone plots in Figure 6. The cell energy (E_{cell}) has been calculated as the integral of the cell voltage under galvanostatic discharge conditions by introducing into the following equation the factor 3600, in order to convert the energy unit from Joule to Wh.

$$E_{cell} = i \int_0^{\tau} \frac{V}{3600} dt \quad (1)$$

where i is the current, V is the cell discharge voltage, and τ is the discharge time. From E_{cell} , the average cell power (P_{cell}) has been calculated according to the following equation.

$$P_{cell} = \frac{E_{cell}}{\tau} \quad (2)$$

For each tested cell, the specific energy (E) and the power density (P) have been calculated according to the following equation.

$$E = \frac{E_{cell}}{m_{cat} + m_{an}} \quad (3)$$

$$P = \frac{P_{cell}}{m_{cat} + m_{an}} \quad (4)$$

where m_{cat} is the experimental mass of the composite cathode (see Table 1), and m_{an} is the mass of the anode. The tested cathodes featured a capacity between 0.5 and 1 mAh,

while the anodic lithium foil was 300 μm thick. The anode theoretical capacity (Q_{Li}) can be calculated by Equation (5).

$$Q_{Li} = Q_{Li}^t \cdot \rho_{Li} \cdot A \cdot t \quad (5)$$

where Q_{Li}^t is the theoretical lithium specific capacity (3860 mA g^{-1}), ρ_{Li} is the lithium density (0.53 g cm^{-3}), A is the electrode area (2 cm^2), and t is the lithium thickness. According to Equation (5), a lithium anode with a thickness of 300 μm features a capacity of 120 mAh, which is c.a. 100 times the one of the prepared cathodes. Therefore, the mass of metallic lithium in a balanced cell can be significantly reduced. A metallic lithium foil of 15 μm with the same area would bring about 6 mAh, which is still from 6 to 15 times the capacity of the tested cathodes. Lithium foils featuring thickness smaller than 15 μm are extremely hard to handle. Indeed, reducing lithium foil thickness below 10 μm is one of the greatest challenges that metallic lithium batteries manufacturers will face in the years to come. A valuable solution is to produce thin lithium films on copper substrates [32].

The specific energy and power values reported in Figure 6, are projected data estimated for lithium metal cells assembled with the cathodes detailed in Table 1 and an optimized lithium foil of 15 μm . The highest values can be delivered by cells with LMNO-PE. The specific energy of the cells ranged from 420 Wh kg^{-1} (at $C/10$) to 355 Wh kg^{-1} (at $C/1$) for LMNO-PE, while the delivered power was between 40 Wh kg^{-1} and 385 W kg^{-1} , respectively. In these evaluations, current collectors, separators, and electrolyte mass were not included. However, we would like to underline that these values should be considered just as preliminary. Indeed, extrapolation of the results achieved at lab-scale to project up-scaled battery performance is a very challenging task that should consider active, composite electrode and electrolyte compositions, composite electrode, current collector, and separator thickness, as well as overall cell size (cylindrical, pouch, or prismatic). In [33], an extremely useful tool for the prediction of full cell performance metrics starting from measurement results on the electrode level was proposed. The impact of “death components” on the gravimetric parameters largely depends on electrode and current collector thicknesses. The higher is the electrode thickness, the higher is the specific energy. In this work, we used thin electrodes; hence, the impact of the separator (1.6 mg m^{-2}) and electrolyte (200 μL) masses was not negligible.

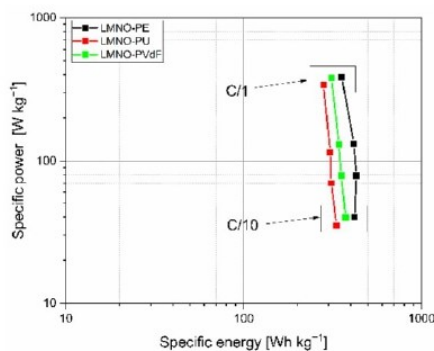


Figure 6. Ragone plot of the lithium metal coin cells with LMNO-PE, LMNO-PU, or LMNO-PVdF cathodes.

Finally, cycling stability tests were performed at $C/1$, which can be considered a preliminary, accelerated condition. Worth noting, we used an as received lithium metal anode and no SEI forming additives were present in the electrolyte. Figure 7 reports the capacity retention (C_{ret}) over cycling, which was calculated according to Equation (6).

$$C_{ret} = Q(t)/Q_0 \quad (6)$$

where $Q(t)$ is the capacity delivered at the i th cycle, while Q_0 is the value exhibited at the first cycle. The cells assembled with the water-processed cathodes featured outstanding

cycle stability. Indeed, LMNO-PU performed like LMNO-PVdF and retained 80% of the initial capacity after 200 cycles. Outstanding is LMNO-PE that features an excellent capacity retention of 100%. This test should be taken as a preliminary one and should be validated by longer cycle-life tests. However, it already clearly demonstrates the better stability of PEDOT:PSS-based cathodes vs. LMNO-PVdF since the first cycles.

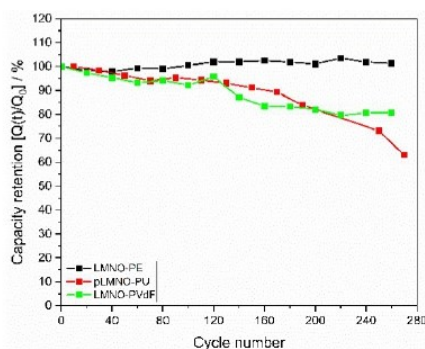


Figure 7. Capacity retention of the tested cell under cycling at C/1.

4. Conclusions

Overall, this paper demonstrates the feasibility of lithium metal battery cells assembled with high potential, water processed cathodes, and the LP30 electrolyte. LMNO electrodes were fabricated using two different water-processable binders: pullulan (PU) or the bifunctional electronically conductive PEDOT:PSS. LMNO was a commercial powder. The voltammetric and galvanostatic tests indicated that PU-based electrodes perform like the conventional PVdF-based ones, and represent a viable alternative to the latter binder. The use of PEDOT:PSS significantly improves specific capacity and capacity retention at different current rates and over cycling. At C/10, LMNO-PE featured 130 mAh g^{-1} , which is even slightly higher than the nominal value reported by the LMNO powder provider (125 mAh g^{-1}). The most interesting result is that lithium metal cells assembled with PEDOT:PSS-based cathode featured an outstanding capacity retention of 100% over 200 cycles carried out at C/1 and with a high cut-off voltage of 5 V. These results are even more important, considering that LMNO-PE is produced in ambient conditions (non-controlled condition), without using toxic solvents. The good cycling stability of LMNO-PE could be related to the ability of PEDOT:PSS to be a “barrier” against undesired side reactions of LMNO with the electrolyte. On the other hand, this effect has already been observed for cathodes produced with PVdF binder and PEDOT:PSS-coated LMNO particles [19–23]. Hence, this work demonstrates that it is possible to produce LMNO cathodes with aqueous binders maintaining the same performance of PVdF, in the case of pullulan, and improving them by the direct use of an electronically conductive binder such as PEDOT:PSS, without the need of LMNO particle coating. Comparison of PU and PEDOT:PSS-LMNO cathodes demonstrates that, besides the possibility of designing sustainable manufacturing, functional polymers with inherent electronic conductivity, play a key role, enabling specific energy and power performances greater than those of PVdF based ones. In addition, our study aims at widening the use of PU and PEDOT:PSS, which are considered key materials in the packaging industry and organic electronics, in an additional, strategic technological sector, namely, LIB manufacturing.

Author Contributions: Conceptualization, F.S.; methodology, F.S.; validation, F.S.; formal analysis, A.B., F.P., E.P., F.M. and F.S.; investigation, F.M., A.B. and E.P.; resources, F.S.; data curation F.M., A.B., F.P. and E.P.; writing—original draft preparation, A.B., F.P., E.P. and F.S.; writing—review and editing, F.S., F.P., A.B. and E.P.; visualization, A.B.; supervision, F.S.; project administration, F.S.; funding acquisition, F.S. All authors have read and agreed to the published version of the manuscript.

Funding: This research was funded by “Piano Triennale di Realizzazione 2019–2021” Accordo di Programma Ministero dello Sviluppo Economico (MISE)- Agenzia nazionale per le nuove tecnologie, l’energia e lo sviluppo economico sostenibile (ENEA) by “New generation of electrochemical energy storage systems” Progetto Alte Competenze per la Ricerca e il Trasferimento Tecnologico POR FSE 2014/2020-REGIONE EMILIA ROMAGNA and by “Programma Regionale attivita’ produttive 2012–2015 (Attivita’ 5.1, Sostegno allo sviluppo delle infrastrutture per la competitività e per il territorio -REGIONE EMILIA ROMAGNA).

Conflicts of Interest: The authors declare no conflict of interest. The funders had no role in the design of the study; in the collection, analyses, or interpretation of data; in the writing of the manuscript, or in the decision to publish the results.

References

- SET-Plan ACTION n°7. Declaration of Intent “Become Competitive in the Global Battery Sector to Drive E-Mobility Forward”. Available online: https://setis.ec.europa.eu/system/files/2021-05/action7_declaration_of_intent_0.pdf (accessed on 20 February 2022).
- Deliverable 3.6. Strategic Research Agenda for Batteries. Available online: https://ec.europa.eu/energy/sites/ener/files/documents/batteries_europe_strategic_research_agenda_december_2020_1.pdf (accessed on 24 February 2022).
- Liang, G.; Peterson, V.K.; See, K.W.; Guo, Z.; Pang, W.K. Developing high-voltage spinel $\text{LiNi}_{0.5}\text{Mn}_{1.5}\text{O}_4$ cathodes for high-energy-density lithium-ion batteries: Current achievements and future prospects. *J. Mater. Chem. A* **2020**, *8*, 15373–15398. [CrossRef]
- Xu, J.; Dou, S.; Liu, H.; Dai, L. Cathode materials for next generation lithium ion batteries. *Nano Energy* **2013**, *2*, 439–442. [CrossRef]
- European Battery Alliance. Available online: https://ec.europa.eu/growth/industry/strategy/industrial-alliances/european-battery-alliance_it (accessed on 24 February 2022).
- Bresser, D.; Moretti, A.; Varzi, A.; Passerini, S. Alternative Binders for sustainable electrochemical energy storage—the transition to aqueous electrode processing and bio-derived polymers. *Energy Environ. Sci.* **2018**, *11*, 3096–3127. [CrossRef]
- REGULATION (EC) No 1907/2006 of the European Parliament and of the Council. Available online: <https://eur-lex.europa.eu/legal-content/EN/TXT/PDF/?uri=CELEX:32006R1907&from=EN> (accessed on 24 February 2022).
- Wood, D.L.; Quass, J.D.; Li, J.; Ahmed, S.; Ventola, D.; Daniel, C. Technical and economic analysis of solvent-based lithium-ion electrode drying with water and NMP. *Dry. Technol.* **2018**, *36*, 234–244. [CrossRef]
- Li, J.; Lu, Y.; Yang, T.; Ge, D.; Wood III, D.L.; Li, Z. Water-Based Electrode Manufacturing and Direct Recycling of Lithium-Ion Battery Electrodes—A Green and Sustainable Manufacturing System. *iScience* **2020**, *23*, 101081. [CrossRef] [PubMed]
- Brilloni, A.; Poli, F.; Spina, G.E.; Samori, C.; Guidi, E.; Gualandi, C.; Maisuradze, M.; Giorgetti, M.; Soavi, F. Easy recovery of Li-ion cathode powders by the use of water-processable binders. *Electrochim. Acta*, 2022; under review.
- Bigoni, F.; De Giorgio, F.; Soavi, F.; Arbizzani, C. New Formulations of High-Voltage Cathodes for Li-Ion Batteries with Water-Processable Binders. *ECS Trans.* **2016**, *73*, 249–257. [CrossRef]
- Malavolta, L.; Terella, A.; De Giorgio, F.; Arbizzani, C. Improved Adhesion of Nafion™-Coated Separator to Water-Processable $\text{LiNi}_{0.5}\text{Mn}_{1.5}\text{O}_4$ Electrodes. *Batteries* **2020**, *6*, 28. [CrossRef]
- Preman, A.N.; Lee, H.; Yoo, J.; Kim, I.T.; Saito, T.; Ahn, S. Progress of 3D network binders in silicon anodes for lithium ion batteries. *J. Mater. Chem. A* **2020**, *8*, 25548–25570. [CrossRef]
- Poli, F.; Momodu, D.; Spina, G.E.; Terella, A.; Mutuma, B.K.; Focarete, M.L.; Manyala, N.; Soavi, F. Pullulan-ionic liquid-based supercapacitor: A novel, smart combination of components for an easy-to-dispose device. *Electrochim. Acta* **2020**, *338*, 135872. [CrossRef]
- Spina, G.E.; Poli, F.; Brilloni, A.; Marchese, D.; Soavi, F. Natural polymers for green supercapacitors. *Energies* **2020**, *13*, 3115. [CrossRef]
- Sun, K.; Zhang, S.; Li, P.; Xia, Y.; Zhang, X.; Du, D.; Isikgor, F.H.; Ouyang, J. Review on application of PEDOTs and PEDOT:PSS in energy conversion and storage devices. *J. Mater. Sci. Mater. Electron.* **2015**, *26*, 4438–4462. [CrossRef]
- Van At Nguyen, V.A.; Kuss, C. Review—Conducting Polymer-Based Binders for Lithium-Ion Batteries and Beyond. *J. Electrochem. Soc.* **2020**, *167*, 065501. [CrossRef]
- Ozerova, V.V.; Stenina, I.A.; Kuz’mina, A.A.; Kulova, T.L.; Yaroslavtsev, A.B. Cathode materials based on lithium iron phosphate/PEDOT composites for lithium-ion batteries. *Inorg. Mater.* **2020**, *56*, 648–656. [CrossRef]
- Liu, J.; Xu, J. Improvement of the Cycle Performance of $\text{LiNi}_{0.5}\text{Mn}_{1.5}\text{O}_4$ Cathode Active Materials by In-Situ Coating with Poly (3,4-Ethylenedioxythiophene). *J. Power Energy Eng.* **2017**, *5*, 28. [CrossRef]
- Su, L.; Smith, P.M.; Anand, P.; Reeja-Jayan, B. Surface Engineering of a LiMn_2O_4 Electrode Using Nanoscale Polymer Thin Films via Chemical Vapor Deposition Polymerization. *ACS Appl. Mater. Interfaces* **2018**, *10*, 27063–27073. [CrossRef] [PubMed]
- Su, L.; Weaver, J.L.; Groenenboom, M.; Nakamura, N.; Rus, E.; Anand, P.; Jha, S.K.; Okasinski, J.S.; Dura, J.A.; Reeja-Jayan, B. Tailoring Electrode–Electrolyte Interfaces in Lithium-Ion Batteries Using Molecularly Engineered Functional Polymers. *ACS Appl. Mater. Interfaces* **2021**, *13*, 9919–9931. [CrossRef] [PubMed]

22. Wu, F.; Liu, J.; Li, L.; Zhang, X.; Luo, R.; Ye, Y.; Chen, R. Surface modification of Li-rich cathode materials for lithium-ion batteries with a PEDOT:PSS conducting polymer. *ACS Appl. Mater. Interfaces* **2016**, *8*, 23095–23104. [[CrossRef](#)]
23. Bae, J.J.; Shin, J.W.; Lee, S.J.; Kim, S.J.; Hong, T.W.; Son, J.T. Effect of PEDOT:PSS (Poly(3,4-ethylenedioxythiophene)—polystyrenesulfonate) Coating on Nanostructured Cobalt-Free $\text{LiNi}_{0.9}\text{Mn}_{0.1}\text{O}_2$ Layered Oxide Cathode Materials for Lithium-Ion Battery. *J. Nanosci. Nanotechnol.* **2020**, *20*, 338–343. [[CrossRef](#)]
24. Das, P.R. Conducting Polymers as Functional Binders for Lithium Ion Battery Positive Electrodes. Ph.D. Thesis, Carl von Ossietzky Universität Oldenburg, Oldenburg, Germany, 2016.
25. Xin, X.; Xue, Z.; Gao, N.; Yu, J.; Liu, H.; Zhang, W.; Xu, J.; Chen, S. Effects of conductivity-enhancement reagents on self-healing properties of PEDOT:PSS films. *Synth. Met.* **2020**, *268*, 116503. [[CrossRef](#)]
26. Higgins, T.M.; Park, S.H.; King, P.J.; Zhang, C.J.; McEvoy, N.; Berner, N.C.; Daly, D.; Shmeliov, A.; Khan, U.; Duesberg, G.; et al. A Commercial Conducting Polymer as Both Binder and Conductive Additive for Silicon Nanoparticle-Based Lithium-Ion Battery Negative Electrodes. *ACS Nano* **2016**, *10*, 3702–3713. [[CrossRef](#)]
27. Chen, H.; Ling, M.; Hencz, L.; Ling, H.Y.; Li, G.; Lin, Z.; Liu, G.; Zhang, S. Exploring Chemical, Mechanical, and Electrical Functionalities of Binders for Advanced Energy-Storage Devices. *Chem. Rev.* **2018**, *118*, 8936–8982. [[CrossRef](#)]
28. Lipomi, D.J.; Lee, J.A.; Vosgueritchian, M.; Tee, B.C.-K.; Bolander, J.A.; Bao, Z. Electronic Properties of Transparent Conductive Films of PEDOT:PSS on Stretchable Substrates. *Chem. Mater.* **2012**, *24*, 373–382. [[CrossRef](#)]
29. Lee, H.D.; Jung, G.J.; Lee, H.S.; Kim, T.; Byun, J.D.; Suh, K.S. Improved stability of lithium-ion battery cathodes using conducting polymer binders. *Sci. Adv. Mater.* **2016**, *8*, 84–88. [[CrossRef](#)]
30. Vuddanda, P.R.; Montenegro-Nicolini, M.; Morales, J.O.; Velaga, S. Effect of plasticizers on the physico-mechanical properties of pullulan based pharmaceutical oral films. *Eur. J. Pharm. Sci.* **2017**, *96*, 290–298. [[CrossRef](#)] [[PubMed](#)]
31. Tong, Q.; Xiao, Q.; Lim, L.T. Preparation and properties of pullulan–alginate–carboxymethylcellulose blend films. *Food Res. Int.* **2008**, *41*, 1007–1014. [[CrossRef](#)]
32. Schönherr, K.; Schumm, B.; Hippauf, F.; Lissy, R.; Althues, H.; Leyens, C.; Kaskel, S. Liquid lithium metal processing into ultrathin metal anodes for solid state batteries. *Chem. Eng. J. Adv.* **2022**, *9*, 100218. [[CrossRef](#)]
33. Heubner, C.; Voigt, K.; Marcinkowski, P.; Reuber, S.; Nikolowski, K.; Schneider, M.; Partsch, M.; Michaelis, A. From Active Materials to Battery Cells: A Straightforward Tool to Determine Performance Metrics and Support Developments at an Application-Relevant Level. *Adv. Energy Mater.* **2021**, *11*, 2102647. [[CrossRef](#)]

2.4 Chapter 2 Conclusion

EESS plays a key role in the energy transition towards a more sustainable and green society. In this scenario, strategies that simultaneously target high energy/power performance, sustainable manufacturing processes, valorization of green raw materials and easy recycling are urgently needed. LIBs technology is the most diffused and forecast estimates a total global capacity of 1,925GWh by 2030, which means an increase of 688% from 244.7GWh in 2021 [21].

Therefore, the scope of this part of my work, described in Chapter 2, tackles the challenge of researching and testing of alternative materials and process to reduce the environmental impact of LIBs manufacturing and improve the recyclability at the end of life.

As of today, in LIBs manufacturing PVdF as binder and NMP as solvent are used for the manufacturing process. Both components are dangerous for humans and environment. In addition, the use of these components requires expensive and energy demanding air recirculation systems. A way to overcome these problems is the use of water processable binders.

In the first part of this section, I have demonstrated the exploitation of Pullulan, a bio-derived polymer, as binder for LIBs. Specifically, the high-potential cathodes PUGLY-NMC, based on NMC532 and pullulan, were produced in the ambient atmosphere, by avoiding the use of toxic solvents and fluorinated binders. Not only the cathodes featured mechanical properties that are suitable for an automatic production by roll-to-roll equipment, but, and mainly, they exhibited excellent cycling stability over 500 cycles along with good capacity retention at high C-rates comparable to that of commercial LIBs. In any case, the proposed procedure could pave the way towards a further reduction of LIB manufacturing costs by reducing active material losses related to production errors and inaccuracies which today account for 26% of the total manufacturing costs. Indeed, NMC could be easily recovered from production scraps and put back in the main production stream. The waste-waters used to wash and recover the NMC-carbon powders are biodegradable, which is of great importance to close the “sustainability chain” loop.

In the second part, I exploited PEDOT:PSS, a well known conductive polymer, as water processable binder. I compared the performance of LMNO-PEDOTPSS to LMNO-PU and LMNO-PVdF electrodes. The 60oltametric and galvanostatic tests indicated that PU-based electrodes perform like the conventional PVdF-based ones and represent a viable alternative to the latter binder, confirming the previous findings. On the other hand, the use of PEDOT:PSS significantly improves specific capacity and capacity retention at different current rates and over cycling. Comparison of PU and

PEDOT:PSS-LMNO cathodes demonstrates that, beside the possibility of designing a sustainable manufacturing, functional polymers, with inherent electronic conductivity play a key role and can enhance performances.

In conclusion, this work demonstrates that the use of well know polymers like PU and PEDOT:PSS, which are already considered key materials in the packaging industry and organic electronics, can be used in the LIBs manufacturing industry. This approach will not only reduce the environmental impact of the manufacturing process but can also reduce the cost thanks to the elimination of toxic components.

Reference Chapter 2

- [1] Brilloni, A.; Poli, F.; Spina, G. E.; Samorì, C.; Guidi, E.; Gualandi, C.; Maisuradze, M.; Giorgetti, M.; Soavi, F. “Easy recovery of Li-ion cathode powders by the use of water-processable binders” *Electrochimica Acta*, 2022, 418, 140376 <https://doi.org/10.1016/j.electacta.2022.140376>.
- [2] Brilloni, A.; Marchesini, F.; Poli, F.; Petri, E.; Soavi, F. “Performance Comparison of LMNO Cathodes Produced with Pullulan or PEDOT:PSS Water-Processable Binders.” *Energies* 2022, 15, 2608. <https://doi.org/10.3390/en15072608>
- [3] Winslow, K. M.; Laux, S. J.; Townsend, T. G. “A review on the growing concern and potential management strategies of waste lithium-ion batteries” *Resources, Conservation and Recycling*, 2018, 129, 263-277, <https://doi.org/10.1016/j.resconrec.2017.11.001>.
- [4] Zheng, X.; Zhu, Z.; Lin, X.; Zhang, Y.; He, Y.; Cao, H.; Sun, Z. “A Mini-Review on Metal Recycling from Spent Lithium Ion Batteries” *Engineering*, 2018, 4, 361-370, <https://doi.org/10.1016/j.eng.2018.05.018>.
- [5] Bresser, D.; Moretti, A.; Varzi, A.; Passerini, S. “Alternative Binders for sustainable electrochemical energy storage—the transition to aqueous electrode processing and bio-derived polymers” *Energy & Environmental Science* 11 (2018) 3096.
- [6] Piątek, J.; Afyon, S.; Budnyak, T. M.; Budnyk, S.; Sipponen, M. H.; Slabon, A. “Sustainable Li-Ion Batteries: Chemistry and Recycling.” *Advanced Energy Materials*. 2021, 11, 2003456. <https://doi.org/10.1002/aenm.202003456>
- [7] Bresser, D.; Buchholz, D.; Moretti, A.; Varzi, A. & Passerini, S. “Alternative binders for sustainable electrochemical energy storage – the transition to aqueous electrode processing and bio-derived polymers” *Energy Environmental Science, The Royal Society of Chemistry*, 2018, 11, 3096-3127 <https://doi.org/10.1039/C8EE00640G>
- [8] Singh, R. S.; Kaur, N.; Hassan, M.; Kennedy, J. F. “Pullulan in biomedical research and development – A review” *International Journal of Biological Macromolecules*, 2021, 166, 694-706, <https://doi.org/10.1016/j.ijbiomac.2020.10.227>.
- [9] Sun, K.; Zhang, S.; Li, P.; Xia, Y.; Zhang, X.; Du, D.; Isikgor, F. H.; Ouyang, J. “Review on application of PEDOTs and PEDOT:PSS in energy conversion and storage devices.” *Journal of Materials Science: Materials in Electronics* 2015, 26, 4438-4462.

- [10] Adekoya, G. J., Sadiku, R. E., Ray, S. S., “Nanocomposites of PEDOT:PSS with Graphene and its Derivatives for Flexible Electronic Applications: A Review” *Macromolecular Materials and Engineering* 2021, 306, 2000716. <https://doi.org/10.1002/mame.202000716>
- [11] Bae, J. J.; Shin, J.W.; Lee, S. J.; Kim, S. J.; Hong, T.W.; Son, J. T. “Effect of PEDOT:PSS (Poly(3,4-ethylenedioxythiophene) – polystyrenesulfonate) Coating on Nanostructured Cobalt-Free $\text{LiNi}_{0.9}\text{Mn}_{0.1}\text{O}_2$ Layered Oxide Cathode Materials for Lithium-Ion Battery.” *Journal of Nanoscience and Nanotechnology* 2020, 20, 338–343.
- [12] Farris, S.; Unalan, I. U.; Introzzi, L.; Fuentes-Alventosa, J. M.; Cozzolino, C. A. “Pullulan-based films and coatings for food packaging: Present applications, emerging opportunities, and future challenges” *Journal of Applied Polymer Science*, 2014, 131
<https://doi.org/10.1002/app.40539>
- [13] Abdul Aziz, A.R.; Tan Hooi, W.; Archina, B. “Two-step purification of glycerol as a value added by product from the biodiesel production process” *Frontiers in Chemistry* 7 (2019) 2296.
<https://doi.org/10.3389/fchem.2019.00774>
- [14] Nguyen Van At, V. A.; Kuss, C. “Review—Conducting Polymer-Based Binders for Lithium-Ion Batteries and Beyond” *Journal of the Electrochemistry Society* 2020, 167, 065501.
- [15] Ozerova, V.V.; Stenina, I.A.; Kuz'mina, A.A.; Kulova, T. L.; Yaroslavtsev, A.B. “Cathode materials based on lithium iron phosphate/PEDOT composites for lithium-ion batteries” *Inorganic Materials* 2020, 56, 648-656.
- [16] Liu, J.; Xu, J. “Improvement of the Cycle Performance of $\text{LiNi}_{0.5}\text{Mn}_{1.5}\text{O}_4$ Cathode Active Materials by In-Situ Coating with Poly (3, 4-Ethylenedioxythiophene)” *Journal of Power and Energy Engineering* 2017, 5, 28.
- [17] Su, L.; Smith, P.M.; Anand, P.; Reeja-Jayan, B. “Surface Engineering of a LiMn_2O_4 Electrode Using Nanoscale Polymer Thin Films via Chemical Vapor Deposition Polymerization” *ACS Applied Materials Interfaces* 2018, 10, 32, 27063–27073 <https://doi.org/10.1021/acsami.8b08711>
- [18] Su, L.; Weaver, J.L.; Groenenboom, M.; Nakamura, N.; Rus, E.; Anand, P.; Jha, S.K.; Okasinski, J.S.; Dura, J.A.; Ree-ja-Jayan, B. “Tailoring Electrode–Electrolyte Interfaces in Lithium-Ion Batteries Using Molecularly Engineered Functional Polymers” *ACS Applied Materials Interfaces*. 2021, 13, 8, 9919–9931

- [19] Wu, F.; Liu, J.; Li, L.; Zhang, X.; Luo, R.; Ye, Y.; Chen, R. “Surface modification of Li-rich cathode materials for lithium-ion batteries with a PEDOT:PSS conducting polymer”. *Applied Materials Interfaces* 2016, 8, 23095-23104.
- [20] Bae, J. J.; Shin, J.W.; Lee, S. J.; Kim, S. J.; Hong, T.W.; Son, J. T. “Effect of PEDOT:PSS (Poly(3,4-ethylenedioxythiophene) – polystyrenesulfonate) Coating on Nanostructured Cobalt-Free $\text{LiNi}_{0.9}\text{Mn}_{0.1}\text{O}_2$ Layered Oxide Cathode Materials for Lithium-Ion Battery.” *Journal of Nanoscience and Nanotechnology* 2020, 20, 338–343.
- [21] EV Battery Supply Chain “Trends, Risks and Opportunities in a Fast-Evolving Sector”. FitchSolutions. 2021. Available on-line: <https://store.fitchsolutions.com/all-products/ev-battery-supply-chain-trends-risks-and-opportunities-in-a-fast-evolving-sector> (accessed on 05 October 2022).

Chapter 3: Semi-solid electrodes

This chapter deals with the findings on a new class of binder-free non-solid electrodes for flowable redox flow batteries, namely semi-solid electrodes (SSEs).

The scope of this part of my work is to enhance the performance of semi-solid electrodes by investigating the effect of super concentrated electrolytes and its beneficial effect on the electrodes stability and performances.

After proving that bio-derived and water processable polymers are a feasible alternative to F-based binder that can reduce environmental impact and cost of the manufacturing process, I focused on a different binder-free class of battery, namely redox-flow battery (RFBs). RFBs is a rechargeable battery that stores electrical energy by the use of two different soluble redox couple present in two flowable electrodes. The liquid components are stored in two external tanks and are pumped inside the reactor where the ion exchange reaction takes place. The power of the RFB is defined by the size and the design of the reactor, while the energy that the RFB can deliver is determined by the volume of the liquid and therefore, by the active species dissolved inside it. Higher the solubility of the active species, higher is the energy density of the RFB.

RFB, thanks to their ability to decouple energy and power, are of fundamental importance for the energy transition because they represent a cost-effective alternative to LIBs for stationary storage. In addition, the manufacturing process of RFB results lower when using 100% of fresh raw materials with respect to LIBs, and can sensibly be reduced by 11% on the “global warming index” when using only 50% of recycled material [1]. Many other strategies can put in place to reduce the environmental impact of RFBs by 20% at the end of life [2,3].

RFBs are very effective in applications that require big implants and long discharge times because they have a flexible design and can be scaled up easily. The main limit to the diffusion of this battery technology is the low energy density, which is around 20-25 Wh/L for the most conventional Vanadium RFB [4], corresponding to a solubility of the electroactive species around 1-2 M.

Instead of trying to increase the solubility of active species, a different solution is proposed with the use of solid active species in the flowing system. This approach opens up the possibility to achieve unprecedented energy density values for RFBs. Therefore, this approach can combine the flexibility of RFBs, specifically decoupling energy and power design, with a high energy density battery system. To reach this goal, an effective way is the use of so-called “*Semi-solid electrodes*” in which solid

active particles are suspended in the electrolyte creating a slurry that is circulated inside the battery system. However, the application of semi-solid electrodes in RFBs requires efficient management of the viscous slurries that results from the particle suspension, a smart management of the slurry flow, and improved reactor design.

Many different chemistries and electrochemical storage systems have been proposed along with semi-solid electrodes [5]. A new concept of flowable supercapacitor, called “electrochemical flow capacitor” (EFC), was proposed by Gogotsi et al. [6]. RFBs featuring semisolid catholytes based on LIBs chemistry like LiCoO_2 (LCO) or $\text{LiMn}_{1.5}\text{Ni}_{0.5}\text{O}_4$ (LMNO) or semisolid anolytes with $\text{Li}_4\text{Ti}_5\text{O}_{12}$ (LTO) or LiFePO_4 (LFP) were also studied [7-11].

Nowadays, the most challenging issues in the developing of high-specific-energy RFBs with semi solid electrodes are related to (i) the formulation of carbonaceous conductive slurries with an efficient electrical percolation network; (ii) the use of stable organic electrolytes to minimize the side reactions with electrolytes and the other cell components, such as the current collectors; and (iii) the achievement of high cell voltages.

In this part of my work I focus on the first and second issues, investigating the effect of the electrolyte ion concentration, from conventional to superconcentrated, on the electronic percolating network of carbonaceous slurries for Lithium-Ion Semiolid RFBs (LI-SSFB).

More specifically, I studied three slurry compositions based on different concentrations of lithium bis(trifluoromethane)sulfonamide (LiTFSI) in tetraethylene glycol dimethyl ether (TEGDME), respectively 0.5 mol/kg (05ME), 3 mol/kg (3ME), and 5 mol/kg (5ME) at different content of Pureblack ® carbon, from 2% wt up to 12 % wt.

In the first part of the study the slurries were investigated by a deep Electrochemical Impedance Spectroscopy (EIS) analysis by using T-shaped cells with two stainless steel blocking electrodes. The EIS results were analyzed referring to the model and electronic equivalent circuits (EEC) proposed by Youssry et al. [12]. With this technique I was able to numerically evaluate the electrical resistance R_e , which is the characteristic resistance of the percolating network formed by the carbonaceous particle suspension. When the concentration of carbon is sufficiently high, a good electronic percolating network is set and the R_e becomes smaller, which is a necessary condition to lower the resistance of semi-solid electrodes in RFBs. The high ionic strength of 3ME mitigates agglomeration and enhances a homogeneous dispersion of the carbon particles. In turn, this facilitates the formation of an efficient percolating network and brings about a higher electrical conductivity with respect to slurries based on more diluted electrolytes like 0.5ME.

To further investigate the formation of the percolating network and better highlight the arrangement of the carbon agglomerates under the effect of superconcentrated electrolyte on the carbonaceous suspension we collected optical fluorescence microscopy images of the slurries. The collected images show that the samples with the higher carbon concentration display a better connection among the carbon particles, which are more inclined to produce an efficient percolating network.

The semi-solid electrode must be flowable inside the volume of the reactor and therefore, to produce the optimal slurry, the electronic conductivity, the carbon percentage and the viscosity must be balanced. A high viscous slurry will result in high conductivity but will consume a lot of energy to be pumped, lowering the overall efficiency of the RFB. Therefore, in the last section of this work I evaluated the viscosity of the different samples with the use of a rheometer. The data demonstrate that all the samples display a non-Newtonian behavior. In fact, the viscosity decreases with the increase of the shear rate. In addition, the higher the carbon content of the slurry, the higher the viscosity of the samples. The experimental methods and the results of this study are reported in [13], which is here attached as complete publication.

Improving the Electrical Percolating Network of Carbonaceous Slurries by Superconcentrated Electrolytes: An Electrochemical Impedance Spectroscopy Study

Alessandro Brilloni, Federico Poli, Giovanni Emanuele Spina, Damiano Genovese, Giorgia Pagnotta, and Francesca Soavi*



Cite This: *ACS Appl. Mater. Interfaces* 2021, 13, 13872–13882



Read Online

ACCESS |



Metrics & More



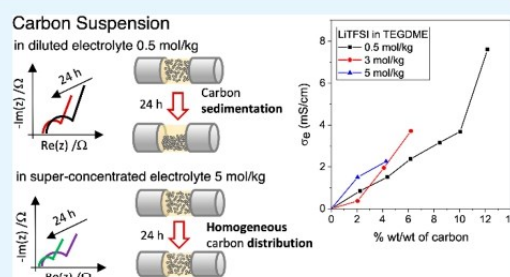
Article Recommendations



Supporting Information

ABSTRACT: Semisolid redox flow batteries simultaneously address the need for high energy density and design flexibility. The electrical percolating network and electrochemical stability of the flowable electrodes are key features that are required to fully exploit the chemistry of the semisolid slurries. Superconcentrated electrolytes are getting much attention for their wide electrochemical stability window that can be exploited to design high-voltage batteries. Here, we report on the effect of the ion concentration of superconcentrated electrolytes on the electronic percolating network of carbonaceous slurries. Slurries based on different concentrations of lithium bis(trifluoromethane)sulfonamide in tetraethylene glycol dimethyl ether (0.5, 3, and 5 mol/kg) at different content of Pureblack carbon (from 2 up to 12 wt %) have been investigated. The study was carried out by coupling electrochemical impedance spectroscopy (EIS), optical fluorescence microscopy, and rheological measurements. A model that describes the complexity and heterogeneity of the semisolid fluids by multiple conductive branches is also proposed. For the first time, to the best of our knowledge, we demonstrate that besides their recognized high electrochemical stability, superconcentrated electrolytes enable more stable and electronically conductive slurry. Indeed, the high ionic strength of the superconcentrated solution shields interparticle interactions and enables better carbon dispersion and connections.

KEYWORDS: semisolid slurry, semisolid redox flow battery, electrical percolating network, superconcentrated electrolyte, electrochemical impedance spectroscopy, optical fluorescence microscopy, semisolid slurry viscosity



1. INTRODUCTION

Boosting the shift to a low carbon society requires a large and widespread diffusion of renewable energy sources such as solar, wind power or ocean wave energy. However, all these sources connected to the power grid are intermittent and can be only partially forecasted. For this reason, the energy network necessitates the development of large electrical energy storage (EES) systems that level loads, shave peaks and improve the overall plant efficiency. One of the most suitable and used EES technology for this purpose is represented by redox flow batteries (RFBs).^{1,2} An RFB is a rechargeable battery that stores electrical energy in two different soluble redox couples. The liquid components are stored in external tanks and are pumped through the reactor, where the reaction and the consequent ion exchange occurs. Therefore, the total capacity and energy of the RFB are related to the volume of the reactants contained in the tanks. Because the active species are dissolved in the electrolyte, the higher is the solubility of the active material, the greater is the capacity and energy densities. The total power output, instead, is determined by the electrode

plate area inside the stack and by the design of the reactor. The main advantage of RFBs is the high flexibility in meeting the demand of the final user. Indeed, energy and power are effectively decoupled. The most diffused technology for RFBs are the vanadium redox flow battery (VRFBs). Despite the long cycle life (>10000 cycles, 10/20 years), these RFBs suffer from low operational potential (<2 V), low energy density, and narrow duty temperature range.^{2–4}

These constraints are pushing researchers to look for new redox couples and designs of RFBs. The main strategies that have been proposed to increase energy and power of RFBs include the use of: (i) organic electrolytes to increase the cell voltage above 2 V and widen the temperature operation, (ii)

Received: February 4, 2021

Accepted: March 1, 2021

Published: March 10, 2021



Table 1. Slurry Identification Code and Composition in Terms of Carbon Mass Percentage and of the Ratio of Carbon Mass to the Electrolyte Volume

		0.5ME-based slurry (0.5 mol kg ⁻¹ LiTFSI)				
sample ID code	PB052	PB054	PB056	PB058	PB0510	PB0512
%C (w/w)	2.23	4.38	6.17	8.3	10.04	12.17
C content (g cm ⁻³)	0.025	0.049	0.071	0.098	0.121	0.150
		3ME-based slurry (3mol kg ⁻¹ LiTFSI)				
sample ID code	PB32	PB34	PB36			
%C (w/w)	2.05	4.1	6.2			
C content (g cm ⁻³)	0.027	0.056	0.086			
		5ME-based slurry (5mol kg ⁻¹ LiTFSI)				
sample ID code	PB52	PB54				
%C (w/w)	2.5	4.2				
C content (g cm ⁻³)	0.029	0.063				

solid metal anodes, and (iii) sulfur- or O₂ (air)-based catholytes to reduce volume and weight, and (iv) semisolid anolyte and/or catholyte to circumvent the active materials solubility limitation of conventional RFBs.^{2,5,6} In the last case, because the redox couples are not molecules in solution but solid particles suspended in the electrolyte, the active species will not crossover through the separator. Ion conduction will take place through the porous voids of the separator, approaching the electrolyte bulk conductivity with advantages in terms of power. However, the development of semisolid RFBs requires efficient management of the viscous slurries that results from the particle suspension, a smart management of the slurry flow, and improved reactor design.⁷ A combination of these different approaches has led to many RFB configurations.^{2–6,8} Gogotsi et al. proposed a new concept of supercapacitor called the “electrochemical flow capacitor” (EFC) that benefits from the major advantages of both supercapacitors and flow batteries.⁹ RFBs featuring semisolid catholytes based on LiCoO₂ (LCO) or LiMn_{1.5}Ni_{0.5}O₄ (LMNO) or semisolid anolytes with Li₄Ti₅O₁₂ (LTO) or LiFePO₄ (LFP) were also studied.^{10–14} The highest specific energy of 500 Wh/kg was demonstrated by combining a lithium metal anode and a semisolid O₂ catholyte made of a suspension of carbon (2%) in a solution of 0.5 *m* solution of lithium bis (trifluoromethane)sulfonamide (LiTFSI) in tetraethylene glycol dimethyl ether (TEGDME) saturated with O₂.^{15,16}

Nowadays, the most challenging issues in the development of high-specific-energy RFBs are related to (i) the formulation of carbonaceous conductive slurries with an efficient electrical percolation network; (ii) the use of stable organic electrolytes to minimize the side reactions with electrolytes and the other cell components, such as the current collectors; and (iii) the achievement of high cell voltages. An efficient electrical percolation network is required to improve the kinetics of the faradaic processes, and, specifically, the electron transfer between the particles and the current collector. The consequence is that ohmic losses are minimized and the power is improved. The rheological and conductive behaviors of the slurries depend on carbon morphology and surface chemistry, which in turn affect particle agglomeration/sedimentation in the electrolyte solution.^{3,13,17–21} In our previous work, we reported that by the proper selection of the carbon, it is possible to formulate slurries with high carbon content characterized by good electrical and rheological properties. Indeed, we compared the electrochemical response of carbonaceous catholytes of semisolid Li/O₂ flowable battery

based on different weight percents of Super-P (spherical particles) and Pureblack (fragmental particles) carbons in 0.5 *m* LiTFSI in TEGDME. According to our findings, the fragmental morphology of Pureblack particles enabled the formulation of pseudoplastic slurries capable of reducing their viscosity at increased shear rate even at high carbon content. In turn, these features positively affected energy and rate performance of the catholyte. In addition, a smooth flow is expected to lower the power consumption of the pump.^{7,14}

Regarding the electrolyte, its composition has to be properly formulated, especially when high-voltage semisolid RFB operation is targeted. In RFBs that exploit the lithium battery chemistries, the solid electrolyte interface (SEI) formation in fluid electrodes represents a critical issue. Indeed, the electronic insulator nature of SEI hinders the electrical contact between the current collector and the particles dispersed in the electrolyte. The use of ionic liquids and superconcentrated (solvent-in-salt) electrolytes with their recognized wide electrochemical stability window, might represent a solution.²² Superconcentrated solutions of LiTFSI in TEGDME are gaining much interest as a new class of stable electrolytes.²³ Furthermore, they represent an extremely interesting platform for the study of the effect of the electrolyte “structure” in terms of ion interactions on the electrochemistry of the systems. Indeed, the increase in LiTFSI concentration from conventional values up to its maximum value, i.e., ca. 5 mol kg⁻¹ at room temperature, modifies the electrolyte behavior from that of a classical salt-in-solvent solution to a solvent-in-salt solution. Increasing LiTFSI concentration from 0.5 mol kg⁻¹ to 5 mol kg⁻¹, changes conductivity from ca. 2 to 0.7 mS cm⁻¹.²⁴ However, the 5 *m* solution of LiTFSI-TEGDME features an extremely high viscosity of 550 cP that might prevent its use as flowable electrolyte. Therefore, a slightly lower concentration of LiTFSI in TEGDME, such as 3 *m*, could represent a good balance between good electrochemical stability, conductivity, and fluidity.²⁴

Here, for the first time to our knowledge, we investigate the effect of the electrolyte ion concentration, from conventional to superconcentrated, on the electronic percolating network of carbonaceous slurries for lithium-ion semisolid RFBs. Specifically, this study mainly focuses on three different concentrations of LiTFSI in TEGDME, namely 0.5, 3, and 5 molal, at different content of Pureblack carbon. The electrical properties of conductive slurries and their dynamic behavior were investigated by a deep electrochemical impedance spectroscopy (EIS) analysis complemented by optical fluorescence microscopy and rheological studies. A model that describes

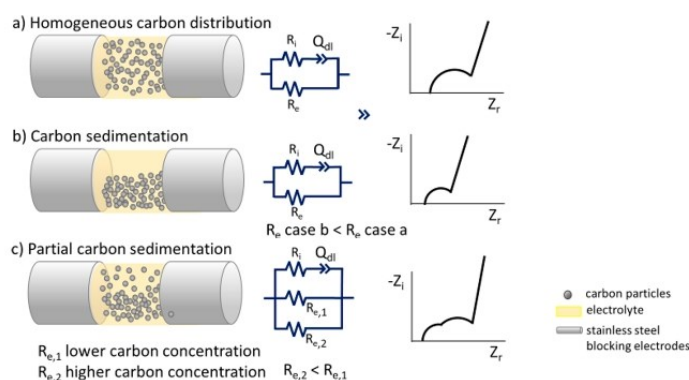


Figure 1. Dispersion of the carbonaceous slurry between the two stainless steel blocking electrodes, the equivalent circuit that models the electrical response of the cell and the corresponding ideal Nyquist plot for (a) homogeneous carbon dispersion, (b) carbon completely sedimented on the bottom of the cell, and (c) partially sedimented.

the complexity and heterogeneity of the semisolid fluids by multiple conductive branches of an equivalent circuit model, is also proposed. Our study demonstrates that superconcentrated electrolytes have a structuring effect on the distribution of carbon particles which positively affects the electronic percolation network of the semisolid slurries of RFBs.

2. EXPERIMENTAL SECTION

2.1. Materials. Two different electrolyte compositions were used to formulate slurries. Tetra-ethylene-glycol-dimethyl-ether (TEGDME, $\geq 99\%$) and lithium bis-tri-fluoro-methan-sulfonimide (LiTFSI, $\geq 99\%$) were purchased by Sigma-Aldrich and used to prepare the electrolytes. The electrolyte 0.5ME featured a LiTFSI molal concentration equal to 0.5 mol kg^{-1} . For the electrolytes, 3ME and SME the LiTFSI molal concentrations were 3 and 5 mol kg^{-1} . Conductivity, density, and dynamic viscosity of 0.5ME, 3ME, and SME were 2.2 mS cm^{-1} (at $30 \pm 0.3 \text{ }^\circ\text{C}$), 1.08 g cm^{-3} , 7.14 cP , 2.0 mS cm^{-1} (at $30 \pm 0.3 \text{ }^\circ\text{C}$), 1.31 g cm^{-3} , 47.1 cP , and 0.8 mS cm^{-1} (at $30 \pm 0.3 \text{ }^\circ\text{C}$), 1.43 g cm^{-3} , 550 cP , respectively.²⁴ The carbon used to compose the slurry was Pureblack 315 (PB), ($\text{BET } 64 \text{ m}^2 \text{ g}^{-1}$) from Superior Graphite. The carbonaceous particles were dispersed at different percentages in the electrolyte solutions. All the slurries were prepared inside a drybox (MBraun LabmasterSP 130) with an argon atmosphere ($\text{H}_2\text{O} < 0.1 \text{ ppm}$, $\text{O}_2 < 0.1 \text{ ppm}$). Before use, LiTFSI was dried in an electric oven at $120 \text{ }^\circ\text{C}$ for 12 h under a dynamic vacuum. PB carbon was dried in the same oven at $120 \text{ }^\circ\text{C}$ for 12 h and both components were stored in the drybox. Table 1 reports the identification codes of the slurries along with their composition in terms of carbon mass percentage and of the ratio of the carbon mass to the electrolyte volume. In the case of the electrolyte 0.5ME we explored a carbon content ranging from ~ 2 to $12 \text{ wt } \%$. For the 3ME electrolyte, the maximum feasible carbon content that enabled a fluid slurry was $6 \text{ wt } \%$. For the SME, it was not possible to add more than $4 \text{ wt } \%$ carbon for the same reason.

2.2. Optical Fluorescence microscopy. To better highlight the arrangement of the carbon agglomerates, we collected optical fluorescence microscopy images of the slurries. The instrument was an Olympus IX71 with $10\times$ objective lens. [9-(2-carboxyphenyl)-6-diethylamino-3-xanthenylidene]-diethylammonium chloride (rhodamine B) was chosen as dye because it can be dissolved, giving fluorescence and making an easier study of the carbon dispersions feasible. For this purpose, $0.1 \mu\text{g}$ of dye was added to $100 \mu\text{g}$ of slurry.

2.3. Electrochemical Impedance Spectroscopy. Electrochemical Impedance measurements were performed by using T-shaped cells with two stainless steel blocking electrodes (Figure S1) (1 cm diameter) at $\sim 1 \text{ cm}$ of distance. The EIS spectra were collected with a BioLogic VSP multichannel potentiostat/galvanostat/FRA

within a 50 kHz to 1 Hz frequency range and 10 mV of perturbation amplitude, acquiring 10 points per decade (selected frequencies ranges are specified when required). EIS spectra collected in a wider frequency range (200 kHz to 100 mHz) are reported in Figure S2. To guarantee the reproducibility of the measurements, we defined a specific procedure for testing. First, we stirred the samples to be tested for 20 min and they were then transferred inside the glovebox to assemble the cells that were previously heated at $30 \text{ }^\circ\text{C}$. When assembled, the cells were stored in a thermostatic oven at $30 \text{ }^\circ\text{C}$ and EIS measurements were performed over time. Specifically, two measurements were carried out immediately after cell assembly in sequence (identified as “-01” and “-02”). The test was repeated after half an hour (identified as “-03”), and the last one after an additional 24 h (identified as “-04”). The overall test spanned for a time of 24.5 h .

2.4. Electrochemical Impedance Spectroscopy Analysis. The EIS spectra of the carbonaceous suspensions were analyzed referring to the model proposed by Youssry et al.¹⁷ Specifically, the impedances of the suspensions have been modeled with the equivalent circuits reported in Figure 1a.

Figure 1a describes the homogeneous dispersion of the carbonaceous slurry between the two stainless steel blocking electrodes, the equivalent circuit that models the electrical response of the cell and the corresponding ideal Nyquist plot. R_e represents the electronic resistance of the dispersed carbon particles, in parallel with the ionic branch R_i, Q_{dl} . R_i is the ionic resistance of the electrolyte, which is in series with the constant phase element Q_{dl} . The latter represents the electrical double-layer capacitance at the blocking electrode/slurry interfaces. When the concentration of carbon in the slurry is extremely low and R_e is much higher than R_i , the R_e branch of Figure 1a is negligible. In this case, the electrochemical response of the cell filled with the slurry corresponds to that of an electrochemical capacitor. At high frequencies (e.g., 50 kHz), the real component of the impedance mainly corresponds to the ionic resistance R_i . At low frequencies, the impedance is dominated by the capacitive accumulation of ions at the surface of the blocking electrodes. Therefore, the corresponding Nyquist plot approximates a straight line parallel to the imaginary axis, with intercepts at high frequencies on the real axis at R_i . When the concentration of carbon is sufficiently high, a good electronic percolating network is set and the R_e branch becomes relevant. Given the high number of carbonaceous particles in contact with each other, at low frequencies, an electronic current through R_e is also observed in parallel with the ionic one associated with the formation of the double layer and that flows through the R_i, Q_{dl} branch. Consequently, the Nyquist plot changes from a straight line to a semicircle. The real axis intercept at high frequencies R_{hf} includes ionic and electronic terms according to the equation:

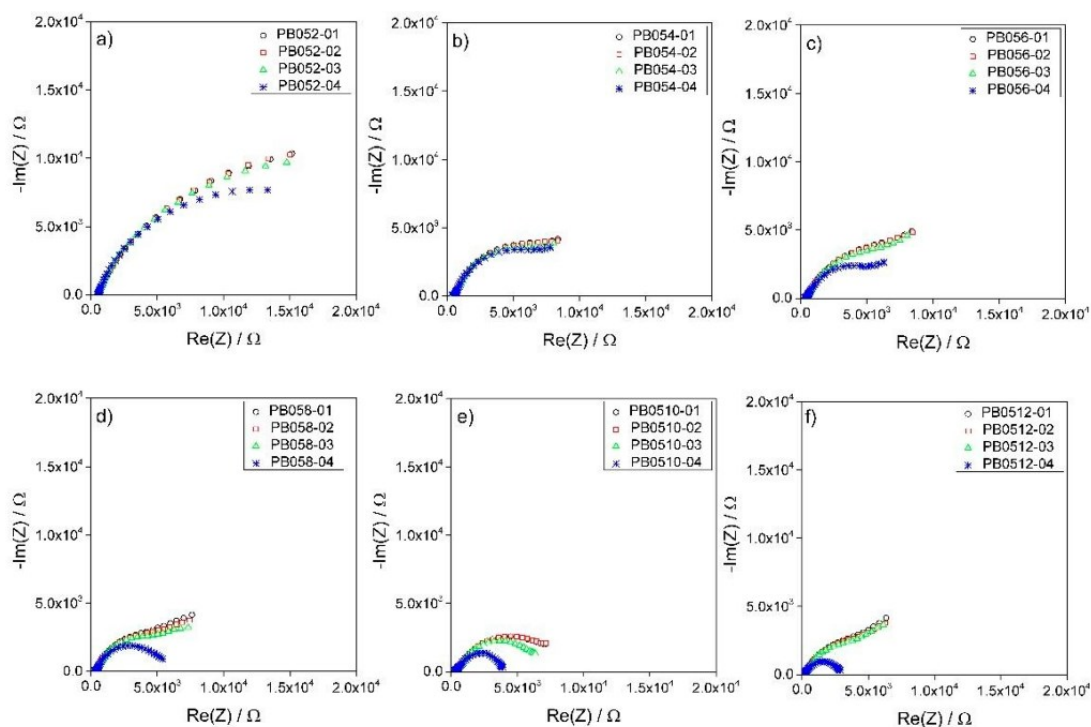


Figure 2. Nyquist plots evolution over time of 0.5ME-based slurries with different carbon percentages of (a) 2, (b) 4, (c) 6, (d) 8, (e) 10, and (f) 12% from 50 kHz to 1 Hz.

$$\frac{1}{R_{hf}} = \frac{1}{R_i} + \frac{1}{R_e} \quad (1)$$

The electronic conductivity of the slurries, σ_e , can be evaluated as reciprocal of R_e

$$\sigma_e = \frac{1}{R_e} \quad (2)$$

where

$$\frac{1}{R_e} = \frac{1}{R_{hf}} - \frac{1}{R_i} \quad (3)$$

In Figure 1a, the semicircle diameter quantifies the resistance of the electronic percolating network R_{pm} . Agglomeration and sedimentation phenomena can give rise to a dynamic electrical response of the slurry. Indeed, Figure 1b represents the case of a slurry where the carbon is sedimented. After sedimentation, carbon particles form aggregates and become better connected. Consequently, R_{hf} and R_e decrease, and the semicircle shrinks and shifts to the left of the Nyquist plot. Hence, it is worth noting that the carbonaceous percolating network should rather be described as a complex system composed of different branches that have different connection paths. The different branches correspond to portions of the slurry that feature different carbon concentration and aggregations status. This is described by Figure 1c, which models a slurry with carbon partially sedimented. In this case, the equivalent circuit is modified by adding different R_e branches that are in parallel with the ionic one. As an example, in Figure 1c, only an additional branch $R_{e,2}$ is added. Therefore, the corresponding Nyquist plot will feature two semicircles, each one representing the two different percolating networks.

2.5. Rheological Measurements. The viscosity of the slurries was evaluated by using Anton Paar MCR 102 rheometer in a plate-plate geometry with a diameter of 25 mm and a gap of 0.5 mm.

measurements were carried out with a shear rate range from 0.01 to 1000 s^{-1} by keeping the temperature constant at 25 °C.

3. RESULTS AND DISCUSSION

The effect of carbon content and electrolyte concentration on the percolating network of the semisolid slurries was evaluated by EIS. Specifically, three different electrolyte concentrations were explored, i.e., 0.5 molal (0.5ME), 3 molal (3ME), and 5 molal (5ME). The next Subsections report the studies carried for each electrolyte composition. Section 3.1 refers to 0.5ME-based slurries, section 3.2 to samples with 3ME electrolyte, section 3.3 compares the results obtained with the different electrolytes formulations, including the 5ME, and finally, section 3.4 reports and discusses the rheological features of the slurries.

3.1. Slurries with 0.5ME Electrolyte. In this section, carbonaceous suspensions with the electrolyte 0.5ME (0.5 molal) at different carbon contents are investigated. Table 1 details the composition of the investigated samples containing a carbon weight percentage ranging from 2.23 to 12.17%. At first, EIS was used to monitor the evolution of the slurry impedance over time. Figure 2 reports the Nyquist plots in the frequency range 50 kHz to 1 Hz for each 0.5ME-based sample, collected immediately after cell assembly (data labeled with “-01” and “-02” were made consecutively), after 30 min (data labeled “-03”), and after 24 h from the last measure (data labeled “-04”). All the plots are representative of slurries featuring both ionic and electronic conductivity. Indeed, as mentioned in section 2.4., they feature large semicircles. The semicircles have a high-frequency intercept on the real axis

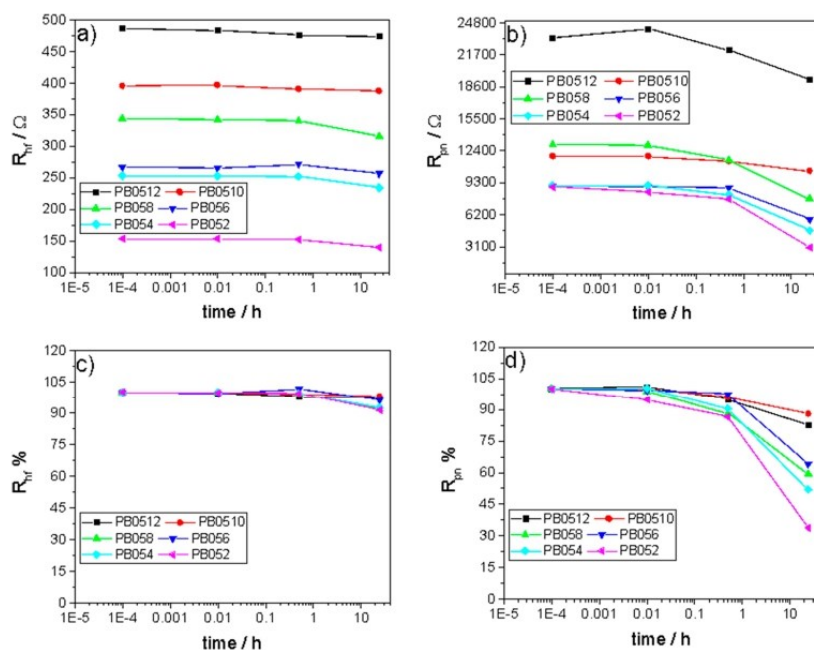


Figure 3. Evolution over time of (a) the high frequency resistance (R_{hf}) and (b) the percolating network resistance (R_{pn}) of 0.5ME-based slurries at different carbon percentages, and of their quantities (c) R_{hf} % and (d) R_{pn} % normalized by their corresponding initial values.

(R_{hf}) that is related to electronic and ionic resistances and a diameter (R_{pn}) that depends on the efficiency of the carbonaceous percolating network. All the samples show a strong time dependence of the impedance spectra over time. Furthermore, the semicircles tend to shrink with the increase of the carbon content. As it concerns the time evolution, for each sample, the two initial measures, -01 and -02, show no significant difference and they almost overlap. After 30 min and, mainly, after 24 h, a strong decrease of the semicircle diameter, and therefore, of the percolating network resistance R_{pn} , is noticeable. In parallel, the semicircles shift to lower R_{hf} values. This is highlighted by Table S1 and Figure 3a and Figure 3b, which report the values of R_{hf} evaluated at 50 kHz and of R_{pn} evaluated over time. The latter was calculated by analyzing the Nyquist plot by a nonlinear fitting procedure referring to the equivalent circuit shown in Figure 1 and discussed in section 2.4. Figure 3c, d reports the values of R_{hf} and R_{pn} normalized with respect to their initial values, i.e., to the values recorded immediately after cell assembly. R_{pn} changed from 23.3 to 19.3 k Ω (82.8%) for PB052, from 11.8 to 10.4 k Ω (88.1%) for PB054, from 13.3 to 6.8 k Ω (51.1%) for PB056, from 9 to 5.7 k Ω (63.3%) for PB058, from 8.9 to 4.6 k Ω (51.7%) for PB0510, and from 8.8 to 3 k Ω (34.1%) for PB0512 (Figure 3b, d). Even for R_{pn} , the percentage variation over time was more evident at high carbon content: for PB052, the R_{pn} decreased by 17%, and for PB0512, R_{pn} decreased by 66%.

Overall, the data reported in this section demonstrate that (i) the increase in carbon content effectively reduces the resistance of the slurries, and (ii) the slurries have dynamic behavior, which changes depending on the carbon content.

Figure 4 reports the optical fluorescence images of 0.5ME-based slurries with different carbon percentages and clearly

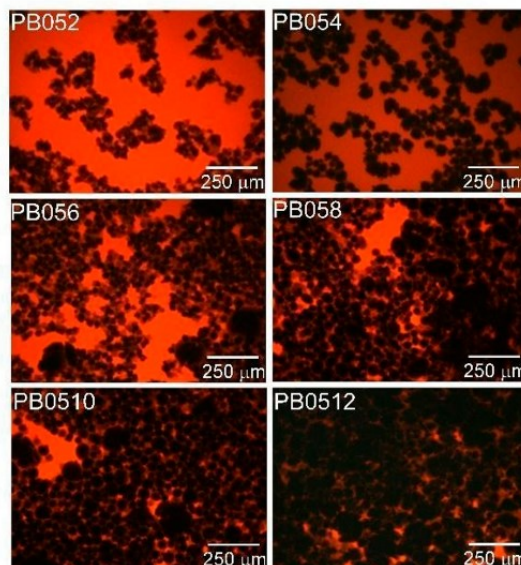


Figure 4. Optical fluorescence images of 0.5ME-based slurries with different carbon content.

shows that the number of carbon particles electrically connected increases when moving from PB052 to PB0512. The images show that the samples with the higher carbon concentration display a better connection among the carbon particles, which are more inclined to produce an efficient percolating network. This explains the observed trends of the

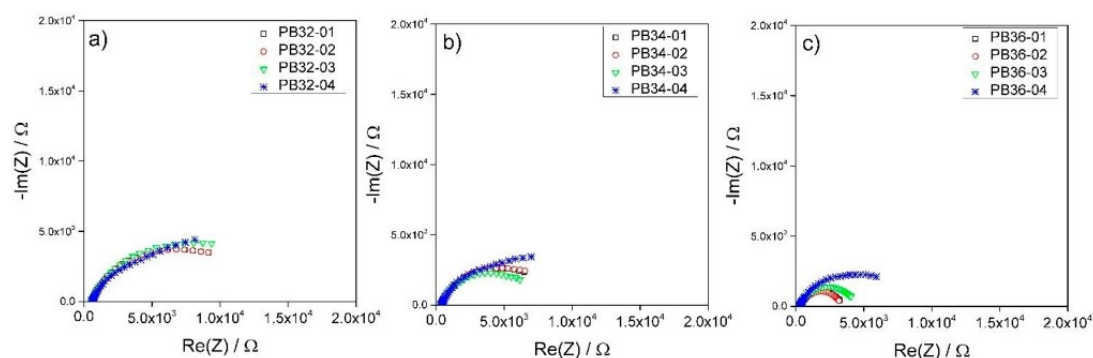


Figure 5. Nyquist plot evolution over time of 3ME-based slurries with different carbon percentages of (a) 2, (b) 4, and (c) 6% from 50 kHz to 1 Hz.

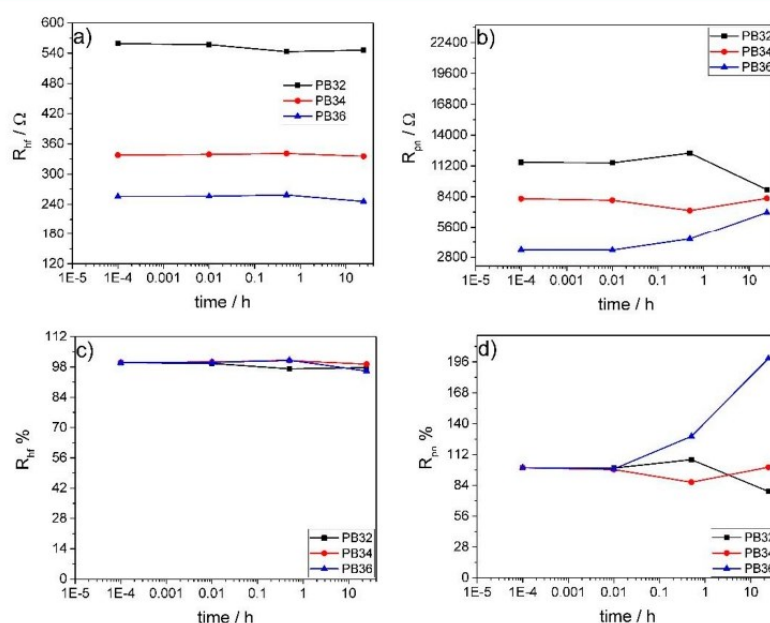


Figure 6. Evolution over time of (a) the high frequency resistance (R_{Hf}) and (b) the percolating network resistance (R_{pn}) of 3ME-based slurries at different carbon percentages, and of their quantities (c) R_{Hf} % and (d) R_{pn} % normalized by their corresponding initial values.

Nyquist diagrams that show a constant reduction in impedance with an increase in carbon content. Figure 4 even suggests that, at high carbon content, the electrolyte is not able to shield the surface interactions among the carbon particles that, as a consequence, exhibit a higher tendency to agglomerate with respect to low carbon content samples. In turn, for the 0.5ME-based slurries, the increase in carbon content accelerates the impedance evolution over time toward lower values. Therefore, this behavior can be explained by the sedimentation or agglomeration of carbon particles in the liquid phase. This process gives rise to additional percolating network branches in parallel to the initial ones. The new branches are generated by the portion of the slurries that feature higher concentration of carbon, and, hence, a lower local R_{pn} . This concept is described by Figure 1, which compares the electric behavior of an homogeneous slurry with carbon particles well distributed

within the liquid phase and of a nonhomogeneous slurry with carbon particles totally or partially agglomerated in the bottom part of the fluid. This is further highlighted by the Nyquist plots of the samples PB052 and PB0512, collected in a wider frequency range (200 kHz to 100 mHz) and shown as an example in Figure S2. The plots indicate the presence of two semicircles that we relate to the presence of two different percolation branches. This is more evident for the slurry PB0512, which has the highest carbon content.

3.2. Slurries with 3ME Electrolyte. This section reports the EIS study of the slurries PB32, PB34, and PB36 that are based on the same superconcentrated electrolyte (3 m LiTFSI in TEGDME) but feature increasing carbon content from 2.05 to 4.1 and 6.2%. It is worth noting that with 3ME electrolyte, it was not possible to obtain a homogeneous slurry with a mass percentage of carbon greater than 6.2% because the fluid was

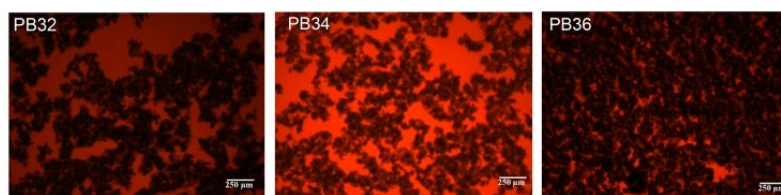


Figure 7. Optical fluorescence images of 3ME-based slurries with different carbon percentage.

too viscous. EIS measurements were carried out and analyzed following the same approach used for 0.5ME carbon slurries. Figure 5 shows the Nyquist plots collected immediately after the cell assembly (data labeled with “-01” and “-02” were made consequentially), after 30 min (data labeled “-03”), and after 24 h from the last measure (data labeled “-04”). Even for 3ME samples, the Nyquist plots are representative of slurries featuring both ionic and electronic conductivity and evolve with a strong dependence on carbon content. The analysis of the Nyquist plots of Figure 5 provided the values of R_{hf} evaluated at 50 kHz and of R_{pn} that are plotted over time in Figure 6a, b and given in Table S2. Figure 6c, d reports R_{hf} and R_{pn} normalized to their initial values. Figure 5 shows that for each sample, the two initial measures -01 and -02 overlap. After 30 min (measure -03), it is not possible to appreciate a clear trend. Indeed, for PB32 and B36, the semicircle slightly widens. For PB34, the semicircle instead shrinks. However, after 24.5 h (measure -04), the Nyquist plots of all the samples seem to evolve into two semicircles that are representative of two different percolating network branches. Given that the two semicircles are not well resolved, R_{pn} was calculated by taking into account only the data in the highest frequency range cut at 8 Hz and excluding those at the lowest frequency. Therefore, the second semicircle was not considered. R_{hf} was found to slightly decrease for all the samples. Indeed, during the 24.5 h, it changed from 559 to 546 Ω (97.7%) for PB32, from 338 to 335 Ω (99.1%) for PB34 and, from 256 to 245 Ω (95.7%) for PB36 (Figure 6, c). The percentage decrease in R_{hf} was 2.3, 0.7, and 3.9% for PB32, PB34, and PB36, respectively. After 24.5 h, R_{pn} of PB32 slightly decreased from 11.5 to 9 k Ω (78.3%), therefore by 22%. For PB34, R_{pn} was instead almost constant at 8.2 k Ω , whereas for PB36, R_{pn} doubled from 3.5 to 7 k Ω (200%) (Figure 6b, d). The comparison of the data reported in this section with those in section 3.1 unveils a specific effect of the electrolyte composition on the resulting impedance of the slurries that will be further discussed in section 3.3.

The main difference is that the R_{pn} values of the PB32 and PB34 slurries are almost 50 and 20% smaller than those of 0.5ME-based samples at the same carbon percentage of 3 and 4%. This indicates that electrical percolation is more efficient when the 3ME electrolyte is used. The ionic strength of the superconcentrated solution might shield interparticle interactions, therefore enabling a better carbon dispersion and electronic connection. This is supported by the fluorescence images of samples PB32, PB34, and PB36 that are reported in Figure 7.

A second effect is that 3ME mitigates the evolution of the Nyquist plots and R_{hf} and R_{pn} over time. Hence, highly concentrated electrolytes are beneficial for the stabilization of carbonaceous slurry. In 3ME samples, a second semicircle at low frequencies appears after 24 h. This can be explained with

the presence of the sedimentation and aggregation processes. Indeed, 3ME fresh samples feature a good percolating network with only one semicircle. After 24 h, sedimentation and agglomeration of carbon provide two branches. The first semicircle at higher frequencies is given by the concentrated portion of agglomerated particles (low R_{pn}). The second one, at lower frequencies, is related to diluted carbon particles that are still suspended in solution (high R_{pn}).

3.3. Comparison of 0.5ME-, 3ME-, and 5ME-Based Slurries. Given that all the slurries exhibited a dynamic behavior, for a comparison of the electrical properties of samples featuring 0.5ME, 3ME, and 5ME electrolyte, we referred to the Nyquist plots collected after 24.5 h. The plots of 0.5ME- and 3ME-based slurries are compared in Figure 8. Data obtained for the electrolytes 0.5ME and 3ME without carbon particles are also included. The Nyquist plots of 5ME-based slurries are reported in Figure S3a, b. In Figure 8, the high-frequency intercepts on the real axis of the plots for 0.5ME and 3ME without carbon provide the ionic resistance of the cells. For 0.5ME it was 623 Ω , lower than that for 3ME (673 Ω), in agreement with the higher conductivity of the former electrolyte with respect to that of the latter. On the contrary, the inset of Figure 8 shows that this trend does not hold for the carbonaceous slurries. Specifically, at a high carbon content, R_{hf} of PB054 (388 Ω) was higher than that of PB34 (335 Ω). This suggests that at high carbon content, the electronic percolation branch is more efficient in 3ME than in 0.5ME.

The electronic conductivity of the slurries σ_e was evaluated as described in section 2.4. The method enabled us to discriminate the electronic conduction provided by the carbon network from the ionic conduction provided by the electrolyte. Figure 9a shows the trend of σ_e vs carbon mass percentage for 0.5ME- and 3ME-based slurries. The electronic conductivity of the slurries featuring 0.5ME increases linearly up to 10% of carbon. In this range, σ_e varies from 0.8 mS cm⁻¹ (2 wt %/wt) to 3.7 mS cm⁻¹ (10 wt %/wt). In the range from 10% to 12 wt %/wt, a sharp increase in σ_e can be observed and the electronic conductivity reaches a value of 7.6 mS cm⁻¹. Youssry et al.¹⁷ reported that the change of the slope of the σ_e vs carbon content plot marks the percolation threshold, i.e., the minimum amount of carbon that provides an efficient percolating network.¹⁶ Therefore, from Figure 9a, it is possible to evince that the percolation threshold of 0.5ME-based slurries corresponds to a carbon content of at least 10%.

Regarding 3ME-based slurries, σ_e linearly increases from 0.4 mS cm⁻¹ at a carbon content of 2 wt %/wt to 3.7 mS cm⁻¹ at 6 wt %/wt. Therefore, it is evident that with 3ME it is possible to achieve the same σ_e of 0.5ME but at a lower carbon mass percentage. For a deeper analysis, it should be considered that 0.5ME and 3ME have different densities, respectively of 1.08 and 1.31 g cm⁻³. Hence, 0.5ME- and 3ME-based slurries with

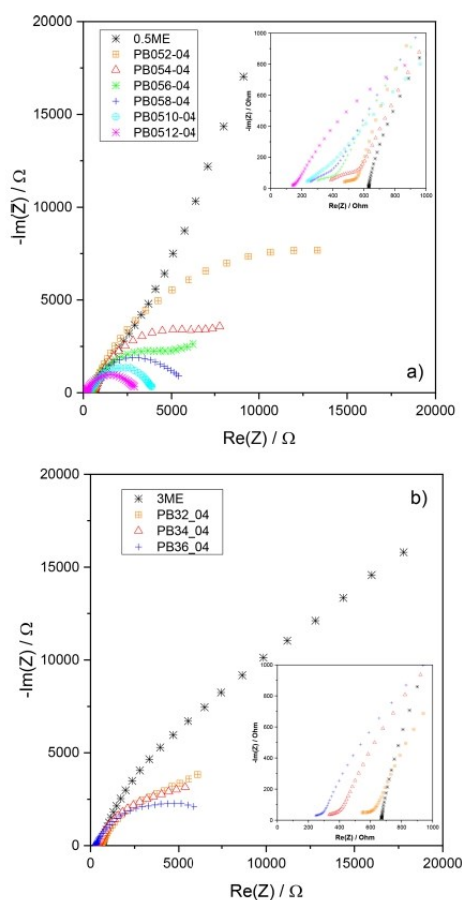


Figure 8. Comparison of the Nyquist plots collected from 50 kHz to 1 Hz, after 24.5 h, of slurries featuring different carbon content and (a) 0.5ME and (b) 3ME electrolytes. The inset reports the magnification of the plots at high frequencies. Data for the 0.5ME and 3ME electrolytes without carbon particles are also included.

the same carbon weight percentage feature a different mass of carbon per volume of solution. Figure 9b shows the trend of σ_e vs the values of carbon mass per volume, which are given for each sample in Table 1. In Figure 9b, the differences in conductivity of 0.5ME- and 3ME-based slurries are less marked than those observed in Figure 9a. However, still, the trend that distinguishes the 0.5ME- and 3ME-based slurries remains evident. Indeed, the σ_e value of 3.7 mS cm^{-1} is obtained at 0.08 g cm^{-3} with 3ME and at 0.12 g cm^{-3} with 0.5ME. This further confirms the positive effect of the higher ion concentration of 3ME vs 0.5ME on the electrical properties of the slurries. The high ionic strength of 3ME mitigates agglomeration and enhances a homogeneous dispersion of the carbon particles (see Figures 4 and 7). In turn, this facilitates the formation of an efficient percolating network and brings about a higher electrical conductivity with respect to slurries based on more diluted electrolytes like 0.5ME.

These findings are further supported by the electronic conductivity of the suspensions PB52 and PB54 that featured the highest LITFSI concentration (5 mol kg^{-1}) and a carbon

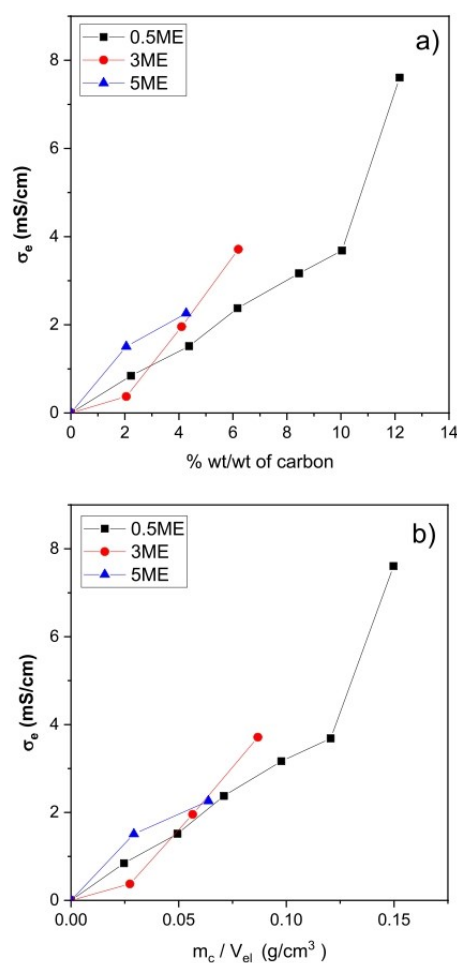


Figure 9. Electronic conductivity of 0.5ME- and 3ME-based slurries at different (a) mass percentages of carbon and (b) mass of carbon per electrolyte volume.

content equal to 2 and 4%, respectively. Indeed, for PB52 and PB54, σ_e was further improved and quantified as 1.50 and 2.26 mS cm^{-1} . These values are included in Figure 9 and are higher than those featured by 0.5ME- and 3ME-based slurries at the same carbon content. The optical fluorescence images reported in Figure S4 highlight the good dispersion of carbon particles in the superconcentrated medium.

3.4. Rheological Properties of 0.5ME-, 3ME-, and 5ME-Based Slurries. Rheological measurements were performed on 0.5ME-, 3ME-, and 5ME-based slurries to evaluate their viscosity at a shear rate ranging from 0.1 s^{-1} to 1000 s^{-1} . Figure 10 shows the viscosity trends in relation with the shear rate applied. All the samples display a non-Newtonian behavior. Indeed, viscosity decreases by increasing the shear rate. Furthermore, the higher the carbon content of the slurry, the higher the viscosity of the samples. In fact, at 0.1 s^{-1} , the viscosity increases from 3 Pa s for PB052 to 628 Pa s for PB0512, from 18 Pa s for PB32 to 338 Pa s for PB36, and from 38.7 Pa s for PB52 to 184 Pa s for PB54. A more detailed

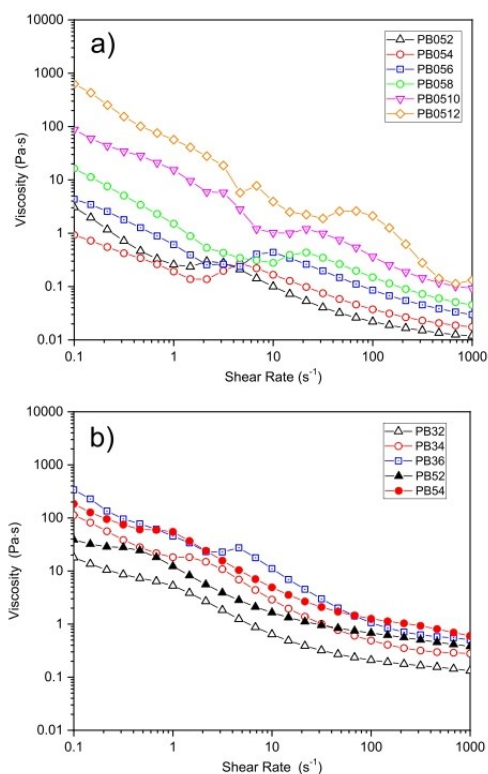


Figure 10. Viscosity response of (a) 0.5ME- and (b) 3ME- and SME-based slurry suspension on a shear rate range from 0.1 to 1000 s^{-1} .

analysis of the plots highlights the presence of three regions for each curve. Viscosity decreases almost linearly at high and low shear rates, and a broad peak can be observed in between. This was also observed by Youssry et al.,^{16,17} who reported a three-phase behavior of the slurries: two shear-thinning phases, at low and high shear rates, separated by a transient shear-thickening phase located at the so-called critical shear rate point. This behavior was attributed to structural changes of the particles under Brownian and hydrodynamic forces that have a different impact on the slurry rheology at different shear rates. The shear thinning observed at low shear rates might be attributed to the breaking up of large agglomerates into smaller ones and to the reduction of the interparticle interactions. In turn, this brings about a lower resistance to the flow. At the critical shear rate point, a new transient phase is established. Here, small aggregates are rearranged as hydroclusters, shaped by the lubricating hydrodynamic forces. These hydroclusters are driven and sustained by the applied shear and contribute to the increase of the resistance to flow, therefore explaining the shear-thickening phase behavior. At the highest shear rates, the hydroclusters break into smaller particles that slide with weak resistance and set up a shear thinning phase. In Figure 10, it is evident that for all the samples, the shear-thickening phase shifts to higher shear rates as a consequence of the carbon content increase. At high carbon percentage, the initial clusters

are strongly connected to each other, as shown by optical fluorescence images (Figures 4 and 7), and require a higher shear rate value to break up into smaller particles. It is worth noting that the shear thickening phases of SME- and 3ME-based slurries are less pronounced and slightly shifted to lower shear rates compared to 0.5ME samples, at the same amount of carbon content. This shift is caused by an easier disaggregation of the initial particles along with the formation of hydroclusters in superconcentrated electrolytes. In 3ME and, mainly, in SME, carbon particles are better distributed and their interactions are shielded by the high ionic strength of the fluids, as remarked by optical fluorescence images (Figure 7) and demonstrated by their efficient electronic percolation.

4. CONCLUSIONS

Semisolid RFBs, like those based on the lithium-ion battery chemistry, represent an emerging technology. Achieving an effective exploitation of the redox species dispersed in the anolyte and catholyte is a requisite. This can be attained by the optimization of the electrical percolating network that is typically realized by the use of carbon particles.

For the first time, to the best of our knowledge, the effect of the electrolyte ion concentration on the electronic percolating network of carbonaceous slurries for lithium-ion semisolid RFBs is here reported by a deep EIS analysis. EIS resulted to be a powerful technique to monitor the electrical properties of conductive slurries and their dynamic behavior. A model that describes the complexity and heterogeneity of the semisolid fluids by multiple conductive branches is proposed.

The study was carried out by taking into account different concentrations of LiTFSI in TEGDME, namely, 0.5 molal (0.5ME), 3 molal (3ME), and 5 molal (5ME) at different concentrations of carbon particles. The 0.5ME- and 3ME-based slurries featured a different dynamic behavior. For 0.5ME suspensions, the electronic component of the impedance decreased over time and the increase in carbon content accelerates the impedance evolution. For 3ME-based slurries, the dynamic behavior was different. The percolating resistance decreased at low carbon concentration but increased at the highest one. The EIS dynamic behavior has been explained with the sedimentation or agglomeration of carbon particles in the liquid phase that, in turn, brings about additional percolating branches with different electronic resistance with respect to fresh samples.

The main result of this work is that the electrical percolation is more efficient when the superconcentrated electrolyte is used. Indeed, the 3ME-slurries with 2 and 4% carbon feature percolating resistances that are almost 50 and 20% smaller than those of 0.5ME-based samples. This is related to a better carbon dispersion and connection in 3ME than in 0.5ME, achieved because of the high ionic strength of the superconcentrated solution that shields interparticle interactions. This was further supported by the results obtained with the SME-based slurries that featured the highest LiTFSI concentration and electronic conductivities.

Therefore, this paper demonstrates an added advantage of superconcentrated electrolytes. Besides their recognized higher electrochemical stability with respect to a conventional solution, they enable a more stable and electronically conductive slurry. Both are key features for the development of semi-solid RFBs, even beyond lithium-ion battery chemistries.

■ ASSOCIATED CONTENT

■ Supporting Information

The Supporting Information is available free of charge at <https://pubs.acs.org/doi/10.1021/acsami.1c02439>.

Cell used for EIS measurements; original R_{fit} data for all the samples; additional EIS spectra of PB052, PB0512, PB52, and PB54 slurries; and optical fluorescence images of PB5-based slurries (PDF)

■ AUTHOR INFORMATION

Corresponding Author

Francesca Soavi – Department of Chemistry “Giacomo Ciamician”, Alma Mater Studiorum Università di Bologna, Bologna 40126, Italy; Bettery Srl, Massafra 74016, Italy; orcid.org/0000-0003-3415-6938; Email: francesca.soavi@unibo.it

Authors

Alessandro Brilloni – Department of Chemistry “Giacomo Ciamician”, Alma Mater Studiorum Università di Bologna, Bologna 40126, Italy; Bettery Srl, Massafra 74016, Italy; orcid.org/0000-0002-9723-1985

Federico Poli – Department of Chemistry “Giacomo Ciamician”, Alma Mater Studiorum Università di Bologna, Bologna 40126, Italy; Bettery Srl, Massafra 74016, Italy; orcid.org/0000-0001-9891-2785

Giovanni Emanuele Spina – Department of Chemistry “Giacomo Ciamician”, Alma Mater Studiorum Università di Bologna, Bologna 40126, Italy; orcid.org/0000-0002-8998-1575

Damiano Genovese – Department of Chemistry “Giacomo Ciamician”, Alma Mater Studiorum Università di Bologna, Bologna 40126, Italy; orcid.org/0000-0002-4389-7247

Giorgia Pagnotta – Department of Chemistry “Giacomo Ciamician”, Alma Mater Studiorum Università di Bologna, Bologna 40126, Italy; orcid.org/0000-0002-8183-4992

Complete contact information is available at: <https://pubs.acs.org/doi/10.1021/acsami.1c02439>

Author Contributions

Conceptualization: F.S. Data curation: A.B., F.P., D.G., and G.P. Formal analysis: A.B., F.P., D.G., and G.P. Funding acquisition: F.S. Investigation: A.B., F.P., D.G., and G.P. Project administration: F.S. Supervision: F.S., Writing—original draft: F.P., A.B., G.E.S., D.G., and F.S. Writing—review and editing: F.P., A.B., G.E.S., D.G., G.P., and F.S. All authors have given approval to the final version of the manuscript.

Notes

The authors declare no competing financial interest.

■ ACKNOWLEDGMENTS

This research was funded by “Piano Triennale di Realizzazione 2019–2021, Accordo di Programma Ministero dello Sviluppo Economico”—ENEA (PTR MISE-ENEA 2019-2021).

■ ABBREVIATIONS

LiTFSI, lithium bis(trifluoromethane)sulfonamide; TEGDME, tetraethylene glycol dimethyl ether; EIS, electrochemical impedance spectroscopy; EES, electrical energy storage; RFBs, redox flow batteries; VRFBs, vanadium redox flow batteries; EFC, electrochemical flow capacitor; LCO, LiCoO₂;

LMNO, LiMn_{1.5}Ni_{0.5}O₄; LTO, Li₄Ti₅O₁₂; LFP, LiFePO₄; 0.5ME, 0.5 molal electrolyte; 3ME and 5ME, 3 molal and 5 molal electrolyte; PB, Pureblack 315; R_e , electronic resistance of the dispersed carbon particles; R_i , ionic resistance of the electrolyte; Q_{dl} , constant phase element for the electrical double-layer capacitance at the blocking electrode/slurry interfaces; σ_e , slurry electronic conductivity

■ REFERENCES

- (1) Uddin, M.; Romlie, M. F.; Abdullah, M. F.; Abd Halim, S.; Abu Bakar, A. H.; Chia Kwang, T. A Review on Peak Load Shaving Strategies. *Renew. Sustain. Energy Rev.* **2018**, *82*, 3323–3332.
- (2) Sánchez-Díez, E.; Ventosa, E.; Guarnieri, M.; Trovò, A.; Flox, C.; Marcilla, R.; Soavi, F.; Mazur, P.; Aranzabe, E.; Ferret, R. Redox Flow Batteries: Status and Perspective towards Sustainable Stationary Energy Storage. *J. Power Sources* **2021**, *481*, 228804.
- (3) Park, M.; Ryu, J.; Wang, W.; Cho, J. Material Design and Engineering of Next-Generation Flow-Battery Technologies. *Nat. Rev. Mater.* **2016**, *2*, No. 1680.
- (4) Dunn, B.; Kamath, H.; Tarascon, J. M. Electrical Energy Storage for the Grid: A Battery of Choices. *Science* **2011**, *334* (6058), 928–935.
- (5) Zhao, Y.; Ding, Y.; Li, Y.; Peng, L.; Byon, H. R.; Goodenough, J. B.; Yu, G. A Chemistry and Material Perspective on Lithium Redox Flow Batteries towards High-Density Electrical Energy Storage. *Chem. Soc. Rev.* **2015**, *44*, 7968–7996.
- (6) Hatzell, K. B.; Boota, M.; Gogotsi, Y. Materials for Suspension (Semi-Solid) Electrodes for Energy and Water Technologies. *Chem. Soc. Rev.* **2015**, *44*, 8664–8687.
- (7) Poli, F.; Ghadikolaei, L. K.; Soavi, F. Semi-Empirical Modeling of the Power Balance of Flow Lithium/Oxygen Batteries. *Appl. Energy* **2019**, *248*, 383–389.
- (8) Ruggeri, I.; Arbizzani, C.; Soavi, F. A Novel Concept of Semi-Solid, Li Redox Flow Air (O₂) Battery: A Breakthrough towards High Energy and Power Batteries. *Electrochim. Acta* **2016**, *206*, 291–300.
- (9) Presser, V.; Dennison, C. R.; Campos, J.; Knehr, K. W.; Kumbur, E. C.; Gogotsi, Y. The Electrochemical Flow Capacitor: A New Concept for Rapid Energy Storage and Recovery. *Adv. Energy Mater.* **2012**, *2* (7), 895–902.
- (10) Hamelet, S.; Larcher, D.; Dupont, L.; Tarascon, J.-M. Silicon-Based Non Aqueous Anolyte for Li Redox-Flow Batteries. *J. Electrochem. Soc.* **2013**, *160* (3), A516–A520.
- (11) Fan, F. Y.; Woodford, W. H.; Li, Z.; Baram, N.; Smith, K. C.; Helal, A.; McKinley, G. H.; Carter, W. C.; Chiang, Y. M. Polysulfide Flow Batteries Enabled by Percolating Nanoscale Conductor Networks. *Nano Lett.* **2014**, *14* (4), 2210–2218.
- (12) Ventosa, E.; Buchholz, D.; Klink, S.; Flox, C.; Chagas, L. G.; Vaalma, C.; Schuhmann, W.; Passerini, S.; Morante, J. R. Non-Aqueous Semi-Solid Flow Battery Based on Na-Ion Chemistry. P2-Type Na_xNi_{0.22}Co_{0.11}Mn_{0.66}O₂-NaTi₂(PO₄)₃. *Chem. Commun.* **2015**, *51* (34), 7298–7301.
- (13) Duduta, M.; Ho, B.; Wood, V. C.; Limthongkul, P.; Brunini, V. E.; Carter, W. C.; Chiang, Y. M. Semi-Solid Lithium Rechargeable Flow Battery. *Adv. Energy Mater.* **2011**, *1* (4), 511–516.
- (14) Mubeen, S.; Jun, Y. S.; Lee, J.; McFarland, E. W. Solid Suspension Flow Batteries Using Earth Abundant Materials. *ACS Appl. Mater. Interfaces* **2016**, *8* (3), 1759–1765.
- (15) Ruggeri, I.; Arbizzani, C.; Soavi, F. Carbonaceous Catholyte for High Energy Density Semi-Solid Li/O₂ Flow Battery. *Carbon* **2018**, *130*, 749–757.
- (16) Soavi, F.; Ruggeri, I.; Arbizzani, C. Design Study of a Novel, Semi-Solid Li/O₂ Redox Flow Battery. *ECs Trans.* **2016**, *72* (9), 1–9.
- (17) Youssry, M.; Madec, L.; Soudan, P.; Cerbelaud, M.; Guyomard, D.; Lestriez, B. Non-Aqueous Carbon Black Suspensions for Lithium-Based Redox Flow Batteries: Rheology and Simultaneous Rheo-Electrical Behavior. *Phys. Chem. Chem. Phys.* **2013**, *15* (34), 14476–14486.

- (18) Barnes, H. A. Thixotropy - A Review. *J. Non-Newtonian Fluid Mech* **1997**, *70*, 1–33.
- (19) Mueller, S.; Llewellyn, E. W.; Mader, H. M. The Rheology of Suspensions of Solid Particles. *Proc. R. Soc. London, Ser. A* **2010**, *466* (2116), 1201–1228.
- (20) Barrie, C. L.; Griffiths, P. C.; Abbott, R. J.; Grillo, I.; Kudryashov, E.; Smyth, C. Rheology of Aqueous Carbon Black Dispersions. *J. Colloid Interface Sci.* **2004**, *272* (1), 210–217.
- (21) Bröckel, U.; Meier, W.; Wagner, G. *Product Design and Engineering*; Bröckel, U., Meier, W., Wagner, G., Eds.; Wiley–VCH: Weinheim, Germany, 2013.
- (22) Ventosa, E.; Zampardi, G.; Flox, C.; La Mantia, F.; Schuhmann, W.; Morante, J. R. Solid Electrolyte Interphase in Semi-Solid Flow Batteries: A Wolf in Sheep's Clothing. *Chem. Commun.* **2015**, *51* (81), 14973–14976.
- (23) Tamura, T.; Hachida, T.; Yoshida, K.; Tachikawa, N.; Dokko, K.; Watanabe, M. New Glyme-Cyclic Imide Lithium Salt Complexes as Thermally Stable Electrolytes for Lithium Batteries. *J. Power Sources* **2010**, *195* (18), 6095–6100.
- (24) Messaggi, F.; Ruggeri, I.; Genovese, D.; Zaccheroni, N.; Arbizzani, C.; Soavi, F. Oxygen Redox Reaction in Lithium-Based Electrolytes: From Salt-in-Solvent to Solvent-in-Salt. *Electrochim. Acta* **2017**, *245*, 296–302.

3.1 Chapter 3 Conclusion

In this chapter the results on the study of SSE for LIB flowable batteries are reported. In the pursuit of lowering the environmental impact of EESS, RFB with SSE are highlighted as a cost-effective and low environmental impact alternative. Here, the effect of the electrolyte ion concentration on the electronic percolating network of carbonaceous slurries for LISSFBS is reported. The study is conducted by a deep EIS analysis. This technique resulted to be effective to monitor the electrical properties of conductive slurries and their dynamic behavior.

The main result of this work is that the electrical percolation is more efficient when the superconcentrated electrolyte is used. Indeed, the 3ME-slurries with 2 and 4% carbon feature R_e resistances that are almost 50% and 20% smaller than those of 0.5ME-based samples with the same carbon percentage. This is related to a better carbon dispersion and connection in 3ME than in 0.5ME, achieved because of the high ionic strength of the superconcentrated solution that shields interparticle interactions. The same behavior was further confirmed with the use of 5ME based slurry.

These results demonstrate an added advantage of superconcentrated electrolytes. Besides their recognized higher electrochemical stability with respect to a conventional solution, they enable a more stable and electronically conductive slurry having a structuring effect on the distribution of carbon particles. Both are key features for the development of semi-solid RFBs, even beyond lithium-ion battery chemistries.

Reference Chapter 3

- [1] da Silva Lima, L.; Quartier, M.; Buchmayr, A.; Sanjuan-Delmás, D.; Laget, H.; Corbisier, D.; Mertens, J.; Dewulf, J. “Life cycle assessment of lithium-ion batteries and vanadium redox flow batteries-based renewable energy storage systems” *Sustainable Energy Technologies and Assessments*, 2021, 46, 101286, <https://doi.org/10.1016/j.seta.2021.101286>.
- [2] He, H.; Tian, S.; Tarroja, B.; Ogunseitan, O. A.; Samuelsen, S.; Schoenung, J. M. “Flow battery production: Materials selection and environmental impact” *Journal of Cleaner Production*, 2020, 269, 121740, <https://doi.org/10.1016/j.jclepro.2020.121740>.
- [3] Díaz-Ramírez, M.C.; Ferreira, V.J.; García-Armingol, T.; López-Sabirón, A.M.; Ferreira, G. Battery Manufacturing Resource Assessment to Minimise Component Production Environmental Impacts. *Sustainability* **2020**, *12*, 6840. <https://doi.org/10.3390/su12176840>
- [4] Lourenssen, K.; Williams, J.; Ahmadpour, F.; Clemmer, R.; Tasnim, S. “Vanadium redox flow batteries: A comprehensive review” *Journal of Energy Storage*, 2019, 25, 100844, <https://doi.org/10.1016/j.est.2019.100844>.
- [5] Sánchez-Díez, E.; Ventosa, E.; Guarnieri, M.; Trovò, A.; Flox, C.; Marcilla, R.; Soavi, F.; Mazur, P.; Aranzabe, E.; Ferret, R. “Redox flow batteries: Status and perspective towards sustainable stationary energy storage” *Journal of Power Sources*, 2021, 481, 228804, <https://doi.org/10.1016/j.jpowsour.2020.228804>.
- [6] Presser, V.; Dennison, C. R.; Campos, J.; Knehr, K. W.; Kumbur, E. C.; Gogotsi, Y. “The Electrochemical Flow Capacitor: A New Concept for Rapid Energy Storage and Recovery.” *Advanced Energy Materials*. 2012, 2 (7), 895–902. <https://doi.org/10.1002/aenm.201100768>
- [7] Hamelet, S.; Larcher, D.; Dupont, L.; Tarascon, J.-M. “SiliconBased Non Aqueous Anolyte for Li Redox-Flow Batteries.” *Journal of Electrochemical Society* 2013, 160 (3), A516–A520.
- [8] Fan, F. Y.; Woodford, W. H.; Li, Z.; Baram, N.; Smith, K. C.; Helal, A.; McKinley, G. H.; Carter, W. C.; Chiang, Y. M. “Polysulfide Flow Batteries Enabled by Percolating Nanoscale Conductor Networks” *Nano Letters* 2014, 14 (4), 2210–2218. <https://doi.org/10.1021/nl500740t>
- [9] Ventosa, E.; Buchholz, D.; Klink, S.; Flox, C.; Chagas, L. G. Vaalma, C.; Schuhmann, W.; Passerini, S.; Morante, J. R. “Non-aqueous Semi-Solid Flow Battery Based on Na-Ion Chemistry. P2-Type $\text{Na}_x\text{Ni}_{0.22}\text{Co}_{0.11}\text{Mn}_{0.66}\text{O}_2\text{-NaTi}_2(\text{PO}_4)_3$ ”. *Chemical Communication* 2015, 51 (34), 7298–7301.

- [10] Duduta, M.; Ho, B.; Wood, V. C.; Limthongkul, P.; Brunini, V. E.; Carter, W. C.; Chiang, Y. M. “Semi-Solid Lithium Rechargeable Flow Battery.” *Advanced Energy Materials* 2011, 1 (4), 511–516. <https://doi.org/10.1002/aenm.201100152>
- [11] Mubeen, S.; Jun, Y. S.; Lee, J.; McFarland, E. W. “Solid Suspension Flow Batteries Using Earth Abundant Materials.” *ACS Applied Materials and Interfaces* 2016, 8 (3), 1759–1765. <https://doi.org/10.1021/acsami.5b09515>
- [12] Youssry, M.; Madec, L.; Soudan, P.; Cerbelaud, M.; Guyomard, D.; Lestriez, B. “Non-Aqueous Carbon Black Suspensions for LithiumBased Redox Flow Batteries: Rheology and Simultaneous RheoElectrical Behavior”. *Physical Chemistry Chemical Physics*. 2013, 15 (34), 14476–14486.
- [13] Brilloni, A.; Poli, F.; Spina, G. E.; Genovese, D.; Pagnotta, G.; Soavi, F.; *ACS Applied Materials & Interfaces* **2021** 13 (11), 13872-13882 <https://doi.org/10.1021/acsami.1c02439>

Chapter 4: Green Supercapacitors

This chapter deals with the achievements in the application of bio-derived components for the design and realization of high voltage green supercapacitors.

After proving the effectiveness of Pullulan as water processable binder for high voltage LIBs cathodes and demonstrated that it can be suitable for a “cradle to cradle” design for LIBs, this part of my work focuses on the exploitation of the same material in Electrical Double Layer Capacitors (EDLCs), both as binder and as separator. With this approach I was able to build, test and evaluate a fully recyclable EDLC.

For this application PU was at first used to manufacture an electrospun separator, provided by the group of Professor Focarete, Laboratory of Polymer Science and Biomaterials of the University of Bologna. The PU electrospun mat was compared with a conventional cellulose triacetate (CTA) electrospun membrane. The two natural polymers have been processed by electrospinning and the outcoming separators tested. The electrochemical and thermal stability features of the two separators were compared in different electrolytes.

The selection of the proper electrolyte is also of fundamental importance in this work. I focused the attention on ionic liquids (ILs) because, thanks to their low flammability, they represent a safer alternative to the more volatile acetonitrile solutions. In addition, ILs are known for their high thermal stability, good conductivity and wide electrochemical stability window (> 3 V).

Therefore, the two separators were tested in three different ILs electrolytes, namely 1-ethyl-3-methyl-Imidazolium bis-(trifluoromethylsulfonyl)imide (EmimTFSi), 0.5 m solution of lithium bis-(trifluoromethylsulfonyl)imide (LiTFSI) in Tetraethylene glycol dimethyl ether (TEGDME), and 1-Butyl-1-methylpyrrolidinium bis-(trifluoromethylsulfonyl)-imide (PYR14TFSI), and their contribution to ionic resistance of the electrolyte has been investigated by Electrochemical Impedance Spectroscopy (EIS) at different temperatures. The tests were carried out using cells with stainless steel blocking electrodes separated by the separator soaked with the electrolyte. It resulted that values of Resistance normalized by the plain area (ohm cm^{-2}) and Mac Mullin number (N_M) of the PU are smaller than those of the CTA in all the tested conditions. In addition, for both membranes, EmimTFSI holds the greater values of N_M with respect to other IL.

The investigation concluded that EmimTFSI-Pu exhibited a resistance considerably smaller than the one obtained with the other electrolytes with PU and that PU showed a lower Mc Mullin number than

CTA with every IL along with a better thermal behavior. Therefore, the pullulan based electrospun membrane and EmimTFSI electrolyte were selected to assemble and test EDLCs

Two different EDLCs, one with low electrode mass loading and high binder content (HBLME) and a second one with high mass loading and low binder content (LBHME) have been produced with PU as binder, EmimTFSI as electrolyte and electrospun PU separator. The EDLCs have been tested by cyclic voltammetry, EIS and galvanostatic charge/discharge cycles. The highest specific capacitance was featured at the lowest scan rate of 5 mV s^{-1} for both devices and was 18 F g^{-1} and 14 F g^{-1} for HBLME-EDLC and LBHME-EDLC, respectively. Both supercapacitors featured a good capacitance retention with the increase of the scan rate that however was higher for HBLME-EDLC (22 %) than LBHME-EDLC (50 %).

For both devices, galvanostatic cycling with high coulombic efficiency (higher than 98%) was demonstrated at high cell voltage of 3.2 V in parallel with a very good cycling behavior over more than 2000 cycles, confirming the stability of the Pu-polymer in EmimTFSI.

The high cell voltage and good specific capacitance provided specific energy of 19.6 Wh kg^{-1} and 7.2 Wh kg^{-1} at 0.5 A g^{-1} that well compare with those of EDLCs featuring the same electrolyte and active carbon but employing a fluorinated binder and fiber glass separators [1]. The highest specific power was 4.6 kW kg^{-1} and 3.7 kW kg^{-1} at $4\text{-}5 \text{ A g}^{-1}$ respectively for HBLME-EDLC and for the LBHME-EDLC

The experimental methods and the results of this study are reported in [2], which is here attached as complete publication.

Article

Natural Polymers for Green Supercapacitors

Giovanni Emanuele Spina[†], Federico Poli[†], Alessandro Brilloni, Daniele Marchese and Francesca Soavi^{*}

Department of Chemistry “Giacomo Ciamician”, Alma Mater Studiorum Università di Bologna, Via Selmi 2, 40126 Bologna, Italy; giovanni.spina3@unibo.it (G.E.S.); federico.poli8@unibo.it (F.P.); alessandro.brilloni2@unibo.it (A.B.); daniele.marchese@studio.unibo.it (D.M.)

^{*} Correspondence: francesca.soavi@unibo.it

[†] These authors contributed equally.

Received: 11 May 2020; Accepted: 10 June 2020; Published: 16 June 2020

Abstract: Water-processable natural polymers represent a valuable alternative for the sustainable manufacturing of electrical double layer capacitors (EDLCs). Here, we demonstrate for the first time the feasibility of the use of pullulan to produce high mass loading electrodes ($>10 \text{ mg cm}^{-2}$) at low binder content (10%) for ionic-liquid based EDLCs. Pullulan has also been processed as a porous separator by electrospinning. Its ionic resistance and thermal stability have been evaluated in different electrolytes and were found to be superior compared to those of a cellulose triacetate electrospun separator. Pullulan-ionic liquid EDLCs were, thus, assembled and charged up to 3.2 V. The EDLCs delivered specific energy and power of 7.2 Wh kg^{-1} and 3.7 kW kg^{-1} and featured good cycling stability over 5000 cycles.

Keywords: green supercapacitor; water processable polymer; pullulan; ionic liquid; electrospinning

1. Introduction

Today one of the biggest challenges our society is facing is how to replace the use of fossil energy sources (coal, oil, gas) with renewable ones (solar and wind). The inherent intermittence of the latter sources requires the development of efficient energy storage systems. Among all the possibilities, electrochemical energy storage by secondary batteries and electrical double layer capacitors (EDLCs) is one of the most efficient approach [1–4]. EDLCs are receiving great attention for their unique characteristics of outstanding power and cycle life, that are related to their electrostatic operating mechanism. However specific energies of EDLCs are one order of magnitude lower than that of batteries.

Commercial EDLCs feature activated carbon (AC) electrodes, a porous polymer separator, and an organic electrolyte, typically a solution of alkylammonium salts in acetonitrile or propylene carbonate. The use of the organic electrolyte enables cell voltages as high as 2.5 V [5].

The energy density of EDLCs can be improved by increasing: (i) the operating voltage window, (ii) electrodes specific capacitance, and (iii) the mass loading of the electrodes.

High operating voltage can be achieved by using an electrolyte with a wide electrochemical stability window, like ionic liquids (ILs) or highly concentrated aqueous electrolytes [6–9]. Electrode specific capacitance can be improved by tailoring carbon porosity to the electrolyte, in order to enhance ion access to the carbon surface. An alternative strategy is represented by the use of redox (pseudocapacitive) electrode materials, like metal oxides or electronically conductive polymers, in asymmetric or hybrid supercapacitors. Regarding the third approach, literature provides a very limited number of publications. Achieving mass loading higher than $5\text{--}10 \text{ mg cm}^{-2}$ is considered a great challenge. Indeed, thick electrodes might delaminate from the current collector that is detrimental for cycling stability. Furthermore, high mass loading may lead to worse ionic and electronic connection between the carbon particles, leading to higher internal resistance [10–12].

Ionic liquids, thanks to their low flammability, represent an even safer alternative to the more volatile acetonitrile solutions. In addition, ILs are known for their high thermal stability, good conductivity and wide electrochemical stability window (>3 V). Despite these interesting properties, they cannot be considered as totally green and strategies to recover them after use are needed. The most investigated ILs for EDLCs are based on the bis(trifluoromethanesulfonyl)imide (TFSI) anion [13–15]. ILs feature bulky ions, therefore in order to promote a high and efficient exploitation of the electron carbon surface of the double layer, the porosity of the carbon has to be properly designed [16,17]. Furthermore, it has been demonstrated that the chemistry of ILs affects the double layer thickness and permittivity, and hence, the electrode capacitance. Indeed, in ref [1,2], the capacitive response of different carbon electrodes in *N*-butyl-*N*-methylpyrrolidinium bis(trifluoromethanesulfonyl)imide (PYR₁₄TFSI), 1-ethyl-3-methylimidazolium bis(trifluoromethanesulfonyl)imide (EmimTFSI) and PYR₍₂₀₁₎TFSI was compared. In EmimTFSI, all the tested electrodes featured a specific capacitance that was double than that exhibited in the other ILs.

In EDLCs the biggest share of the cost is related to electrodes (28%) and electrolytes (27%). Electrodes are processed by casting slurries made of AC, conductive carbon, binder, and suitable solvents on metal current collectors. The binder material itself does not contribute significantly to the overall cost. However, its chemistry drives the selection of the solvent used for electrode processing, that has a great economic and environmental impact on EDLCs manufacturing [18]. Indeed, nowadays, commercial AC electrodes are mostly fabricated with F-based polymers as binders, such as poly(vinylidene difluoride) (PVdF) which needs *N*-methyl-2-pyrrolidone (NMP) as solvent/dispersant, both very toxic for humans and environment. This process requires expensive atmosphere-controlled environments [19].

In light of that and to meet the requirements of sustainable and cheaper production processes, much effort is being devoted to the substitution of F-based components with alternative ones. Transition to aqueous electrode preparation by non-toxic binders is expected to provide a great step forward towards an ideally sustainable and environmentally friendly technology for energy storage systems [20,21].

Carboxymethyl cellulose (CMC) represents the state of the art of water-soluble binders [10,21–24]. One of the first attempts of substituting F-based compounds with CMC, was reported by Bonnefoi et al. in 1999 [25]. Two of the major drawbacks in the use of CMC, are: (i) the relatively low achievable electrode mass loading, and (ii) the brittleness shown after the drying step. Winter et al. [23], first proposed Natural Cellulose (NC). While NC is cheaper (0.5–1.5 EUR kg⁻¹ vs. 1–2 EUR kg⁻¹) and more abundant than CMC, it cannot be dissolved in water nor in almost all organic solvents while being soluble in certain ionic liquids [26–29]. Varzi et al. dissolved NC in 1-ethyl-3-methylimidazolium acetate (EmimAc) and demonstrated that NC has enhanced stability at high voltages. An EDLC assembled with electrodes featuring 10 % NC binder and a mass loading of c.a. 3 mg cm⁻² and PYR₁₄TFSI ionic liquid electrolyte, exhibited a specific capacitance of c.a. 13 F g⁻¹ at 10 mA cm⁻², and a capacitance retention of 52%, after cycling for 750 h at 3.7 V [30]. Pursuing the research of even more eco-friendly binders, potato starch, a highly abundant polysaccharide that can be extracted from non-edible potatoes, was also proposed. By the use of this polysaccharide, the production of thick electrodes (240 μm, 9.3 mg cm⁻²) was demonstrated [18]. These electrodes were used to assemble a 2.5 V-EDLC with 1 M Et₄NBF₄ in propylene carbonate (PC) electrolyte, that delivered 0.36 F cm⁻² at 10 mA cm⁻².

Recently, we demonstrated the use of the biodegradable biopolymer pullulan (Pu) as a water processable separator and binder for EDLCs. Specifically, the separator was obtained by electrospinning and the EDLCs featured EmimTFSI electrolyte and pepper seed derived biochar carbon. The EDLC was able to operate at 3.2 V and delivered up to 5 kW kg⁻¹ specific power and 27.8 Wh kg⁻¹ specific energy. Its performances were compared with that of conventional electrical double-layer capacitor, with the added value of being eco-friendly and cheap.

Furthermore, the smart combination of the water-soluble, biodegradable Pu with the hydrophobic ionic liquid EmimTFSI, enabled a novel and easy approach for the recovery of EDLC

components at the end-of-life. Indeed, the IL and carbon easily separate when immersed in water. The expensive IL can therefore be recollected for a second use [31].

Following these preliminary results, here we report the challenging study that aims to demonstrate the feasibility of the use of Pu to process electrodes at low binder content (10 %) and high mass loading ($>10 \text{ mg cm}^{-2}$). In the first part of our work we compare the electrochemical response and thermal stability of Pu and cellulose triacetate (CTA) in different electrolytes, namely EmimTFSI, 0.5 m LiTFSI TEGDME, PYR₁₄TFSI. The two natural polymers have been processed by electrospinning and their contribution to ionic resistance of the electrolyte has been investigated by Electrochemical Impedance Spectroscopy (EIS) at different temperatures. On the basis of this investigation, Pu and EmimTFSI were selected to assemble two different EDLCs, one with low electrode mass loading and high binder content (HBLME) and a second one with high mass loading and low binder content (LBHME). The EDLCs have been tested by cyclic voltammetry, EIS and galvanostatic charge/discharge cycles. A deep analysis of the EDLCs performance is reported and discussed to demonstrate that natural polymers and, specifically Pu, may pave the way towards a new approach for a green manufacturing of EDLCs.

2. Materials and Methods

2.1 Materials

N-butyl-*N*-methylpyrrolidinium bis(trifluoromethanesulfonyl)imide (PYR₁₄TFSI, purity >99.9 %) was purchased from Solvionic (Toulouse, France). 1-Ethyl-3-methylimidazolium bis(trifluoromethanesulfonyl)imide (EmimTFSI, purity >99 %) was purchased from Solvent Innovation (Köln, Germany). Lithium bis(trifluoromethanesulfonyl)imide and tetraethylene glycol dimethyl ether (TEGDME) (purity >99 %) were both purchased from Sigma-Aldrich (St. Louis, Mo, USA). Activated carbon PICA^{CTIF} was purchased from PICA (Basiano, Italy). Conductive carbon additive (SUPER C45) was purchased from TIMCAL (Bodio, Switzerland). Pullulan (P0978, $\eta = 15.0 \div 180.0 \text{ mPa s}$, 10 % in H₂O at 30 °C) was purchased from TCI Europe (Zwijndrecht, Belgium). Cellulose triacetate (CTA, $M_w = 74,000 \text{ g/mol}$, DS 3.0) was purchased from Honeywell Fluka (Charlotte, NC, USA). Glycerol (purity $>99\%$) was purchased from Sigma-Aldrich. Nickel foam was purchased from Alantum (Munich, Germany).

2.2. Preparation of the Electrospun Separator

Electrospinning was used to prepare the non-woven separator. In particular an home-made electrospinning apparatus has been used, this consisted of a high-voltage power supply (SL 50 P 10/CE/230, Spellman, West Sussex, UK), a syringe pump (200 series, KD Scientific, Holliston, MA, USA), a glass syringe containing the polymer solution and connected to a stainless-steel blunt-ended needle (inner diameter = 0.51 mm) through a polytetrafluoroethylene (PTFE) tube. The Pu membrane was electrospun starting from a 23 % *w/v* solution of pullulan in Milli-Q water. The solution was spun at 18 kV at 20 cm from the collector with a flow rate of 1 mL h⁻¹. The cellulose triacetate (CTA) separator has been electrospun starting from a 6 % *w/v*. solution in DCM/EtOH 80/20 solution. The solution was spun at 15 kV and at a 15 cm distance from the collector with a flowrate of 2 mL/h, at room temperature (RT) with a relative humidity of 40–50%. After electrospinning the mat has been soaked into a 0.1 M solution of sodium hydroxide in a mixture of Ethanol and water 4:1 *v/v* for 24 h. In the end the electrospun separator was washed in MilliQ water twice for fifteen minutes each.

2.3. Membrane Characterization

Electrospun membranes have been characterized at first by scanning electron microscopy (SEM) using an EVO 50 apparatus (Zeiss, Oberkochen, Germany). The feasibility of the use of the electrospun mats as separators was evaluated by EIS. Swagelok-type cells with two stainless steel blocking electrodes (0.9 cm diameter), separated by the membranes (dried overnight before use at RT) soaked in the different investigated electrolytes, were used. The EIS spectra were collected by a VSP multichannel potentiostat/galvanostat/FRA (BioLogic, Seyssinet-Pariset, France) within 500

kHz–100 mHz frequency range and 5 mV AC perturbation, acquiring 10 points per decade. The cells were thermostated at 30, 40 and 60 °C by a thermostatic oven. The bulk conductivity of the electrolytes without membranes were measured by a CDM 210 Conductivity Meter (MeterLab, Milano, Italy) with an Amel standard cell (platinum electrodes). The temperature was controlled by a DC50 K40 thermocryostat (Haake, Thermo Fisher Scientific, Karlsruhe, Germany) with an accuracy of 0.1 °C. Samples were thermostated for 1 h before every measurement.

2.4. Preparation of the Electrodes

Electrodes were prepared using the mesoporous carbon PICA^{CTIF} from PICA (BP10) as reported in [8] and described in Figure S1a. BP10 featured a Brunauer, Emmett and Teller (BET) specific surface >2000 m² g⁻¹ and a pores size distribution centered at 2.7 nm [8]. Two water processable formulations have been studied. A first one with 70 % BP10, 10 % Carbon black, 20 % pullulan-glycerol (1:1 wt) and low mass loading (3.6–4.6 mg cm⁻²) is referred in the following text as high binder low mass electrode (HBLME). A second one with 85 % BP10, 5 % Carbon black, 10 % pullulan-glycerol and higher mass loading is labelled as low binder high mass electrode (LBHME). Electrodes have been obtained by casting on pre-cut nickel foams (diameter 0.9 cm) a slurry containing 23.5 mg of BP10, 3.5 mg of carbon black (as conducting additive), 6.7 mg of pullulan (P0978, TCI) and glycerol in 0.8 g of MilliQ water for HBLME. For LBHME the ink was composed of 40.2 mg of BP10, 2.3 mg of carbon black (as conducting additive), 4.7 mg of pullulan and glycerol in 0.57 g of MilliQ water. The electrodes were then dried in an oven (under vacuum) overnight at room temperature (Büchi glass oven B-585). The composite electrode loadings (excluding the nickel foam mass) are reported in Table 1.

Table 1. Composition and mass loading of High Binder Low Mass Electrode (HBLME) and Low Binder High Mass Electrode (LBHME).

Name	Composition	Mass Loading Range *
HBLME	70 % BP10/10% CB/20 % binder	3.6–4.6 mg cm ⁻²
LBHME	85 % BP10/5% CB/10 % binder	6.3–7.5 mg cm ⁻²

* single electrodes mass loading.

2.5. Supercapacitor Assembly

A T Swagelok-type cell assembly (BOLA Cell made from Teflon, BOLA GmbH, Grünsfeld, Germany) with a silver quasi-reference electrode disk and stainless-steel current collectors was used. Cells were assembled in a dry box (Labmaster 130, H₂O, and O₂ <0.1 ppm MBraun, Garching, Germany). The separator (12 mm diameter) and the electrodes (9 mm diameter) were soaked under vacuum together with the IL before the assembly. The ratio of the positive to negative electrode composite loading was >1 to achieve cell voltages higher than 3 V [32]. EDLCs were assembled with two carbon based composite electrodes alienated by a circular sheet of electrospun pullulan separator, with 1-ethyl-3-methylimidazolium bis(trifluoro-methylsulfonyl) imide IL (EmimTFSI) as the electrolyte, as described in Figure S1b.

2.6. Supercapacitor Characterization

The electrochemical tests consisted in EIS, cyclic voltammetry (CV) and galvanostatic (GCPL) tests and were performed in a thermostatic oven at 30 °C using a BioLogic VSP multichannel potentiostat/galvanostat/FRA. EIS was performed with a 100 kHz–100 mHz frequency range and 5 mV AC perturbation, acquiring 10 points per decade. To evaluate the impedance of each of the EDLC electrodes, three electrode measurements, have been done. A silver disk has been used as pseudo reference. Here, the working electrode was the tested one and counter the other. To evaluate the complete cell impedance, two electrode measurement have been done. For two electrode measurements, the silver disk was disconnected, the EDLC positive electrode was the working, and the EDLC negative electrode was connected to the counter and reference instrument plugs.

CV discharge curves were analyzed to get a first evaluation of the EDLC specific capacitance (C_{EDLC}). Specifically, C_{EDLC} was calculated from the slope of the voltammetric plots of the discharge capacity vs. cell voltage. The capacity was calculated by the integral of the CV current over time. The slope values were divided by the total composite mass of the two electrodes (m_{tot}).

The GCPL curves were analyzed to quantify the equivalent series resistance (ESR) and the C_{EDLC} , the specific energy and power of the devices at different discharge currents. ESR was calculated according to Equation (1), where ΔV_{ohmic} is the ohmic voltage drop at the beginning of discharge, and i is the current density ($A\ cm^{-2}$):

$$ESR = \Delta V_{ohmic} / (2 \times i) \quad (1)$$

C_{EDLC} was calculated from the reciprocal of the slope of the GCPL voltage profile during the discharge (dt/dV) by Equation (2):

$$C_{EDLC} = i \times dt/dV / m_{tot} \quad (2)$$

The single electrode specific capacitance ($C_{electrode}$) was therefore calculated from the EDLC's one by Equation (3)

$$C_{electrode} = 4 \times C_{EDLC} \quad (3)$$

The EDLCs specific energy (E) and power (P) were calculated from the GCPL discharge curves through Equations (4) and (5):

$$E = i \int V \times dt / (3600 \times m_{tot}) \quad (4)$$

$$P = 3600 \times E / \Delta t \quad (5)$$

where Δt is the discharge time in seconds.

3. Results

3.1. Electrospun Separator and Electrolyte Selection

Figure 1a,b report the SEM images of the electrospun Pu and CTA membranes, respectively. They feature interconnected fibers, randomly deposited, with a low number of defects. The Pu mat thickness was $55\ \mu m$ and the mean fiber diameter was around $0.3\ \mu m$. The CTA mat thickness was $22\ \mu m$ and the mean fiber diameter was around $0.6\ \mu m$. The fiber thickness of the two mats is in line with the value already reported for electrospun separators obtained with different polymers [33]. Furthermore, the PU and CTA mat thicknesses were adequate for an easy handling and assembly of the EDLCs. In addition to the difference in fiber diameter, the two polymers differ in terms of fiber diameter distribution, the CTA fibers being less homogeneous with a broader distribution.

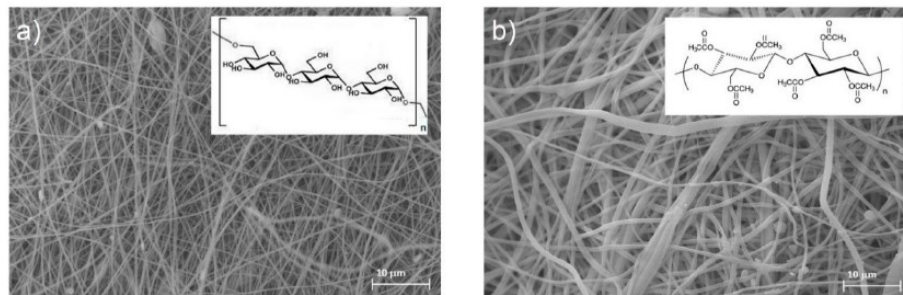


Figure 1. SEM images of electrospun membrane of (a) pullulan and (b) cellulose triacetate with their molecular structures.

Before the evaluation of the ionic conductivity response of the membranes, at first bulk conductivity of the electrolytes was measured. The values at different temperatures are reported in Table 2. The ionic conductivity of all the tested electrolytes grows with temperature. Among the considered electrolytes, the most conductive one is the EmimTFSI. Specifically, at 30 °C EmimTFSI features 12.6 mS cm⁻¹, which is 5-fold higher than the conductivity of 0.5 m LiTFSI in TEGDME (2.05 mS cm⁻¹) and PYR₁₄TFSI (3.01 mS cm⁻¹).

Table 2. Ionic conductivity of the tested electrolytes at different temperatures.

Conductivity (mS cm ⁻¹)	σ (30°)	σ (40°)	σ (60°)
EmimTFSI	12.60	15.10	25.70
0.5 m LiTFSI in TEGDME	2.05	2.63	4.82
PYR ₁₄ TFSI	3.01	3.90	6.30

The separators of the EDLCs should be designed in order to achieve low ESR. This can be obtained by minimizing their hindrance to the ion flow during the charge/discharge, while guaranteeing the electronic separation of the two electrodes.

In order to evaluate the contribution of the investigated separators and electrolytes to ESR, EIS measurements were performed. The tests were carried out using cells with stainless steel blocking electrodes separated by the separator soaked with the electrolyte. EIS was carried out at constant interval of time (24 h) and at different temperature (30 °C, 40 °C and 60 °C) to check the chemical and electrochemical stability of the different membranes in the tested electrolytes.

As an example, Figure 2 reports the Nyquist plots of the electrospun pullulan separator in EmimTFSI over time at the different tested temperatures. The Nyquist plots for all the combination of Pu and CTA membranes with the different electrolytes are reported in Figure S2.

In Figure 2, the impedance spectra of the Pullulan membrane resemble a straight line. This response can be modelled with a resistance (R) in series with a constant phase element (Q), therefore the resulting impedance is given by the following equation:

$$Z = R - 1/(j \omega Q)^n \quad (6)$$

In Equation (6), R is the equivalent resistance of the separator soaked in the electrolyte and can be evaluated from the intercept with the real axis in the 150–300 kHz frequencies region. It includes the electronic resistance of the current collectors and the ionic resistance of the cell which reasonably dominates the response. When $n = 1$, the plot is a line parallel to the imaginary axis and Q represents the capacitive response of the cell. When $n = 0.5$, the plot is a line with a slope of 45° and Q corresponds to the Warburg element that is representative of diffusion-controlled processes.

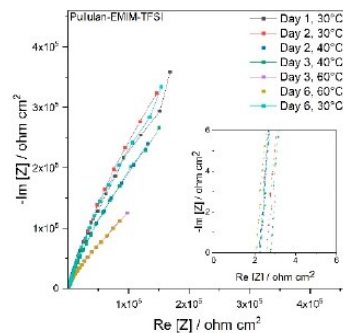


Figure 2. Nyquist plot of Pullulan electrospun membrane in EmimTFSI electrolyte.

Figure 2 shows that the temperature increase leads to the decrease of the resistance of the cell that is related to the increase of the electrolyte conductivity (cf. Table 2). In parallel, it is noticeable that the slope of the Nyquist plot decreases, unveiling that ion diffusion through the membrane becomes more sluggish.

This behaviour could be explained with the swelling of the membrane at the highest temperature that, in turn, brings about thickening of the fibres and narrowing of the inter-fibre voids. This might result in a more tortuous path for ion conduction.

Tables S1 and S2 and Figure 3a,b report the values of resistance of Pu and CTA membrane respectively, at different temperatures over time, in the different electrolytes. The values are in the same order of magnitude and span between c.a. 2 and 5 ohm cm². The first day at 30 °C, Pu features 2, 3 and 3.5 Ohm cm² when soaked with EmimTFSI, 0.5 m LiTFSI TEGDME and PYR₁₄TFSI, respectively. CTA exhibits 2, 3 and 3.5 Ohm cm² with EmimTFSI, 0.5 m LiTFSI TEGDME and PYR₁₄TFSI. Therefore, resistance values are similar for both membranes in the same electrolytes, with EmimTFSI accounting for the smallest values. A more straightforward comparison must consider the mat thickness of both separators and can be carried out referring to the effective resistivity (ρ_{eff}) of the membrane-electrolyte system. The value of ρ_{eff} can be obtained by Equation (7):

$$\rho_{\text{eff}} = S \times R/L \quad (7)$$

where R is the resistance (in Ohm), L is the membrane thickness (cm), and S is the current collector area (cm²).

As commented above, Pu separator features a thickness of 55 μm that is almost 2.5 times larger than the CTA's that is 22 μm . Therefore, ρ_{eff} of Pu at 30 °C in EmimTFSI results 450 Ohm cm and is almost half than CTA's (over 1000 Ohm cm). This can be related to the thinner fibres of the former membrane (0.3 μm) vs. the latter (0.6 μm). Thinner fibres provide a greater surface area and a greater density of free volume that can be exploited by ions to achieve higher conductivity. Noticeably, the resistance values of Pu at the different temperatures keep almost constant during time. At the contrary, those of CTA membrane gradually increase achieving 5 Ohm cm² at 60 °C, after 5 days, a value that doubles the Pu ones. Furthermore, after six day, the temperature was lowered to 30 °C. The resistance of Pu-EmimTFSI went back to its initial value while the CTA-EmimTFSI ones doubled (4 Ohm cm²). This indicates that the swelling process promoted by the increase of temperature is reversible for Pu but not for CTA. Overall, the data of Figure 2 suggest that Pu membrane is more stable than CTA.

In order to get further insight into the contribution of the separator to the ESR, the Mac Mullin number (N_M) has been calculated for all the tested systems. Indeed, N_M quantifies the increase of resistivity of the separator soaked in the electrolyte (ρ_{eff}) with respect to the bulk resistivity of the electrolyte solution (ρ_0), and it is calculated after Equation (8):

$$N_M = \rho_{\text{eff}}/\rho_0 \quad (8)$$

where ρ_{eff} has been evaluated by Equation (6) using the resistance values listed in Tables S3 and S4. In turn, ρ_0 is the reciprocal of the electrolyte conductivity (σ_0) and is calculated by Equation (9):

$$\rho_0 = 1/\sigma_0 \quad (9)$$

The N_M values for the different separator/electrolyte combinations at the different temperatures are reported in Tables S5 and S6 and in Figure 3c,d as comparative histograms.

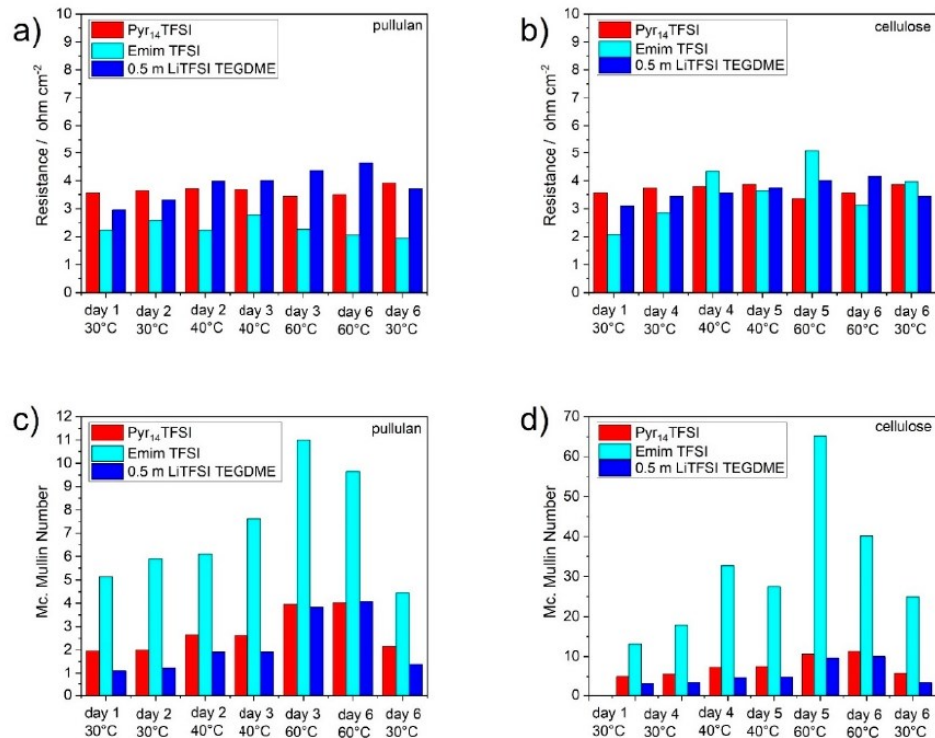


Figure 3. Resistance normalized by the plain area and MacMullin number of (a,c) Pullulan and (b,d) Cellulose triacetate electrospun separators in different tested electrolytes.

The values of the Pu are always smaller than those of the CTA in all the tested condition. For both membranes, in all the tested conditions, EmimTFSI holds the greater values of N_M , while the smaller ones are exhibited by 0.5 m LiTFSI in TEGDME. The first day at 30 °C, Pu features N_M of 5, 1 and 2 when soaked with EmimTFSI, 0.5 m LiTFSI TEGDME and Pyr₁₄TFSI, respectively. For CTA, N_M is 13, 3 and 5 with EmimTFSI, 0.5 m LiTFSI and PYR₁₄TFSI, respectively. These trends indicate that EmimTFSI is the electrolyte that has a conductivity that is more affected by the presence of the membranes. In turn, this can be explained taking into account the protic behaviour of EmimTFSI. Indeed, unlike the other electrolytes, EmimTFSI features an acidic proton in alpha position in the imidazolium ring, that contributes to its bulk ionic conductivity. When EmimTFSI is in contact with the membranes this proton drives specific acid-base interactions that decrease its activity. Specifically, it can be claimed that hydrogen bond with the carboxyl functionalities of the membranes are formed (Figure 1).

For both separators soaked with EmimTFSI, N_M increases with temperature. In case of Pu, it reaches a maximum of 11 on the day 3 at 60 °C. For CTA N_M is 65 during the day 5 at the same temperature. Once cooled at 30 °C (day 6), Pu-EmimTFSI's N_M reversibly reduces to 4 that is even smaller than its initial value, in agreement with the resistance trend (Figure 3a). At the contrary CTA-EmimTFSI's N_M does not recover its initial value and doubles (25).

To conclude this section, EmimTFSI-Pu featured a resistance considerably smaller than the one obtained with the other electrolytes. Pu exhibited a lower McMullin number than CTA along with a better thermal behaviour. Therefore, the pullulan based electrospun membrane and EmimTFSI were selected to assemble and test EDLCs as described in the next section below.

3.2. Supercapacitor Testing

The EDLCs featured the commercial high surface area carbon BP10 and the conductive additive Super C45. We already demonstrated the good binding properties of the pullulan: glycerol mixtures, that was therefore selected for the aqueous processing of the carbon composite electrodes [31].

The following sections report the electrochemical characterization of EDLCs assembled with 20% binder and low composite electrode mass loading ($3.6\text{--}4.6\text{ mg cm}^{-2}$), referred as high binder low mass electrode (HBLME, Section 3.2.1), and with 10% binder and higher mass loading, labelled as low binder high mass electrode (LBHME, Section 3.2.2). The first composition was meant to verify the feasibility of the use of Pu binder and Pu membrane in the tested electrolyte while the second is meant to reach a formulation closer to that exploited commercial EDLCs. Section 3.2.3 compares the performances of HBLME and LBHME based EDLCs.

The electrochemical tests at first included EIS measurements of both the individual electrodes and of the full cell. These tests enable the evaluation of the EDLCs ESR that accounts for the contributions of (i) the contact resistance between composite material and current collector and (ii) the ionic resistance of the separator/electrolyte. Two electrodes cyclic voltammetry (CV) experiments have been carried out between 0 V and 3.2 V to evaluate the electrochemical stability and the capacitance of the EDLC as function of the scan rate. Galvanostatic (GCPL) charge/discharge measurements between 0 and 3.2 V (GLV) at different specific currents were subsequently performed to evaluate the specific energy and power. Finally, GCPL cycling has carried out at 1 A g^{-1} in order to evaluate the stability of the proposed EDLCs.

3.2.1. High Binder Low Mass Loading Electrodes (HBLME)

In this section, the results of the electrochemical characterization of the HBLME-EDLCs are reported. Figure 4a shows the Nyquist plots of the HBLME-EDLC single electrodes and the full cell. The three Nyquist plots share all the same shape. They can be divided into three components: (i) a high frequencies semicircle, (ii) a middle frequencies line with a slope of c.a. 45° , and (iii) a low frequency line that approaches a slope of 90° . The intercepts at the highest frequencies of the semicircles represents the ohmic resistances (electronic and ionic) of the electrodes and electrolyte-separator system. Values of 1.4, 1.5 and 3.3 Ohm cm^2 have been measured, respectively for the negative, the positive electrode and the full cell. The small semicircle has been attributed to (i) the ion transport at the electrolyte-carbon interface and (ii) the contact between the electrode and the current collector [34]. For the full cell the semicircle diameter is 0.3 Ohm cm^2 . The middle frequency line with 45° slope is representative of diffusion limited phenomenon. Specifically, it refers to diffusion of ions required to charge inner pores of the carbon electrodes. The low frequency line represents the capacitive behavior of the electrodes and the EDLC. For an ideal EDLC, a vertical line is expected. In Figure 4a the lines deviate from this ideal behavior because of the presence of different class of pores [35]. The real axis intercept of the linear fit of the cell low frequency line gives the ESR that was quantified in 6.4 ohm cm^2 .

Figure 4b reports the CVs of the full HBLME-EDLC cell at different scan rate, between 0 and 3.2 V. The voltammogram are symmetric and box shaped, which indicates the absence of faradic secondary process and an electrical double layer driven process. The maximum current of 3 A g^{-1} (25 mA cm^{-2}) is reached with a scan rate of 200 mV s^{-1} , this value is comparable with the ILs based EDLC already reported in literature [8]. Figure 4c reports the trend of C_{EDLC} versus the scan rate. The highest specific capacitance of HBLME-EDLC is 18 F g^{-1} at 5 mV s^{-1} and decreases to 14 F g^{-1} at 200 mV s^{-1} . This trend has been widely discussed in literature and is attributed to the ionic diffusion limitation upon the double layer formation in the smallest pores at fast scan rates [36]. Indeed, micropores with an internal area less exposed to the electrolytes need more time for the creation of the electrical double layer than bigger pores. At low scan rate, the polarization is slow and ions have enough time to access the internal area of micro-pores. Increasing the scan rate, only the external surface of the pores becomes easily accessible. This process also explains the 45° Warburg line of the Nyquist plot of Figure 4a.

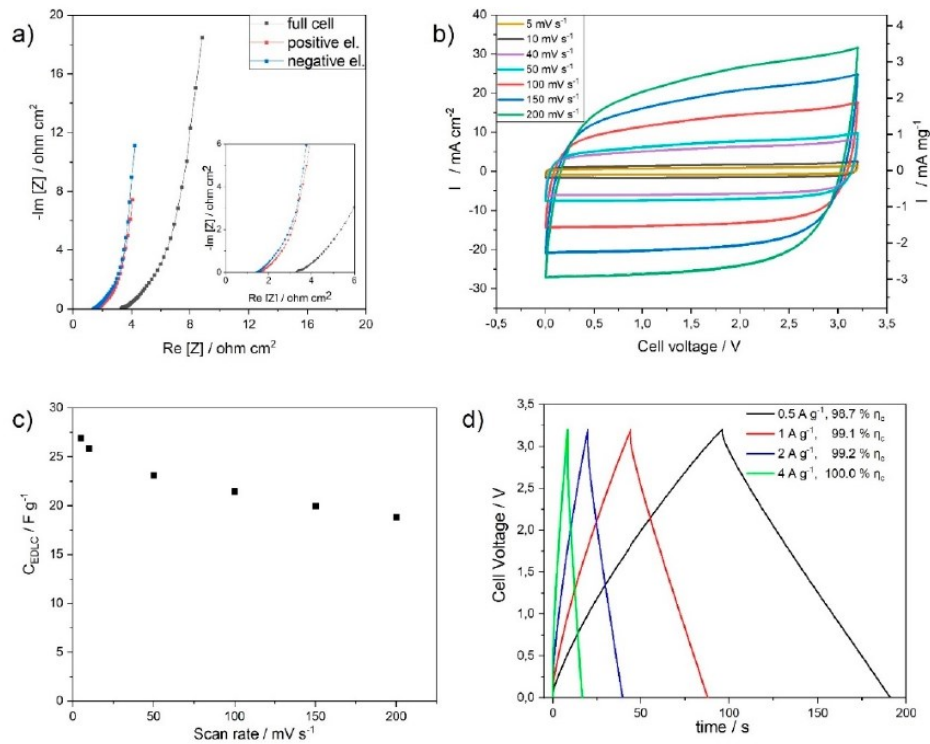


Figure 4. Electrochemical characterization of HBLME-EDLC (a) Nyquist plots of the (black) full cell, (red) positive and (blue) negative electrodes (500 kHz and 100 mHz), (b) 2-electrode CVs at different scan rate from 5 mV s^{-1} to 200 mV s^{-1} , between 0 V and 3.2 V, (c) Capacitance of the EDLC evaluated by CV reported as function of the scan rate; and (d) selected galvanostatic charge/discharge cycles between 0 V and 3.2 V at different current densities from 0.5 A g^{-1} to 4 A g^{-1} .

Figure 4d reports selected voltage profiles of the HBLME-EDLC under galvanostatic charge/discharge cycles at different current density, between 0 and 3.2 V. The voltage profile of the cell has a symmetric, triangular shape which is characteristic of electrical double layer driven process. Increasing the current from 0.5 to 4 A g^{-1} leads, as expected, to the decrease of the charge/discharge time. Coulombic efficiency (η_c), i.e., the ratio between the charge released during discharge and the charge stored during charge, is reported as inset in Figure 3d. This quantity is always greater than 98 % and reaches the highest value of 100 % at 4 A g^{-1} . The GCPL ohmic drops were analyzed to quantify ESR of the device and resulted in 5.9 Ohm cm^2 , that well compares with the value obtained by EIS. EDLC. Specific capacitance C_{EDLC} has been calculated from the slope of the GCPL discharge profile and for HBLM-EDLC resulted in 15.9 , 15.4 , 14.6 and 13.7 F g^{-1} at 0.5 , 1 , 2 and 4 A g^{-1} , respectively. The corresponding single electrode specific capacitances ($C_{electrode}$) are 63 , 61 , 58 and 54.8 F g^{-1} . These values well compare with those of electrodes featuring the same electrolyte and carbon but employing a fluorinated binder [8]. Table 3 reports the ESR and C_{EDLC} at 0.5 A g^{-1} of the HBLME-EDLC along with the EDLC areal capacitance.

Table 3. Gravimetric and surface quantities of HBLME-EDLC and LBHME-EDLC .

Electrode Label	HBLME-EDLC	LBHME-EDLC
Mass loading (mg cm ⁻²)	9.3	13.8
ESR (ohm)	5.9	7.9
Capacitance *(F g ⁻¹)	15.9	6.2
Areal capacitance (mF cm ⁻²)	148.0	85.5
Specific energy** (Wh kg ⁻¹)	19.6	7.2
Specific power*** (kW kg ⁻¹)	4.6	3.7
Areal energy density (μWh cm ⁻²)	182.3	99.4
Areal power density (mW cm ⁻²)	42.8	51.1

* Capacitance has been calculated from the CV at 50 mV s⁻¹, ** Specific energy has been calculated from GCPL at minimum current (0.5 A g⁻¹), *** Specific power has been calculated at maximum current (4 and 5 A g⁻¹).

3.2.2. Lower Binder High Mass Loading Electrodes (LBHME)

In this section, the results of the electrochemical characterization of the LBHME-EDLCs are reported. Figure 5a shows the Nyquist plots of the LBHME-EDLC single electrodes and full cell.

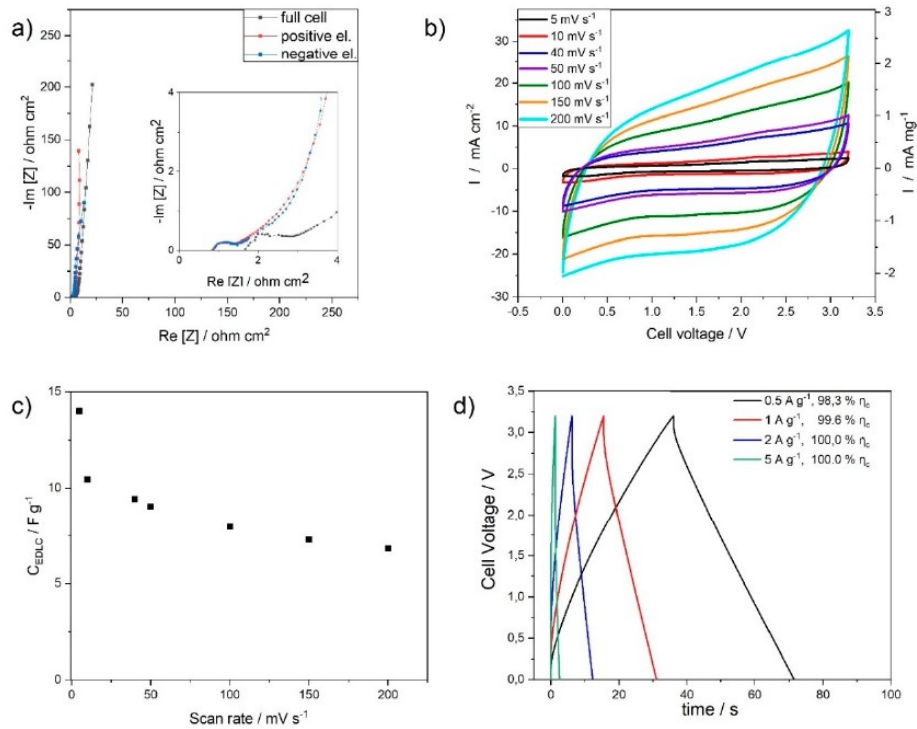


Figure 5. Electrochemical characterization of LBHME-EDLC (a) Nyquist plots of the (black) full cell, (red) positive and (blue) negative electrodes (500 kHz and 100 mHz), (b) 2-electrode CVs at different scan rate from 5 mV s⁻¹ to 200 mV s⁻¹, between 0 V and 3.2 V, (c) Capacitance of the EDLC evaluated by CV reported as function of the scan rate; and (d) selected galvanostatic charge/discharge cycles between 0 V and 3.2 V at different current densities from 0.5 A g⁻¹ to 5 A g⁻¹.

Like for HBLME, the three Nyquist plots share all the same shape. For the physical interpretation of the Nyquist plots, the considerations that have been drawn in the previous section are still valid. The high frequency intercepts with the real axis of the semicircles are 0.8, 0.9 and 1.7 $\Omega \text{ cm}^2$ for the positive and negative electrodes and full cell, respectively. Noticeably these values are halved with respect to those of the HBLME electrodes and EDLC (cf. Figure 4a). In LBHME formulation, the quantity of binder and conductive carbon are halved compared to the HBLME one. Therefore, the decrease of the high frequency impedance achieved by LBHME can be explained with the decrease of the insulating component of the electrode, i.e., the binder. Comparing the high frequency semicircles in Figures 4a and 5a, it is possible to notice that the LBHME's is wider than HBLME's. Indeed, the LBHME-EDLC semicircle diameter is 1.3 $\Omega \text{ cm}^2$ while the HBLME's is 0.3 $\Omega \text{ cm}^2$. This difference is due to the high mass loading of LBHME with respect to HBLME (1.5-fold), that brings about a worse ionic and electronic connection between the carbon particles [10]. The LBHME-EDLC middle frequency line (45° slope) span across the same range of resistance with respect to the HBLME-EDLC. The ESR of the LBHME-EDLC was evaluated from the real axis intercept of the low frequency line and resulted in 7.6 $\Omega \text{ cm}^2$.

Figure 5b reports the CVs of the full LBHME-EDLC cell at different scan rate, between 0 and 3.2 V. From these measurements, voltammetric specific capacitance values have been calculated and are reported as function of the scan rate in Figure 5c. The highest specific capacitance is 14 F g^{-1} at 5 mV s^{-1} and decreases to 7 F g^{-1} at 200 mV s^{-1} . Therefore, from 5 mV s^{-1} to 200 mV s^{-1} there is a 50 % specific capacitance reduction, that is higher than what observed for HBLME-EDLC (22 %). This can be related to a not optimized electronic and ionic connection of the electrodes carbon particles that has been highlighted by the Nyquist plot analysis reported above (Figure 5a).

The LBHME-EDLC galvanostatic charge/discharge profiles at different current are reported in Figure 5d. The coulombic efficiency was 98.3 %, 99.6 %, 100 %, 100 % at 0.5, 1, 2, 5 A g^{-1} , respectively. These values are slightly higher than those that have been observed for the HBLME. The ESR was 7.9 $\Omega \text{ cm}^2$ in agreement with the EIS value. The C_{EDLC} was 6.2, 5.8, 5.3 and 4.2 F g^{-1} at 0.5, 1, 2 and 5 A g^{-1} . These values are lower than those featured by HBLME-EDLC and this can be explained with the not optimized ionic and electronic connection highlighted by Table 3 that reports the ESR and C_{EDLC} at 0.5 A g^{-1} of LBHME-EDLC. The EDLC areal capacitance is also reported in the Table.

3.2.3. Cycling Stability, Energy and Power of HBLME- and LBHME-EDLCs

Figure 6a reports the trends of the specific capacitance of the two EDLCs over cycling at 1 A g^{-1} . The values are normalized by the value of the specific capacitance of the first cycle. Both devices show a good stability with capacitance retention of 90 % at the 2000th cycle. This result demonstrates the feasibility of the use of pullulan as alternative separator and binder for green supercapacitors.

Note that the cycling stability of LBHME-EDLC at low binder content was further evaluated even over 5000 cycles (Figure S3). The test indicated that also over prolonged cycling, a capacitance retention of 77% can be obtained.

The specific energy and power values of the two EDLCs, calculated through Equations (4) and (5) are compared in the Ragone plot reported in Figure 6b. Both devices deliver the maximum specific energy at the lowest current, and the maximum power is delivered at the highest current.

Indeed, at 0.5 A g^{-1} , the specific energy is 19.6 Wh kg^{-1} and 7.2 Wh kg^{-1} for HBLME-EDLC and LBHME-EDLC, respectively. At 4 A g^{-1} , the specific power is 4.7 kW kg^{-1} for the HBLME EDLC and 3.8 kW kg^{-1} for the LBHME-EDLC. These values are reported in Table 3. If energy and power are normalized by the electrode area, they become 182 $\mu\text{Wh cm}^{-2}$ and 42.8 mW cm^{-2} for the HBLME-EDLC, and 99.4 $\mu\text{Wh cm}^{-2}$ and 51 mW cm^{-2} for the LBHME-EDLC (Table 3). These results clearly demonstrate that increasing electrode thickness is detrimental for energy and power performance. Indeed, specific energy of LBHME-EDLC is lower than HBLME-EDLC and this is mainly related to an inefficient exploitation of the electrode carbon surface. This is highlighted by the comparison of the area capacitance of HBLME-EDLC (148 mF cm^{-2}) and LBHME-EDLC (85.5 mF cm^{-2}). Therefore, in LBHME-EDLC, the increase of the electrode mass is not enough to offset such specific energy decrease, and the areal energy density keeps lower than that of HBME-EDLC. However, power

performance of the two EDLCs are comparable, suggesting that the decrease of the binder content has a positive effect.

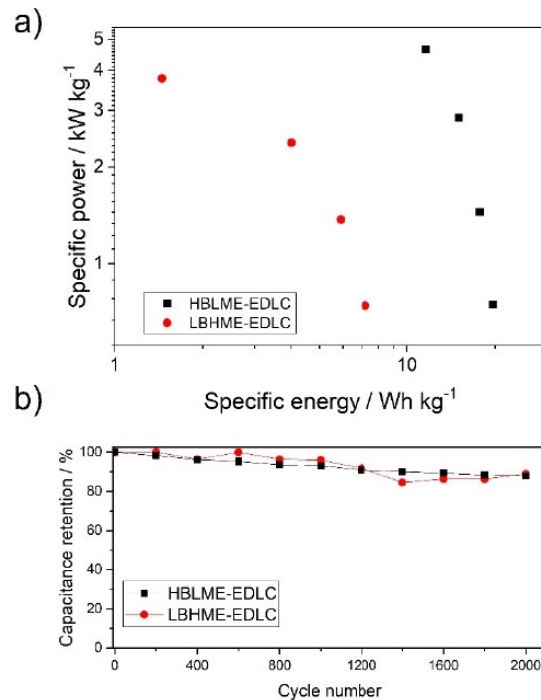


Figure 6. EDLC comparison by galvanostatic tests. (a) Trend of the capacitance percentage normalized by the value at first cycle the as function of the cycle number (at 1 A g⁻¹, cell voltage cut-off: 0 V–3.2 V) and (b) Ragone plots of HBLME-EDLC and LBHME-EDLC.

4. Discussion

Today many efforts are being devoted to increasing the specific energy of supercapacitors by different strategies. Among them promises are held by the use of ionic liquids, thick electrodes and pseudocapacitive active materials [2,6,12]. Ionic liquids enable high practical voltage (>3 V) and therefore energy density, but their major drawbacks are the greater ESR respect to commercial electrolytes and high cost. The use of thick electrodes (>10 mg cm⁻²) may seem the simpler solution, but the achieving high performance with thick electrodes is still an unsolved problem [10,11]. Indeed, thick electrodes suffer of poor electronic and ionic connection between the particles, and only the external portion of the electrodes take part in the charge/discharge processes.

The increasing market for supercapacitors requires that sustainable manufacturing processes and materials are exploited to manufacture green supercapacitors. Aqueous processable bio-derived polymers represent a valuable alternative to today's fluorinated separators and binders. Furthermore, we have already demonstrated that the smart combination of a water processable binder and separator (like pullulan) and a hydrophobic ionic liquid electrolyte (EmimTFSI) enables an easy recovery of the expensive ionic liquid [31]. Indeed, the pullulan-IL-based EDLC can be readily separated into each of its components by immersion in water. After these very interesting but preliminary results, in this paper we have carried out a study to get further insight into the impact of the use of natural polymer in supercapacitors performance. We have investigated the use of cellulose, which is the most widely studied bio-based polymer for green supercapacitors, and pullulan, that we have proposed for the first time in [31]. CTA and Pu separators were processed as self-standing mats

by electrospinning. Their permeability to different electrolytes (EmimTFSI, 0.5 m LiTFSI TEGDME, PYR₄TFSI), which is critical in the formation of the electrical double layer, has been evaluated by EIS and quantified referring to the Mac Mullin number. This characterization has been done at different temperatures over one week, in order to get insight on the thermal and chemical stability of the tested bio-polymer in the selected electrolytes. Both membranes at 30 °C featured the lower resistance (Pu 2 Ohm cm² CTA 2 Ohm cm²) when soaked with EmimTFSI. However, given that the thickness of Pu (55 μm) was higher than that of CTA (22 μm), the resistivity of the Pu-EmimTFSI system was considerably smaller (0.407 kOhm cm vs. 1.041 kOhm cm). Furthermore, Pu-EmimTFSI exhibited a better thermal stability respect to the CTA-EmimTFSI. Notably, the N_M for the Pu is always smaller than that of CTA, in particular, in EmimTFSI values of 5 and 12 were found, respectively. Overall, this study highlighted the presence of different and specific interactions between the tested electrolytes and the membranes that affect the ionic permeability and stability. It also indicated Pu-EmimTFSI as the best system. Indeed, Pu-EmimTFSI was the combination capable to minimize the ESR and avoid performance degradation due to temperature changes.

On the basis of these results, Pu was selected as separator and binder for EmimTFSI-based EDLCs. The big challenge we faced in this study was to reach high electrode mass loading at low binder content.

Two EDLCs have been assembled featuring two different formulations, one with lower mass loading and high binder content (HBLME) and a second one with higher mass loading and lower binder content (LBHME). These have been characterized electrochemically to evaluate how binder decrease and mass loading increase affect performance. In particular, these devices have been characterized at first by EIS. Analysis of the Nyquist plots highlighted an increase of the ESR moving from the HBLME-EDLC to the LBHME-EDLC, (5.9 Ohm cm² vs. 7.6 Ohm cm²). This trend was mainly related to the increase of the ionic and electronic contact resistances between carbon particles with the increase of electrode mass loading (1.5-fold from HBLME-EDLC to LBHME-EDLC).

For both devices' CVs have shown the absence of faradaic parasitic reactions within the cell voltage range 0 to 3.2 V. This wide range is feasible thanks to the good electrochemical stability of Pu-EmimTFSI. Specific capacitances have been calculated for both EDLCs. The highest specific capacitance was featured at the lowest scan rate of 5 mV s⁻¹ for both devices and was 18 F g⁻¹ and 14 F g⁻¹ for HBLME-EDLC and LBHME-EDLC, respectively. Both supercapacitors featured a good capacitance retention with the increase of the scan rate that however was higher for HBLME-EDLC (22 %) than LBHME-EDLC (50 %).

GLV cycling with high coulombic efficiency (higher than 98 %) was demonstrated for both devices at the high cell voltage of 3.2 V. Noticeably, the EDLC featured a very good cycling behaviour demonstrated over more than 2000 cycles even at low binder content, confirming the stability of the Pu-polymer in EmimTFSI.

The high cell voltage and good specific capacitance provided specific energy of 19.6 Wh kg⁻¹ and 7.2 Wh kg⁻¹ at 0.5 A g⁻¹ that well compare with those of EDLCs featuring the same electrolyte and active carbon but employing a fluorinated binder and fiber glass separators [16]. The highest specific power was 4.6 kW kg⁻¹ and 3.7 kW kg⁻¹ at 4–5 A g⁻¹ respectively for HBLME-EDLC and for the LBHME-EDLC

The gravimetric performance of the HBLME-EDLC is superior respect to that of the LBHME-EDLC. This is due to the lower specific capacitance of the latter vs. the former. In turn, this is due to an inefficient ionic electronic contact between electrode carbon particles that leads to a partial exploitation of the electrodes surface.

5. Conclusions

This work demonstrates that aqueous processable biodegradable polymers such as pullulan can be effectively exploited for the development of the major components (separator and binder) of ionic-liquid-based green EDLCs. After studying different combinations of biopolymer and organic electrolyte, pullulan-EmimTFSI was found to be the best system in terms of resistivity and thermal behavior. Therefore, we assembled Pu-based EDLCs with EmimTFSI as electrolyte. Our study

demonstrates for the first time the feasibility of the use of pullulan to produce high mass loading electrodes at low binder content for high voltage EDLCs. We prepared electrodes with mass loadings up to 13.84 mg cm⁻² with 10 % binder content. Pullulan-EmimTFSI EDLCs were charged up to 3.2 V with good cycling stability over 5000 cycles. Pullulan-EmimTFSI EDLCs featured specific energy and power comparable with those of supercapacitors based on the same activated carbon and ionic liquid, but with fluorinated binder and fiberglass separator.

Further work is in progress to improve the specific capacitance of these thick electrodes by using high surface area carbons with tailored porosity, different conductive carbon additives, and by exploring different electrolytes.

Supplementary Materials: The following are available online at www.mdpi.com/xxx/s1, Figure S1. Schemes of the casting preparation of the pullulan-based electrodes and of the supercapacitor assembly, Figure S2. Nyquist plot of Pullulan electrospun membrane soaked with (a) PYR₁₄TFSI, (c) EmimTFSI, (e) 0.5 m LiTFSI TEGDME and Cellulose triacetate electrospun membrane soaked with (b) PYR₁₄TFSI, (d) EmimTFSI, (f) 0.5 m LiTFSI TEGDME, Figure S3. Trend of the capacitance percentage normalized by the value at first cycle as function of the cycle number (at 1 A g⁻¹, cell voltage cut-off: 0 V–3.2 V), Table S1. Resistance normalized by the plain area of Pullulan electrospun separator in different tested electrolytes, Table S2. Resistance normalized by the plain area of Cellulose triacetate electrospun separator in different tested electrolytes, Table S3. Resistivity of Pullulan electrospun separator in different tested electrolytes, Table S4. Resistivity of Cellulose triacetate electrospun separator in different tested electrolytes, Table S5. Mac Mullin number of Pullulan electrospun separator in different tested electrolytes, Table S6. Mac Mullin number of Cellulose triacetate electrospun separator in different tested electrolytes.

Author Contributions: Conceptualization: F.S. Data curation: G.E.S., F.P. Formal analysis: G.E.S., F.P., Funding acquisition: F.S. Investigation: G.E.S., F.P. Project administration: F.S. Supervision: F.S., Writing—original draft: G.E.S., F.P., A.B., D.M., F.S. Writing—review & editing: G.E.S., F.P., A.B., D.M., F.S. All authors have read and agreed to the published version of the manuscript.

Funding: This research was funded by the Italy-South Africa joint Research Programme 2018–2020 (Italian Ministers of Foreign Affairs and of the Environments) and “Piano Triennale di Realizzazione 2019–2021, Accordo di Programma Ministero dello Sviluppo Economico”—ENEA.

Acknowledgments: Maria Letizia Focarete (University of Bologna) and her research group are acknowledged for their precious contribution and support on electrospinning of natural polymers.

Conflicts of Interest: All The authors declare no conflict of interest for this manuscript.

References

- Dunn, B.; Kamath, H.; Tarascon, J.M. Electrical energy storage for the grid: A battery of choices. *Science* **2011**, *334*, 928–935.
- Yang, Z.; Zhang, J.; Kintner-Meyer, M.C.W.; Lu, X.; Choi, D.; Lemmon, J.P.; Liu, J. Electrochemical energy storage for green grid. *Chem. Rev.* **2011**, *111*, 3577–3613.
- Chen, G.Z. Supercapacitor and supercapattery as emerging electrochemical energy stores. *Int. Mater. Rev.* **2017**, *62*, 173–202.
- Poonam; Sharma, K.; Arora, A.; Tripathi, S.K. Review of supercapacitors: Materials and devices. *J. Energy Storage* **2019**, *21*, 801–825.
- Schütter, C.; Pohlmann, S.; Balducci, A. Industrial Requirements of Materials for Electrical Double Layer Capacitors: Impact on Current and Future Applications. *Adv. Energy Mater.* **2019**, *9*, 1900334.
- DeVos, N.; Maton, C.; Stevens, C. v. Electrochemical Stability of Ionic Liquids: General Influences and Degradation Mechanisms. *ChemElectroChem* **2014**, *1*, 1258–1270.
- González, A.; Goikolea, E.; Barrena, J.A.; Mysyk, R. Review on supercapacitors: Technologies and materials. *Renew. Sustain. Energy Rev.* **2016**, *58*, 1189–206.
- Lazzari, M.; Mastragostino, M.; Soavi, F. Capacitance response of carbons in solvent-free ionic liquid electrolytes. *Electrochem. Commun.* **2007**, *9*, 1567–1572.
- Mauger, A.; Julien, C.M.; Paolella, A.; Armand, M.; Zaghbi, M. A comprehensive review of lithium salts and beyond for rechargeable batteries: Progress and perspectives. *Mater. Sci. Eng. R Rep.* **2018**, *134*, 1–2110.

10. Ruschhaupt, P.; Varzi, A.; Passerini, S. Natural Polymers as Green Binders for High-Loading Supercapacitor Electrodes. *ChemSusChem* **2020**, *13*, 763–770.
11. Arbizzani, C.; Yu, Y.; Li, J.; Xiao, J.; Xia, Y.; Yao, Y.; Yang, Y.; Santato, C.; Raccichini, R.; Passerini, S. Good practice guide for papers on supercapacitors and related hybrid capacitors for the Journal of Power Sources. *J. Power Sources* **2020**, *450*, 227636.
12. Stojanovska, E.; Kilić, A. Carbon nanofibers as thick electrodes for aqueous supercapacitors. *J. Energy Storage* **2019**, *26*, 100981.
13. Krause, A.; Balducci, A. High voltage electrochemical double layer capacitor containing mixtures of ionic liquids and organic carbonate as electrolytes. *Electrochem. Commun.* **2011**, *13*, 814–817.
14. Krummacher, J.; Balducci, A. Al(TFSI)₃ as a Conducting Salt for High-Voltage Electrochemical Double-Layer Capacitors. *Chem. Mater.* **2018**, *30*, 4857–4863.
15. Krummacher, J.; Hess, L.H.; Balducci, A. Al(TFSI)₃ in Acetonitrile as Electrolytes for Electrochemical Double Layer Capacitors. *J. Electrochem. Soc.* **2019**, *166*, A1763–A1768.
16. Lazzari, M.; Soavi, F.; Mastragostino, M. Mesoporous carbon design for ionic liquid-based, double-layer supercapacitors. *Fuel Cells* **2010**, *10*, 840–847.
17. Chmiola, J.; Largeot, C.; Taberna, P.L.; Simon, P.; Gogotsi, Y. Desolvation of ions in subnanometer pores and its effect on capacitance and double-layer theory. *Angew. Chem. Int. Ed.* **2008**, *47*, 3392–3395.
18. Varzi, A.; Passerini, S. Enabling high areal capacitance in electrochemical double layer capacitors by means of the environmentally friendly starch binder. *J. Power Sources* **2015**, *300*, 216–222.
19. Ahmed, S.; Nelson, P.A.; Gallagher, K.G.; Dees, D.W. Energy impact of cathode drying and solvent recovery during lithium-ion battery manufacturing. *J. Power Sources* **2016**, *322*, 169–178.
20. Mauger, A.; Julien, C.; Paolella, A.; Armand, M.; Zaghib, K. Recent Progress on Organic Electrode Materials for Rechargeable Batteries and Supercapacitors. *Materials* **2019**, *12*, 1770.
21. Bresser, D.; Buchholz, D.; Moretti, A.; Varzi, A.; Passerini, S. Alternative binders for sustainable electrochemical energy storage—the transition to aqueous electrode processing and bio-derived polymers. *Energy Environ. Sci.* **2018**, *11*, 3096–3127.
22. Yamagata, M.; Ikebe, S.; Soeda, K.; Ishikawa, M. Ultrahigh-performance nonaqueous electric double-layer capacitors using an activated carbon composite electrode with alginate. *RSC Adv.* **2013**, *3*, 1037–1040.
23. Böckenfeld, N.; Jeong, S.S.; Winter, M.; Passerini, S.; Balducci, A. Natural, cheap and environmentally friendly binder for supercapacitors. *J. Power Sources* **2013**, *221*, 14–20.
24. Dühnen, S.; Betz, J.; Kolek, M.; Schmuck, R.; Winter, M.; Placket, T.; A. Toward Green Battery Cells: Perspective on Materials and Technologies. *Small Methods* **2020**, 2000039, doi:10.1002/smt.202000039.
25. Bonnefoi, L.; Simon, P.; Fauvarque, J.F.; Sarrazin, C.; Sarrau, J.F.; Dugast, A. Electrode compositions for carbon power supercapacitors. *J. Power Sources* **1999**, *80*, 149–155.
26. Phillips, D.M.; Drummy, L.F.; Conrady, D.G.; Fox, D.M.; Naik, R.R.; Stone, M.O.; Trulove, P.C.; de Long, H.C.; Mantz, R.A. Dissolution and regeneration of Bombyx mori silk fibroin using ionic liquids. *J. Am. Chem. Soc.* **2004**, *126*, 14350–14351.
27. Swatloski, R.P.; Spear, S.K.; Holbrey, J.D.; Rogers, R.D. Dissolution of Cellulose with Ionic Liquids. *J. Am. Chem. Soc.* **2002**, *124*, 4974–4975.
28. Recham, N.; Armand, M.; Tarascon, J.M. Novel low temperature approaches for the eco-efficient synthesis of electrode materials for secondary Li-ion batteries. *Comptes Rendus Chim.* **2010**, *13*, 106–116.
29. Heinze, T.; Dorn, S.; Schöbitz, M.; Liebert, T.; Köhler, S.; Meister, F. Interactions of Ionic Liquids with Polysaccharides—2: Cellulose. *Macromol. Symp.* **2008**, *262*, 8–22.
30. Varzi, A.; Balducci, A.; Passerini, S. Natural Cellulose: A Green Alternative Binder for High Voltage Electrochemical Double Layer Capacitors Containing Ionic Liquid-Based Electrolytes. *J. Electrochem. Soc.* **2014**, *161*, A368–A375.
31. Poli, F.; Momodu, D.; Spina, G.E.; Terella, A.; Mutuma, B.K.; Focarete, M.L.; Manyala, N.; Soavi, F. Pullulan-ionic liquid-based supercapacitor: A novel, smart combination of components for an easy-to-dispose device. *Electrochim. Acta* **2020**, *338*, 135872.
32. Arbizzani, C.; Lazzari, M.; Soavi, F.; Mastragostino, M.; Conte, M. ILHYPOS Ionic Liquid-Based Supercapacitors. *ECS Trans.* **2010**, *25*, 25–30.
33. Li, Y.; Li, Q.; Tan, Z. A review of electrospun nanofiber-based separators for rechargeable lithium-ion batteries. *J. Power Sources*, **2019**, *443*, 227262.

34. Yoo, H.D.; Jang, J.H.; Ryu, J.H.; Park, Y.; Oh, S.M. Impedance analysis of porous carbon electrodes to predict rate capability of electric double-layer capacitors. *J. Power Sources* **2014**, *267*, 411–420.
35. Conway, B.E. *Electrochemical Supercapacitors: Scientific Fundamentals and Technological*; Springer Science & Business Media: Berlin, Germany, 2013.
36. Kötz, R.; Carlen, M. Principles and applications of electrochemical capacitors. *Electrochim. Acta* **2000**, *45*, 2483–2498.



© 2020 by the authors. Licensee MDPI, Basel, Switzerland. This article is an open access article distributed under the terms and conditions of the Creative Commons Attribution (CC BY) license (<http://creativecommons.org/licenses/by/4.0/>).

4.1 Chapter 4 Conclusion

Among the EESSs exploited to accelerate the transition to a low carbon society, the Electrical Double Layer Capacitor (EDLC) is gaining great interest thanks to its peculiarity of high power device. EDLC are preferred to LIBs in applications where high current and short discharging time are involved. In the manufacturing process of these devices, also EDLCs exploit the use PVdF as binder.

After demonstrating the effective use of PU on LIBs, in this chapter I focused on the exploitation of PU to realize high voltage ionic liquid based EDLCs. For this device, PU was also used to manufacture an electrospun separator.

As first, I studied different combinations of biopolymer and organic electrolyte. Finally, pullulan-EmimTFSI was found to be the best system in terms of resistivity and thermal behavior. Therefore, I assembled Pu-based EDLCs with EmimTFSI as electrolyte.

I prepared two types of electrodes with PU as binder, one with low electrode mass loading and high binder content (HBLME, $3.6 - 4.6 \text{ mg cm}^{-2}$) and a second one with high mass loading and low binder content (LBHME, $6.3 - 7.5 \text{ mg cm}^{-2}$).

The assembled EDLCs provided specific energy of 19.6 Wh kg^{-1} and 7.2 Wh kg^{-1} at 0.5 A g^{-1} that well compare with those of EDLCs featuring the same electrolyte and active carbon but employing a fluorinated binder and fiber glass separators. The highest specific power was 4.6 kW kg^{-1} and 3.7 kW kg^{-1} respectively for HBLME-EDLC and for the LBHME-EDLC.

Pullulan-EmimTFSI EDLCs were charged up to 3.2 V with good cycling stability over 5000 cycles with high coulombic efficiency (around 98 %) and featured specific energy and power comparable with those of supercapacitors based on the same activated carbon and ionic liquid, but with fluorinated binder and fiberglass separator.

This work demonstrates, as for battery electrodes, the feasibility of the use of pullulan to produce high mass loading electrodes at low binder content for high voltage EDLCs. Future work will be done to increase the specific capacitance of these thick electrodes by the use of high surface area carbons with tailored porosity, different conductive carbon additives, and by exploring different electrolytes.

Reference Chapter 4

[1] Lazzari, M.; Soavi, F.; Mastragostino, M. “Mesoporous carbon design for ionic liquid-based, double-layer supercapacitors.” *Fuel Cells* 2010, 10, 840–847.

<https://doi.org/10.1002/fuce.200900198>

[2] Spina, G.E.; Poli, F.; Brilloni, A.; Marchese, D.; Soavi, F. “Natural Polymers for Green Supercapacitors.” *Energies* 2020, 13, 3115. <https://doi.org/10.3390/en13123115>

Chapter 5: Supercapacitor for improved RFBs performances in hybrid systems

Chapter 5 shows the preliminary results achieved combining two different electrochemical storage systems, namely Supercapacitors and Redox-Flow Batteries, in order to exploit the advantages of both systems in a hybrid combination.

This part of my work was conducted under the European project HyFlow (H2020-LC-BAT-9-2020), at the Technologiezentrum Energie (TZE) Hochschule Landshut, where I spent 3 months of my PhD. The HyFlow project deals with the “Development of a sustainable hybrid storage system based on high power vanadium redox flow battery and supercapacitor–technology”. The aim of the project is to develop a hybrid energy storage system (HESS) that is capable of meeting high-energy and high-power requirements from the grid/customer. To this end, a high-power vanadium redox flow battery (HP-VRFB) and a supercapacitor (SC), operating as two distinct systems, are electrically hybridized by the means of a bidirectional power converter (BC). Hybridization of EESS will also lead to more efficient storage systems, with longer lifetimes and with the ability to operate on all time-scale applications, from seconds to days. This feature can be beneficial for applications like virtual inertia or special large-scale uninterruptible power supply. Overall, the HyFlow concept aims at improving efficiency and performance, reducing the environmental impact, and extending lifespan along with optimizing costs. Therefore, the final real scale device of the HyFlow project will be composed of three main parts: the HP-VRFB, the SC and the BC. This last component is the only one not dedicated to energy storage but it affects the overall efficiency by a 2-5% by absorbing and dissipating energy through its internal circuit: inside the converter there are switches and electronic components that dissipate energy in order to stabilize the voltage of the connected devices. The most relevant impact that the converter has on the whole battery system is the final cost: 100 k€ MW⁻¹ for the converter shares a 5-10% of the total price of the full system [1]. The exclusion of this device from the whole system will reduce the overall production cost of the energy storage system and the environmental impact.

Therefore, my idea is to evaluate the elimination of the BC by directly connecting low environmental impact SC, like those developed in Chapter 4, to the cells of the HP-VRFB. The result will be a hybrid vanadium flow cell that can deliver high power peak and pulsed power signals for frequency regulation. As a preliminary study, I explored this concept by using commercial SCs.

In the first part of this work, I studied the power and energy response of the HP-VRFB single cell with specific discharge protocols in order to separate the effect of the combination with SC, that is at the base of the study. The cell was provided by one of the partners of the project, PinFlow Energy Storage S.r.o. (PinFlow). In the second part I did the characterization of small size commercial supercapacitors with different discharge current and setting cut-off voltages in the range of the HP-VRFB single cell. In the last part, I report the results of the discharge curves for the vanadium cell connected in parallel with SC with increasing capacitance.

The aim of the study is to evaluate the benefits and the influence of a direct parallel connection of commercial supercapacitor of different capacitance with a vanadium redox flow single cell. The SC connected in parallel should, at first instance, reduce the discharge overvoltages that characterize the high current discharge curves of the VRFC, while increasing energy yield.

5.1 High Power Vanadium Redox Flow Battery

The Vanadium Redox Flow Cell (VRFC) used for the testing was provided by PinFlow Energy Storage S.r.o. (PinFlow), which is a company that produces high power VRFBs based in Czech Republic and partner of the project HyFlow.

The cell has an active area of 4 cm² that locates a polyacrylonitrile (PAN)-derived activated mat of the same size for both electrodes. PAN activated carbon felt mats are widely used as current collectors, both for cathode and anode, of RFBs because of their high BET surface, that can reach up to 373 m²/g [2] and the possibility to functionalize the surface to increase the power density of the cells [3]. The anion exchange membrane (AEM), the plates with flow field and other internal components were fixed and provided by PinFlow as part of the project. Also the 1.6 M V₂O₅ in 2M H₂SO₄ vanadium electrolyte was provided by the company.

The setup, visible in Figure 5.1 is composed of the cell with positive (red cables) and negative (blue cable) side, 2 tank filled with 50 mL (total of 100 mL) of vanadium electrolyte, a peristaltic pump serving both the positive and negative line and two stirrers for mixing the electrolyte in the tank. The theoretical capacity of the electrolytes can be calculated with the formula:

$$Q_{TEO} = \frac{1}{2} \cdot V_{tot} \cdot c_v \cdot F \quad (5.1)$$

where V_{tot} is the total electrolyte volume of the cell (anolyte + catholyte), c_v is the molarity of the electrolyte (M) and F is the Faraday constant (26.801 Ah/mol). The cell results to have a total theoretical capacity of 2144 mAh. In all the tests, the cell is cycled in a potential window of 0.85V, i.e. the lower potential is set at +0.8 V, while the charging cut-off voltage is set at +1.65V. All the experiments are conducted at a flow rate of 10 mL/min (which corresponds to 10 rpm).

The cell is connected to a VSP multichannel potentiostat/galvanostat/FRA (BioLogic, Seyssinet-Pariset, France). The PEIS are collected by applying a perturbation of 5 mV within 10 kHz–100 mHz frequency range, acquiring 10 points per decade. The GEIS are collected by applying a perturbation of 50 mA within 10 kHz–20 mHz frequency range, acquiring 10 points per decade, limiting the potential to ± 2.5 V.



Figure 5.1 Setup of the testing bench with the VRFB cell and all the ancillary equipment.

At the beginning, the vanadium electrolyte is unique for both the electrodes, positive and negative side, and has an oxidation value of $V^{+3.5}$, which corresponds to a SOC of -50%. Therefore, it must be activated in two different redox couples, V^{II}/V^{III} for the anode, and V^{IV}/V^V for the cathode, with a specific protocol that is provided by the company. The protocol consists in a series of charge/discharge cycle and positive/negative current scan, interspersed with EIS to monitor the state of internal materials.

EIS measurements were performed at the beginning of the tests with -50% SOC (PEIS), after the activation protocol at +50% SOC (GEIS) and with the electrolyte flowing at 10 mL/min at +50% SOC. The compared results are shown in Figure 5.2 where the Nyquist plot of the three measurements is plotted.

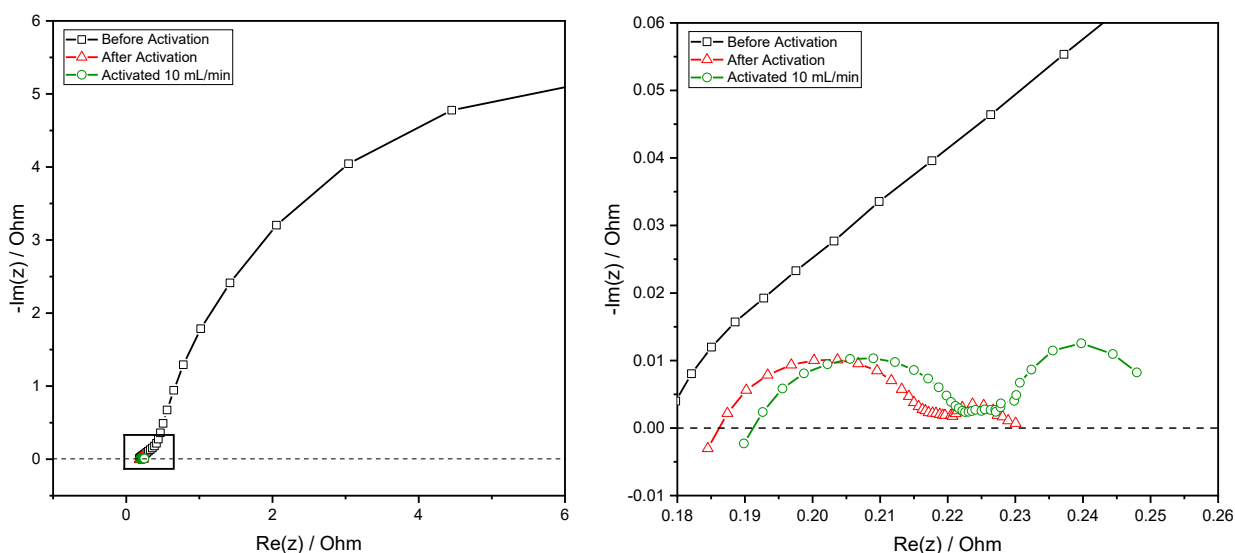


Figure 5.2 Comparison of the EIS measurements for the VRFC before the activation (blue curve), after the activation (red curve) and while the electrolyte is flowing after the activation (green curve). On the left, full scale graph, on the right, magnification of the graph in the rectangle

The EIS was used to analyze the polarization of the PAN electrodes and evaluate the Equivalent Series Resistance (ESR) of the cell in order to compare it with that of supercapacitors.

For the EIS shown in Figure 5.2, more specifically after the activation of the electrolytes, the first semicircle at high frequency region is attributed to the charge-transfer (kinetic) resistance, the second semicircle, at low frequency, is ascribed to the mass transfer (finite length diffusion) resistance, and high-frequency intercept on the real axis of the high frequency semicircle is related to the ohmic resistance. The ohmic resistance includes the ionic resistance of the membrane, electrolyte, and interfacial interface between the cell components (e.g. membrane/ electrode, electrode/flow field). The contribution of the electronic resistance to overall ohmic impedance is usually lower compared to the membrane and distributed porous ionic resistance [4,5]. Given the complexity of the interpretation of the Nyquist plot, for the preliminary study, I just used the Nyquist plot to get an indication of the ESR from the intercept of the real axis of the low frequency semi-circle, at the lowest frequency, therefore including electronic and ionic resistance, charge transfer resistance and diffusion impedance. The resulting ESR is c.a 0.23 ohm.

Following the activation process, the VRFC was further cycled at a rated current of 600 mA, corresponding to 150 mA cm⁻² with discharging cut-off voltage of 0.8V and charging cut-off voltage of 1.65V, for 20 cycles. The discharge/charge voltage profile are shown in Figure 5.3a and the capacity trend over cycles is shown in Figure 5.3b. The capacity shown by the VRFC in the first cycles is around 1550 mAh, that is 72% of the theoretical value calculated by Equation 5.1. The round-trip coulombic efficiency of the VRFC (η_i) is defined conventionally as the ratio of the total discharge capacity with respect to that of the charge capacity, as for the Equation 5.2.

$$\eta_i(\%) = \frac{Q_i(\text{discharge})}{Q_i(\text{charge})} \times 100 \quad (5.2)$$

Through the charge discharge cycles, the conventional round-trip coulomb efficiency (η_i) of the VRFC remained relatively constant at ~95 % as shown in Figure 5.4b. On the other hand, the energy storage capacity of VRFC decreased over the 20 cycles by 7%. Therefore, the conventional round-trip efficiency of the VRFB system, which is generally used for the major performance indicative of flow batteries, cannot account for the change in energy storage capability of the VRFC, which depends largely on the physicochemical and electrochemical states of the electrolytes. The fading in the cycling capacity of the cell depends on the balance of charge between the two electrolytes that can be unbalanced due to i) the high internal cell resistance, ii) the higher rate of ion crossover with a continuously decreasing vanadium concentration in one of the two electrolytes, and iii) the aggravation of imbalance in the valence states of vanadium ions between the positive and negative electrolytes [6].

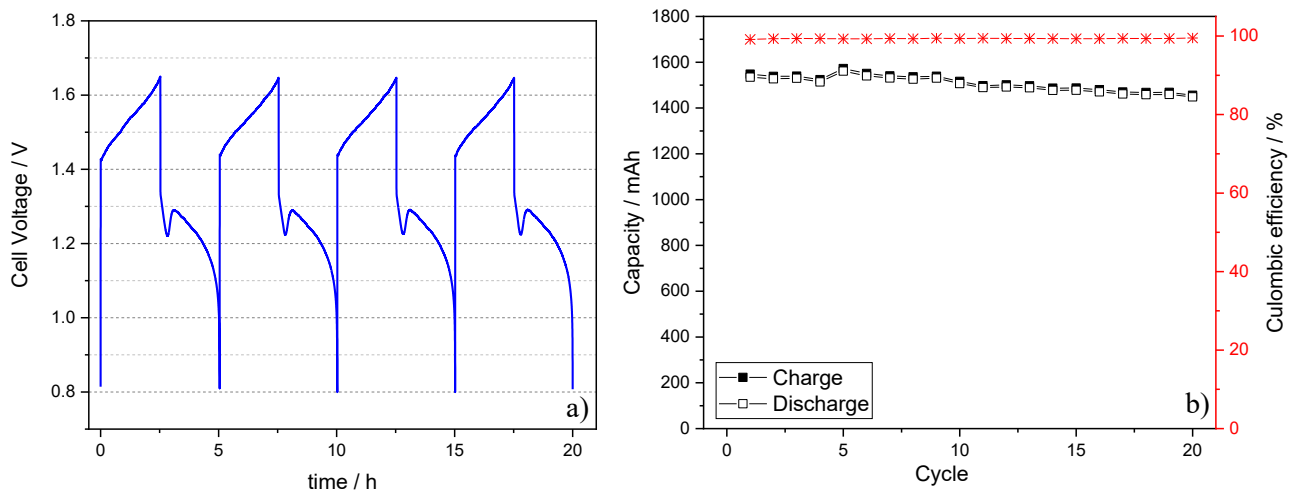


Figure 5.3 Cycling performance of the VRFC showing a) few representative cycles of the discharge profile and b) trends of the specific capacity and coulombic round-trip efficiency over 20 cycles.

Another phenomenon that affects the VRFC is the appearance of a sudden drop in the voltage profile that lasts for some minutes soon after the discharge starts. This feature is called the “power drop

effect” and is attributed to an increase in membrane resistance due to the accumulation of V^V complexes or temporary precipitation of V_2O_5 within the pores of the anion membrane facing the positive half-cell. This can occur especially when high current densities $>100 \text{ mA cm}^{-2}$ are applied, at high percentage of SOC of the positive electrolyte and with anion exchange membrane, which I used in this setup [7,8].

After the first cycles, the VRFC was tested with discharge currents at different rates by a specific protocol. A full charge at 100% SOC was performed, and then the VRFC was put in OCV reaching a steady voltage at c.a. 1.5 V. When the voltage stability was reached, I applied a discharge current for only 5 seconds (I_{pulse}) at 400 mA, 600 mA, 800 mA, 1 A, 2 A, 4 A and 6 A. Between the discharge phase, the cell was left in OCV for 60 s in order to reach a steady OCV voltage. The discharge voltage profiles are shown in Figure 5.4: the complete profile on the left and a magnification of the charging part of the profile on the right. In Table 5.1, values of discharge overvoltages and energy for a 5 second discharge current of the VRFC are summarized. For the highest currents, 10 A to 4 A, the

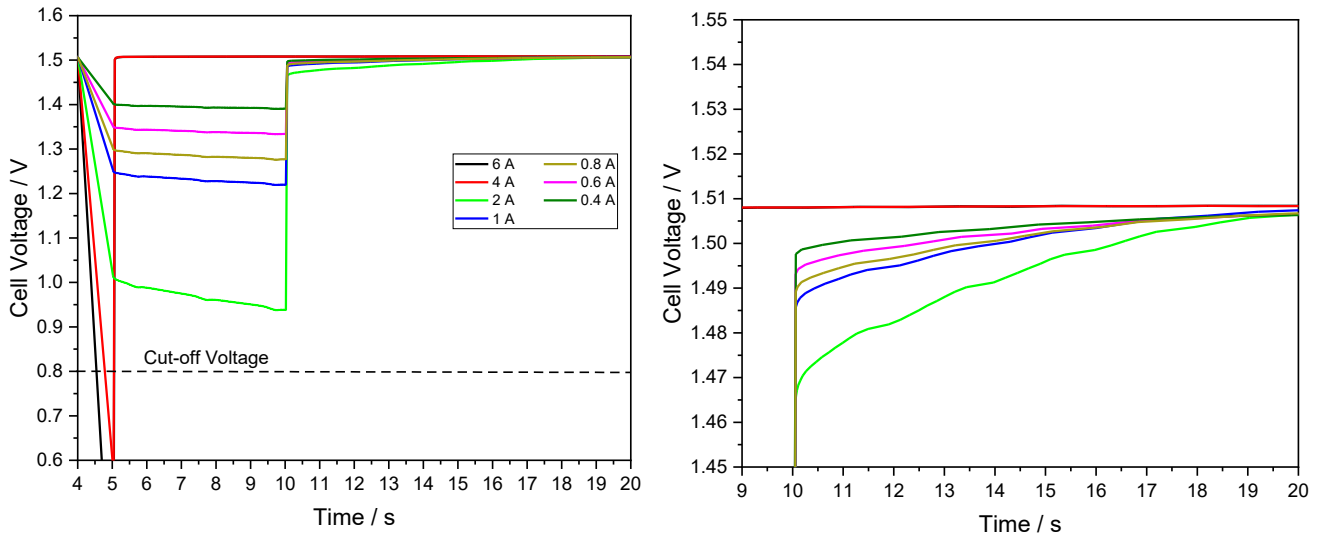


Figure 5.4 Discharge profile of the VRFC at different discharging currents, from 6A to 0.4A. The complete profile is shown on the left and a magnification of the charging part of the profile on the right.

VRFC suddenly reaches the lower cut-off voltage of 0.8 V, therefore little or no energy is yielded during the discharge.

From the discharge curves and the evaluation of the ohmic drop of the VRFC (ΔV_{ohmic}), it is possible to calculate the ESR of the VRFC (ESR_{VRFC}) with Equation 5.3, which results to be 250 m Ω .

$$ESR = \frac{\Delta V_{ohmic}}{I_{pulse}} \quad (5.3)$$

Table 5.1 Values of discharge overvoltages and energy for a 5 second discharge current on the VRFC

Discharge Current (A)	Discharge time (s)	VRFC ΔV_{ohmic} (V)	VRFC Capacity (mAh)	VRFC Energy (mWh)
10	---	---	---	---
6	5	1.3 V(lim)	0	0
4	5	0.9 V (lim)	0	0
2	5	0.5	2.8	2.71
1	5	0.25	1.4	1.72
0.8	5	0.20	1.12	1.44
0.6	5	0.15	0.8	1.12
0.4	5	0.10	0.56	0.78

5.2 Commercial Supercapacitors

Different commercial supercapacitors, purchased from EATON (Figure 5.5), were investigated in this work, at first studied separately and then connected in parallel with the VRFC. This section reports about the electrochemical tests run on single SCs. The characteristics of the supercapacitors, extrapolated from the device datasheets provided by the manufacturer, are shown in Table 5.2. The main difference consists in the nominal capacitance that was 1 F, 3 F, 5 F, 34 F and 100 F, respectively. The 9 F system was built by the parallel direct connection of three different SC: one of 1 F, one of 3 F and one of 5 F. The related characteristics have been extrapolated from those of the composing SC units and further confirmed by galvanostatic tests. All the commercial SC can be operated up to 2.7 V and feature ESRs that decrease with the reciprocal of their size: from 0.2 ohm to 0.011 ohm moving from the 1F-SC to the 100 F-SC.



Figure 5.5 Example of the commercial SC5F

Table 5.2 Commercial Supercapacitors characteristics

Acronym	Capacitance (F)	Initial ESR (Ω)	τ – Time constant (s)	Working Potential (V)	E max (mWh)	P max (W)	Continuous discharging current (A)
SC1F	1	0.200	0.20	0-2.7	1	9.1	0.8
SC3F	3	0.080	0.24	0-2.7	2	23	1.6
SC5 F	5	0.040	0.20	0-2.7	5.1	46	2.3
SC9 F*	9*	0.023*	0.21	0-2.7	8.8*	46*	2.3*
SC34F	34	0.016	0.54	0-3.0	42.5	141	6.5
SC100F	100	0.011	1.1	0-3.0	125	205	11.7

* values for 9F supercapacitor were calculated from test results

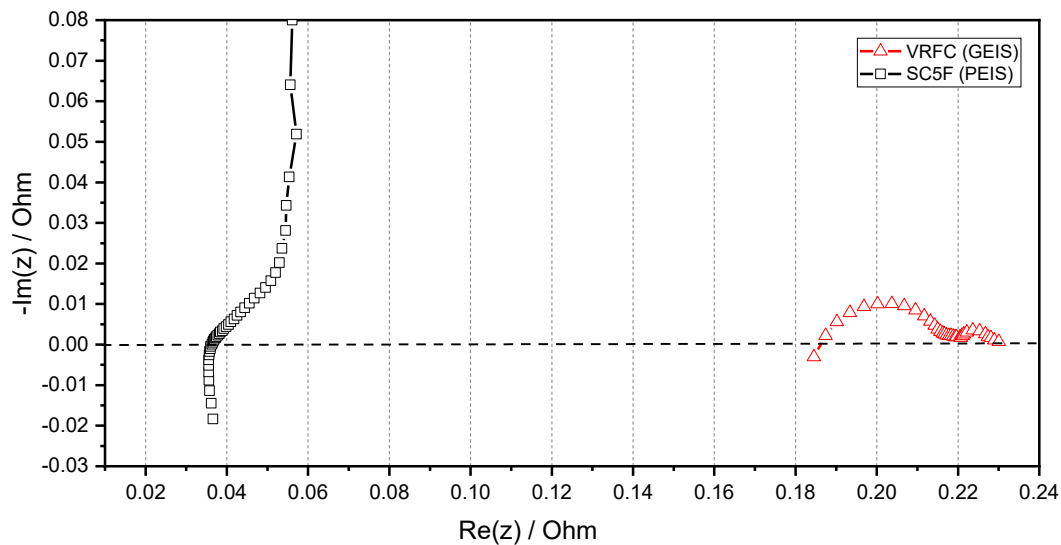


Figure 5.6 Comparison of the Nyquist plots of the SC5F (PEIS) and VRFC (GEIS)

As an example, Figure 5.6 compares the Nyquist plot for the SC5F (black line) and for the VRFC (red line) after the activation cycles. In the case of 5F-SC, EIS was performed by potentiostatic EIS in the 10 kHz – 10 mHz frequency range with $V_a = 5$ mV, while the EIS for the VRFC was performed in galvanostatic mode between 10 kHz – 10 mHz frequency range with $I_a = 50$ mA. The Figure 5.6 highlights the lowest impedance of the SC5F with respect to the VRFC. The nominal SC capacitance C and ESR were used to calculate the time constants (τ) by:

$$\tau = C \times ESR \quad (5.4)$$

The τ values range from 0.2 s for 1F-SC to 1.1 s for 100 F-SC. The energy (E_{max} , in mWh) and Pulse Power (P_{max}) values reported in Table 5.3 are the maximum values that are calculated by Equation (5.5) and (5.6), respectively:

$$E_{MAX} (mWh) = \frac{1}{2} \cdot C \cdot V_{MAX}^2 \cdot \frac{1000}{3600} \quad (5.5)$$

$$P_{MAX} (W) = \frac{1}{4} \cdot V^2 \cdot \frac{1}{ESR} \quad (5.6)$$

Where V_{MAX} is the maximum cut-off voltage (2.7 V), C the nominal capacitance and ESR the equivalent series resistance.

The nominal maximum charge voltage of the adopted commercial SCs (2.7 V) is much higher than what can be reached when the SC is charged by the VRFC under a direct, parallel connection. In this case, and considering negligible any loss related to leakage currents and self-discharge, the SC should reach c.a. 1.5 V as maximum value.

In order to simulate the SC behavior during the parallel connection with an VRFC we tested the SCs according to the following protocol: galvanostatic charge at 1.45 V (chosen because it is comparable with the open-circuit voltage, OCV, featured by the tested VRFC) followed by a potential step at 1.45 held for 20 s and the subsequent galvanostatic discharge with cell cut-off voltage of 0.8 V and cut-off discharge time of 5 s. The discharge was interrupted when one of the two cut-offs was reached. The charge and discharge steps were run at the same currents that varied from 400 mA up to 10 A (like for the VRFC tests reported in the previous section). The test was performed with a VSP multichannel potentiostats/galvanostats (Bio-Logic Science Instruments) at room temperature. All data were analyzed using Bio-Logic program EC-Lab 10.23.

As an example, Figure 5.7 shows the voltage profile of the SC34F under these tests. From the figure, it is possible to appreciate that the voltage decreases linearly in time, indicating that the discharge is driven only by an electrical double layer process and that these devices behave like an ideal capacitor

in series with a negligible resistance (ESR). At the highest current of 6 A, the SC34F reaches the 0.8 V cut-off voltage after 2.68 s delivering 4.8 mWh of energy at a maximum power of 8.2 W.

Table 5.3 reports the SC34F capacitance, discharge time (Δt) and final discharge voltage and the practical energy (E) and power (P) evaluated by the analysis of the discharge curves. Capacitance, energy and power were evaluated by the following Equations:

$$C = \frac{I_{discharge}}{\Delta V / \Delta t} \quad (5.7)$$

$$E = I_{discharge} \cdot \int_0^t \frac{V}{3600} \cdot dt \quad (5.8)$$

$$P = E / \Delta t \cdot 3.6 \quad (5.9)$$

As expected, the lower V_{max} affects (slightly decrease) the nominal value of C, E and P.

Table 5.3 SC34F capacitance, discharge time (Δt) and final discharge voltage and the practical energy (E) and power (P) evaluated by the analysis of the discharge curves

Current (A)	Capacitance (F)	Discharge time (s)	Final Discharge voltage (V)	Practical Energy (mWh)	Practical Power (W)
0.4	29.47	5	1.37	0.78	0.56
0.6	29.46	5	1.33	1.16	0.83
0.8	29.35	5	1.30	1.52	1.09
1	29.27	5	1.26	1.87	1.34
2	28.89	5	1.07	3.46	2.49
4	28.29	4.21	0.8	5.13	4.38
6	28.13	2.68	0.8	4.80	6.45

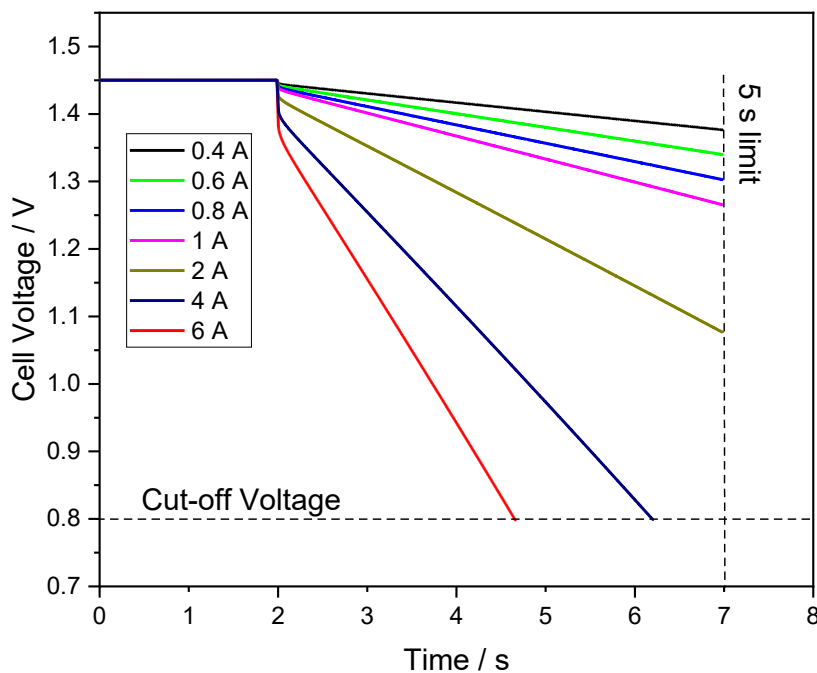


Figure 5.7 Voltage profile of SC34F under pulsed discharge curves of 5 s at different currents

5.3 Combining high power VRFC with Supercapacitors

Tests similar to SC's reported in the previous section, were run for the VRFC-SC system, where the supercapacitors were connected in parallel with the vanadium cell. Four different systems were tested: VRFC-SC5F, VRFC-SC9F, VRFC-SC34F, VRFC-SC100F. The connection in parallel between the VRFC and the SC was made through two wiring with alligator clip heads, as shown in Figure 5.8. The wiring has a negligible ohmic resistance. The VSP instrument was then connected to the SC. The protocol adopted for the testing was studied to simulate discharge peak loading without charging the SC. Therefore, the first step provides the VRFC a full charge with 600 mA, up to the cut-off charging voltage that is set at 1.65V which is held for 5 minutes. The VRFC-SC system is then left in open circuit and the



Figure 5.8 Setup for the system VRFC-SC

corresponding system open circuit voltage (OCV) is measured; this is defined as rest condition. The highest voltage featured by the cell in rest is named OCV_{max} . Finally, galvanostatic discharge (GCPL) at a defined current (I_{pulse}) with time and discharge voltage cut-offs of 5 s and 0.8 V is performed. The 5 seconds discharge time was decided considering SC time constants defined in Table 5.2 . The data acquisition for the discharge curve occurs every 0.1 mV or at intervals of 0.002 s. As soon as the discharge currents start to flow into the system, the voltage is subjected to a vertical drop due to the ohmic resistance of the systems (mainly related to electronic and ionic resistances of electrodes and electrolyte), ΔV_{ohmic} . Knowing the ohmic drop, it is possible to calculate the equivalent series resistance (ESR) of the VRFB-SC system according to Equation 5.10:

$$ESR = \frac{\Delta V_{ohmic}}{I_{pulse}} \quad (5.10)$$

After the ohmic drop of ΔV_{ohmic} , that starts from the OCV_{max} , the voltage keeps decreasing with different slopes according to the applied current density. The slope (Δs) is defined as the variation

of voltage over time (dV/dt). The capacitance of the system (C_{sys}) can be calculated according to Equation 5.11:

$$Capacitance = \frac{I_{pulse}}{\Delta s} \quad (5.11)$$

The results of the discharge curves for the four different VRFC-SC systems are showed in Figure 5.9. The experimentation allows extracting important data such as ohmic drop (ΔV_{ohmic}), capacitance, specific energy and power of the VRFB-SC system. Energy and power are also important parameters to be measured. The energy of the pulse (E_{pulse}) is calculated from the GCPL discharge curves according to Equation 5.12. Results of the discharged curves are reported in Table 5.4 .

$$E_{pulse} = I_{pulse} \cdot \int_0^t \frac{V}{3600} \cdot dt \quad (5.12)$$

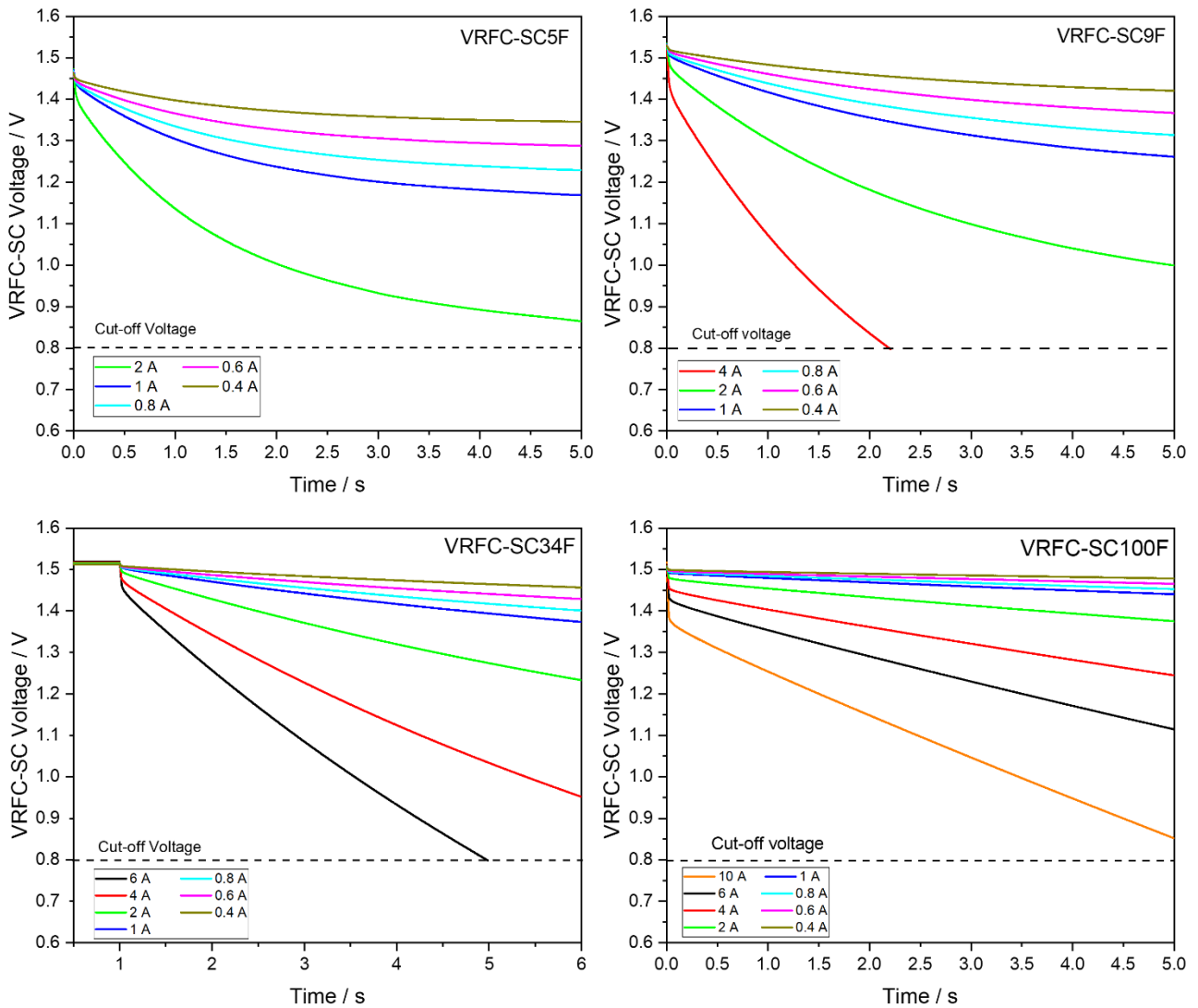


Figure 5.9 Discharge profile of the 4 different VRFC-SC for different discharging currents

Table 5.4 ΔV_{ohmic} , Capacity of the systems and energy delivered for every current applied to every different system combination of VRFC-SC

Disch. Current (A)	VRFC ΔV_{ohmic}	VRFC mAh	VRFC mWh	VRFC+ SC5F ΔV_{ohmic}	VRFC+ SC5F mAh	VRFC+ SC5F mWh	VRFC+ SC9F ΔV_{ohmic}	VRFC+ SC9F mAh	VRFC+ SC9F mWh	VRFC+ SC34F ΔV_{ohmic}	VRFC+ SC34F mAh	VRFC+ SC34F mWh	VRFC+ SC100F ΔV_{ohmic}	VRFC+ SC100F mAh	VRFC+ SC100F mWh
10 A	---	---	---	---	---	---	---	---	---	---	---	---	130	13.98	15.35
6A	1.3 V (lim)	---	---	---	---	---	---	---	---	58	6.66	7.3	80	8.39	10.57
4 A	0.9 V (lim)	---	---	---	---	---	93	2.47	2.61	37	5.59	6.61	53	5.60	7.51
2 A	500	2.8	2.71	56	2.77	2.80	46	2.79	3.26	18	2.8	3.77	26	2.79	3.98
1 A	250	1.4	1.72	30	1.38	1.72	23	1.4	1.88	9	1.4	2	13	1.4	2.05
800 mA	200	1.12	1.44	23	1.10	1.45	18	1.12	1.54	7	1.11	1.62	10	1.12	1.64
600 mA	150	0.8	1.12	17	0.83	1.10	14	0.84	1.19	5	0.84	1.22	8	0.83	1.24
400 mA	100	0.56	0.78	11	0.55	0.76	9	0.56	0.81	3	0.56	0.82	5	0.55	0.83

The three different scenarios that can occur when connecting in parallel the VRFC with SCs are shown in Figure 5.10: in the upper section of the figure the scheme of the connection is shown, while at the bottom the corresponding voltage cell behavior are plotted with time for the SC34F and VRFC-SC34F.

In the VRFC-SC system, the current generated by the VRFC charges the external SC up to a voltage that corresponds to the highest voltage of the VRFB exhibited in open circuit (OCV_{max}). This process happens all the time because the SC have an ESR (11-40 m Ω) much lower than that of the VRFC (250 m Ω), and therefore, when the system is in open circuit or when it is working, the SC is charged by the VRFC with the corresponding current I_{VRFC} . The comparison of the ESR can be seen in Figure 5.6. This occurs only in absence of leakage currents. The time required to charge the SC when the system is in OCV, is related to the ESR of the SC and its time constant, τ (see Table 5.2). This case is represented in Figure 5.10a. The SC can then deliver the stored charge while being disconnected to the VRFB, like shown in Figure 5.10b. In alternative, like in the test reported in this section, the SC can undergo discharge at a current I_{pulse} while being connected to the VRFB, like it is represented in Figure 5.10c.

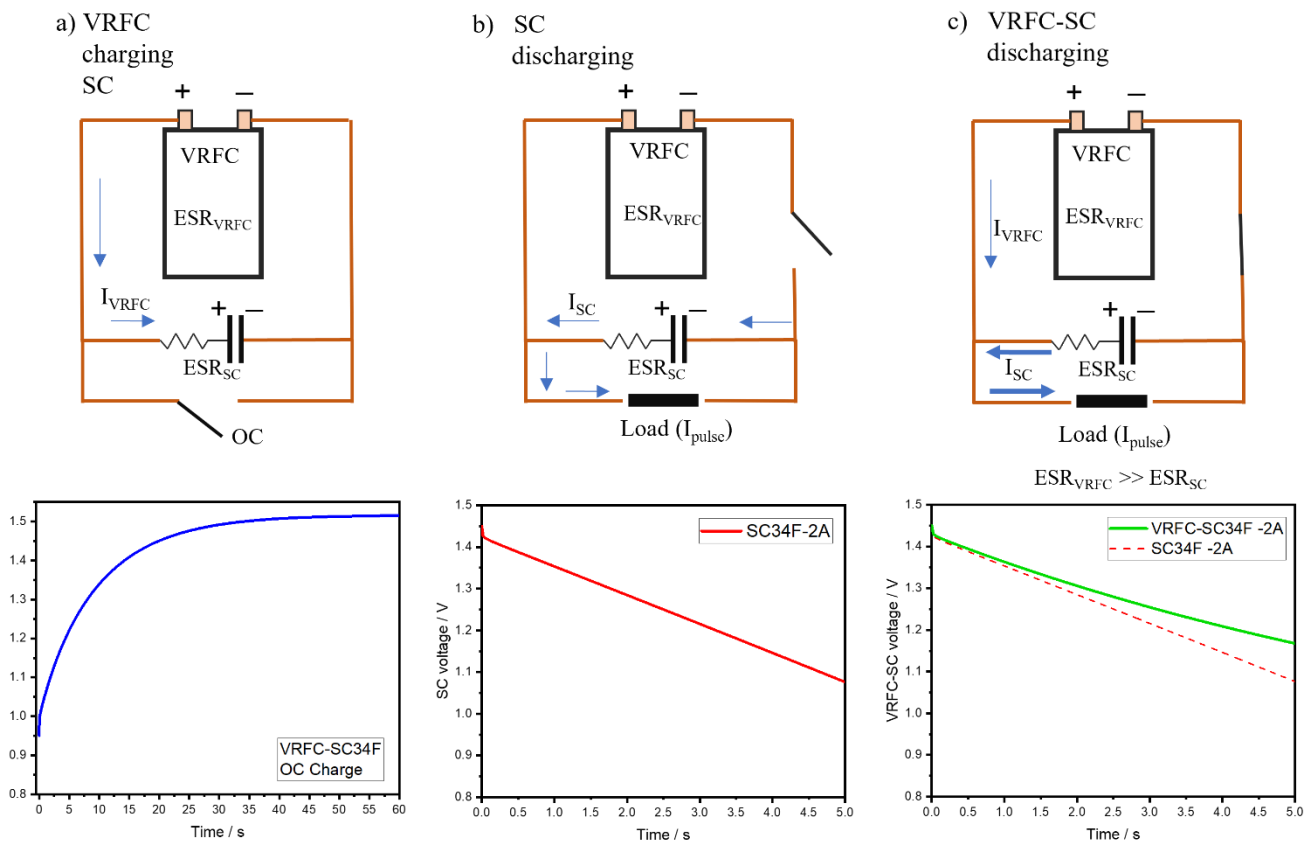


Figure 5.10 Scheme of equivalent circuits describing the parallel connections of the VRFC with the SCs. Below the real response with the VRFC and the SC34F are represented to better underline the behavior.

Concerning the SC branch, I_{SC} flows in the opposite direction than the charging I_{VRFB} current. When the SC is disconnected from the VRFB (Figure 5.10b), during the galvanostatic discharge at current $I_{SC}=I_{pulse}$, the discharge profile will linearly decrease over time following the characteristic behavior of a conventional SC. In this case, the delivered charge (Q) is calculated according to Equation 5.13 and the capacitance is therefore calculated according to Equation 5.14

$$Q = I_{SC} \cdot dt \quad (5.13)$$

$$C_{SC} = \frac{Q}{\Delta V_{SC}} = \frac{I_{SC} \times t}{\Delta V_{SC}} \quad (5.14)$$

When the SC is discharged while being connected with the VRFC, the discharge behavior will be different. This is because the SC will deliver energy at the designated current I_{SC} while being virtually recharged by the VRFC at I_{VRFC} . The total charge delivered by the VRFB-SC when being connected is calculated in Equation 5.15.

$$Q = (I_{SC} + I_{VRFC}) \cdot dt \quad (5.15)$$

In this case, the integrated system features an apparent capacitance C_{APP} which is higher than the capacitance exhibited by the SC alone, as shown in Equation 5.16

$$C_{SC} = \frac{dQ}{dV} = (I_{SC} + I_{VRFC}) \times \frac{dt}{dV} \quad (5.16)$$

This phenomenon can be clearly seen in the discharge curve shown in Figure 5.10c that highlights the difference between the conventional SC discharge and the VRFC-SC34F discharge profile. As an example, in Figure 5.11 the three different discharge curves are compared for two different discharge currents. More specifically, the curves shown are VRFC-SC34F (dashed line), SC34F (solid thick line) and VRFC (solid thin line) with discharge currents of 0.8 A (blue lines) and 2 A (red lines). From the comparison of the three different discharge curves we can notice that the connection in parallel of the SC to the VRFC also dramatically reduces the ΔV_{ohmic} ohmic drop allowing the system to discharge smoothly allowing the functioning even at high discharge currents. The VRFC alone showed 250 m Ω of ESR that is reduced in the range of 30 to 9 m Ω which correspond to a minimum reduction by 88% of the ohmic drop. Being lower the ohmic drop and higher the cell voltage, also the energy yield (mWh) in the initial part of the discharge increases with the scaling up of the capacitance of the SC connected. For example, for a discharge current of 2 A, if connected with SC5F the energy yield increases by 3%, with SC9F increases by 20%, with SC34F increases by 39% and with SC100F increases by 46%, from 2.71 mWh to 3.98 mWh. We can confirm this data from Table 5.4.

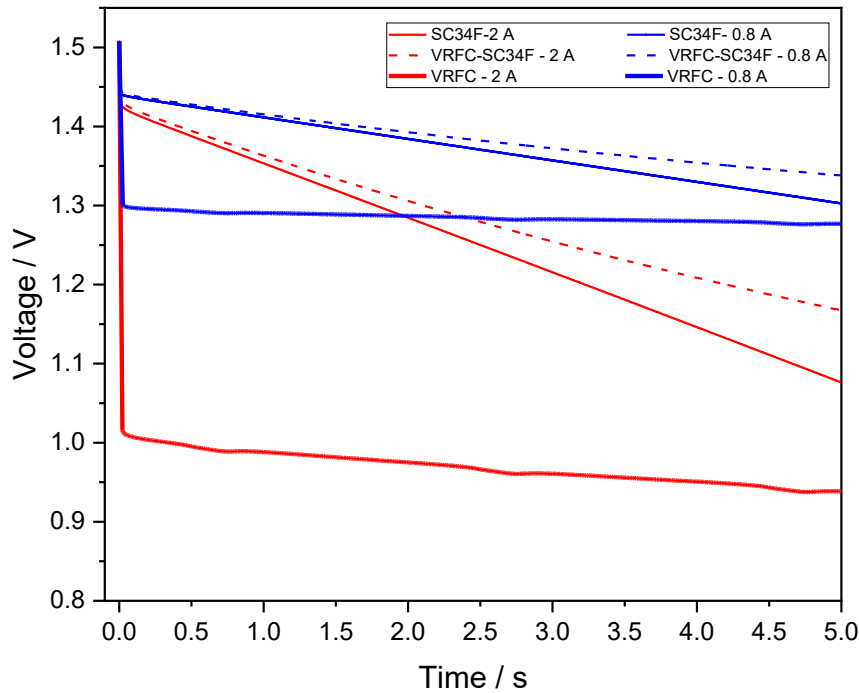


Figure 5.11 Comparison of discharge curves for VRFC-SC34F (dashed line), SC34F (solid thick line) and VRFC (solid thin line) with discharge currents of 0.8 A (blue lines) and 2 A (red lines)

5.4 Chapter 5 Conclusion

EESS can be grouped also into “power devices” and “energy devices”. The combination of these two different classes of devices could be a leap forward into the spread adoption of “battery systems”. Projects on the hybridization of battery devices are already ongoing, like the HyFlow project. This explorative part of my work was, in fact, conducted under the HyFlow project. The aim of the project is to hybridize a high power vanadium redox flow battery with the use of supercapacitors to enhance the power response of the whole system. Vanadium redox flow battery will be therefore connected to the supercapacitive device by a bidirectional converter. However, the use of the converter reduces the overall efficiency, being a power device that dissipate energy, and increases the final cost of the system.

In this chapter I showed the results of connecting directly in parallel a vanadium redox flow cell (VRFC) with supercapacitors, therefore eliminating the use of the bidirectional converter. At first, I studied the vanadium redox flow cell, that was provided by a partner of the project, in all the detail and electrical response to different pulsed discharge currents. I started with the activation of the VRFC and performed 20 cycles in order to run the cell stable. Through the discharge curves I was

able to calculate the equivalent series resistance of the cell (ESR_{VRFC}), the capacity and the energy delivered in a 5 second discharge. The open circuit voltage (OCV) of the VRFC resulted to be c.a. 1.5 V and the ESR_{VRFC} about 250 m Ω . I was not able to perform discharging cycles with current above 2 A because the voltage of the cell suddenly reached the lowest cut-off voltage of 0.8V.

In the second part, I tested the performances of four different commercial supercapacitors (SC), namely a 5 F, 9 F, 34 F and 100 F. As for the vanadium redox flow cell, I performed 5 second discharge at increasing current, from 400 mA up to 10 A for the 100 F supercapacitor. The 5 seconds discharge time was chosen according to the time constants τ of the supercapacitors. The ESR of the capacitors (ESR_{SC}) are ranging from 40 m Ω for the 5 F SC to 11 m Ω for the 100 F SC. The ESR_{VRFC} resulted to be one order of magnitude higher than that of all the SCs.

In the third section I performed the same protocol of 5 second discharge on the VRFC connected directly in parallel with the SCs. The connection reduced dramatically the ohmic drop that was previously on the VRFC alone, and also enhanced the performance of the SC. Since the ESR_{SC} is much lower than ESR_{VRFC} , the SC is always charged by the VRFC, even when the system VRFC-SC is being discharged: this behavior of the system modified the expected discharge curve of the SC and showed what I termed an “apparent capacitance”.

Overall, the connection of the VRFC with the SC made it possible to reduce the ohmic drop of the VRFC extending its range of use to currents higher than 2 A, up to 10 A with the connection to the 100 F SC, increasing the energy delivered by 46%. The system also highlighted that the discharge curve of the SC was modified by the simultaneous charging of the SC by the VRFC while the system is discharging and put in evidence the so-called “*Apparent Capacitance*”. These are preliminary studies, and following the successful results, I will further investigate the direct connection of vanadium redox flow batteries made of multiple cells in series with SC to verify the possibility of scaling up this technique. I believe that this approach can contribute to increase the adoption of VRFB system opening the possibility to install even in private households by reducing the price and expanding the operational potentiality with a more innovative cell integrated with supercapacitors.

In addition, I am planning to demonstrate a hybrid system where commercial supercapacitors are substituted by greener cells, by following the approaches presented in Chapter 4. To this aim, modeling of the hybrid connection will be extremely important to accelerate the research activity, by identifying the proper size of the VRFB and SC to be connected to power specific applications.

Reference Chapter 5

- [1] Minke, C.; Kunz, U.; Turek, T. “Techno-economic assessment of novel vanadium redox flow batteries with large-area cells” *Journal of Power Sources*, 2017, 361, 105-114, <https://doi.org/10.1016/j.jpowsour.2017.06.066>.
- [2] Yusof, N.; Ismail, A.F. “Post spinning and pyrolysis processes of polyacrylonitrile (PAN)-based carbon fiber and activated carbon fiber: A review” *Journal of Analytical and Applied Pyrolysis*, Volume 93, 2012, Pages 1-13, <https://doi.org/10.1016/j.jaap.2011.10.001>
- [3] Sankaralingam, R. K.; Seshadri, S.; Sunarso, J.; Bhatt, A. I.; Kapoor, A. “Overview of the factors affecting the performance of vanadium redox flow batteries” *Journal of Energy Storage*, 2021, 41, 102857, <https://doi.org/10.1016/j.est.2021.102857> .
- [4] Daugherty, M. C.; Hsieh, C.-T.; Aaron, D. S.; Ashraf Gandomi, Y.; Li, J.; Zheng, Y.; Pflieger, W. “Enabling high rate capability, low internal resistance, and excellent cyclability for vanadium redox flow batteries utilizing ultrafast laser-structured graphite felt” *Electrochimica Acta*, 2020, 344, 136171, <https://doi.org/10.1016/j.electacta.2020.136171>.
- [5] Bourke, A.; Miller, M.A.; Lynch, R.P.; Gao, X.; Landon, J.; Wainright, J.S.; Savinell, R.F.; Buckley, D.N. “Electrode Kinetics of Vanadium Flow Batteries: Contrasting Responses of V^{II} - V^{III} and V^{IV} - V^V to Electrochemical Pretreatment of Carbon” *Journal of the Electrochemical Society* 163 (2016) A5097-A5105.
- [6] Lim, H.; Yi, J. S.; Lee, D. “Correlations of Through-Plane Cell Voltage Losses, Imbalance of Electrolytes, and Energy Storage Efficiency of a Vanadium Redox Flow Battery” *ChemSusChem* 2019, 12, 1459-1468 , <https://doi.org/10.1002/cssc.201802633>
- [7] Roznyatovskaya, N.V.; Fühl, M., Roznyatovsky; V.A., Noack, J.; Fischer, P.; Pinkwart, K.; Tübke, J. “The Influence of Free Acid in Vanadium Redox-Flow Battery Electrolyte on “Power Drop” Effect and Thermally Induced Degradation” *Energy Technology*, 2020 8: 2000445. <https://doi.org/10.1002/ente.202000445>
- [8] Bhattarai, A.; Whitehead, A. H.; Schweiss, R.; Scherer, G. G.; Skyllas-Kazacos, M.; Wai, N.; Nguyen, T. D.; Ghimire, P. C.; Ohnmar Oo, M.; Hoon Hng, H. “Anomalous Behavior of Anion Exchange Membrane during Operation of a Vanadium Redox Flow Battery” *ACS Applied Energy Materials* 2019 2 (3), 1712-1719, <https://doi.org/10.1021/acsaem.8b01816>

Chapter 6: Conclusion

The biggest challenge of our century will be the dramatical reduction of CO₂ emission into the atmosphere as to slow down the effects of the climate change. The continuous growth of the global population both in number and pro-capita energy consumption, especially in developing economies such as India or Brazil will significantly impact the success of global mitigation effort of all the other countries. The resulting growth demand for energy in form of electricity will increase the load on world global energy grid and related infrastructures. Cleaner energy production systems are those that take advantage of renewable energy sources, but they have low efficiency and the widespread use of energy production systems like photovoltaic and wind power will further load the electrical grid. The solution is in the massive adoption of electrochemical energy storage systems (EESS), that can store energy in the form of electricity, guaranteeing high efficiency and reducing at the minimum energy losses. At this outcome, also EESS must have a low environmental impact. For this reason, my Ph.D studies, have been focused on studying strategies to lower the environmental impact of EESS, in particular Lithium-ion batteries (Li-ion), supercapacitors (SC), and innovative redox flow battery (RFBs). In addition, I conducted a preliminary study on combining SC and RFBs in a hybrid system.

Lithium-ion batteries are the most diffused battery technology and therefore they must be manufactured in the view of recycling. An effective way to accomplish this goal is to use water processable binder, instead of the commonly used poly(vinylidene difluoride) (PVdF), that simultaneously reduces the manufacturing energy costs and environmental impact facilitating the recycling at the end of life of the cell. In the first part of my work, I used Pullulan (PU), a bio-derived polymer, as a water processable binder to produce a high potential cathode with Li(Ni_{0.5}Mn_{0.3}Co_{0.2})O₂ (NMC532) active powder. The cathode went through a manufacturing process based on water and exhibited excellent cycling stability for over 500 cycles and delivering up to 115 mAh g_{NMC}⁻¹. The electrode powder was then recovered using a water spray and the washing waste-water made of pullulan and glycerol resulted to be 100% biodegradable in just 15 days under anaerobic conditions. After using PU, I exploited PEDOT:PSS, a well known conductive polymer, as a water processable binder. PEDOT:PSS, PU and PVdF-based electrodes were manufactured and compared. The voltammetric and galvanostatic tests underline that PU-based electrodes can perform like the conventional PVdF-based electrodes, while PEDOT:PSS significantly improve the performances. The first outcome of my work is that the well know polymers like PU and PEDOT:PSS can be used in the LIBs manufacturing industry as water processable binders. This manufacturing process will not only reduce the environmental impact of Li-ion cell production but can also reduce the

manufacturing cost avoiding the use of toxic solvents, that needed tailored controlled environments and recycling facilities, in favor of water.

After proving PU and PEDOT:PSS as water processable polymers to be a feasible alternative to F-based binder, I focused on a binder-free class of battery, namely redox-flow battery (RFBs). RFBs have liquid electrodes and the important characteristic to decouple energy and power. Thanks also to their manufacturing processes, they represent a cost-effective alternative to LIBs for stationary storage. Nowadays RFBs are being exploited also with the use of conventional Li-ion material dispersed in a liquid solvent through the use of semi-solid electrodes. In Chapter three, I investigate the influence of superconcentrated electrolytes for Li-ion RFB. My work demonstrated that the electrical percolating network made by carbonaceous suspension is more efficient when the superconcentrated electrolyte is used. Indeed, I was able to reduce the internal resistance of the semisolid electrodes by a 50% with respect to conventional electrolytes demonstrating an added advantage of superconcentrated electrolytes, besides their recognized wide electrochemical stability.

EESS not only relies on the faradaic processes of conventional batteries, but also supercapacitors have a great importance in the energy transition. In the fourth Chapter, I focus on the manufacturing process of “green supercapacitors”. After demonstrating the effectiveness of PU as a water processable binder for high voltage Li-ion batteries, I proved the exploitation of the same material in Electrical Double Layer Capacitors (EDLCs), both as binder and as separator. PU was used first to manufacture an electrospun separator and it was compared with a conventional cellulose triacetate (CTA) electrospun membrane. The compatibility of the separator with the electrolyte is of fundamental importance, and in order to manufacture a more safe and recyclable device, I used ionic liquids (IL). Therefore, the two separators were tested in three different ILs electrolytes and experimentation concluded that EmimTFSI IL with Pu mat exhibited the best performance and the lower resistance. Afterwards, I manufactured EDLC that showed a specific energy of 19.6 Wh kg^{-1} and 7.2 Wh kg^{-1} at 0.5 A g^{-1} that well compared with those of EDLCs featuring the same electrolyte and active carbon but employing a fluorinated binder and fiber glass separator. In conclusion, because PU dissolves in water, IL it is not mixable with water and I was able to filter the carbon powder and physically separate the EDLC components. With this approach I was able to build, test and evaluate a fully recyclable EDLC.

In the last part of my work, I focused on hybrid EESS, more precisely on the integration of RFB with SC. Hybrid systems can benefit from the best features of the two building blocks, namely the RFB and the SC. The study was conducted under the European project HyFlow. Here, preliminary investigated the direct parallel connection of SC of different capacitance (5 F, 9 F, 34 F and 100 F)

with vanadium redox flow cell (VRFC). The hybrid system was discharged with increasing pulsed currents, from 0.4 A to 10 A, for 5 seconds, and the resulting curves were compared with the ones of SC and VRFC alone. The main result was a noticeable reduction of the ohmic drop of the hybrid system and the parallel increase by 46% of the energy delivered under pulse discharges. In addition, the discharge curve of the SC was modified by the simultaneous charging of the SC by the VRFC. Indeed, the analyses of the discharge curves evidenced what I termed an “*Apparent Capacitance*” increase. This study represents a first proof-of- concept, that will be further investigated by proposing a tailored model to understand the effect of the SC connection to the VRFN and by the substitution of the commercial SC with green SC from Chapter 4.

Overall, these results highlight that it is possible to effectively reduce the carbon footprint of EESS with the use of bio-derived materials, like PU for the production of Li-ion batteries and SC, or by smart design of battery systems, like semi-solid electrodes or hybrid systems. These approaches can reduce the environmental impact of both the materials used as components and of the manufacturing processes, making the production of a cell less “polluting”. In addition, this aim can be pursued without affecting the performances of commercial devices based on the current technologies, which is of fundamental importance to accelerate the energy transition to a more sustainable society. With my Ph.D. thesis I aimed at proving that all the “ingredients” for a real green energy transition are available. Now, it is the responsibility of the manufacturing companies to put in place all the activity and resources to lower the environmental impact and emission related to EESS.

Acknowledgments

First of all, I would like to thank my supervisor Professor Francesca Soavi, for her support all along this learning experience, both as a person and as a scientist, for her patience and determination on always giving me the best suggestions. I would like to thank Professor Maria Letizia Focarete and Professor Chiara Gualandi, along with their research group, for the support in many aspects of my research: for their exceptional work in electrospinning of natural polymer, for the help in testing mechanical properties of electrodes and for their experience with viscous media. Heartfelt thanks also to Professor Marco Giorgetti and his group for their material characterization, Prof. Damiano Genovese for his contribution and help on microscopy analyses and Prof. Dr. Karl-Heinz Pettinger for welcoming me into his research group and giving me the chance to work with RFBs. Finally, I would like to thank all the people that helped me in this three-year journey, those who spent even little time teaching me something new and those who listened to me, and most of all my colleagues, that are also my friends.

I am grateful for all the experience had, and also the failures that I had to face, because they are both part of my growth, and are necessary. I will keep failing hard and studying harder.

I would also like to acknowledge the following international and national project for the financial support:

1. Italy-South Africa joint Research Programme 2018-2020 (Italian Ministers of Foreign Affairs and of the Environment and NRF of South Africa, grant No. 113132)
2. Fondazione CARISBO (Progetto Bando Ricerca n° 354)
3. Piano Triennale di Realizzazione 2019-2021, Accordo di Programma Ministero dello Sviluppo Economico” ENEA
4. HyFlow H2020-LC-BAT-9-2020 HyFlow-Development of a sustainable hybrid storage system based on high power vanadium redox flow battery and supercapacitor technology (ID 963550, <https://cordis.europa.eu/project/id/963550/it>)

7 Project, publication and contribution

7.1 National and International Projects

During my Ph.D. I've been working under the following national and international projects:

[1] Italy-South Africa joint Research Programme 2018-2020 (Italian Ministers of Foreign Affairs and of the Environment and NRF of South Africa, grant No. 113132)

[2] Fondazione CARISBO (Progetto Bando Ricerca n° 354)

[3] Piano Triennale di Realizzazione 2019-2021, Accordo di Programma Ministero dello Sviluppo Economico” ENEA

[4] HyFlow H2020-LC-BAT-9-2020 HyFlow-Development of a sustainable hybrid storage system based on high power vanadium redox flow battery and supercapacitor technology (ID 963550, <https://cordis.europa.eu/project/id/963550/it>)

7.2 List of Publication

[1] Spina, G.E.; Poli, F.; Brilloni, A.; Marchese, D.; Soavi, F. *Natural Polymers for Green Supercapacitors*. *Energies* 2020, *13*, 3115. <https://doi.org/10.3390/en13123115>

[2] A. Brilloni, F. Poli, G. E. Spina, D. Genovese, G. Pagnotta, and F. Soavi; *Improving the Electrical Percolating Network of Carbonaceous Slurries by Superconcentrated Electrolytes: An Electrochemical Impedance Spectroscopy Study*; ACS Applied Materials & Interfaces

[3] Mutuma, B.K., Sylla, N.F., Bubu, A., Ndiaye, N.M., Santoro, C., Brilloni, A., Poli, F., Manyala, N., Soavi, F., “Valorization of biodigestor plant waste in electrodes for supercapacitors and microbial fuel cell”, (2021) *Electrochimica Acta*, 391, art. no. 138960. <https://doi.org/10.1016/j.electacta.2021.138960>

[4] A. Brilloni, F. Poli, G. E. Spina, C. Samori, E. Guidi, C. Gualandi, M. Maisuradze, M. Giorgetti, F. Soavi, *Easy recovery of Li-ion cathode powders by the use of water-processable binders*, *Electrochimica Acta*, Volume 418, 2022, 140376

[5] Brilloni, A.; Marchesini, F.; Poli, F.; Petri, E.; Soavi, F. Performance Comparison of LMNO Cathodes Produced with Pullulan or PEDOT:PSS Water-Processable Binders. *Energies* **2022**, *15*, 2608. <https://doi.org/10.3390/en15072608>

[6] F. Soavi, A. Brilloni, F. De Giorgio, F. Poli, *Semi-solid lithium/oxygen flow battery: an emerging, high-energy technology*, *Current Opinion in Chemical Engineering*, Volume 37, 2022, 100835.

7.3 List of Contribution to Conferences: posters and oral presentations

Oral Presentation

- 1 F. Poli, A. Brilloni, F. De Giorgio, F. Soavi, “Design of Novel Redox Flow Batteries”, 69th Annual meeting of the International Society of Electrochemistry, Oral Presentation 2-7/09/18, Bologna (Italy).
- 2 A. Brilloni, F. Poli, F. De Giorgio, F. Soavi, “Next-Generation Lithium Batteries: Challenges in High-Energy Semi-Solid Lithium/Oxygen Flow Batteries”, Metal advanced Batteries International Congress November 6-7,2019, Pamplona
- 3 F. Soavi, A. Brilloni, F. Poli, D. Marchese, G. E. Spina, “Water processable polymers for supercapacitors and Li-ion batteries” Nano Innovation Conference and Exhibition, 15-18 Sept 2020, Rome
- 4 Alessandro Brilloni, Federico Poli, Giovanni Emanuele Spina, Francesca Soavi, “Super-concentrated electrolytes based slurries for advanced flow batteries”, Flow Camp for Next generation – flow battery conference and networking event, Thursday, 11th march, 2021 – online

- 5 Alessandro Brilloni, Federico Poli, Francesca De Giorgio, Francesca Soavi, “New High-Energy Semi-Solid Lithium/Oxygen Flow Battery: from research to spinoff company”, 72th Annual meeting of the International Society of Electrochemistry, 29/08/21 - 3/09/21, Jeju, Korea
- 6 Alessandro Brilloni, Federico Poli, Michele Rizzotti, Francesco Marchesini, Francesca Soavi, “Green design of lithium metal battery” , Nano Innovation Conference and Exhibition 2021, 21-24/09/2021, Rome, Italy

Poster contribution

- 7 F. De Giorgio, L. Morici, F. Poli, A. Brilloni, Francesca Soavi, “Study of Semi-Solid Li-Ion Anolytes”, 69th Annual meeting of the International Society of Electrochemistry, Poster, 2-7/09/18, Bologna (Italy).
- 8 A. Brilloni, N. Mancuso, F. De Giorgio, F. Poli, A. Ceruti, F. Soavi, “Using Batteries to supply Unmanned Aerial Vehicles (UAV): a tradeoff analysis”, 69th Annual meeting of the International Society of Electrochemistry, 2-7/09/18, Bologna (Italy), Participation with poster contribution.
- 9 F. Soavi, F. De Giorgio, J. Seri, A. Terella, F. Poli, A. Brilloni, D. Fabiani, M. L. Focarete, C. Santato, “Bio-Inspired Components of Supercapacitors”, 69th Annual meeting of the International Society of Electrochemistry, 2-7/09/18, Bologna (Italy).
- 10 Alessandro Brilloni, Giovanni Emanuele Spina, Michele Rizzotti, Francesco Marchesini, Giovanni Battista Appetecchi, Francesca Soavi, “Cycling stability of Li-metal anodes in new ionic liquids solutions”, 72th Annual meeting of the International Society of Electrochemistry, 29/08/21 - 3/09/21, Jeju, Korea, Poster contribution
- 11 Alessandro Brilloni, Elisabetta Petri, Federico Poli, Francesca Soavi, “Application of WISE Electrolytes for all aqueous low environmental impact supercapacitors” International Symposium on Enhanced Electrochemical Capacitors , 7th Annual edition , 11st-15th July 2022, Bologna, Italy
- 12 Alessandro Brilloni, Giovanni Emanuele Spina, Federico Poli, Michele Rizzotti, Francesco Marchesini, Giovanni Battista Appetecchi, Francesca Soavi, “Novel methods for increasing energy and reducing environmental impact of lithium batteries” , XXVII Congresso nazionale della società chimica italiana, 14-23/09/2021 , online

Thesis co-supervision

1. *Studio di liquidi ionici per batterie al litio metallico*, Michele Rizzotti, MSc. in “Ingegneria Energetica” Anno Accademico 2020/2021 Sessione I
2. *Water processable polymers for high voltage cathodes in next generation lithium batteries*, Francesco Marchesini, MSc. in “Ingegneria Energetica” Anno Accademico 2020/2021 Sessione I
3. *Batterie redox a flusso al vanadio con elettrodi semi-solidi*, Andrei Timofte, Laurea triennale in Chimica e Chimica dei Materiali del Dipartimento di Chimica “Giacomo Ciamician”, Anno Accademico 2020/2021 Sessione II